Technical University of Delft

MSc. Thesis

Three Dimensional Plasmonic Back Reflector for Solar Cells

Brian Carlsen
Student Nr. 4512677

supervised by
Ir. Olindo Isabella
Dr. Rudi Santbergen
Nasim Rezaei

EEMCS Faculty
Department of Electrical Engineering
Electrical Sustainable Energy
Photovoltaic Materials and Devices Group

October 20, 2017

Abstract

Two dimensional plasmonic back reflectors have shown the ability to match the scattering performance of standard back reflectors. However, three dimensional plasmonic structures have not yet been thoroughly investigated. Here, the scattering properties of a 3D plasmonic structure are approached at three levels of system. First, the scattering properties of different types of particles are investigated. An optimum particle size is found for both spherical and cylindrical silver particles. The interaction of two particles is then studied. By comparing numerical and analytic results, the strength of different effects is explored. It is found that dipole-dipole interactions can not be ignored within the structure. Finally, the effect of the lattice structure on the scattering properties is probed. A new lattice summation method is developed, revealing that only particles near the point of interest must be considered. Several 3D devices were fabricated to investigate the properties of self forming metal island films. It was found that the surface morphology of layers deposited on top of these films, do not depend on the properties of the film.

Thank you to my mother, father, and grandparents
for supporting me during these studies.

Contents

Chapter 1

Introduction

1.1 Why Plasmonics?

As the world turns to renewable energy as it's primary energy source, the volume of installed solar power continues to increase. However, to make solar energy a mainstay of global energy production several factors must be taken into account to allow continued scaling. To allow for large volume installations, abundant materials must be used in solar cell production, and ideally in as small amounts as possible [1]. This can be accomplished by making the wafer of the solar cell as thin as possible. By decreasing the wafer thickness carrier extraction efficiency also increases.

As wafers become thinner, though, less light is absorbed. This is especially true for wavelengths that are a significant fraction of the thickness of the absorber material. To increase the absorption of these thin wafers the optical path length the light travels must be increased. This can be accomplished by both reflecting and scattering the light at the back side of the solar cell. By scattering the light at a high angle, a significant increase in the optical path length occurs. Further, if the light is scattered outside the critical angle for total internal reflection, essentially all the light can be absorbed. Thus, the ultimate goal of a scatterer is to redirect all incident light, regardless of angle or polarization, outside the critical angle.

There are many ways to increase light absorption, but three are especially popular. The first is by texturing the surface of the active layer. As seen in Fig. 1.1a, texturing the surface of the absorber layer has two effects. Not only is the reflected light directed towards another part of the cell allowing a second chance for absorption, it also enters the absorber at a modified angle, increasing the optical path length and, thus, the likelihood of absorption. This method can also be enhanced by modulating the size of the texturing, combining large and small variations [2]. However, the sizes of the features required to achieve light trapping effects are the same as the cell thickness for thin-films, creating significant defects in the material, reducing their efficiency [3].

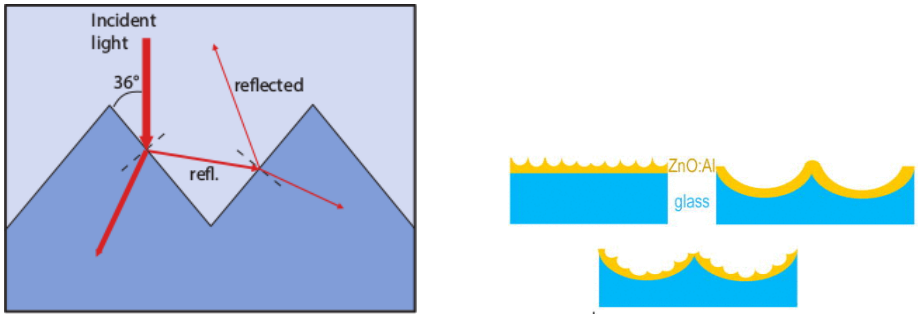

(a) (b)

Figure 1.1: Illustration of light trapping by texturing. (a) Schematic of light path under textured surface [4, Ch. 10]. (b) Schematic of modulated surface texture, incorporating both large and small feature sizes [5].

The second popular method of trapping light is to paint the back surface of the cell white. The white paint consists of titanium dioxide (TiO_2) nanoparticles suspended in a binder, as seen in Fig. 1.2a. These particles act as Mie scatterers

over a wide range of wavelengths, scattering the light in a narrow cone about the surface normal. Thus, although the light is reflected at the back surface, much of it escapes after only the first reflection.

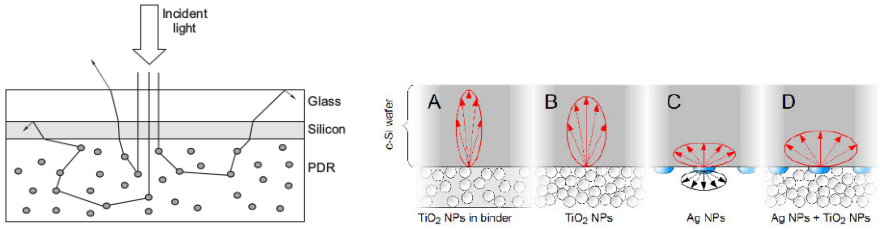

(a) (b)

Figure 1.2: (a) Illustration of light trapping with paint [6]. (b) Schematic results showing the larger angular intensity distribution when combining metal nanoparticles with paint [7]

Finally, and the subject of this work, metal nanoparticles can be used to trap light. These particles act as a sea of free electrons embedded in a dielectric. This allows the electrons to vibrate within the confines of the metal against a fixed backdrop of the positively charged metal ions. Acting as damped oscillators, the electrons can experience a resonant frequency when driven by the electric field of incident light. It is this property that is exploited to create an efficient back reflector.

Plasmonic reflectors can overcome the challenges of both the textured and painted reflectors. Implemented through an additional layer placed on the back of the solar cell, these reflectors do not disturb the quality of the absorber layer as texturing does. This also allows the reflector to be easily integrated into the production process as an additional step. Metal nanoparticles can also increase the angular distribution of reflected light. As seen in Fig. 1.2b, when included in the painted back reflector, the angular intensity distribution of the reflected light widens significantly. Unfortunately, the particles also increase absorption, so the overall reflected intensity may decrease. This is especially true as particle size decreases or the frequency of the light increases [7]. These issues can be overcome by tuning the particle size to interact with the electric field of light only over a specific range of wavelengths. Further, the cross sectional area with which the particles can interact with light can be up to ten times their geometric cross section [8]. This allows a surface coverage of only 10% to optically cover the entire cell, reducing material costs. Combined, these effects can improve light trapping compared to other reflector types [9].

1.2 Current State of Research

There are a wide range of factors affecting the behavior of a plasmonic structure. The most general is whether the structure is periodic or not. 1D and 2D periodic structures have shown a great ability to couple light into the absorbing layer, increasing the efficiency of an amorphous silicon cell from 4.5% to 6.2% [10]. However, both of these structures suffer from sensitivity to the angle of incident light, losing effectiveness as the light deviates from the normal of the surface. In addition, 1D structures are sensitive to the polarization of the incident light, coupling only transverse electric (TE) waves. Non-periodic structures, while not sensitive to the incident angle, can not be tuned to a specific range of wavelengths. Thus, they will not be as effective in coupling light as their periodic counterpart. A possible compromise to the issues of both periodic and non-periodic structures may lie in a quasicrystal structure, however little research has been pursued along this path [11].

The size and shape of the metal nanoparticles making up the plasmonic structure also play a significant role in their response to light. In general, as the particles become larger the wavelengths they interact with red-shift and their resonant peak broadens. As particles become larger they also gain more resonant modes due to excitations of higher order terms in the multipole expansion [12]. Both of these effects are observed in Fig. 1.3. However, the specific shape of the particles has a more dramatic influence over how a particle behaves. Spheroids, hemispheres, and cylinders are the most studied shapes. Spheres can be modeled using Mie theory, giving exact solutions to Maxwell's equations under certain assumptions, serving as a nice baseline with which to compare other geometries. These solutions show that spheres mostly scatter forward, with the effect becoming more pronounced as the particle size increases, as seen in Fig. 1.4. This effect is compounded if the particle is at the interface with a high dielectric material [13].

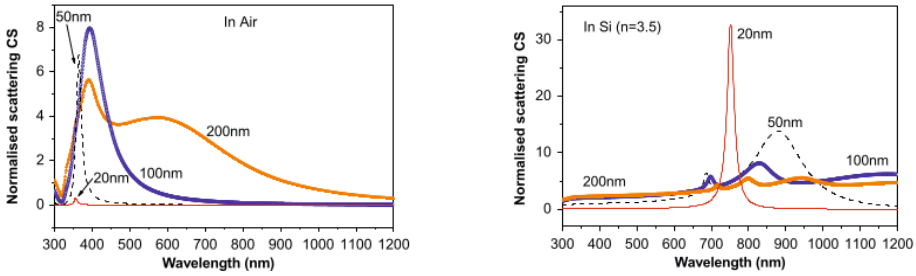

(a) (b)

Figure 1.3: Illustration of how size affects a plasmonic particle's interaction with light. The particles were simulated in (a) air, and (b) silicon. As the particle size increases the resonant peak red-shifts and broadens, and more resonant modes appear [12].

While most spheroids behave similarly, hemispheres show slightly different behavior, and cylinders diverge significantly. Using finite difference time domain (FDTD) calculations it was found that of the three shapes, cylinders are the best scatterers, but suffer from the highest absorption losses. Interestingly though, the albedo seems to be almost independent of particle shape [13]. It was also found that both hemispheres and cylinders have a more pronounced coupling

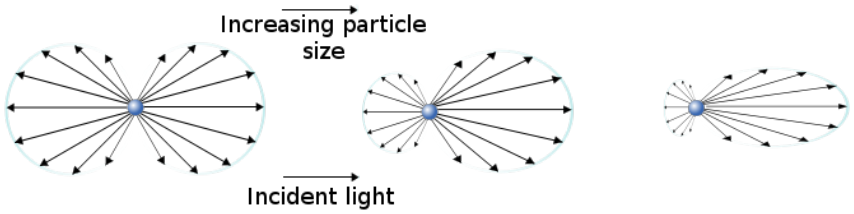

Figure 1.4: Illustration of Mie scattering with light incident from the left [14]. As the particle becomes larger, from left to right, the incident light is experiences forward scattering more prominently.

into the dielectric due to a stronger near field coupling of their electric fields. This effect can be seen in Fig. 1.5 [9].

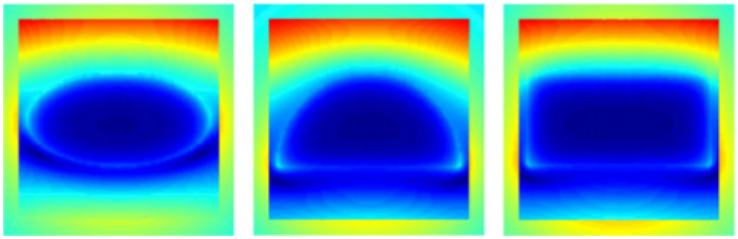

Figure 1.5: Finite difference time domain calculation showing the effect of particle shape on light scattering [13].

Another major contributor affecting how the particles perform is the material they are made out of and the material of the surrounding dielectric. The noble metals have been the main area of study so far, especially gold and silver. This arises because their high conductivity allows for a large ratio between their extinction and geometric cross-section [15]. Both these metals, however, are relatively scarce and expensive. This will create issues if the production of plasmonic solar cells scales up. Thus, both aluminum and copper have been proposed as alternative materials that are still effective, but much more abundant and cheaper. The surrounding material's largest effect comes from its refractive index. As the contrast between the refractive index of the particles and the surrounding materials grows, scattering and reflection effects change significantly [12]. This then offers another option for tuning the resonant frequency of the plasmonic particles.

There are several other design parameters that affect how well these structures perform. For instance, the distance between the absorber layer and the metal particles can have a significant impact on how well light is coupled into the absorber. By properly spacing the two layers, the driving field of the particles can be increased 14 times [16]. The coverage density of the particles also affects how the particles behave. For a given particle type and size, there is a strong dependence of both reflectance and absorption on surface coverage, yielding an optimum value. If coverage is below this level, there is a steep decrease in the absorption of light in the absorber. If this optimum is exceeded, the plasmonic resonance of the particles is red shifted, and absorption is reduced [17]. Interestingly, having sufficient coverage can also reduce the effective resistance of the

cell, allowing more efficient collection of charge carriers [10].

These metal nanostructures can also be utilized in differing manners. If metal particles are placed on the front side of the solar cell they can be used as scattering elements as depicted in Fig. 1.6 (a). The scattered light has an increased optical path through the absorber material, thereby increasing the cell's efficiency. In Fig 1.6 (b), it is shown how metal nanoparticles embedded into the absorber layer can be used to create charge carriers directly. When these particles absorb light and become excited their near-field resonance couples energy into the absorber layer. This energy is then used to create the charge carriers. Instead of metal nanoparticles, a periodic waveguiding structure can also be created, as seen in Fig 1.6 (c). This structure acts as a standing wave guide for incident light. The incoming light is effectively rotated by 90 degrees and absorbed along the interface of the waveguide and absorbing layer [8].

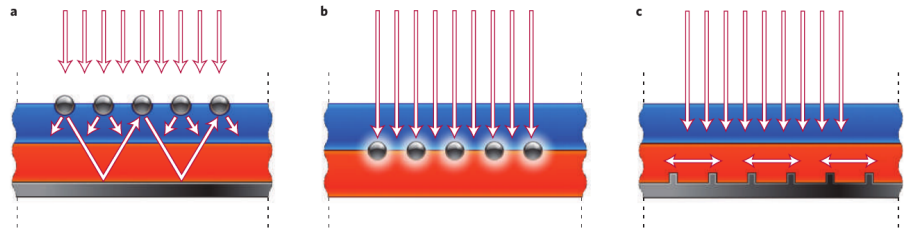

Figure 1.6: (a) Metal nanoparticles at the front side of a solar cell acting as scatterers. (b) Metal nanoparticles embedded in a semiconductor directly creating charged particles. (c) A metal nanostructure at the back of the solar cell that increases absorption [8].

Metal nanoparticles can also be embedded on the back side of a solar cell to act as a reflector, as seen in Fig. 1.7. This configuration has several benefits over the others mentioned. By being on the back side, unnecessary absorption caused by the particles is reduced as the light has already made a single pass through the active layer. This is most apparent in a comparison with the front side scatterer and more prominent for longer wavelengths. Another main advantage of the back reflector is that it can be detached from the electrically active layers of the cell. Thus, it does not interfere with the charge carriers after they are created, as is the case with the embedded nanoparticles. Finally, because the particles exhibit a large scattering cross-section relative to their geometry, less material is needed to cover the cell compared to a waveguide structure. The waveguide also suffers from high absorption losses, decreasing its appeal relative to the back reflector [8].

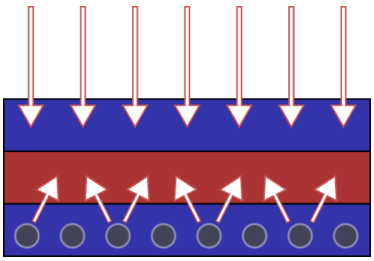

Figure 1.7: Schematic of a plasmonic back reflector.

1.3 This Work

There are still many research problems that must be tackled to fully utilize plasmonics for use in solar cells. One of the main issues is that there is little known about how the size, shape, and surface coverage interact to affect an incident light field other than the general trends presented. To probe this issue further, the plasmonic effects of an individual particle can be isolated by modeling it in vacuum. Once these effects are understood, more particles can be added in varying arrangements to address inter-particle interactions.

Most previous work has investigated 2D structures, leaving several degrees of freedom untouched. By utilizing a 3D structure, more efficient light scattering may be achieved. Using a periodic structure, interference patterns directing the radiated power can be engineered, allowing a high percentage of the power to be scattered outside the critical angle. A 3D structure may also allow tuning to a wider range of frequencies through two methods. First, the periodicity in the third dimension can be set to interact with a specific wavelength independent of the particle's interactions. Also, particle properties can be tuned layer-by-layer to optimize their interaction and driving field for the specific wavelength prominent at their location within the reflector.

To investigate how a lattice of plasmonic particles can be used to increase light scattering, an analytic model was created. Using the model, an understanding of important aspects of the lattice can be gained. In parallel, a study of how actual particles compare to an ideal plasmonic particle was performed using numerical models. From this study particle parameters optimizing desired effects can be obtained. Finally, several devices were fabricated to study how the particles form, and how a random array of particles scatters light.

Chapter 2

Modeling Theory

To investigate different aspects of the reflector, several models were used and compared against each other. This allows the strength of different effects to be determined. The effect of the lattice structure on the scattered field was studied using a new lattice sum technique. This method allows the most significant areas of the lattice to be identified, reducing the computational time required to study a certain lattice structure, compared to a complete numerical solution. The interaction of scattered fields from two particles was probed using a simple dipole radiation model. This allows for quick analysis of multiple dipoles. The behavior of an individual particle was examined using Mie Theory, which gives critical parameters about how a particle will react to a driving field when embedded in a given material. Both of these results were then compared with numerical simulations. These simulations take in to account the material properties of the particles and the environment, and their interaction with each other, giving a more complete view of the system's behavior.

2.1 Lattice Sum

When considering the construction of a multi-layered back reflector, the width and length are much greater than its depth. This allows the approximation that each layer consists of an infinite plane of plasmonic particles. It is also likely that a carefully designed arrangement of the particles will give a more favorable scattering profile than randomly placed particles. Further, a regular lattice could be an ideal structure to allow a scattering profile to be engineered due to its periodicity and reproducibility.

The proposed structure consists of several 2D layers stacked on top of each other. Thus, there are several parameters that can be adjusted in each layer: the size and shape of the particles, the lattice vectors, the parallel displacement relative to the other layers, and the spacing between the layers. Trying to optimize these parameters without an understanding of how the lattice structure of the particles effects the radiation field would be a search in the dark. By creating a model that illuminates the lattice's effects, a more directed approach to designing the reflector can be taken.

2.1.1 Phased Array Antennas

As a first attempt to find the radiation pattern from a lattice of dipoles the methods of a phased array antenna can be used. Immediately though, the assumption is made that all distances not related to phase changes are equal [18, Ch. 6]. This assumption holds well for points far from the radiation sources. However, when considering points nearer the radiation sources, such as those relevant for this study, this assumption no longer holds. An illustration of the validity of this assumption is seen in Fig. 2.1.

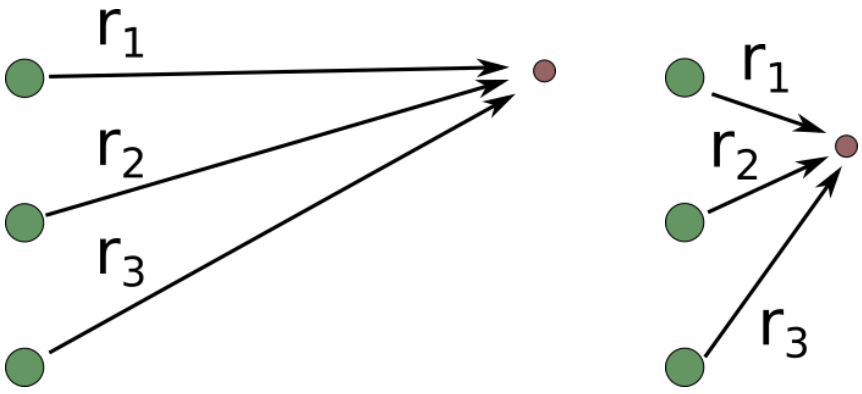

(a) (b)

Figure 2.1: In the phased antenna array model, points far from the source are considered to all have the same distance unless dealing with phase. Thus, in (a) $r_1 = r_2 = r_3$. However, for the situation in this study, the point of interest is closer to the radiation sources. Hence, in (b) r_1, r_2, and r_3 are not equal, invalidating the results from the phased antenna array model.

Another standard approach to solving a lattice sum of this sort would be to use Floquet modes. Again, however this theory has been mostly developed for the far-field regions of infinite radiating arrays. Chou has begun working on a near-field theory, but only deals with rectangular lattices, severely limiting its usefulness for this application [19].

2.1.2 General Method

The full theory of this lattice summation technique is developed in Appendix D, here only the general ideas and main results will be presented. The theory is based around two main assumptions. Because the observation point is near the radiating particles, the first assumption is that, far away from the observation point when looking in a particular direction ϕ, the change in distance between consecutive lattice points $\delta\mathscr{r}(\phi)$ is constant. This is depicted in Fig. 2.2 where $r_2 \asymp r_1 + \delta\mathscr{r}(\phi)$. The second assumption is that the driving field of each particle is the same. This allows the simplification that the radiation pattern of each particle is the same. Because the field of a particle only depends on the vector between the particle and the observation point $\boldsymbol{\mathscr{r}}$, all the particles can be collapsed to a single point. This is depicted in Figs. 2.3a and 2.3b. So, instead of summing over the infinite fields produced by each particle at the observation point, the field of a single particle can be summed over infinitely many observation points. Although this seems like a small change it is a massive simplification. In the original sum the coordinate system of each particle must be considered. In the transformed lattice, though, only one coordinate system is needed.

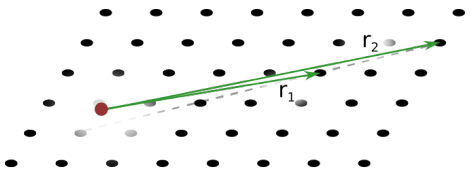

Figure 2.2: Far from the observation point, the distance change between consecutive lattice points is constant.

To perform the sum, the lattice is divided into regions via a stereographic projection as seen in Fig. 2.3c. A radius is set dividing the lattice in to a near region and a far region. In the near region a direct sum of the lattice points is performed. In the far region, the distance change between the points is assumed constant. Here, all the observation points are collapsed along the midline of the region. The number of points in the region, and their offset from the midline are both considered. Then, the field at each of the points is summed in each region.

The situation of interest, however, is a lattice in a layer, meaning reflections and absorption must be accounted for. Absorption is accounted for using the Beer-Lambert law

$$I = I_0 e^{-\eta \mathscr{r}} \tag{2.1}$$

where the initial intensity is I_0, η is the absorption constant, and $\mathscr{r}$ is the distance traveled through the layer. To account for reflections, imagine laying between two mirrors, surrounded by a 2D lattice. When looking in the mirrors you would actually see a 3D lattice, where each point in the 2D lattice has a 1D lattice caused by the reflections associated to it. By considering the points in the 3D lattice as "real" the field from reflections can be accounted for by transforming the 2D lattice in to a 3D lattice. This is depicted in Fig. 2.4.

Assuming that each particle scatters light as a dipole results in the total field

$$
\begin{aligned}
\mathbf{E}_{int} = \sum_i \sum_j & \boldsymbol{P}\hat{\boldsymbol{\theta}'}_{i,j} e^{-i\omega t} \exp\left[i\frac{\omega}{c}\boldsymbol{r}_{\beta_{i,j}}\right] \exp\left[-\eta \boldsymbol{r}_{\beta_{i,j}}\right] \frac{\left[\nu_{i,j}^1\right]^{-\beta_{i,j}} e^{-i\zeta_{i,j}^1 \beta_{i,j}}}{\delta \boldsymbol{r}(\theta_i, \phi_j)} \\
& \times \exp\left[-i2\pi \frac{\boldsymbol{r}_{\beta_{i,j}} \sin\theta_i}{\lambda_0} \sin\theta_0 \cos(\phi_j - \phi_0)\right] r_1^{m_1'} r_2^{m_2'} \\
& \times \frac{-p\omega^2\mu_0}{4\pi} \sin\left(\theta(\boldsymbol{T}\boldsymbol{r}_{i,j})\right) \\
& \times \left\{ \begin{array}{l}
\left[\begin{array}{l} \dfrac{\exp\left[i\delta \boldsymbol{r}(\theta_i, \phi_j + \frac{\pi}{2}) \delta \boldsymbol{r}(\theta_i + \frac{\pi}{2}, \phi_j) \zeta_{i,j}^2\right]}{2i \sin\left(\delta \boldsymbol{r}(\theta_i, \phi_j + \frac{\pi}{2}) \zeta_{i,j}^2\right)} \\ \quad \times \displaystyle\sum_{\gamma=\beta_{i,j}}^{\infty} \left(\frac{1}{\gamma} + \frac{1}{\gamma^2} + \frac{1}{3\gamma^3}\right) \left[\nu_{i,j}^1\right]^{\gamma} e^{i\zeta_{i,j}^1 \gamma} \\ \qquad \times \exp\left[i\gamma^2 \delta \boldsymbol{r}^2(\theta_i, \phi_j) \Delta\phi_j \Delta\theta_i \zeta_{i,j}^2\right] \end{array} \right] \\
- \left[\begin{array}{l} \dfrac{\exp\left[-i\delta \boldsymbol{r}(\theta_i, \phi_j + \frac{\pi}{2}) \delta \boldsymbol{r}(\theta_i + \frac{\pi}{2}, \phi_j) \zeta_{i,j}^2\right]}{2i \sin\left(\delta \boldsymbol{r}(\theta_i, \phi_j + \frac{\pi}{2}) \zeta_{i,j}^2\right)} \\ \quad \times \displaystyle\sum_{\gamma=\beta_{i,j}}^{\infty} \left(\frac{1}{\gamma} + \frac{1}{\gamma^2} + \frac{1}{3\gamma^3}\right) \left[\nu_{i,j}^1\right]^{\gamma} e^{i\zeta_{i,j}^1 \gamma} \\ \qquad \times \exp\left[-i\gamma^2 \delta \boldsymbol{r}^2(\theta_i, \phi_j) \Delta\phi_j \Delta\theta_i \zeta_{i,j}^2\right] \end{array} \right] \\
- \left[\ln\left(1 - \nu_{i,j}^1 e^{i\zeta_{i,j}^1}\right) + \displaystyle\sum_{\gamma=1}^{\beta_{i,j}-1} \frac{\left[\nu_{i,j}^1\right]^{\gamma} e^{i\zeta_{i,j}^1 \gamma}}{\gamma}\right] \\
- \left[\mathrm{Li}_2\left(\nu_{i,j}^1 e^{i\zeta_{i,j}^1}\right) + \displaystyle\sum_{\gamma=1}^{\beta_{i,j}-1} \frac{\left[\nu_{i,j}^1\right]^{\gamma} e^{i\zeta_{i,j}^1 \gamma}}{\gamma^2}\right] \\
- \frac{1}{3}\left[\mathrm{Li}_3\left(\nu_{i,j}^1 e^{i\zeta_{i,j}^1}\right) + \displaystyle\sum_{\gamma=1}^{\beta_{i,j}-1} \frac{\left[\nu_{i,j}^1\right]^{\gamma} e^{i\zeta_{i,j}^1 \gamma}}{\gamma^3}\right]
\end{array} \right\}
\end{aligned}
\tag{2.2}
$$

with

$$\nu_{i,j}^1 = \exp\left[-\eta \delta \boldsymbol{r}(\theta_i, \phi_j)\right] r_1^{m_1''} r_2^{m_2''} \tag{2.3a}$$

$$\zeta_{i,j}^1 = \frac{\omega}{c} \delta \boldsymbol{r}(\theta_i, \phi_j) - 2\pi \frac{\delta \boldsymbol{r}(\theta_i, \phi_j) \sin\theta_i}{\lambda_0} \sin\theta_0 \cos(\phi_j - \phi_0) \tag{2.3b}$$

$$\zeta_{i,j}^2 = -\frac{2\pi \sin\theta_i}{2\delta \boldsymbol{r}(\theta_i, \phi_j + \frac{\pi}{2}) \lambda_0} \sin\theta_0 \sin(\phi_0 - \phi_j) \tag{2.3c}$$

In Eq. (2.2) the sum takes place over the regions of the stereographic projection, where θ_i and ϕ_j are the midline angle of the $(i,j)^{th}$ region. $\boldsymbol{P}\hat{\boldsymbol{\theta}'}_{i,j}$ is the direction of the field at the observation point. The driving electric field has frequency ω and unit strength. $\boldsymbol{r}_{\beta_{i,j}}$ is the vector from the origin to the nearest

point in the $(i,j)^{th}$ region, and $\beta_{i,j}$ is the number of lattice points in the (θ,ϕ) direction needed to reach the far region in that direction. the layer has absorption constant η, and reflection coefficient r_1 at the top interface and r_2 at the bottom interface. m_1 and m_2 account for how many reflections the light experiences at each observation point. The incident driving field approaches the top interface from the (θ_0,ϕ_0) direction. p is the dipole moment and $\sin(\theta(\boldsymbol{T}\hat{\boldsymbol{\theta}'}_{i,j}))$ accounts for the polar angle of the observation point relative to the dipole. $\Delta\phi$ and $\Delta\theta$ account for the width of the region. Li_n is the polylogarithm of order n.

The dipole moment p is found from the plasmonic effects derived in Eq. (A.16).

$$\mathbf{p} = \epsilon_0\epsilon_D\alpha\mathbf{E_0} = 4\pi\epsilon_0\epsilon_D a^3\frac{\epsilon-\epsilon_D}{\epsilon+2\epsilon_D}\mathbf{E_0} \tag{2.4}$$

where the normal font weight indicates the magnitude of the corresponding vector (E.g. $p = |\mathbf{p}|$). The field from light paths that don't interact with particles, *free light paths*, can also be accounted for using the classical geometric series technique.

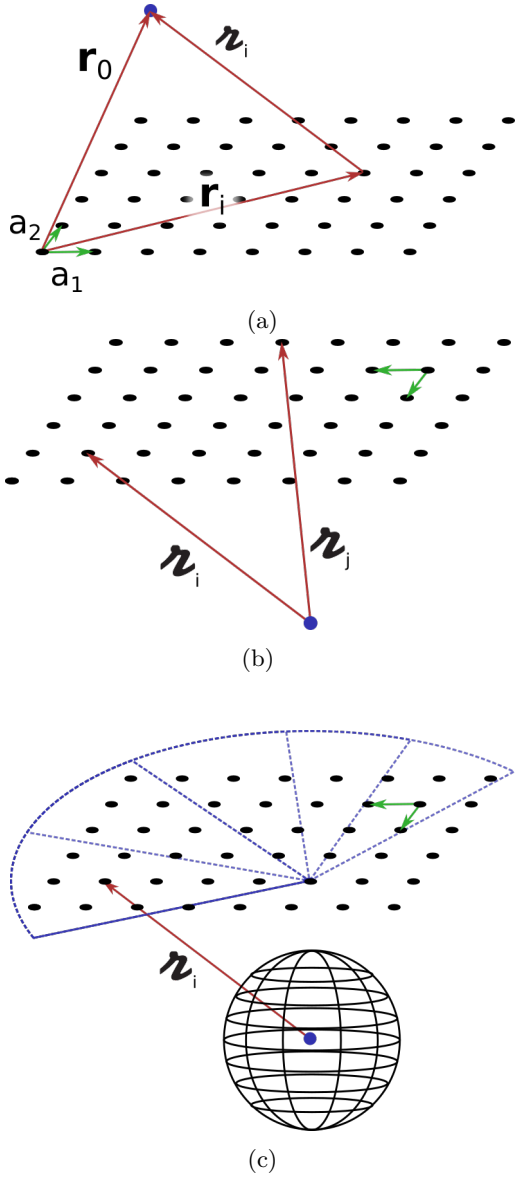

Figure 2.3: Illustrations of the steps leading to the lattice summation process investigated. (a) The original lattice, with green lattice vectors. (b) Viewing the lattice points shifted to the origin, creating a new conjugate lattice. The new conjugate lattice vectors are in green. (c) The stereographic projection that divides the conjugate lattice. The blue point in the lattice from which the divisions emanate is the projection of the origin on to the lattice plane, but is not necessarily a lattice point.

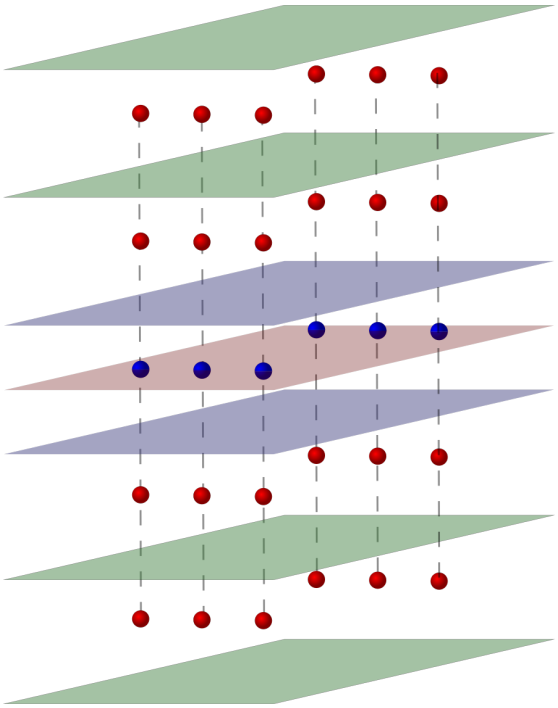

Figure 2.4: The virtual lattice created by the reflections from the real lattice. The original lattice points are indicated by the blue points lying in the red plane with blue layer boundaries. The virtual lattice is indicated by the green layer boundaries and red particles.

2.2 Modeling Methods

The effect of the lattice structure on the fields with in the reflector can be investigated using the techniques presented in Sec. D.1.1, however this ignores how the particles interact with each other. Using both simplified analytic models, and numerical models, these interactions can be accounted for and incorporated into our understanding of the reflector's behavior.

2.2.1 Mie Theory and Individual Particle Behavior

To study how an individual particle reacts to a driving field, Mie theory can be used. Mie theory make two assumptions. First is that the particle is spherical, allowing the scattered field to be represented naturally as spherical harmonics. Second, the particle is assumed small enough that the driving field is constant across the particle's cross section.

To find the Mie theory results, MiePlot was used. It is a software package developed by Philip Laven and based on the results of Bohren and Huffman as discussed in Appendix B [20]. It is able to calculate scattering profiles and cross sections for spherical particles under various conditions. By comparing these theoretical results to those of the numerical models the validity of the numerical models can be verified. Any deviation between the two results will also provide insight into non-ideal processes that are occurring in the system.

2.2.2 Interfering Dipole Fields

As discussed in Appendix A, plasmonic particles can be modeled as radiating dipoles. To study how the radiation from a small number of dipoles interact the fields can simply be summed. To accomplish this, a pure dipole radiation model was created in Mathematica using Eq. (A.18). Because Eq. (A.18) gives the field in the local coordinate frame of the dipole, a transformation from each dipole's local frame to the global system frame was needed to create a system of dipoles. In this vein, consider a dipole $\mathbf{p}$ with local frame $\Sigma' = \{\mathbf{e}'_x, \mathbf{e}'_y, \mathbf{e}'_z\}$, where $\mathbf{e}'_z = \hat{\mathbf{p}}$. Then the transformation from the global frame Σ to the local frame Σ' is

$$\boldsymbol{P} = \frac{1}{p}\begin{bmatrix} \frac{p_x p_z}{p_\parallel} & \frac{p_y p_z}{p_\parallel} & -p_\parallel \\ -p\frac{p_y}{p_\parallel} & p\frac{p_x}{p_\parallel} & 0 \\ p_x & p_y & p_z \end{bmatrix} \tag{2.5}$$

where $p_\parallel$ is the length of $\mathbf{p}$ projected into the x-y plane, $p_\parallel = \sqrt{p_x^2 + p_y^2}$. The transformation from Σ' to Σ is

$$\boldsymbol{T} = \frac{1}{p}\begin{bmatrix} p_z + \frac{p_y^2}{p_\parallel}(p - p_z) & -\frac{p_x p_y}{p_\parallel}(p - p_z) & p_x \\ -\frac{p_y p_x}{p_\parallel}(p - p_z) & p_z + \frac{p_x^2}{p_\parallel}(p - p_z) & p_y \\ -p_x & -p_y & p_z \end{bmatrix} \tag{2.6}$$

If the origins of the two frames do not coincide then a simple translation $\boldsymbol{P}(x - x_0, y - y_0, z - z_0) = \boldsymbol{P}(\mathbf{r} - \mathbf{r_0})$ remedies the situation, where $\mathbf{r}_0$ is the displacement vector from the origin of Σ to Σ'. Using these transformations, the Σ' coordinates of a vector $\mathbf{v}$ in Σ are found by $\mathbf{v}' = \boldsymbol{P}\mathbf{v}$. Conversely, the Σ coordinates of a vector given in Σ' are found by $\mathbf{v} = \boldsymbol{T}\mathbf{v}'$. Note that unprimed and primed vectors of the same name represent the same geometric vector, while the priming of it indicates the coordinate system of its components. The derivation of these transformations can be found in Appendix C.

Thus, the total electric field at a point $\mathbf{r_0}$, of a system of pure dipoles, $\mathbf{p}_i$, is obtained by summing the field from each dipole, $\mathbf{E}_i$.

$$\mathbf{E}(\mathbf{r}_0) = \sum_i \mathbf{E}_i(\mathbf{r}_0 - \mathbf{r}_i) = \sum_i \boldsymbol{T}\mathbf{E}_i(\boldsymbol{P}\boldsymbol{\imath}_i) \tag{2.7}$$

where $\boldsymbol{\imath}_i = \mathbf{r}_0 - \mathbf{r}_i$.

2.2.3 Numerical Models Using HFSS

Unfortunately, Maxwell's equations, describing the complete set of interactions for an EM field, can only be solved for very simple situations. Thus, for a more complete view of how a system of these particles will behave, a numerical solver must be used. For this, High Frequency Structural Simulator (HFSS) by Ansoft was used. HFSS uses the Finite Element Method (FEM) to solve the system in a self-consistent manner, within some given energy error.

Finite Element Method

There are three main steps in the finite element method. First, the system is divided into discrete regions creating a 3D mesh of polygons. Next, polygons in contact with the excitations are given their initial conditions, matching the excitations. In each of these regions, then, the EM field is propagated through the polygon, treating it as an area of constant dielectric properties. After propagation through the polygon, the EM field is matched at the boundaries of adjacent polygons using Maxwell's equations. In this way the excitation is propagated through the entire structure. Finally, an energy error is calculated by comparing the energy of the current solution with the previous solution. If this error is less than a given amount the simulation stops. Otherwise the mesh is refined, and the process is iterated again.

For this project, of interest is how the back reflector structure will respond to incident solar light. This situation is modeled as an incident plane wave from the top of the structure. Because HFSS only calculates the total field, the incident and scattered fields are separated manually.

$$\mathbf{E}_t = \mathbf{E}_i + \mathbf{E}_s \tag{2.8}$$

Where $\mathbf{E}_t$ is the total field, $\mathbf{E}_i$ is the incident field, and $\mathbf{E}_s$ is the scattered field. It is assumed that the incident field is a perfect plane wave, taking the form

$$\mathbf{E}_i = \mathbf{E}_0 e^{i(k(z-h)+\phi)} \tag{2.9}$$

where $\mathbf{E}_0$ is a constant vector indicating the polarization and magnitude of the incident field, h is the excitation height of the incident wave, and ϕ is the phase of interest.

By comparing the results from these different simulation methods, the strength of different effects can be evaluated. Individual particles can be designed to radiate as an ideal dipole. The interaction of the particles from multiple layers can be used to create a desired interference pattern. And the lattice structure can be tuned to increase or decrease the impact of the particles far away from a given point. The strongest effects of these can then be incorporated in to the design of a reflector.

Chapter 3

Modeling Results and Analysis

To build an understanding of how a reflector will behave it was divided into three levels of subsystem. At the lowest level, the properties of individual particles can be explored. Using Mie Theory the scattering efficiency of a single particle embedded in different materials can be predicted. Comparing the theoretical results to numerical results obtained with HFSS, how well particles of different size and shape fit the theory can be assessed. Two dipole systems can then be investigated to determine possible interference patterns. These interference patterns can be used to direct scattered power in to directions to ultimately increase absorption. Comparing these results with those of HFSS will reveal how strongly the particles influence each other. Finally, the lattice structure can be evaluated using the lattice summation technique developed. Combining these results a reflector structure that optimally scatters light can be arrived at.

3.1 HFSS Settings

HFSS provides several parameters when solving systems. Among these are the minimum and maximum number of passes to converge a system, the number of passes the system should stay converged for, and the allowed energy error to define convergence. As with all numerical methods, the more accurate the desired result, the more computation resources are required, be it time or processing power. Thus, through early stages of trial and error a balance of the two was struck. The nominal values for these parameters can be found in Table 3.1.

In addition, radiated fields were calculated at ten degree intervals of an

Property	Value
Maximum Number of Passes	16
Minimum Number of Passes	4
Energy Error	0.02
Number of Converged Passes	2

Table 3.1: The nominal parameters used during HFSS simulations.

infinite sphere in both the polar and azimuthal directions. As the polar angle varies from 0 to 180 degrees, and the azimuthal angle varies from 0 to 360 degrees, except at the poles, this gives $(17 \times 36 + 2) = 614$ field points.

Each model in HFSS consists of the system of interest, embedded in a medium, and surrounded by a boundary. Because the radiation pattern is of interest, the *radiation boundary* was used around the entire system. This acts as a perfect absorber, simulating an open system. The HFSS manual suggests placing the boundary at least a quarter wavelength away from the system of interest to reduce near-field effects [21, p25]. To keep the models conservative, though, at least one wavelength was provided in all directions for each model.

Symmetries of a system can also be exploited using the *symmetry boundary*. By dividing a model in to symmetric sections the effective volume requiring computation can be significantly reduced, and along with it the computational resources required to converge the system. In instances where symmetry was exploited, a perfectly conducting boundary is place perpendicular to the driving electric field, and a perfect magnetic boundary is placed parallel to it, both along the corresponding planes of symmetry.

In the simulations four types of materials were used: vacuum, an ideal dielectric, silver, and SiO_2. Vacuum and the ideal dielectric were both simulated by setting a constant relative permittivity and a relative permeability of 1. Silver was modeled using the n-k data of Johnson and Christy [22]. Although this data is optimistic as pointed out by Pahud *et al.*, it is the data typically found in literature [23]. The ϵ_1 and ϵ_2 values are seen in Fig. 3.1. Because the real part of the permittivity ϵ_1 is at least one order of magnitude larger than the imaginary part ϵ_2, in the wavelengths above 700 nm, only ϵ_1 will be considered when evaluating the scattering cross sections. Finally, SiO_2 was simulated using HFSS's native values.

3.1.1 Boundaries

Because the radiation pattern of the structure is of primary interest, the boundaries of the HFSS simulations are important. Both Radiation and Perfectly Matched Layer (PML) boundaries were tested using an incident plane wave traveling through vacuum and an ideal dielectric. The mean radiation pattern of each boundary type is seen in Fig. 3.2. Because the wave is traveling in the 180° polar direction through a homogeneous medium, it would be expected that all the radiation energy would be at 180°. Unexpectedly though, some of the energy is scattered. This may be a result of numerical noise or indicate that an artificial interface is being encountered at the radiation boundary. Because the radiation boundary is closer to the expected radiation pattern of having all the radiation at 180°, and because it seems to be more efficient time-wise, it will be used for all other simulations.

3.2 Single Particles

To verify the models, as well as establish which particle size and shape to use for further simulations, the properties of a single particle were investigated using HFSS. In the Scattering Theory section, Appendix B, the scattering profile of a spherical particle is discussed. It would be convenient to match simulation

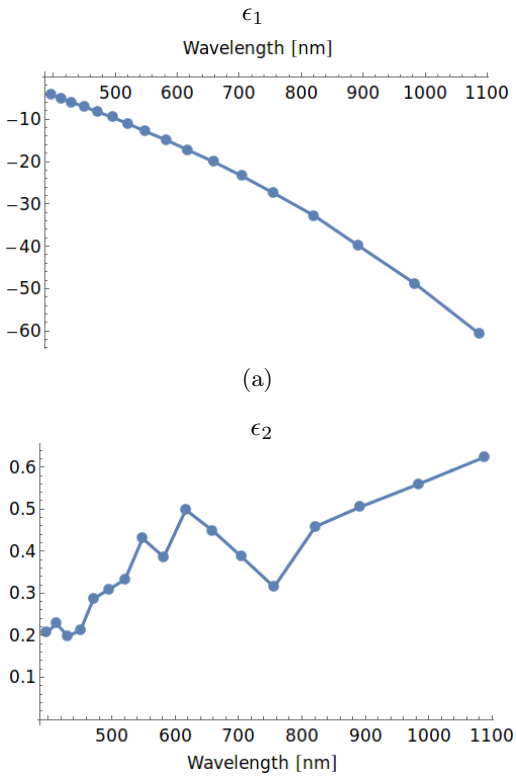

(a)

(b)

Figure 3.1: The relative permittivity (a) ϵ_1 and (b) ϵ_2 of silver from Johnson and Christy [22].

results to the theory in simple cases to validate the model. Then, more complex simulations could be used for the entire structure and the best actually fabricated. However, fabricating spherical particles is quite difficult. Thus, in addition to simulating spherical particles, cylinders were also simulated. As will be discussed in Part 4, which addresses fabrication, cylindrical particles are more feasible to create.

Through this study, the frequency range of interest can also be narrowed. Because the reflector is integrated at the rear of the solar cell, longer wavelengths of light are of greater interest. In Table 3.2 some key wavelengths and frequencies are shown for convenience. Assuming a silicon absorber layer, the longest wavelength of relevant light is 1107 nm. This serves as a good maximum for the models as well because, of common absorbers, silicon has one of the smaller band gaps. Thus, when the size of the particle is compared to the calculated absorption, an upper bound for the frequency can be set.

Frequency [THz]	400	333	286
Wavelength [nm]	750	900	1050

Table 3.2: Frequencies and their corresponding wavelengths.

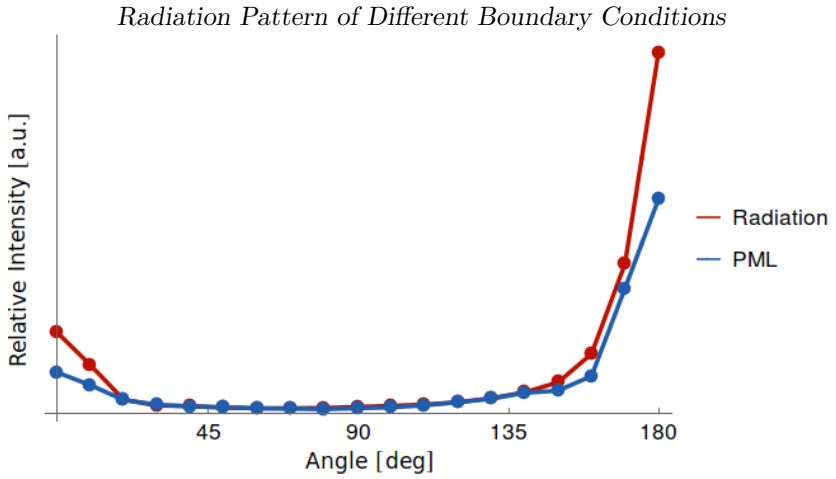

Figure 3.2: Mean radiation pattern of a plane wave traveling through vacuum with radiation and PML boundary conditions.

To compare how the two canonical shapes of this study react to incident light, both were modeled in vacuum. The radius of the sphere, and the radius and aspect ratio of the disk were varied and the absorption and scattering profiles calculated. Using this information, the size of each shape was set for the remainder of the models.

3.2.1 Mie Theory

From Eqs. (B.18), the absorption and scattering cross sections of a sphere are given by a power series of Bessel functions [24]. In the small particle limit, for a sphere with radius a and incident plane wave with wavenumber k, this power series can be reduced to Eqs. (B.19), reproduced in Eqs. (3.1).

$$C_{sca} = \frac{8\pi}{3} k^4 a^6 \left| \frac{\epsilon - \epsilon_m}{\epsilon + 2\epsilon_m} \right|^2 \tag{3.1a}$$

$$C_{abs} = 4\pi k a^3 \,\mathrm{Im}\left[\frac{\epsilon - \epsilon_m}{\epsilon + 2\epsilon_m} \right] \tag{3.1b}$$

Here ϵ is the relative permittivity of the particle and ϵ_m is the relative permittivity of the surrounding material. The scattering cross section is the effective area required such that if the absorbed incident power is radiated isotropically, the power density delivered to the observation point matches the measured power density. Similarly, the absorption cross section defines the equivalent area if all power is absorbed. Thus, these give a measure of the interaction size of the particle. The ratio of the scattering cross section with the geometric cross section, which is the scattering efficiency Q_{sca}, then gives a relative measure of how well the particle scatters.

To tune the silver particles to their plasmon frequency, the dielectric of the surrounding medium must be chosen to minimize the denominator of the cross sections. The dielectric function of silver, measured by Johnson and Christy, is

seen in Fig. 3.1. For the wavelengths of interest (longer than 700 nm), ϵ_1 is two orders of magnitude larger than ϵ_2, so ϵ_2 will be ignored. Unfortunately, between 700 and 1000 nm wavelengths, ϵ_1 varies from roughly -25 to -50, meaning the surrounding material should have a permittivity of at least 12 to achieve resonance. For visible light though, transparent materials have permittivity between 1 and 10, meaning only specialized materials that are both transparent and have a high permittivity could be used.

In comparison, by using MiePlot to calculate the full series expansion in Eq. (B.18a) a more interesting result is found. In this more complete analysis several peaks of the scattering cross section are found. This is seen in Figs. 3.3 and 3.4 where the scattering efficiency of a silver sphere with 100 nm radius has been plotted against the incident wavelength and surrounding permittivity, respectively. The scattering efficiency, Q_{sca} is the scattering cross section normalized to the geometric cross section of the particle, A.

$$Q_{sca} = \frac{C_{sca}}{A} \tag{3.2}$$

As expected from the limiting case in Eq. (3.1a) , a higher permittivity of the embedding material redshifts the peaks. However, this analysis reveals several resonant peaks, as opposed to the singular peak of the limiting case. Fortunately, for ϵ_m between 2 and 3, a resonance occurs around 1000 nm. This is an excellent match for the present situation as transparent conductive oxides (TCOs) have permittivities in this range, and, as discussed in Sec. 5.2, the ability to use a TCO may prove very important.

Under the small particle assumption, a single resonance peak is expected when varying them environment's permittivity. However, the full Mie theory calculation shows multiple peaks. This indicates that the particles under consideration are not small enough for the small particle assumption. So the simple equations in (3.1) are not sufficient to describe the particles behavior, and a more complete approach must be used.

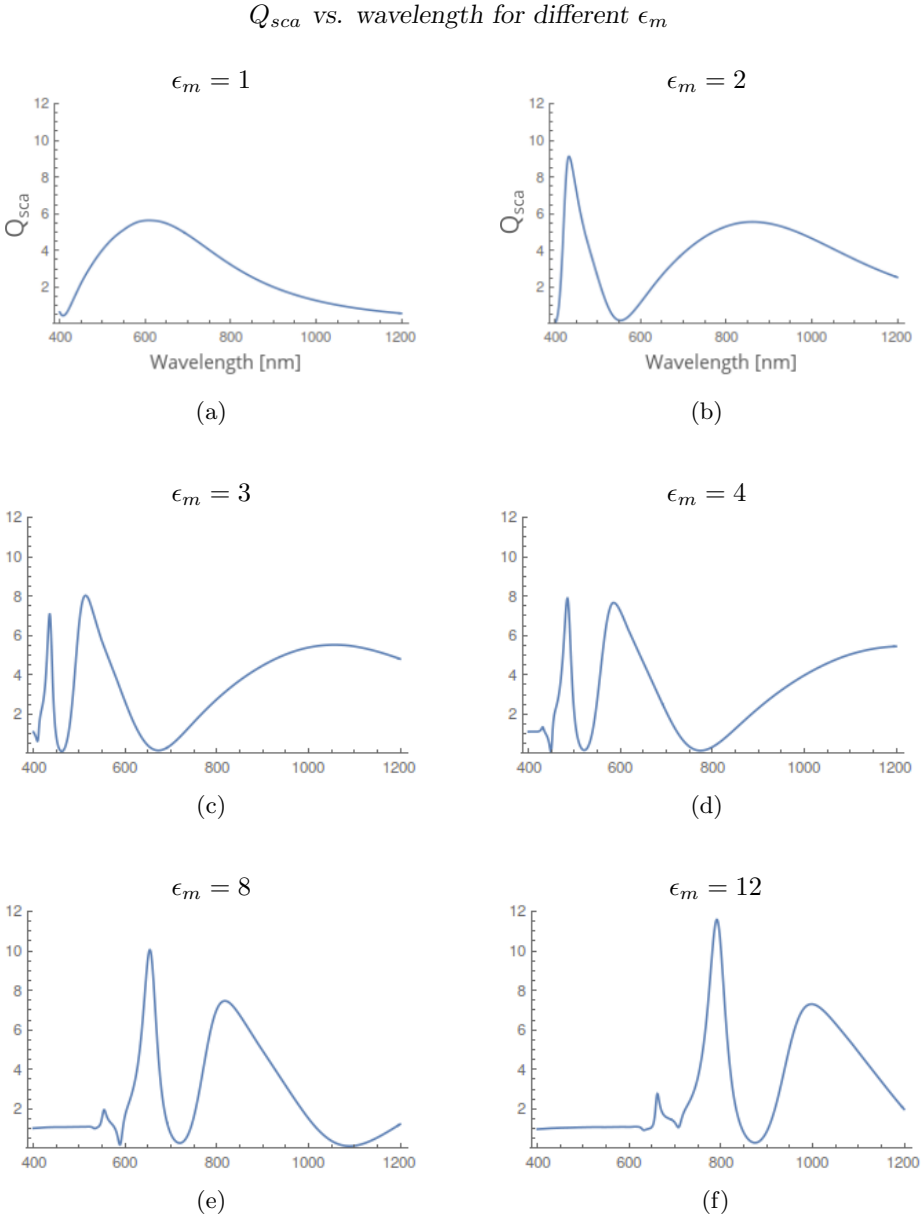

Figure 3.3: Scattering efficiency of a 100 nm silver sphere embedded in material with relative permittivity (a) 1, (b) 2, (c) 3, (d) 4, (e) 8, (f) 12. Wavelength, on the x-axis is in nm, and the scattering cross section on the y-axis is in relative units.

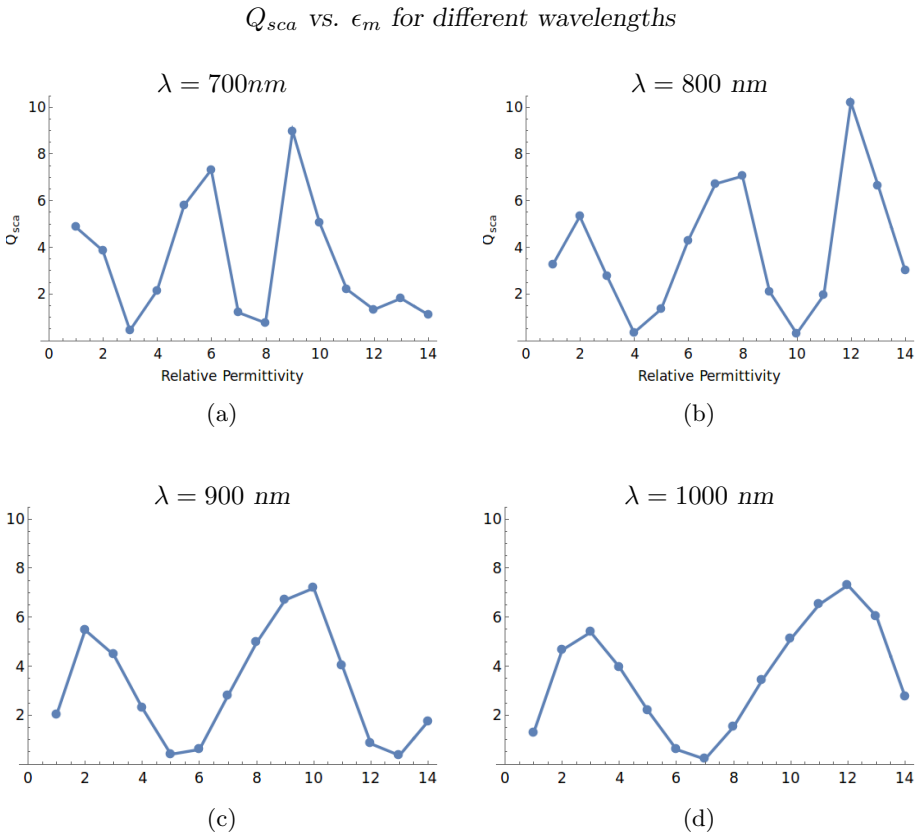

Figure 3.4: Scattering efficiency of a 100 nm silver sphere embedded in material with incident wavelengths (a) 700, (b) 800, (c) 900, and (d) 1000 nm.

3.2.2 Scattering Cross Section

To validate the HFSS results against theory, the scattering cross section, also called the radar cross section, was computed for a 100 nm silver sphere; identical to that used in the Mie theory calculations in Sec. 3.2.1. In Fig. 3.5 the relative scattering cross section is plotted against wavelength for different surrounding permittivities, and in Fig. 3.6 the relative scattering cross section is plotted against permittivity for different incident wavelengths. (In Fig. 3.6c, the permittivities with two values were caused by an overlap in HFSS evaluations when an analysis parameter was changed for accuracy) Unfortunately, in both situations there is significant disagreement between the numerical HFSS results, and the theoretical MiePlot results. This indicates that either the small particle assumption is being violated, or there are additional effects due to the material properties.

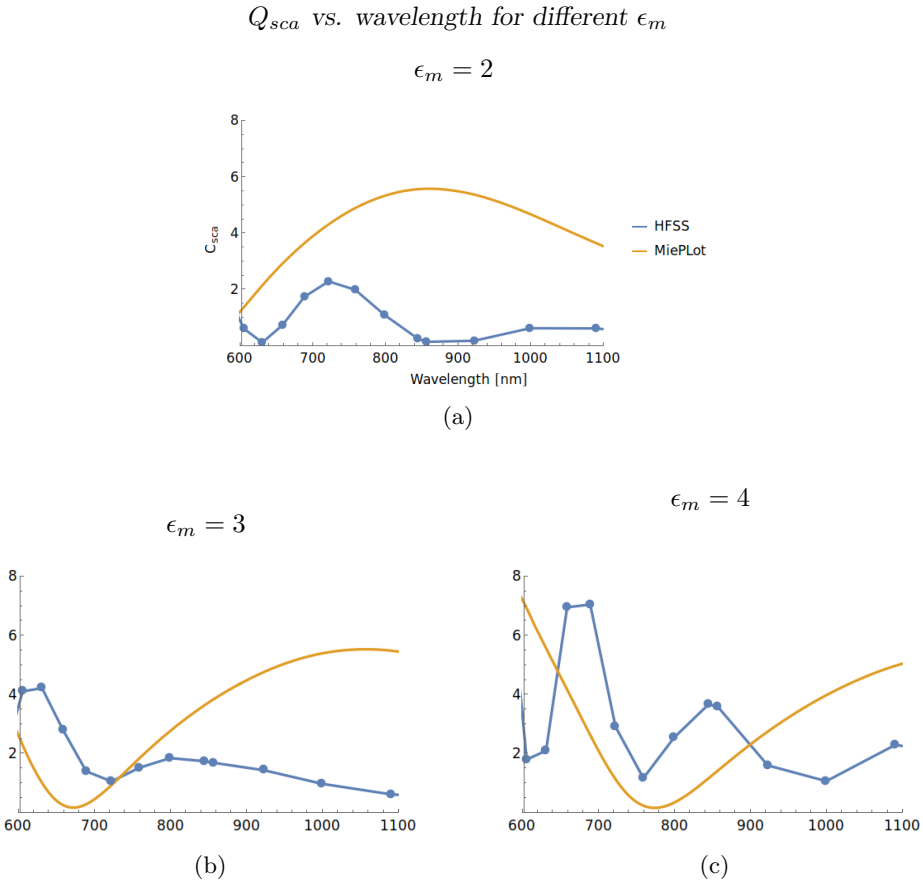

Figure 3.5: The relative radar cross section plotted against wavelength for a 100 nm silver sphere as computed by HFSS and MiePlot. The surrounding permittivity is (a) 2, (b) 3, and (c) 4.

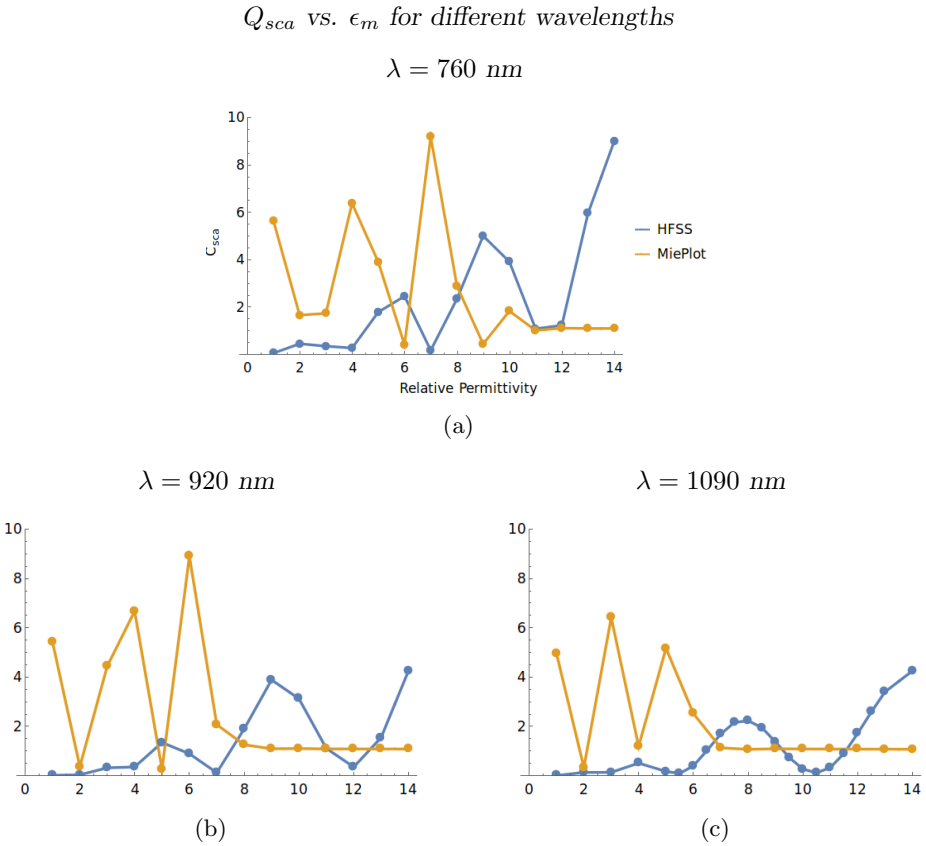

Figure 3.6: The relative scattering cross section against relative permittivity for a 100 nm silver sphere as computed by HFSS and MiePlot. The incident wavelength is (a) 760, (b) 920, and (c) 1090 nm.

3.2.3 Absorption

To determine the size and shape of the best particles to use, the average absorption density was simulated using HFSS for spheres and cylinders of various sizes. The average absorption density is defined as the total absorbed power divided by the total volume of the object. The results for a sphere of varying radius are seen in Fig. 3.7. Over the wavelengths of interest, these results show that to reduce absorption a radius between 150 and 200 nm or 350 to 400 nm should be used. The larger radii have two downsides though. First, their size compared to the wavelength of light will begin to mitigate the plasmonic effects of interest. And second, due to fabrication limitation, discussed in Sec. 4, particles of this size could not be produced. Thus, spherical particles with radius between 150 and 200 nm should be used.

When analyzing the absorption of a sphere, only one parameter could be tuned, namely its radius. However, there are two parameters that can vary in the disk: the volume and the radius to height ratio. For a fixed 1:1 ratio, varying the volume of the cylinder results in the average absorption in Fig. 3.8. The regular downward trend with increasing volume exhibits an a^{-1} trend, as

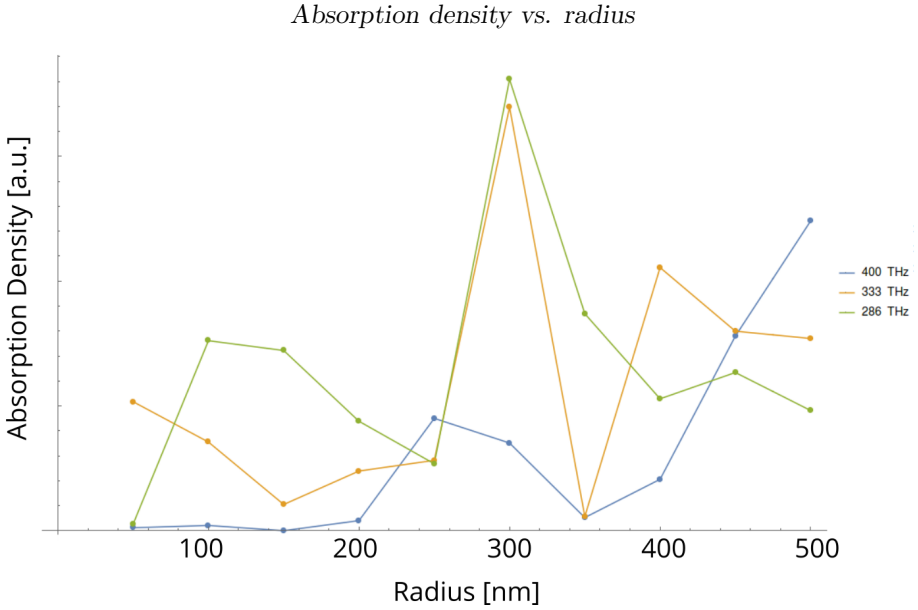

Figure 3.7: Average absorption density of a silver sphere in vacuum with varying radius at different incident frequencies.

seen in the inset. Fitting this trend to the data, the coefficient of a^{-1} was found to be roughly 8×10^{-3} for all three frequencies. So for a radius of more than 90 nm, the magnitude fo the slope is less than 1. Thus 90 nm can be used as a lower bound to mitigate absorption. For cylinders with radii smaller than 90 nm absorption increases rapidly, but for those with a radius larger than 90 nm absorption is roughly constant.

Now, using a fixed volume of $\pi \cdot 100^3$ nm^3 and varying the aspect ratio of the cylinder results in the average absorption seen in Fig. 3.9. The ratio was varied from 1:8 to 8:1, the former being a thin rod, and the latter resembling a flat disk. The two higher frequencies have an almost linear trend, while 286 THz deviates from this a bit. It is difficult to tell whether the 286 THz trend is in fact nonlinear due to the cutoff point of the plot, however. The linear trends seen in these results are quite interesting. The two parameters changing in these situations are the cross sectional area exposed to the incident field, and the depth of the particle. The volume V, and aspect ratio σ of a cylinder are given by

$$V = \pi r^2 h \tag{3.3}$$

$$\sigma = \frac{r}{h} \tag{3.4}$$

for radius r, and height h. If the absorption was dependent on only the area exposed to the incident wave, a $\sigma^{3/2}$ dependence would be expected as $\sigma \propto A^{3/2}$. This is not observed, though. Thus, the aspect ratio of the particle plays a role in the absorption, especially towards the higher frequencies, and a smaller aspect ratio should be used for less absorption.

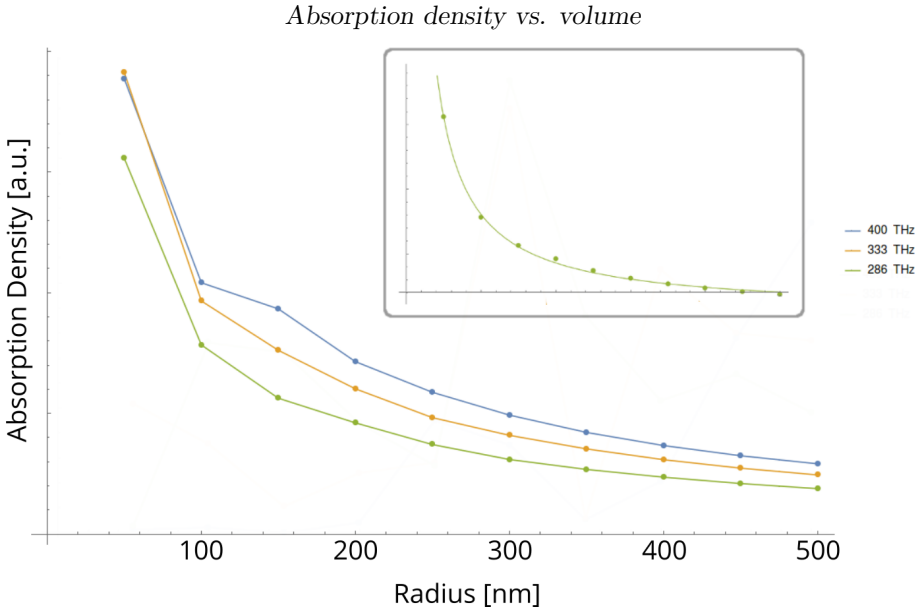

Figure 3.8: Average absorption density of a cylinder in vacuum with a fixed aspect ratio of 1:1 radius to height, but varying volume for different incident frequencies. **Inset:** The 286 THz data plotted with trend line of the form $1 + x^{-1}$.

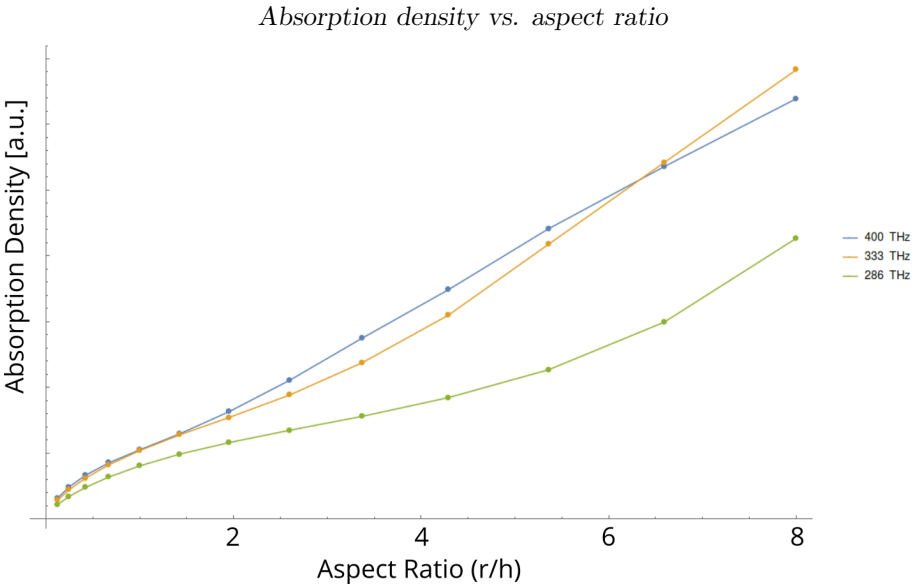

Figure 3.9: Average absorption density of a cylinder in vacuum with a fixed volume but varying aspect ratio.

3.2.4 Particle Size and Radiation

In Appendix A, when deriving properties of plasmonic particles, especially in Eq. (A.18) showing that particles act as dipoles, it is assumed that the particle is small compared to the wavelength of the driving field. By comparing the radiation pattern of the HFSS simulations with this idealization, the "dipoleness" of a particle can be assessed and a limit for the small particle assumption can be established. To find the size at which the dipole approximation becomes valid, silver spheres with radius from 5 to 100 nm in 5 nm steps, from 110 to 200 nm in 10 nm steps, and from 300 to 1000 nm in 100 nm steps were simulated. Each particle was placed in vacuum and excited at 400, 333, and 286 THz.

As explained in Sec. 3.3.2, to make comparisons more tenable, the radiated field is integrated around the azimuth for each polar angle measurement and the field is normalized so the total radiated time-averaged power is 1. Under these calculations, an ideal dipole has the radiation pattern shown in Fig. 3.10. It should be noted that the data from HFSS is the total field, while the data the dipole model is only the radiated field. Ideally the scattered field of the HFSS simulations could be obtained by subtracting the incident field from the total field $E_{sca} = E_{tot} - E_{inc}$. Unfortunately, due to absorption of energy in the particles and the non-ideal results of a free wave discussed in Sec. 3.1 this resulted in negative field magnitudes.

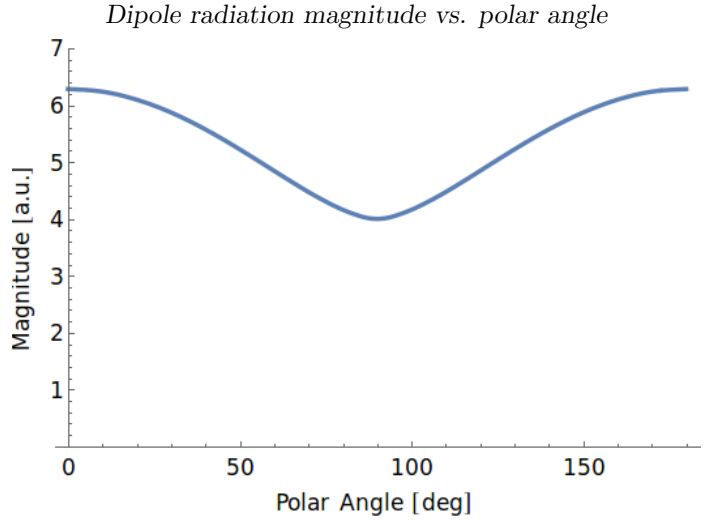

Figure 3.10: Calculated radiation pattern in the polar direction of an ideal dipole with unit strength.

The radiation pattern of the all the simulations, is seen in Fig. 3.11. For almost every particle size there is a significant disagreement from the ideal pattern, however between 130 and 200 nm the dipole approximation holds quite well. To investigate further, the 3D radiation patterns can be examined, a selection of which are in Fig. 3.12. Interestingly, small particles vary significantly from the ideal case, the opposite trend of what would be expected given the small particle approximation. At these small sizes though, absorption is becoming large enough that the radiation pattern is disrupted.

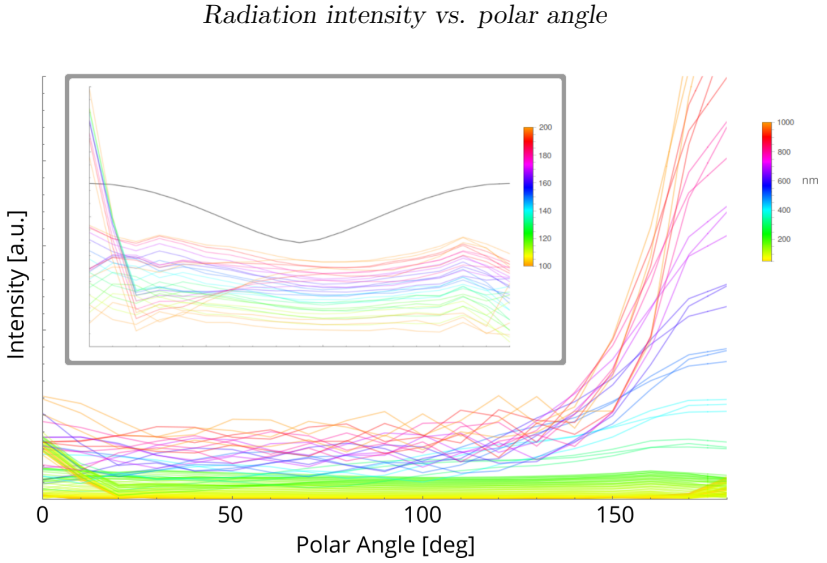

Figure 3.11: Radiation pattern of spheres from 5 to 1000 nm radius excited at three different frequencies. **Inset:** A scaled and recolored plot showing detail of the particles from 100 to 200 nm. The black line is the ideal dipole radiation pattern.

By scaling the ideal radiation pattern, the error between each particle radius and the ideal pattern can be quantified. To find the scaling factor m, the root mean square (RMS) of the data was minimized giving

$$m = \frac{\sum_i d_i e_i}{\sum_i d_i^2} \tag{3.5}$$

where the sums are taken over the data points of a single particle, with d_i the calculated ideal value at the i^{th} angle, and e_i the simulated value. The RMS of the relative errors for each particle can then be computed, resulting in Fig. 3.13. As expected the longer wavelengths give a smaller error due to the small particle approximation. Taking the average of the RMS values across each frequency results in Fig. 3.14a, showing the particle radius behaving most like a dipole across the range of frequencies occurs at 180 nm. It appears that the data follows a smooth function, however, the form of this function was not obtained. The standard deviation of these values also follows a smooth trend, as seen in Fig. 3.14b. The decreasing deviation means that as particle increase in size they behave more uniformly across the frequency range, so a more consistent radiation pattern can be expected.

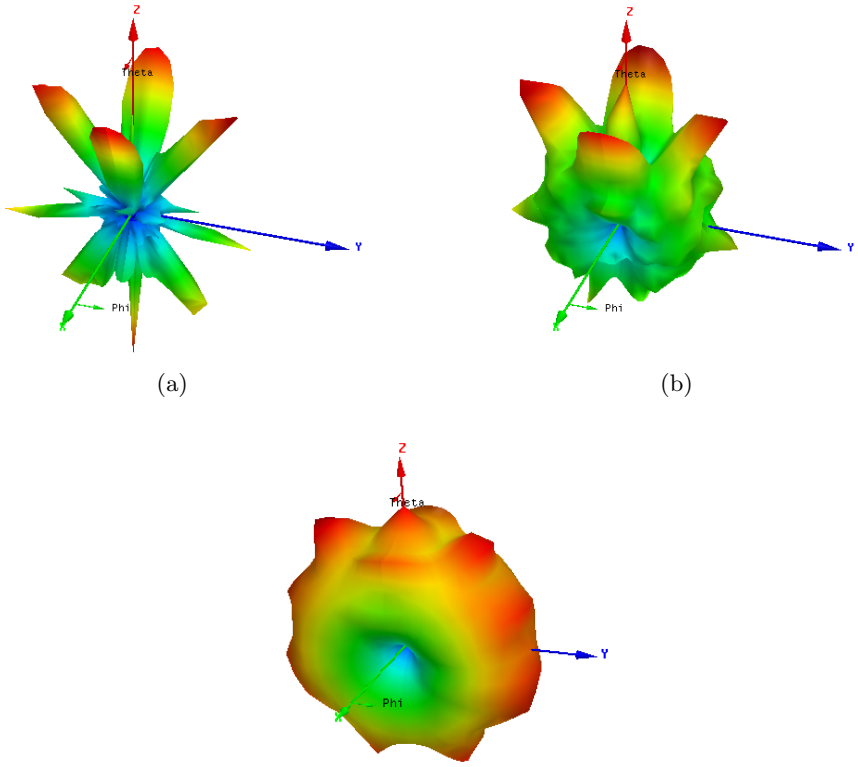

(a) (b)

(c)

Figure 3.12: Radiation patterns of the (a) 50, (b) 100, and (c) 200 nm radius particles.

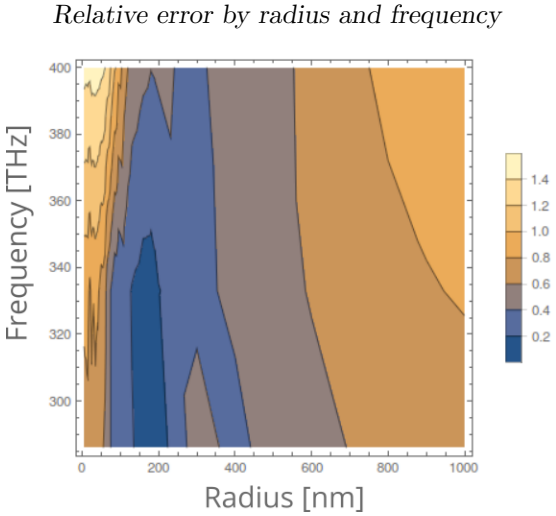

Figure 3.13: Interpolated RMS of the relative error for each particle and frequency combination.

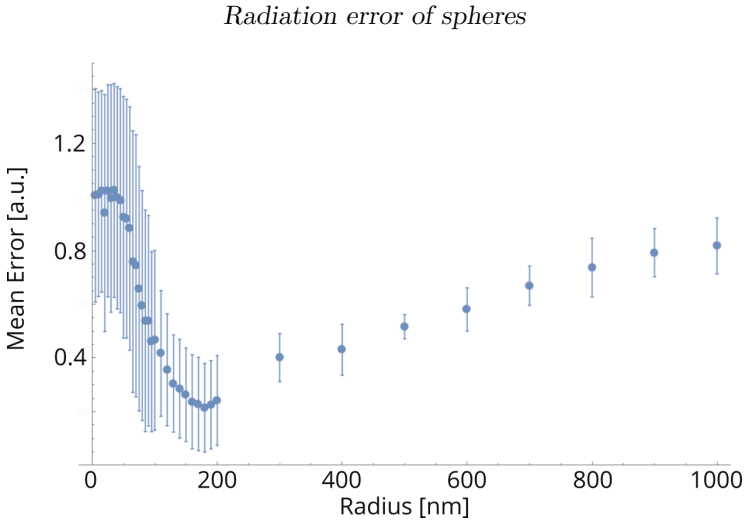

(a)

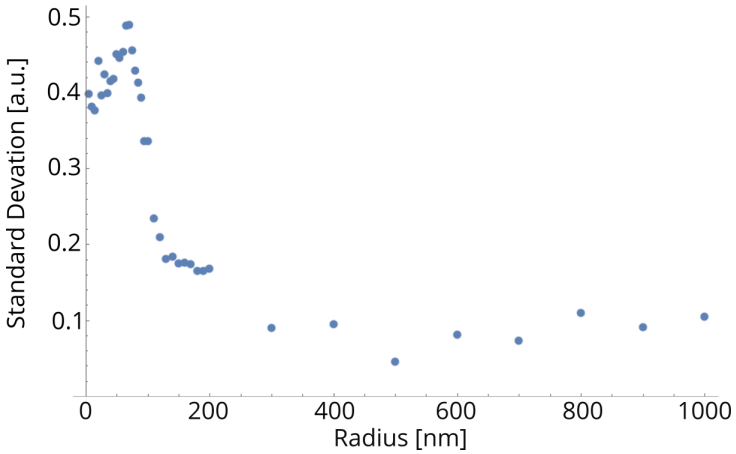

(b)

Figure 3.14: The (a) mean and (b) standard deviation of the RMS of the relative errors across frequency.

The same analysis was carried out for disks. As discussed in Sec. 3.2.3 disks with a fixed aspect ratio but varying volume, and a fixed volume but varying aspect ratio were simulated. The results for the disks with a fixed aspect ratio of $\sigma = 1$ and varying volume $V = \pi r^3$ are shown in Fig. 3.15a. The same pattern is seen here as with the spheres. Small volumes deviated quickly from the ideal radiation pattern, and larger volume diverge more slowly. Interestingly, the ideal volume again occurs with a radius of around 180 nm. While the volume of the cylinder and the sphere are not the same in this case, the cross sectional area is. This may point to the shape of the particle mattering less than its cross sectional area.

Fig. 3.15b shows the relative errors in radiation for disks with a fixed volume of $V = \pi 100^3$ nm^3 and varying aspect ratio. Here a relatively steady reduction in error is seen as the aspect ratio increases. This means that shorter, wider cylinders are acting more like dipoles than taller thinner ones. A line of the form $(1 + \sigma^{-1})$ was fitted to the data. This resulted in the fitted equation $(0.52 + 0.11\sigma^{-1})$. Using this equation, an aspect ratio of 0.33 has a slope of -1. So aspect ratios less than this will have a quick departure form the ideal, while aspect ratios larger than this will depart slowly.

From these studies we have found that for both spheres and disks there is an optimal volume to reproduce the radiation pattern of an ideal dipole. For disks it was also found that a larger aspect ratio mimics dipole radiation more closely.

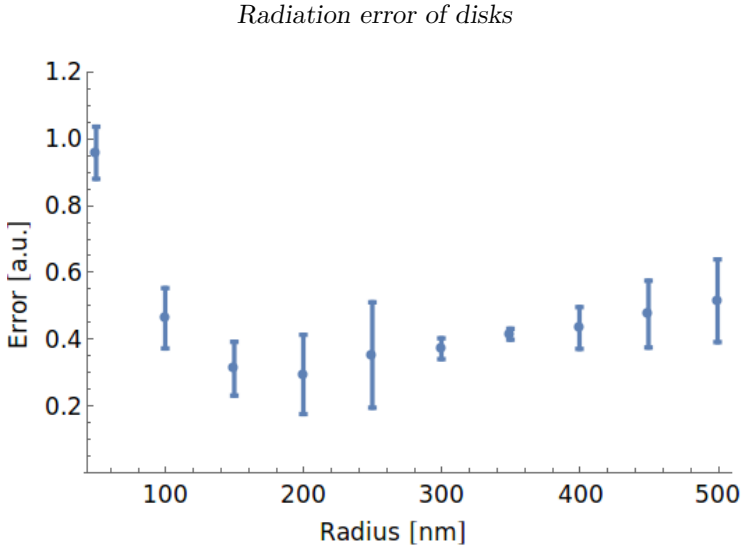

(a)

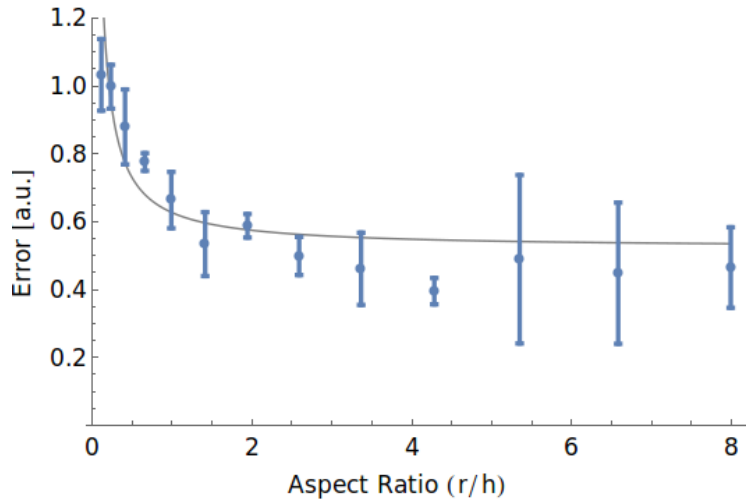

(b)

Figure 3.15: The RMS of the relative errors across frequency for disks with varied (a) volumes and (b) aspect ratios. In (b) the gray line is fitted to the data with form $1 + \sigma^{-1}$.

3.3 Two Particles

3.3.1 Non-interacting Dipoles

To gain an understanding of how scattered light can be directed, the dipole approximation of the scattering particles was used. Two non-interacting dipoles were placed at varying orientations relative to each other. To model the same driving field for both particles, each dipole had the same orientation and magnitude, with a phase difference corresponding to their separation. An illustration of this is shown in Fig. 3.16. Each of the relative positions in Table 3.3 was modeled, where the separation was relative to the radiated wavelength. A phase delay was also accounted for between the particles, representing the difference in position relative to the incoming plane wave.

In Fig. 3.17, two of the radiation patterns from these configurations are seen. From these preliminary results it is clear that, at least in the non-interacting dipole idealization, quite interesting scattering patterns can be obtained. By comparing these non-interacting results to results of interacting particles in the same configurations, the divergence from the ideal case can be evaluated. This can reveal how strongly the presence of one particle effects the radiation pattern of the other.

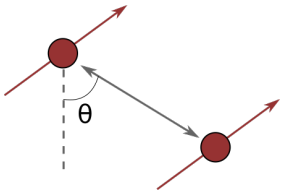

Figure 3.16: An example of the two dipole system.

Separation	*0.1 - 3.0 in 0.1 steps*
Angle	*0, 20, 30, 40, 50, 60, 80*
Polarization	*TE, TM*

Table 3.3: The combinations of parameters used to investigate two particle systems.

Radiation of two ideal dipoles

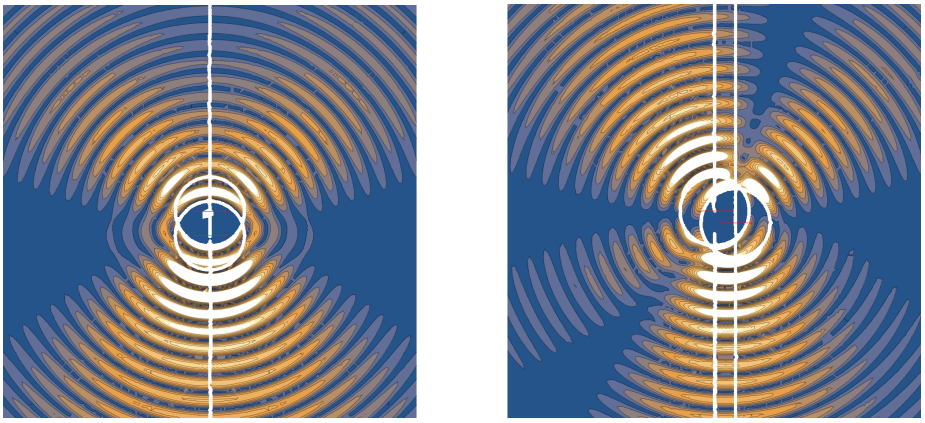

(a) (b)

Figure 3.17: Two examples of a radiation pattern that two dipoles can create. The interference pattern allows power to be directed. Both dipoles are separated by 0.7λ and have (a) $\theta = 0$, and (b) $\theta = 60$ degrees.

3.3.2 Interacting Particles

To compare the realistic scattering patterns of two plasmonic particles with those of the idealized radiating dipole model discussed in Sec. 3.3.1, both canonical shapes were simulated in HFSS. Using the same combinations as in Table 3.3, and surroundings of varying permittivity, each situation can be compared against the ideal dipole model. This will reveal how strong the dipole-dipole interaction is between the two particles.

To facilitate the comparison between the two sets of results, each set was normalized such that the total radiated time-averaged power was 1. Because only the radiation in the polar direction is of interest, to reduce the complexity of the situation the power of all the azimuthal angles at a given polar angle was summed together. This reduced the dimensions of each comparison from 614 field points, found in Sec. 3.1, to 19 field points, each representing a 10 degree step in the polar direction. Then, by comparing the amount of power radiated at each polar angle the radiation patterns were compared. Some examples of these comparisons can be seen in Fig. 3.18 where the two examples in the left column match relatively well, and the two on the right are mismatched. By computing the absolute and relative differences in radiation at each angle, and taking the root sum squared (RSS) of these values, as in Eq. (3.6), several measures of how well the radiation patterns matched were calculated.

$$M_{abs} = \sqrt{\sum_{\theta} \left(E_{\text{Dipole}} - E_{\text{HFSS}}\right)^2 \Big|_{\theta}} \tag{3.6a}$$

$$M_{rel} = \sqrt{\sum_{\theta} \left(\frac{E_{\text{Dipole}} - E_{\text{HFSS}}}{E_{\text{HFSS}}}\right)^2 \Big|_{\theta}} \tag{3.6b}$$

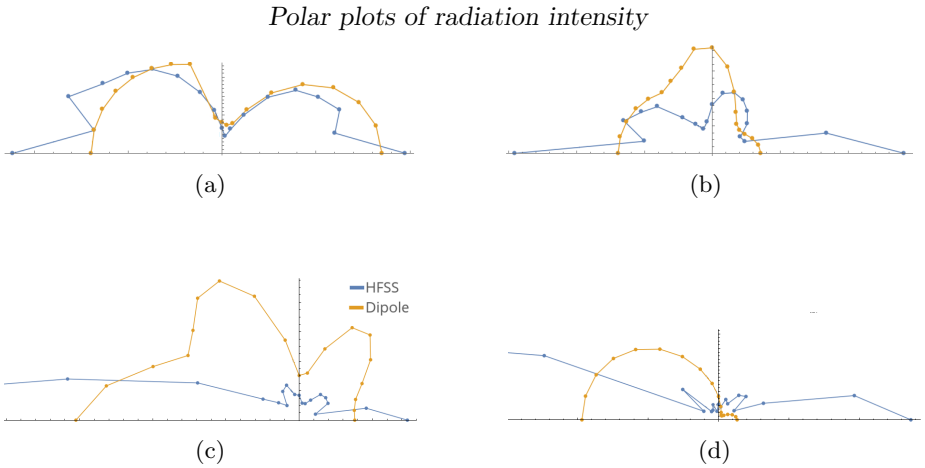

Figure 3.18: Examples of the radiation pattern comparison used for comparing the ideal dipole to the HFSS results. (a) and (c) match fairly well, while the (b) and (d) do not resemble each other much.

Spheres in Vacuum

Plotted in Figs. 3.19a and 3.19b are the magnitude of the absolute and relative errors of every orientation combination, with the mean value indicated by the disks. The first thing to notice is that the largest absolute mismatches occur near polar angles of 0 and 180 degrees. This occurs because the HFSS field values near these angle is much larger than those seen in the dipole model. When viewing the relative errors, though, the largest mismatches occur near 120 degrees. The absolute value of the relative errors over all angles have a mean value of $(47 \pm 56)\%$, indicating that the spheres do not match the ideal dipole model well.

Disks in Vacuum

Moving towards the more realizable particle structures, disks in vacuum were modeled in HFSS and compared to the ideal dipole model. The same analysis as was carried out for the spheres was carried out for the disks, and the errors are seen in Figs. 3.20a and 3.20b. The absolute value of the relative errors over all angles have a mean value of $(40 \pm 47)\%$, indicating that the disks match the ideal model no better than the spheres. Interestingly though, the shape of the errors for the disks and the spheres maintain roughly the same shape, with the largest absolute errors occurring near 0 and 180 degrees, and the largest relative errors near 120 degrees.

There may be the possibility that instead of a situation in HFSS matching the same situation in the dipole model, it may better match a situation with different parameters. For example, the HFSS model at 286 THz (1050 nm) with a 1.0λ separation and 30 degree angle between the particles may match the dipole simulation at 1.0λ but a 40 degree offset. To evaluate this, the relative errors for each dipole simulation were computed against each HFSS simulation. Then, the RSS of the errors where computed for each comparison as in Eq. (3.6), as resulting in a single value to compare how well the simulations

matched. The results of this comparison are seen in Fig. 3.21a, where each dipole model represents a row, and each HFSS simulation represents a column. The simulations are organized such that TE polarization occupy the the first half of the rows and columns, and TM the second half. Within each of these quadrants smaller separations are first, with increasing angle. Once all angles at that separation have been listed, then the separation is increased by one step. If the same situations matched best, diagonal lines of low error values would be expected within each of these sub-blocks. Instead of diagonal lines, though, horizontal and vertical lines of high and low error values seem to be present. In general the top-left corners of each sub-block appear to have higher error values indicating that the HFSS results match the ideal results better when the bottom particle is not being shaded.

A histogram of the RSS errors with a matching extreme value distribution (EVD) is shown in Fig. 3.21b. The errors follow closely the EVD which represents the distribution of extremum points of independent populations with identically distributed random variables. The EVD takes the form of

$$\frac{e^{(\alpha - x)/\beta}}{e^{e^{(\alpha - x)/\beta}}} \tag{3.7}$$

where $\alpha = 7.0$ is the location parameter, and $\beta = 2.7$ is the scale parameter. Given the origins of the error data and the EVD, it is unclear why they match so well.

Because no strong patterns were easily found in the RSS data, DBSCAN was used to cluster the results. A seven dimensional space was used to classify the data points, with parameters of the HFSS particle separation, angle, and frequency; the difference between the HFSS and ideal model's separation, angle, and polarization; and with the error value. This resulted in 83 clusters, too many clusters to easily recognize any patterns in. To simplify the dataset dimensional reduction was used, projecting the cluster centers to both a 2- and 3D subspace. However, still no trends were observed. Due to the lack of easily identifiable trends it does not appear that there is a correlation between the HFSS and dipole models.

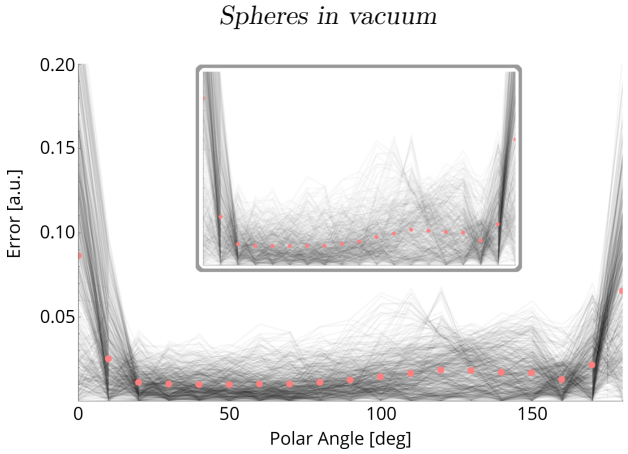

(a)

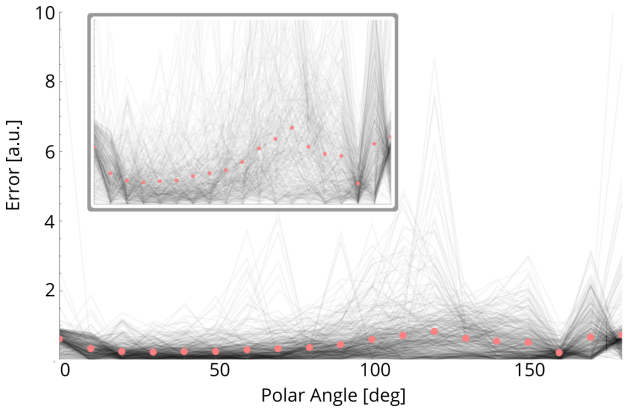

(b)

Figure 3.19: (a) Absolute and (b) relative error in radiation between of spheres in vacuum and ideal dipoles in the same arrangement. Each line represents a single arrangement. Mean values across all arrangements are indicated by the pink disks. **Insets:** Scaled images to show detail.

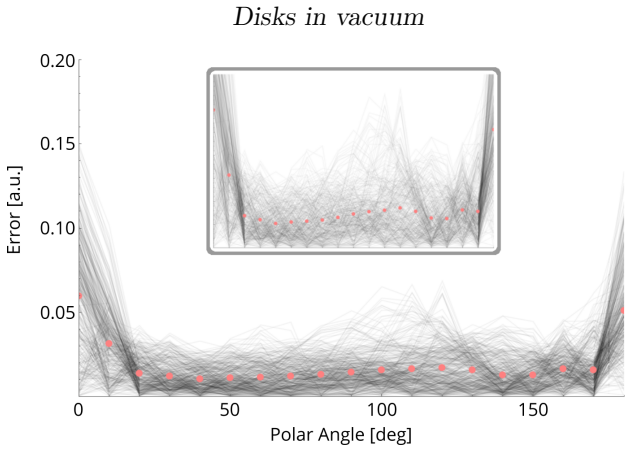

(a)

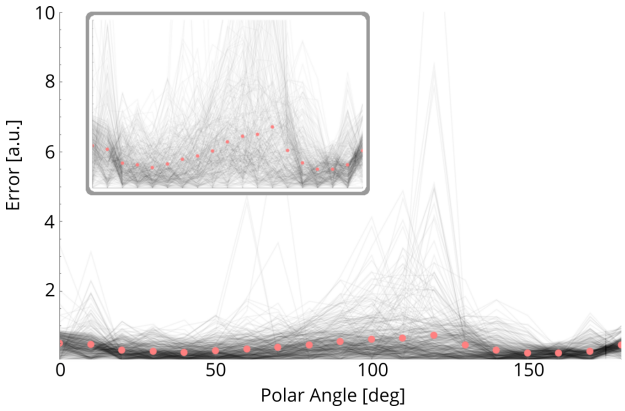

(b)

Figure 3.20: (a) Absolute and (b) relative error in radiation by direction of disks in vacuum. Mean values are indicated by the disks. **Insets:** Scaled images to show detail.

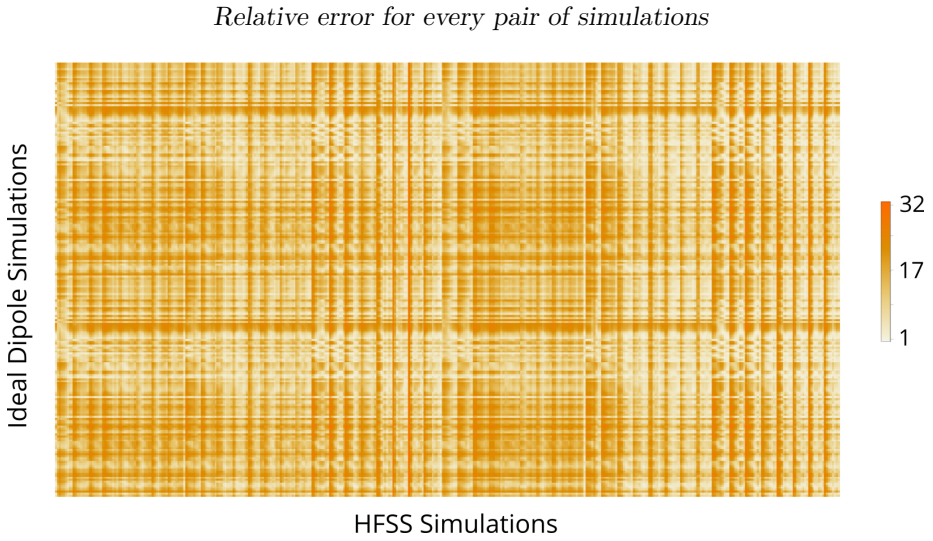

(a)

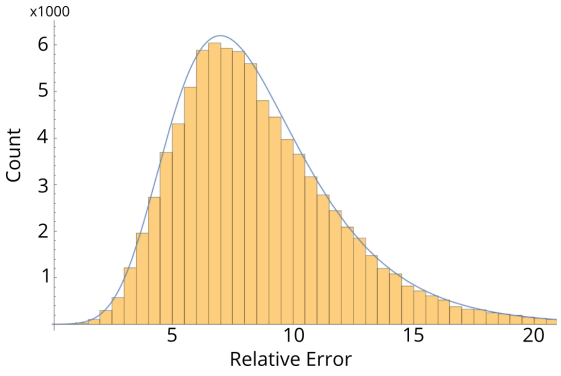

(b)

Figure 3.21: (a) RSS error in radiation by direction of disks in vacuum. The rows are the mathematical model and the columns are HFSS models. (b) A histogram of the RSS error values with the matching extreme value distribution.

Disks in Dielectric

Adding in a dielectric surrounding with relative permittivity of 1, 2, 3, or 4 to the disks, the same analysis carried out for the spheres was performed again. The results of the absolute and relative errors can be seen in Figs. 3.22a and 3.22b, respectively. Again, no clear pattern emerges for the error's dependence on the situation of the particles, or the relative permittivity. The mean of the absolute value of the relative error of all the permittivities was $(400 \pm 2300)\%$, with the individual permittivity statistics seen in Table 3.4. While a relative permittivity of 4 matches the ideal dipole model significantly better than the other situations, the matching is still quite bad.

Rel. Permittivity	1	2	3	4
Mean Rel. Error (%)	600 ± 3700	300 ± 900	600 ± 2600	100 ± 100

Table 3.4: Absolute value of the relative errors for disks embedded in materials of different permittivity.

Conclusion

By comparing HFSS results to an ideal dipole model of two particle in differing situations of separation, relative angle, embedding permittivity, polarization, and driving frequency it was found that significant errors between the radiation patterns exist. Further, by comparing the results of different situations together, it does not appear that there is a correlation between any of the HFSS results and the ideal model. There may have been the opportunity to add an extra component to the results of one of the models to allow easier modeling of these situations using the ideal dipole setup, however, due to the lack of consistency in the errors, it does not appear a simple term like this exists. However, the errors at 0 and 180 degrees are significantly larger in every situation than the intermediate angles. Therefore, it appears that using an ideal dipole model will not provide strong insight into how either an HFSS or actual model will behave. Due to the discrepancy between the ideal dipole model and the HFSS results, one must be chosen as "correct". As HFSS intrinsically accounts for more effects than the ideal dipole model, it will be used.

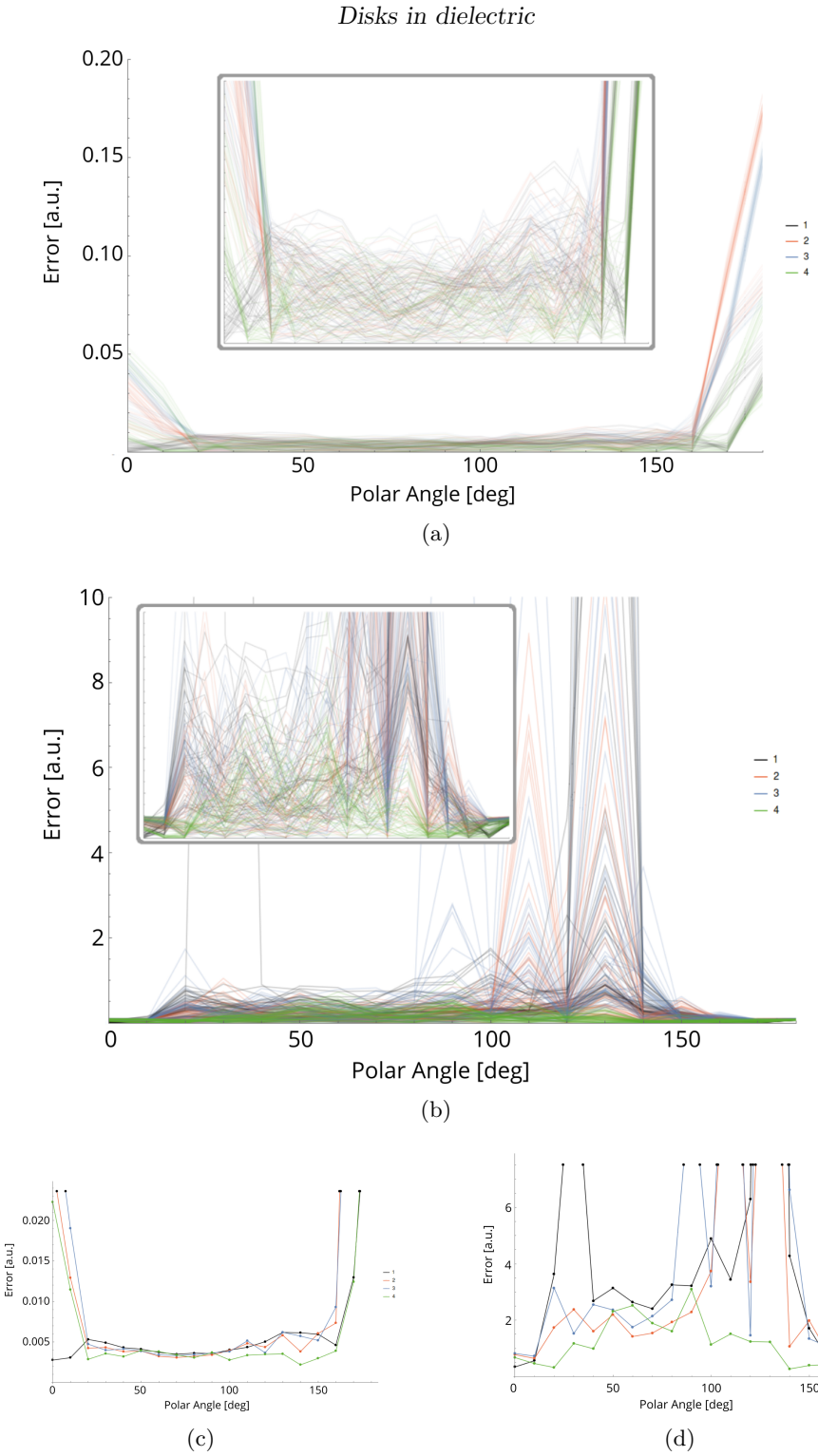

Figure 3.22: (a) Absolute and (b) relative error in radiation by direction of disks in a dielectric medium with varying relative permittivities. **Insets:** Scaled plots showing detail of lower error values. Mean value of the (c) absolute and (d) relative errors.

3.3.3 Radiation Analysis

Using the HFSS results, examining the two disk system in dielectric may provide insight into which array structures will yield the best scattering results. Fig. 3.23 shows the radiation patterns of each set up under differing permittivities of the surrounding material. All of the situations have high radiation in the forward (180 degrees) and backwards (0 degrees) directions with a relatively low scattering at the mid angles of interest. The $\epsilon = 4$ case does show a slight increase in towards $\pi/2$ but this is accompanied by a trade off in a smaller scattering cross section as discussed in Sec. 3.2.2, thus the effectiveness may be mitigated. It is somewhat surprising how similar the scattering patterns of these differing situations are, given that both the scattering cross section and wavelength of the radiated waves are affected.

Disks surrounded by different permittivities

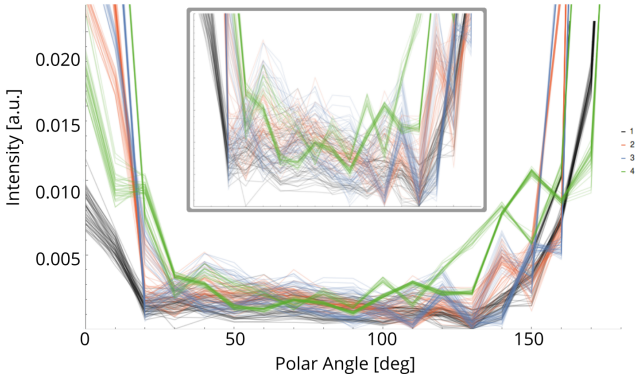

(a)

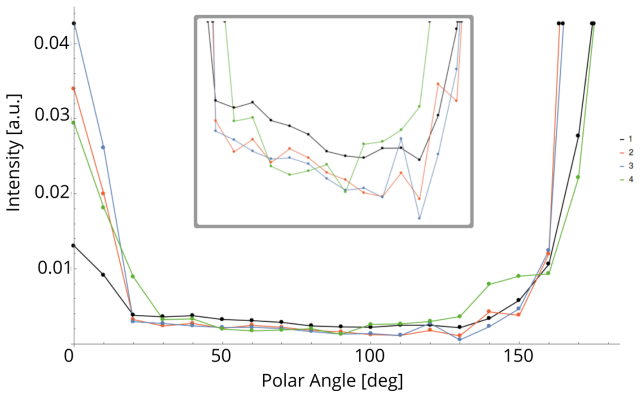

(b)

Figure 3.23: Selected data of the (a) raw and (b) mean radiation patterns by surrounding permittivity. Each line in (a) is the radiation pattern of a single simulation with a different set of separation and relative angle parameters. **Insets:** A scaled version of the plots to reveal detail.

In Figs. 3.24 radiation patterns from a selection of particle separations are

seen. While some data was excluded for illustrative purposes, the conclusions drawn used all available data. As with the permittivity, there is a strong forward and back scattering component of the radiation patterns, with much less towards the $\pi/2$ directions. There also doesn't appear to be any correlation of the particle separation and the radiation pattern, with little variation of the mean.

Disks separated by different lengths

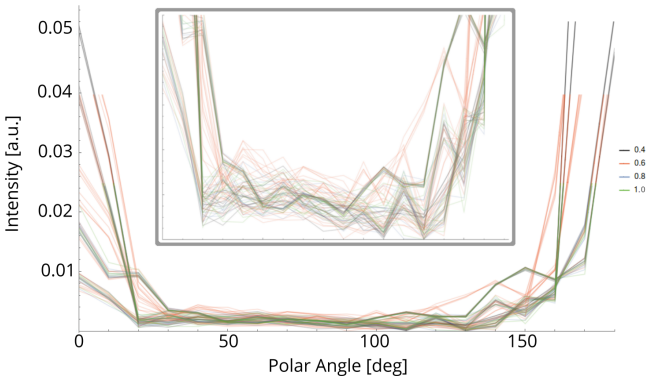

(a)

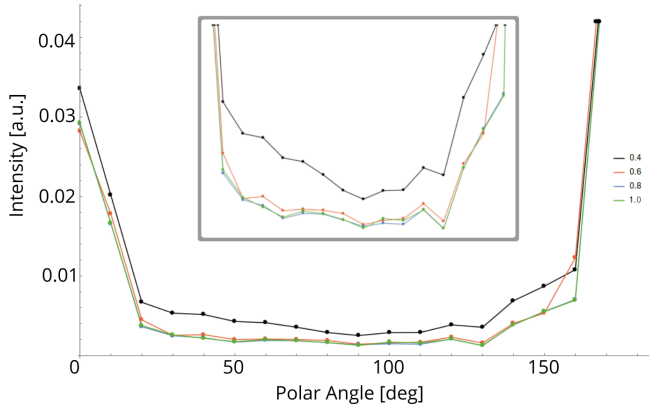

(b)

Figure 3.24: Selected data of the (a) raw and (b) mean radiation patterns by particle separation relative to the incident wavelength. Each line in (a) is the radiation pattern for a single simulation. **Insets:** A scaled version of the plots to reveal detail.

Figs. 3.25 shows the radiation patterns of selected particle angles. Again, illustrated data was limited for illustrative purposes, but conclusions were drawn for all data. The same pattern is seen with the correlation of angle and radiation pattern as with permittivity and separation. There is no general trend of the pattern that depends on the particle angle, with a low intermediate angle scattering and large scattering components at 0 and 180 degrees.

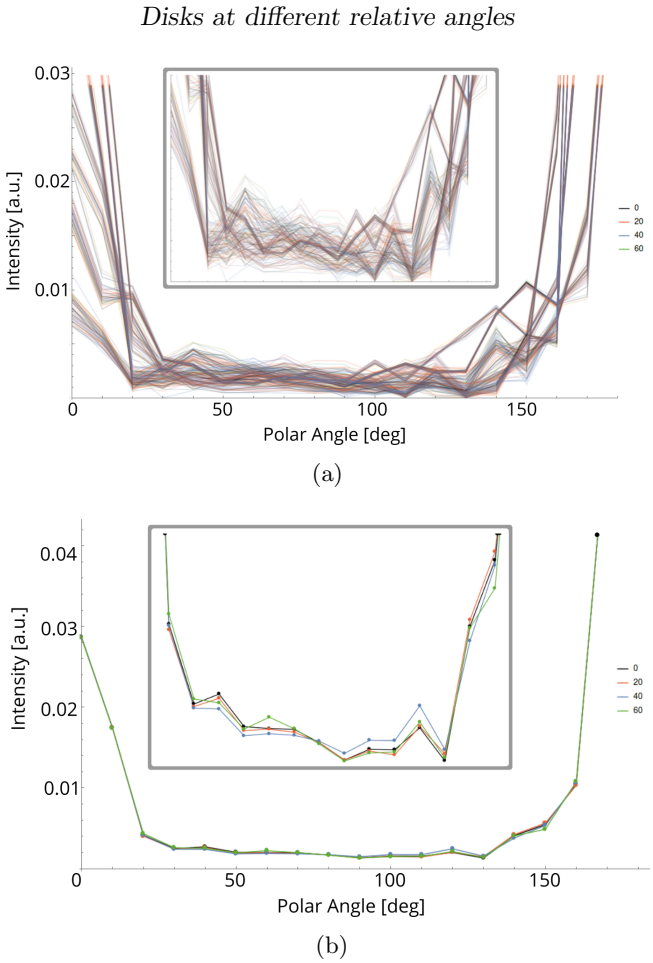

Figure 3.25: Selected data of the (a) raw and (b) mean radiation patterns by the relative angle of the particles. Each line in (a) is the radiation pattern for a single simulation. **Insets:** A scaled version of the plots to reveal detail.

Ideal Dipole Model

The same analysis that was carried out for the HFSS data was performed on the ideal dipole radiation patterns. Because permittivity only affects the wavelength of the radiated fields in the ideal model, it is not relevant as this is already accounted for via the separation parameter. Thus, an increasing particle separation parameter can be interpreted as either the particle separation being increased for a constant driving field frequency, or as the driving field frequency being increased for a constant article separation.

Fig. 3.26 shows the mean radiation patterns based on particle separation. As the separation increases there is a clear shift from back to forward scattering. Thus, as the particles move further apart, or the driving frequency becomes faster, more forward scattering is expected. In Fig. 3.27 the mean radiation pattern is seen as the angle between the particles varies. Here it is seen that as the angle of the particles increases there is a shift from forward scattering to

backscattering. Both of these results are in stark contrast to the HFSS results which showed no clear trend. This is another indication that the HFSS models are taking into account a more complicated situation than the dipole model, and that the dipole model is insufficient to model the actual situation.

Dipoles with different separation

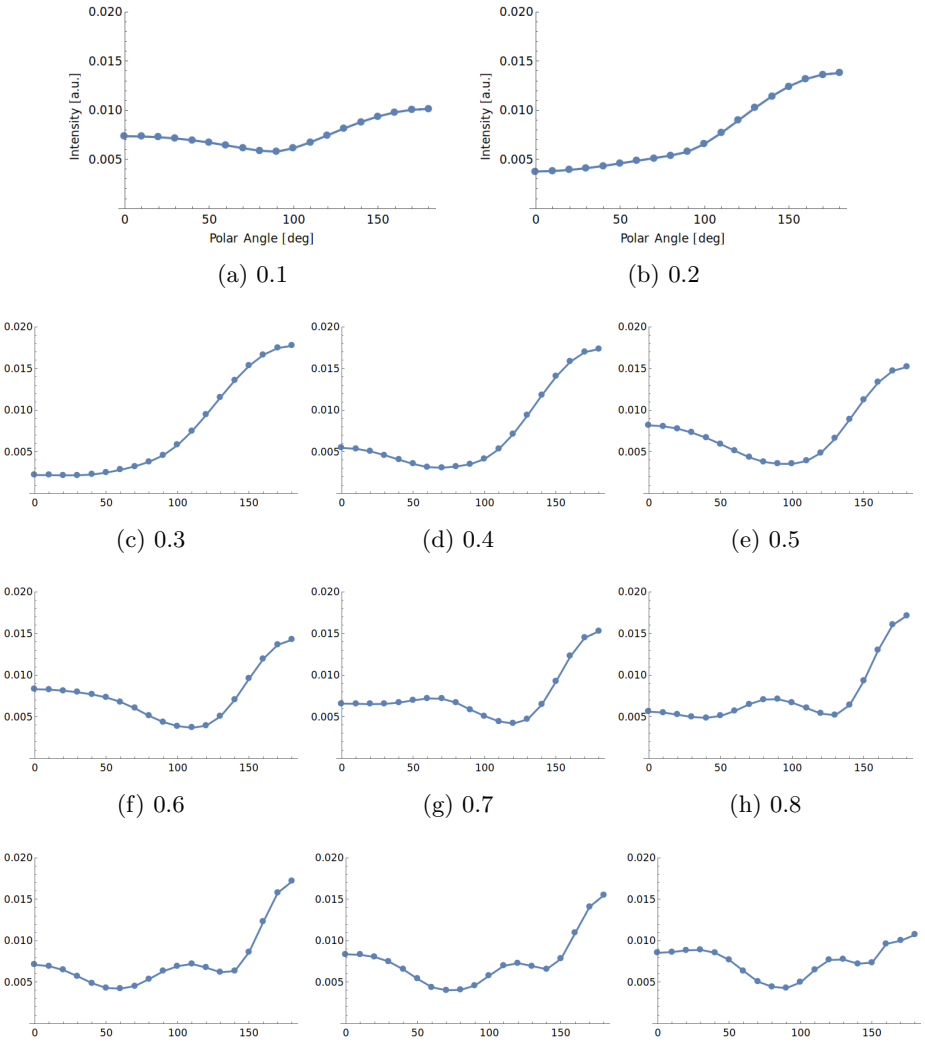

(a) 0.1 (b) 0.2

(c) 0.3 (d) 0.4 (e) 0.5

(f) 0.6 (g) 0.7 (h) 0.8

(i) 0.9 (j) 1.0 (k) 1.1

Figure 3.26: Mean radiation pattern of ideal dipoles with varying separation. The separation, given in the caption, is relative to the radiated wavelength.

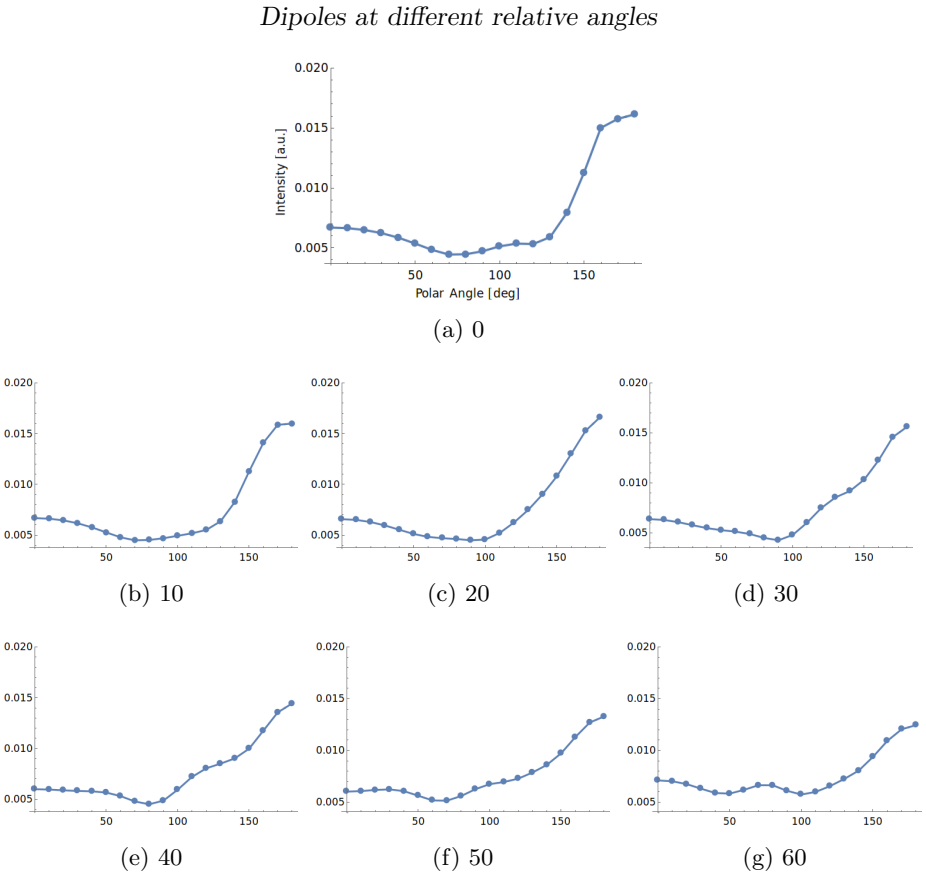

(a) 0

(b) 10 (c) 20 (d) 30

(e) 40 (f) 50 (g) 60

Figure 3.27: Mean radiation pattern of ideal dipoles with varying angle relative to each other.

3.4 Periodic Systems

3.4.1 Lattice Sum

When developing the lattice summation technique for both 2D and 3D lattices is Secs. D.1.1 and D.2.2, it is easy to get confused by the details and long equations[1]. Thus it pays off to examine an overview of the process that was followed in these derivations. To begin, space was broken into near and far regions, and the far region was further divided into regions ρ. In each region ρ the radiation function of interest $\mathbf{f}$ was placed at origin points γ creating a 1D lattice. This function only depended on the distance to the observation point $\hat{r}$, giving $f(\hat{r})$. $\mathbf{f}$ was then multiplied by a magnitude function M which depended on the lattice point and the position vector $\boldsymbol{\hat{r}}$. This resulted in a

[1]When deriving these equations in Appendix D, a formal approach was taken and terms were labeled precisely. However, these notations make the equations more cumbersome. At this point a bit of comfort is assumed with how the notation is being used, and some of the notation will be suppress in exchange for readability.

general equation of the form

$$\mathbf{E} = \sum_{\rho} \sum_{\gamma} \mathbf{f}(\imath) M(\gamma, \boldsymbol{\imath}) \tag{3.8}$$

For each ρ, $\hat{\mathbf{f}}$ was considered constant and f took the form $c_\rho \cdot \exp(ih(\imath))/\imath$ for $c_\rho = c(\delta\imath, \rho)$ constant and real in each region, and linear function h. The magnitude function could be divided into a part that only depends on γ and a part that only depends on $\hat{\boldsymbol{\imath}}$, $M(\gamma, \boldsymbol{\imath}) = M'(\hat{\boldsymbol{\imath}}) \times M''(\gamma)$.

$$\mathbf{E} \sim \sum_{\rho} c_\rho M'(\hat{\boldsymbol{\imath}}) \hat{\mathbf{f}} \sum_{\gamma} M''(\gamma) \frac{\exp\left(ih(\imath)\right)}{\imath} \tag{3.9}$$

$\imath$ was then approximated by $\imath \sim \imath_\beta + \gamma\delta\imath$ as $\imath \to \infty$, and $\imath_\beta \approx \beta\delta\imath$ was used in the magnitude giving

$$\begin{aligned}
\mathbf{E} &\sim \sum_{\rho} c_\rho M'(\hat{\boldsymbol{\imath}}) \hat{\mathbf{f}} \sum_{\gamma=0} M''(\gamma) \frac{\exp\left(ih(\imath_\beta + \gamma\delta\imath)\right)}{(\beta+\gamma)\delta\imath} \\
&= \sum_{\rho} c_\rho M'(\hat{\boldsymbol{\imath}}) \hat{\mathbf{f}} \sum_{\gamma=\beta} M''(\gamma-\beta) \frac{\exp\left(ih(\imath_\beta + (\gamma-\beta)\delta\imath)\right)}{\gamma\delta\imath} \\
&= \sum_{\rho} c_\rho M'(\hat{\boldsymbol{\imath}}) \frac{\exp\left(ih(\imath_\beta - \beta\delta\imath)\right)}{\delta\imath} \hat{\mathbf{f}} \sum_{\gamma=\beta} M''(\gamma-\beta) \frac{\exp\left(i\gamma h(\delta\imath)\right)}{\gamma}
\end{aligned} \tag{3.10}$$

As the observation point changes $\imath_\beta$ is the only parameter in the expression that changes. So each lattice region has a constant magnitude, regardless of the observation point, but a varying phase.

Field Evolution

To see how the phase of the field changes through the structure, recall that $\imath_\beta = |\mathbf{r}_0 - \mathbf{r}_\beta|$ with $\mathbf{r}_\beta = \alpha^i_\beta \mathbf{a}_i$. The evolution of the field can then be determined by taking the derivative of it relative to the observation point.

$$\begin{aligned}
\frac{\partial \mathbf{E}}{\partial \mathbf{r}_0} &= \sum_{\rho} \mathbf{E}_\rho \times i \frac{\partial}{\partial \mathbf{r}_0} h(\imath_\beta) \\
&= \sum_{\rho} \mathbf{E}_\rho \times i \frac{\partial}{\partial \mathbf{r}_0} h\left(\left[\left(r^j_0 - \alpha^i_\beta a^j_i \right)^2 \mathbb{1}_j \right]^{1/2} \right)
\end{aligned} \tag{3.11}$$

where $\mathbf{E}_\rho$ is the electric field from region ρ. In both the 2D and 3D cases h is a constant within each region, $h(\imath_\beta) = h_\rho \imath_\beta$. So

$$\frac{\partial}{\partial \mathbf{r}_0} h\left(\left[\left(r^j_0 - \alpha^i_\beta a^j_i \right)^2 \mathbb{1}_j \right]^{1/2} \right) = h_\rho \frac{\partial}{\partial \mathbf{r}_0} \left[\left(r^j_0 - \alpha^i_\beta a^j_i \right)^2 \mathbb{1}_j \right]^{1/2}$$

Finding the gradient for the directional derivative gives

$$\begin{aligned}\frac{\partial}{\partial r_0^{j_0}}\left[\left(r_0^j-\alpha_\beta^i a_i^j\right)^2\mathbb{1}_j\right]^{1/2} &= \frac{r_0^{j_0}-\alpha_\beta^i a_i^{j_0}}{\left[\left(r_0^j-\alpha_\beta^i a_i^j\right)^2\mathbb{1}_j\right]^{1/2}}\\ &= \frac{r_0^{j_0}-\alpha_\beta^i a_i^{j_0}}{\mathscr{r}_\beta}\\ &= \frac{\mathscr{r}_\beta^{j_0}}{\mathscr{r}_\beta}\end{aligned} \tag{3.12}$$

Yielding

$$\nabla\left[\left(r_0^j-\alpha_\beta^i a_i^j\right)^2\mathbb{1}_j\right]^{1/2} = \hat{\boldsymbol{\mathscr{r}}}_\beta \tag{3.13}$$

So changing $\mathbf{r}_0$ by $\mathbf{v}$ changes the electric field as

$$\left.\frac{\partial\mathbf{E}}{\partial\mathbf{r}_0}\right|_{\mathbf{v}} = \sum_\rho \mathbf{E}_\rho \times ih_\rho\hat{\boldsymbol{\mathscr{r}}}_\beta\cdot\mathbf{v} \tag{3.14}$$

If $\mathbf{v}$ is perpendicular to $\hat{\boldsymbol{\mathscr{r}}}_\beta$, this means the $\mathbf{E}_\rho$ does not change. Thus, fields from the far region are constant along spheres with centers at the β points in the lattice. Also, due to the factor of i, only a phase change can occur and there is no reliance on the distance the field is being observed from the source point. Note that this is different from a traveling EM spherical wave as the direction of the fields is also constant along these surfaces, as seen in Fig. 3.28.

Considering the separation function, Eqs. (D.120) and (D.130), the symmetry of the lattice is such that the separation from opposing directions is equal. In the 2D lattice this gives $\delta\mathscr{r}(\phi) = \delta\mathscr{r}(\phi+\pi)$, and in the 3D case $\delta\mathscr{r}(\theta,\phi) = \delta\mathscr{r}(\pi-\theta,\pi+\phi)$. Because the field strength is constant, and only a phase change occurs depending on the observation point, this halves the number of regions that must be considered when finding the total far region field.

Component Analysis and Region Limits

As the boundary between the near and far regions of the sum are pushed away from the origin more directions are included in the far region sum, making the model more accurate. If the β point for each lattice vector is the same β_0, then there are $(2\beta_0)^3$ lattice points in the near region and the number of directions included in the far region is the number of co-prime triplets with all elements less than or equal to β_0. This seems to grow exponentially fast, as seen in Fig. 3.29, so a balance between accuracy and required computational resources must be found [25].

In Figs. 3.30 the near region electric field magnitude is plotted for β_0 from 1 to 3. Comparing the square from $(-1,-1)$ to $(1,1)$ across the cases shows that the general radiation pattern remains the same across the three cases. However, the maximum magnitude of the field is much larger in $\beta_0 = 2$ than $\beta_0 = 1$, and roughly the same for $\beta_0 = 2$ and $\beta_0 = 3$.

In Figs. 3.31 the far region electric field magnitude as for the near region field, and in Figs. 3.32 the magnitude of the field from each region is shown.

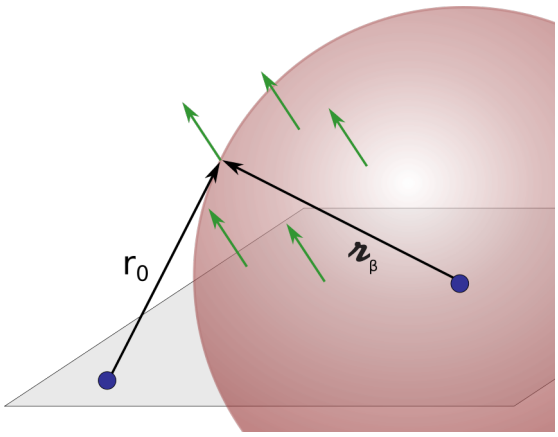

Figure 3.28: The constant spherical field emanating from a β point of the lattice. The field vectors, in green, are constant on the surface and only change phase between surfaces.

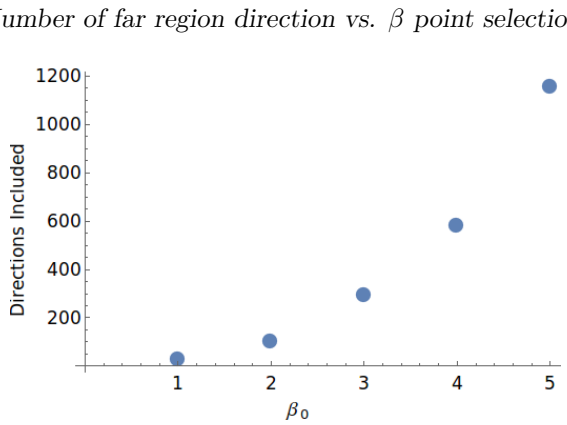

Figure 3.29: The number of directions in the far region sum when each lattice vector has the same bound.

Again, moving from $\beta_0 = 1$ to $\beta_0 = 2$ shows a significant change, especially in the region magnitudes, while moving from $\beta_0 = 2$ to $\beta_0 = 3$ does not have a significant impact. Combining the near region field and the far region field gives the total field, seen in Figs. 3.33 Here, the same pattern is seen when change the β_0 value.

The computational resources required to calculate the fields in the near and far region scale roughly linearly with the number of points in that region. Thus, if the time to calculate the fields with $\beta_0 = i$ is t_i, then $t_2 = 2t_1$ and $t_3 = 4t_1$. Balancing the the gain inaccuracy with the resources, it was decided to use $\beta_0 = 2$ for further results, unless specified.

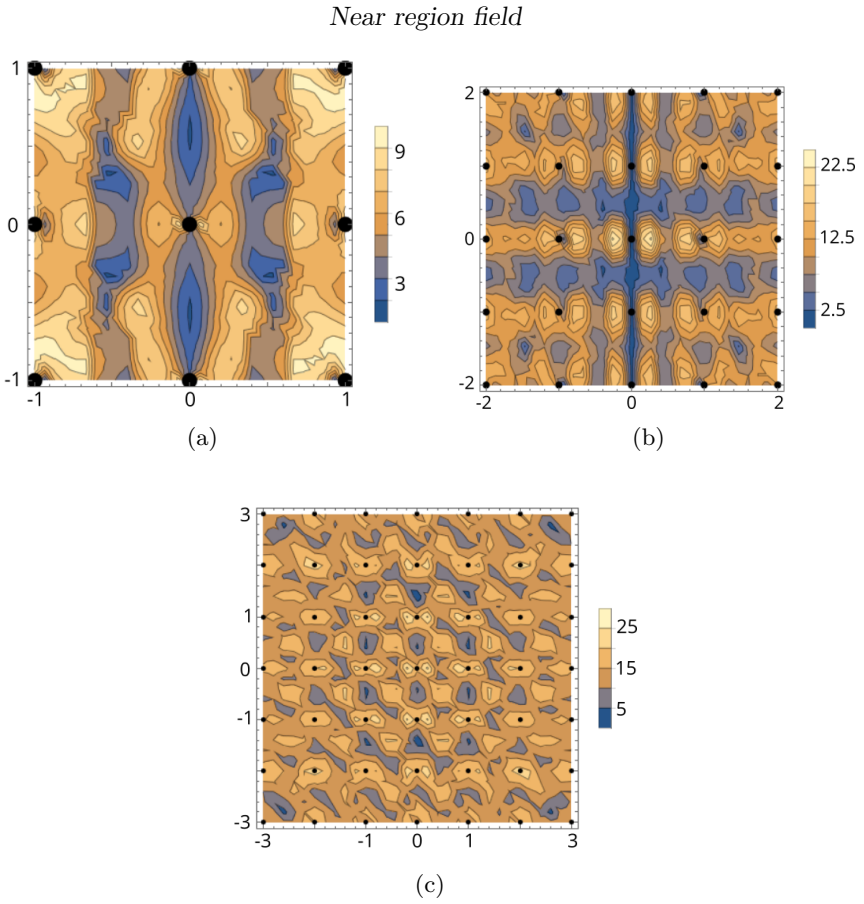

Figure 3.30: The electric field magnitude of the near region, computed directly, with each lattice vector have the equal β points of (a) 1, (b) 2, and (c) 3. The black points indicate the position of the lattice points in the XY plane.

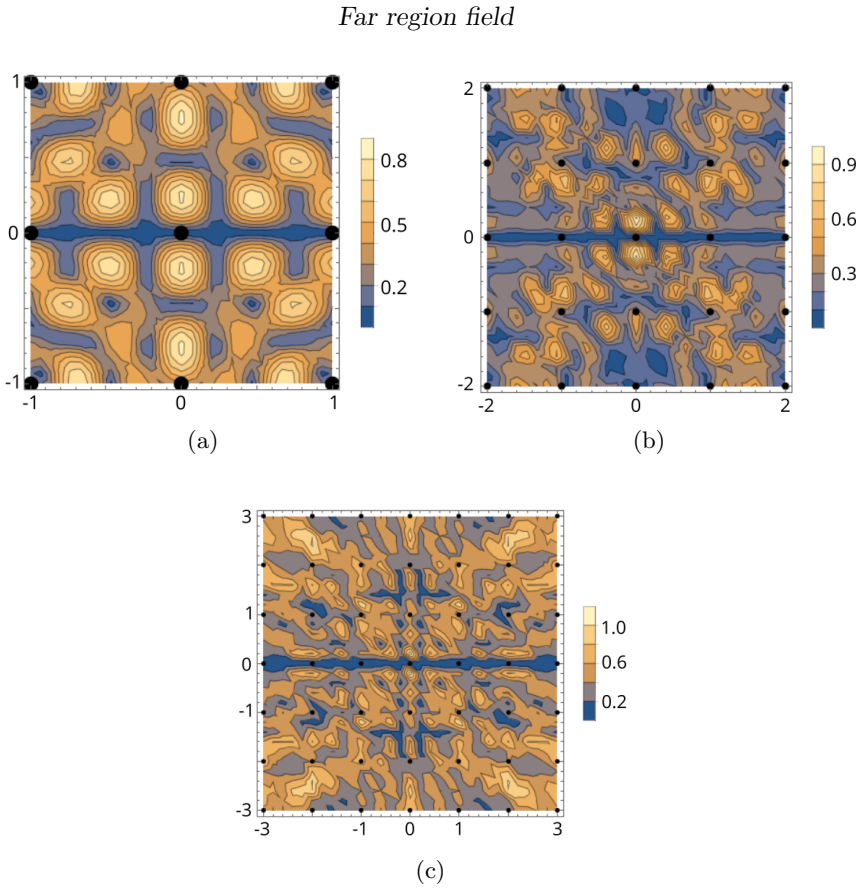

Figure 3.31: The electric field of the far region with each lattice vector have the equal β points of (a) 1, (b) 2, and (c) 3. The black points indicate the position of the lattice points in the XY plane.

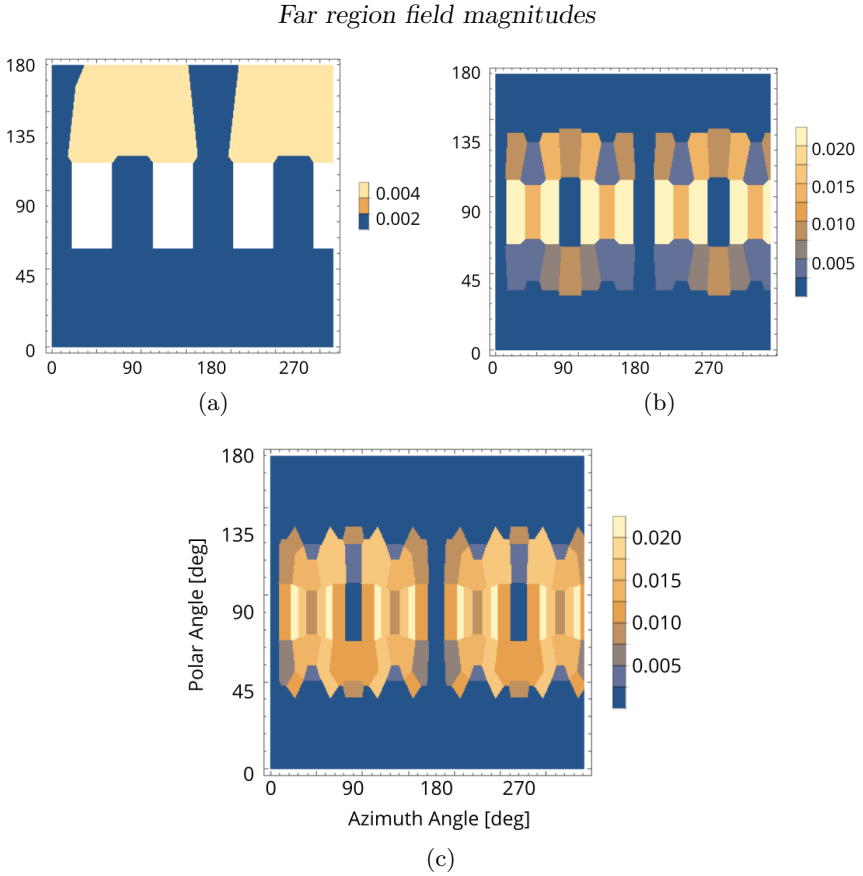

Figure 3.32: The electric field magnitude of the far regions, with each lattice vector have the equal β points of (a) 1, (b) 2, and (c) 3. The white space is a large region without a direction.

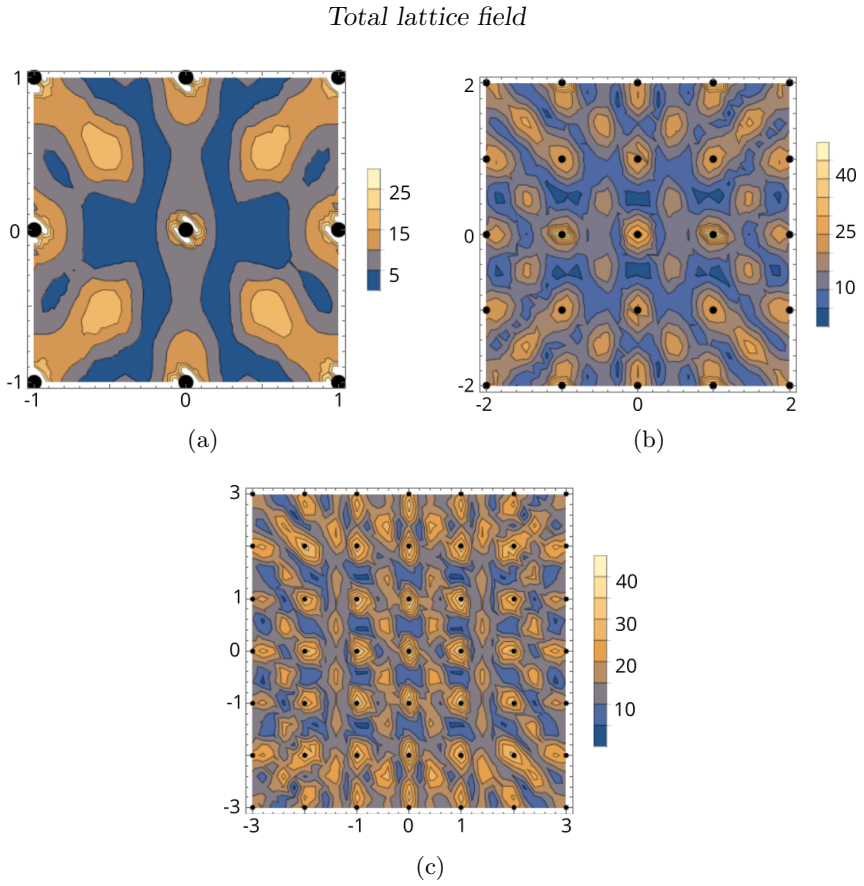

Figure 3.33: The total electric field magnitude, with each lattice vector have the equal β points of (a) 1, (b) 2, and (c) 3. The black points indicate the position of the lattice points in the XY plane.

3.4.2 Dominant Region

In the far region each direction has a maximum magnitude given by $c_\rho M'(\hat{\boldsymbol{r}})$. However, this magnitude is scaled by

$$\sum_\gamma M''(\gamma)\frac{\exp(ih(r))}{r} \tag{3.15}$$

This term takes into account the phase shift between particles in the given direction, accounting for the interference of their fields. So by adjusting the lattice parameters to minimize or maximize this term for a given direction, the relevance of the far region field from that direction can be tuned. To determine when the far region terms dominate the field and when the near region terms dominate the maximum field magnitudes from each can be evaluated.

From Eq. (2.2), the maximum magnitude for a given region occurs when $\nu^1 = 1$, corresponding to the case of no absorption and perfect reflection at both interfaces, and when $\zeta^2 = 0 \mod 2\pi$. Recalling the equations for ζ^1 and ζ^2 are

$$\zeta^1 = \frac{\omega}{c}\delta r(\theta,\phi) - 2\pi\frac{\delta r(\theta,\phi)\sin\theta}{\lambda_0}\sin\theta_0\cos(\phi-\phi_0) \tag{3.16a}$$

$$\zeta^2 = -\frac{2\pi\sin\theta}{2\delta r(\theta,\phi+\frac{\pi}{2})\lambda_0}\sin\theta_0\sin(\phi_0-\phi) \tag{3.16b}$$

ζ^2 can be substituted in to the second term of ζ^1, giving

$$\zeta^1 = \frac{\omega}{c}\delta r(\theta,\phi) + 2\frac{\delta r(\theta,\phi)\delta r(\theta,\phi+\frac{\pi}{2})}{\tan(\phi_0-\phi)}\zeta^2 \tag{3.17}$$

Assuming that $\phi_0 \neq \phi$, then

$$\zeta^1 = \frac{\omega}{c}\delta r(\theta,\phi) \tag{3.18}$$

So ζ^1 represents how in-phase the particles are due to their separation. It will also be assumed that r_β and $\boldsymbol{r}$ are such that the factors involving them are maximized, and constants will be ignored. With these assumptions the first two term in the brackets of Eq. (2.2) are equal, and thus cancel, leaving the maximum angle for a region of

$$E_{max} = -\frac{e^{i\zeta^1\beta}}{\delta r(\theta,\phi)} \tag{3.19}$$

$$\times\left\{\begin{array}{l}\left[\mathrm{Li}_1\left(e^{i\zeta^1}\right)+\sum_{\gamma=1}^{\beta-1}\frac{e^{i\zeta^1\gamma}}{\gamma}\right]\\ +\left[\mathrm{Li}_2\left(e^{i\zeta^1}\right)+\sum_{\gamma=1}^{\beta-1}\frac{e^{i\zeta^1\gamma}}{\gamma^2}\right]\\ +\frac{1}{3}\left[\mathrm{Li}_3\left(e^{i\zeta^1}\right)+\sum_{\gamma=1}^{\beta-1}\frac{e^{i\zeta^1\gamma}}{\gamma^3}\right]\end{array}\right\} \tag{3.20}$$

where $\mathrm{Li}_1(z) = \ln(1-z)$.

Figs. 3.34 show the real part, imaginary part, and norm of the polylogarithm functions. Both Li_2 and Li_3 stay finite, however Li_1 diverges for arguments equal to $0 \mod 2\pi$. The summation term corresponding to the Li_1 component adds an oscillatory behavior to the real and imaginary parts but leaves the shape of the norm unaffected. The summation terms for the Li_2 and Li_3 components do not drastically change their behavior, only modifying their amplitude.

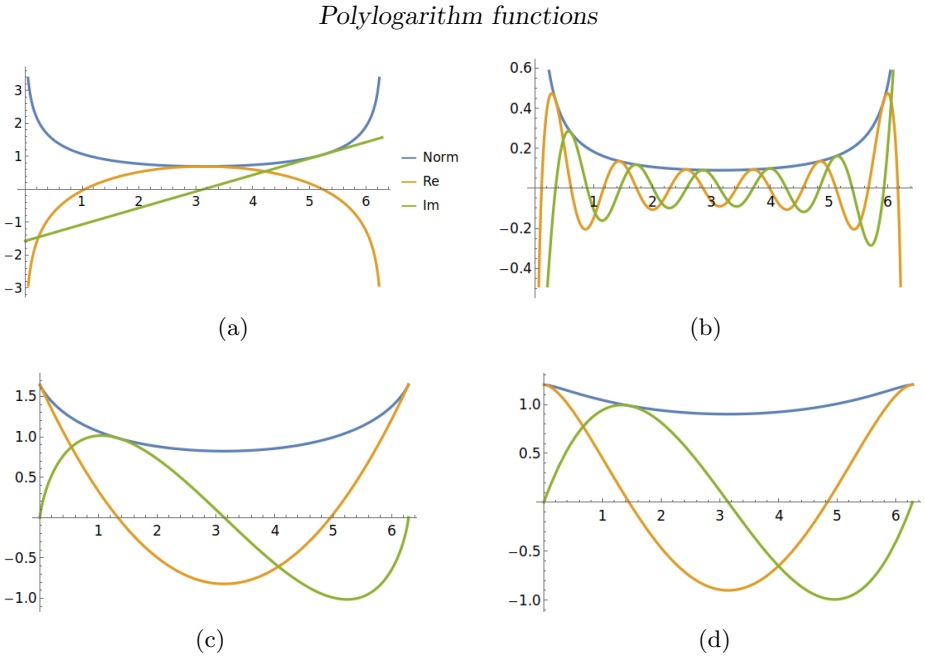

Figure 3.34: The real part, imaginary part, and norm of (a) $\mathrm{Li}_1(e^{ix}) = \ln(1 - e^{ix})$, (b) $\mathrm{Li}_1(e^{ix}) + \sum_\gamma e^{ix}/\gamma$ with $\gamma = 5$, (c) $\mathrm{Li}_2(e^{ix})$, and (d) $\mathrm{Li}_3(e^{ix})$.

To determine how precisely the separation of the particles must be to be in resonance something similar to the half width at half maximum (HWHM) can be computed. Here, though, the divergence does not allow a maximum to be calculated. Instead the half width will be calculated at a multiple of the minimum value of the norm (HWMN). A somewhat arbitrary, but natural, choice of the multiple is e. The minimum value of $\left|\mathrm{Li}_1(e^{ix})\right|$ occurs at $x = \pi$ and has value $\ln 2$. Thus the half width will be determined at $e \ln 2$. Using

$$\begin{aligned} a &= \left|1 - e^{i\zeta^1}\right| = \sqrt{(1 - \cos\zeta^1)^2 + \sin^2\zeta^1} \\ b &= \arg\left(1 - e^{i\zeta^1}\right) \end{aligned} \tag{3.21}$$

For an arbitrary value c

$$\begin{aligned} c &= \left|\mathrm{Li}_1\, e^{i\zeta^1}\right| \\ &= \left|\ln(1-e^{i\zeta^1})\right| \\ &= \left|\ln(ae^{ib})\right| \\ &= \sqrt{\ln^2 a + b^2} \end{aligned} \tag{3.22}$$

Because the resonant peak is of interest ζ^1 will be small mod 2π, $\zeta^1 \to 0$ mod 2π. Taking the first order Taylor expansion of the trigonometric functions in Eqs. (3.21) has $a \to (1-\cos\zeta^1)$ and $b \to 0$. This assumption allows Eq. (3.22) to be solved, but also underestimates the HWMN.

$$\begin{aligned} c &= \sqrt{\ln^2 a + b^2} \\ &\leq \sqrt{\ln^2 a} \\ &\leq |\ln a| \end{aligned}$$

Because $a = \left(1-\cos\zeta^1\right) < 1, \ln a < 0$, so

$$\begin{aligned} c &\leq -\ln a \\ e^{-c} &\leq 1-\cos\zeta^1 \\ \zeta^1 &\leq \arccos\left(1-e^{-c}\right) \end{aligned} \tag{3.23}$$

Fig. 3.35a shows the HWMN for a given multiplier c. For $c = e\ln 2$, the HWMN is 32 degrees. Assuming that the values of the separation function are randomly distributed mod 2π, as shown in Fig. 3.35b, the percentage of regions that are considered in-phase for a given frequency is HWMN$/\pi$. So for $c = e\ln 2$, 17.8% of the regions will be in phase. Thus, to make the far region relevant, a lattice structure that concentrates the separation function within the HWMN mod 2π should be constructed.

In this vein, 500 lattices were randomly generated. The angle between the lattice vectors was uniformly distributed between 0.001 and π, and the ratio of their norms between 1 and 15, as seen in Fig. 3.35d. Fig. 3.35c shows a histogram of lattices by the percent of far regions within the HWMN of $c = e\ln 2$ centered at 0. On average, (17.8±1.5)% of the far regions fell within the HWMN, matching the random distribution extremely closely. This analysis was run for several other lattice parameter distribution with no significant change to this number. Thus, it appears regardless of the lattice, the separation function is evenly distributed mod 2π. If $\phi_0 = \phi$, the same analysis holds because only a phase shift is incurred.

So far only the maximum possible magnitude for each region has been analyzed. One of the largest factors that has been ignored in this analysis is the reflection coefficients. In an actual reflector, although the bottom interface will be mirrored, the top interface, with the absorbing layers, will have a small reflection coefficient to allow light to be re-absorbed. This further diminished the role of the far regions. Combined with the analysis, this points to the far region only being of consequence under extremely specific conditions. Thus, only the near region should be considered to design the back reflector.

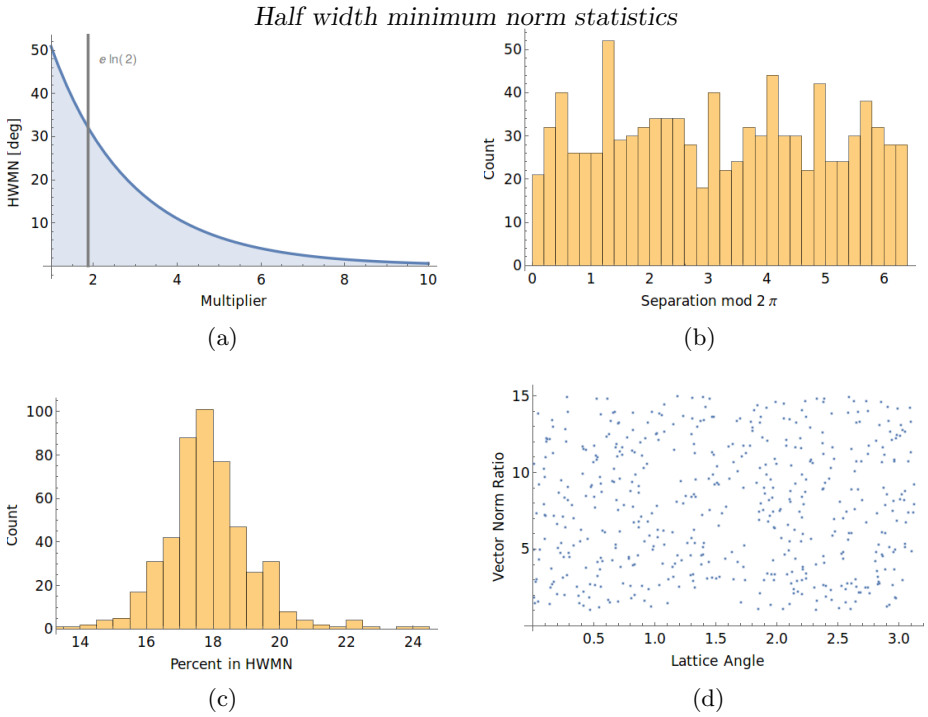

Figure 3.35: (a) The half width min norm (HWMN) for different multiplier values, with the gray line indicating $e \ln 2$. (b) The separation for regions in a square lattice with unit vectors and lattice constants up to 40. (c) The percentage of lattice direction within the HWMN of randomly generated lattices. (d) The distribution of lattice parameters for the randomly generated lattices.

3.4.3 Near Region Field

Considering only the near region field, a preliminary investigation in to the possible fields was performed. Several structures with two particle layers were modeled. An example of the near region virtual lattice for one of these devices is seen in Fig. 3.36. The fields for several of these devices are seen in Figs. 3.37. From the limited set of examples explored, all the fields were similar to the ones shown. Unfortunately none of these fields showed promise to scatter in an efficient manner.

3.5 Realistic System

To mimic the realistic systems measured in Sec. 6.3.1 a model with particles mimicking the statistics of sample 1.6 in Table 6.1 was created. Two of these layers were created so the devices fabricated in Table 6.2 could be simulated. Images of these layers are in Fig. 3.38, and the statistics are in Table 3.5. All particles had a height of 20 nm.

The simulated model varies from the realistic devices in several ways. First, the surface morphology of the SiO_2 was not replicated. This is because it is unknown how the particles form on a rough surface, discussed in Sec. 6.3.2.

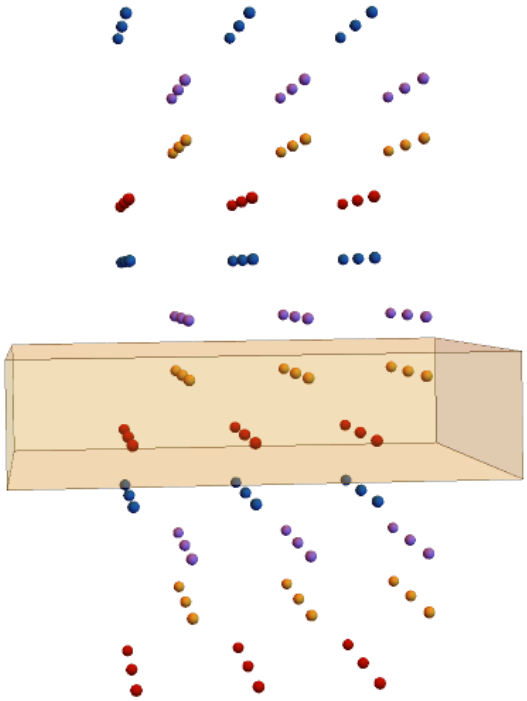

Figure 3.36: The virtual lattice of a device with two particle layers. Both layers have a square unit cell with unit side length. The bottom layer is offset by $(1/2, 1/2)$ relative to the top layer.

Possible examples are shown in Fig. 3.39. This is also why the particle statistics for particles on a flat surface were used for both layers. As discussed in Sec. 6.3, the top layer of particles in the fabricated devices actually have a smaller particle radius than the first layer of particles.

The model consisted of a half infinite air and a half infinite SiO_2 layers. The particles were embedded in the SiO_2 layer with the top layer either 50 or 100 nm from the interface with air, called the *buffer* length. The bottom layer of particles had a center-to-center distance of either 50 or 100 nm from the top layer, known as the *layer separation*. Simulations were run between 750 and 1050 nm at 50 nm steps to be compared with the angular intensity distribution measurements discussed in Sec. 6.4. Table 3.6 provides the frequencies of the relevant wavelengths.

In Fig. 3.40a the radiation pattern of each of the four simulation config-

Layer	Radius [nm]	Coverage [%]
Top	159 ± 39	61.2
Bottom	159 ± 38	61.3

Table 3.5: Layer properties for realistic simulation.

urations at each wavelength is visible. All of the simulations follow the same general shape with a small amount of back scattering up to 30°, then a slowly increasing intensity through 140°, and finally a greater intensity increase to forward scattering at 180°. Fig. 3.40b shows the radiation patterns of the samples averaged over frequency. There is no significant difference of trends in the data, showing that the frequency does not have an overall effect on the radiation pattern. Fig. 3.40c shows the radiation pattern averaged over the separation and buffer thickness, listed respectively in the legend. Here a trend does appear. The simulations with the same separation have roughly equivalent radiation patterns, with the large separation leading to more scattering.

Frequency [THz]	286	300	315	333	353	375	400
Wavelength [nm]	1050	1000	950	900	850	800	750

Table 3.6: A conversion table for selected wavelengths.

Fields of multi-layered structures

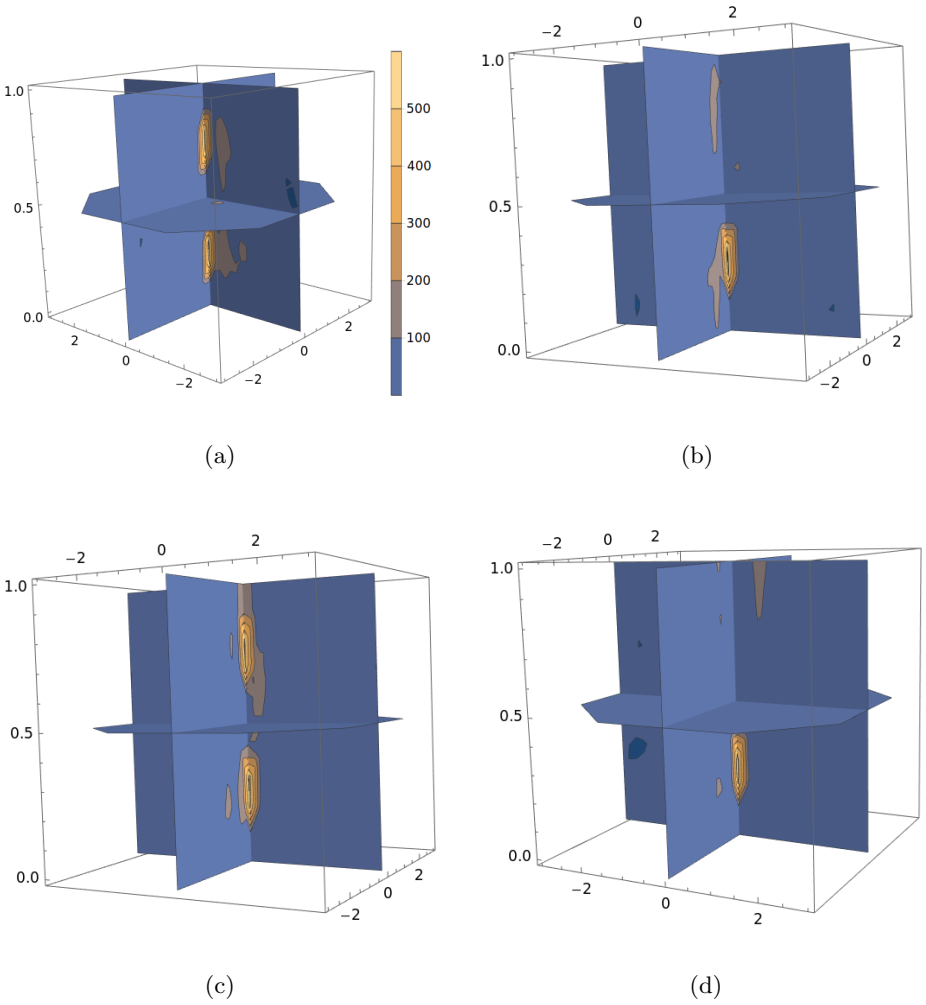

Figure 3.37: The electric field magnitudes for varying devices with two lattices. The top lattice in each case had a unit length square unit cell. The bottom layer in (a), (b), and (d) had the same unit cell, but was offset by (a) $(0, 0)$, (b) $(0.25, 0)$, (d) $(0.25, 0.25)$. In (c) the bottom lattice is not offset, but has lattice vectors each with unit length, but with 45 degrees between them. The field in the XY-plane is the field at the top interface of the device.

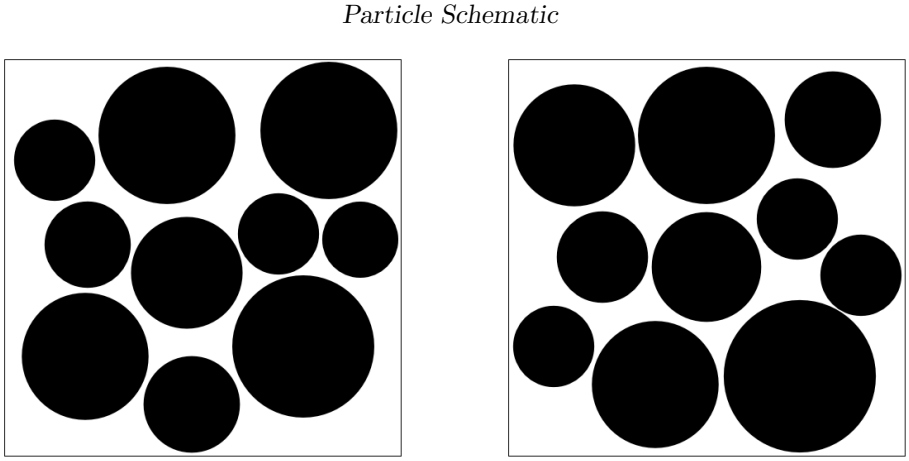

(a) (b)

Figure 3.38: Layout of the (a) top and (b) bottom layer used in the HFSS simulations.

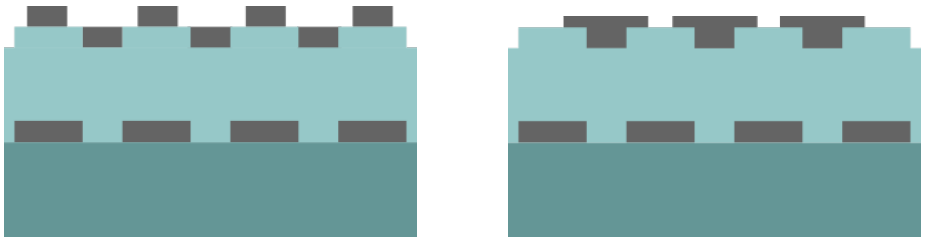

(a) (b)

Figure 3.39: Schematics of possible particle morphologies when deposited on a rough surface.

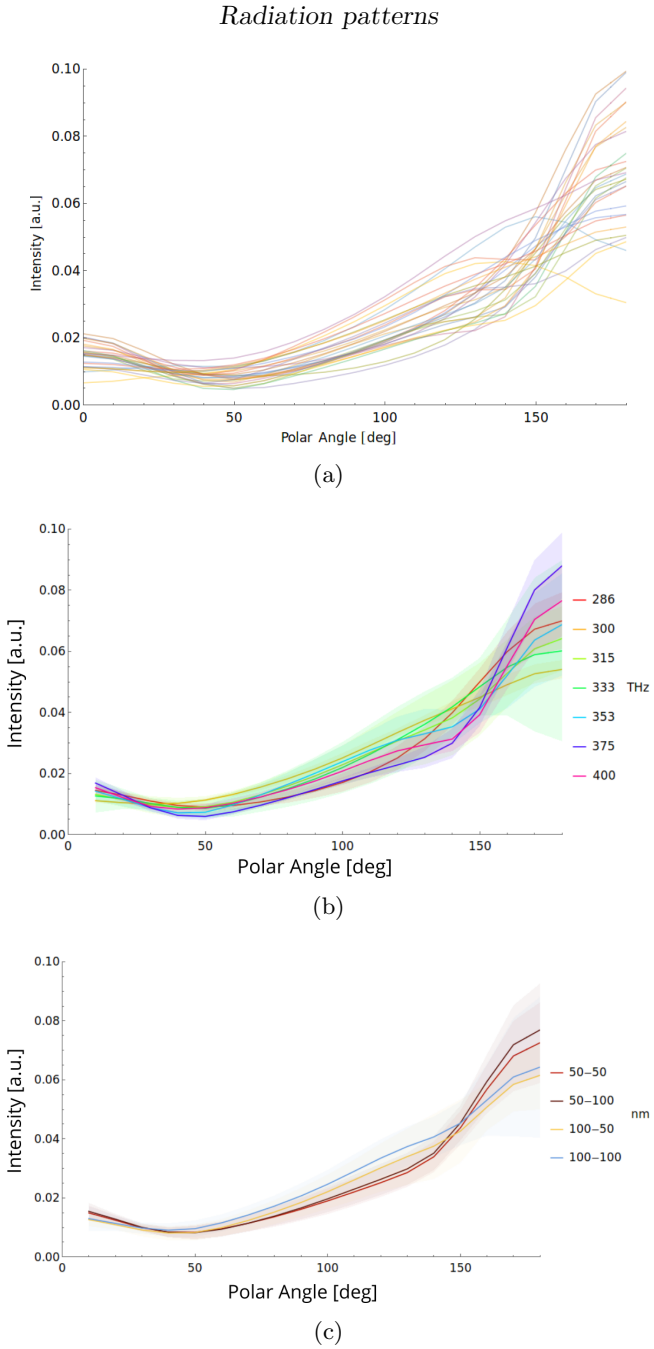

Figure 3.40: (a) Radiation pattern of all simulations. (b) Radiation pattern of the simulations averaged by frequency. (c) Radiation pattern averaged over separation and buffer thickness, represented respectively in the legend. Lines are the mean values and shaded areas represent errors.

Chapter 4

Modeling Conclusion

To better understand how a reflector made from layers of plasmonic particles behaves, the system was decomposed into several parts. First, the behavior of individual particles were investigated using Mie Theory and HFSS simulations. Through these investigations it was found that there is an optimal particle size to produce ideal dipole radiation. If the particles become too small absorption effects quickly take over, while particles that are too large slowly deviate from the ideal case. For cylinders, it was also found that the radius to height ratio of the particle affects its radiation pattern, with a larger radius to height ratio leading to more absorption. The scattering cross sections were also investigated with the HFSS results showed a significant divergence from Mie theory.

A two dipole system was then considered so the effects of interference could be evaluated. Comparing an ideal dipole model to HFSS results showed that the field from each particle affects the radiation of the other significantly. The radiation patterns of the HFSS results and ideal dipole model were then considered separately. The HFSS results showed that forward scattering to 180° and backscattering to 0° are most dominant regardless of the particle orientations. The ideal dipole model, however, showed that as the orientation of the particles relative to each other change, the radiation pattern varies as well. While forward scattering remained most dominant, a relatively large amount of power could also be back scattered.

To investigate the effect of the lattice, the lattice summation technique developed in Appendix D was used. By taking the extreme values for each far region in a lattice it was determined that the field from the far regions are only significant in very specific situations. Thus, only the field in the near region, which is calculated directly, must be considered.

Finally, using parameters measured from fabricated devices, a realistic HFSS model of a two-layered lattice structure was simulated. The simple model matched the radius and distribution of particle sizes but did not take in to account the surface morphology. The results showed a similar radiation pattern regardless of incident wavelength or buffer layer thickness. However, the separation between the bottom and top layer of particles played a role in the radiation pattern, with a larger separation scattering more strongly.

Chapter 5

Fabrication Theory

5.1 Lithography

Lithography allows the creation of nanoscale structures, using a masking method to create layers of different patterns.

5.1.1 Optical Lithography

One of the major lithography processes, optical lithography, uses light exposure to alter the properties of a material. This material can then be etched away in a negative or positive pattern, allowing only parts of the desired material to be manipulated. There are four major steps in this lithographic process. First the sample is spin coated in resist. The sample is then placed under a mask of the desired pattern and illuminated for a brief period suing short wavelength light. If a positive resist pattern is used, the bonds in the exposed are of the resist are weakened. In a negative resist the exposed area are strengthened. After the exposure, the sample is washed in developer, removing the more weakly bound resist areas. Thus, the resist of a positive pattern remains in the unexposed areas, while a negative pattern retains its resist in the exposed areas. An illustration of this difference can be seen in Fig. 5.1.

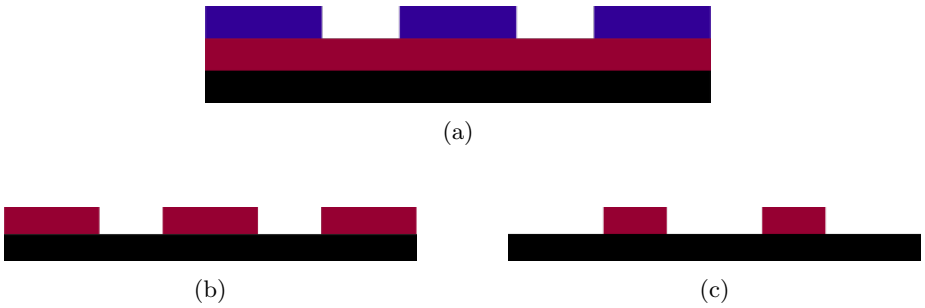

Figure 5.1: The mask in blue, resin in red, and substrate in black (a) before etching, and after etching of a (b) positive resist, and (c) negative resist.

After the resist is in place, the sample can receive a deposition. The mask acts to block the deposition on certain areas of the sample. Finally, after the deposition, the resist is then etched away in a chemical bath, leaving behind the desired pattern of deposited material. By repeating this process, layers of different patterns can be constructed on a sample.

There are several considerations that must be taken in to account during the lithographic process, here though, only the two most relevant will be addressed. First, by modifying the thickness of the resist and exposure time different vertical patterns can be created during the development phase. If the exposure is longer than the minimum amount of time to modify the resist's bonds, called the *critical dose*, spill over occurs. This modifies the vertical angle of the walls at the boundary of development, called the *contrast*. A longer exposure will cause more spill over and a lower contrast. However, spill over can also be used to increase the pattern size relative to the mask, effectively causing an exposure under the masked area. This technique is known as *dose to size*.

Second, as light penetrates through the mask it is absorbed. Thus, the bottom of the mask will receive a lower dose than the top. If this effect is strong

enough, a low contrast boundary is developed resulting in pyramidal structure as with the spill over effect. If a positive resist is used this results in upright pyramids. However, if a negative resist is used, the pyramids are inverted, resulting in *undercuts*. So, as material is deposited it becomes discontinuous at the undercuts. When the resist is then etched away, a clean pattern is left behind. This technique, shown in Fig. 5.2, is known as *lift off*.

(a) (b)

Figure 5.2: The resist pattern left behind due to overexposure of a (a) positive and (b) negative resist using the same mask pattern as in Fig. 5.1a.

5.1.2 Ultraviolet Nanoimprint Lithography

Ultraviolet nanoimprint lithography (UV-NIL) uses essentially the same processing techniques as optical lithography, described in Section 5.1.1. The only difference comes when curing the photoresist. After the photoresist is deposited on the substrate, instead of placing an optical mask over the resist to prevent it from curing, a stamp is used to mold the resist to the desired shape. The stamp, made of material transparent to the relevant wavelengths, is pressed into the resist layer. The sample is then cured as normal and the stamp is removed. Processing then continues as normal.

Because the resist is removed mechanically by the stamp from the positions where it is unwanted, this process only uses negative resist. The mechanical nature of UV-NIL also means that the inverted pyramid structures that could be formed using optical lithography for a clean lift off process can no longer be manufactured. However, NIL has some key advantages over optical lithography, especially for use in solar cells. Because the process is mechanical, and the same stamp can be re-used many times UV-NIL is much cheaper, more reproducible, and allows for smaller feature sizes [26]. Thus, when scaling up production UV-NIL is often a better choice.

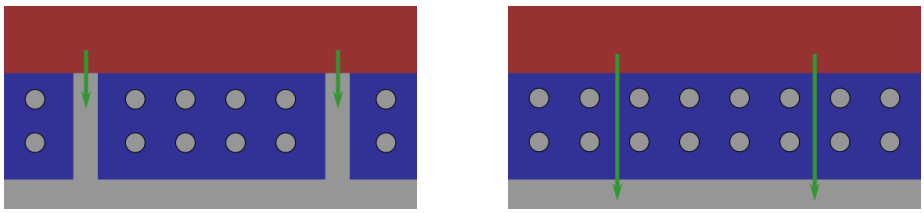

(a) (b)

Figure 5.3: Depending on the conductivity of the embedding material, the back reflector may need to use vias to connect the absorbing layers to the back contact, as in (a). If a conductive material is used for embedding, electron transport can occur directly through the embedding material, as in (b).

5.2 Structure

There are two possible constructions for a back reflector of this type depending on the embedding material. If the embedding material is a dielectric, then connections from the absorbing layers to the back contact must be made with vias through the embedded layer, as seen in Fig. 5.3. If, however, the embedding material is conductive vias are no longer required.

Chapter 6

Fabrication Methods, Results, and Analysis

6.1 Optical Lithography

Due to time constraints, only masks that could be created quickly were available for testing. This limited the options to creating a mask through the formation of metal island films, or using a mask that was already made.

6.1.1 Metal Island Films as Masks

To create a mask for lithography, metal island films were created in the vein of Tan and Santbergen [15, 27]. Using plasma deposition, a 12 nm layer of silver was deposited at 0.1 nm s^{-1} onto five SiO_2 substrates. Two of the samples were annealed for 1 hour, two for 1.5 hours, and one for 0.5 hours, all at 400° C. One of the 1 hour and one of the 1.5 hour annealed samples then received an SiO_2 deposition of 100 nm at 0.5 nm s^{-1} to prevent oxidation. These films then constitute a random arrangement of particles that can be used to create the 3D structure.

Using an NTEGRA Prima AFM machine with NOVA 1508 software, measurements of the films were obtained. For each mask a statistical average of each property was calculated over five samples regions.

6.1.2 Results

Using the masks several attempts were made to create a resist pattern. AZ 2020 negative photoresist was deposited on to a glass substrate with thicknesses ranging from 700 nm to 1.5 μm. Samples were then dried for 1 minute at 100° C. Using a Karl Suss MA6 for exposure, times for each thickness were varied between 5.0 and 30.0 seconds, after which the samples were dried for one more minute. The samples were then developed in MF322 solution for between 30 seconds and 1 minute.

Unfortunately, no resist remained on the substrate after any of these trials. This occurred because the wavelength of the exposure light is more than 400 nm from a mercury lamp, while particle sizes were found to be at most 250 nm from AFM measurements. So, due to diffraction effects the particle did not prevent any exposure. This means that when the samples were developed the bonding strength over the entire sample was uniform, and the developer simply removed all the resist with the same characteristic development time.

6.2 Nanoimprint Lithography Stamps

The issues that arose using optical lithography, discussed in Section 6.1, can be overcome using NIL. Unfortunately, an NIL stamp could not be obtained. However, given the advantages discussed in Section 5.1.2, NIL is a strong candidate for not only prototyping 3D plasmonic back reflectors, but also producing them at scale.

6.3 Metal Island Films

Because optical lithography was unsuccessful and an NIL mask could not be obtained, the use of self-forming metal island films directly on the substrate was used to create the plasmonic particles. Unfortunately, this comes with several downsides. Most prominently this means a controlled structure in the plane could not be created. Also, because an annealing process must occur for each layer, all previously deposited layers are annealed again. Thus, if there are three layers of plasmonic particles, the first layer is annealed two additional times. This may cause diffusion of the plasmonic material into the embedding material, or may lead to oxidation.

Using this method, there are three properties that can be controlled: the average particle size, the area coverage, and the distance between plasmonic layers. From Tan and Santbergen's work, it was found that varying the amount of deposited silver affects the area coverage, and the annealing time affects particle size [28, Ch. 3]. The best coverage results for a single layer reflector are obtained for a 12 nm film deposition, which will be held constant to narrow the investigation.

6.3.1 Particle Properties

To establish the fabrication process for the reflectors, self-forming particles were created varying several parameters using a similar process as in Sec. 6.1. To begin, 12 nm of silver was deposited on glass. Samples were then heated to 400° C in a Carbolite AAF 1100 oven with a nitrogen flow of 20 liters per minute to prevent oxidation. After cooling, a buffer layer of SiO_2 of different depths was deposited. A schematic of the samples are seen in Figs. 6.1. The samples were measured with the NTEGRA AFM and analyzed using Gwyddion and NOVA. Example AFM scans are seen in Fig. 6.2, and analysis results are in Table 6.1. Samples 1.1, 1.2, and 1.3 were used as controls to determine how the morphology of the SiO_2 depends on the underlying nanoparticles, so no silver was deposited on them. To validate the AFM measurements, samples 1.1, 1.2, and 1.3 were also measured using a Hitachi s4800 SEM, confirming the results.

(a) (b)

Figure 6.1: Schematic of the single layered device (a) without and (b) with an SiO_2 deposition on top of the particles

There are three properties of primary concern for the particles: coverage, particle radius, and aspect ratio. Coverage is the percentage of the surface covered by particles. Particles were delineated using a height threshold mask in Gwyddion. This is not the best technique as the particle properties are quite sensitive to the mask, however an effort was made to represent the particle

consistently by varying the threshold value. The particles are quite densely packed as seen in Figs. 6.2, which is in agreement with the results of Tan and Santbergen [29, 27]. There also isn't any significant difference between the 45, 60 and 120 minute anneal times, having coverage $(59 \pm 4)\%$, $(61 \pm 2)\%$, and $(61 \pm 4)\%$, respectively.

Particle radius was determined from samples 1.4, 1.6, and 1.8. The radius was calculated by

$$r = \sqrt{\frac{A\sigma}{\pi N}} \tag{6.1}$$

where r is the radius, A is the area of the scan, 5x5 μm^2 in these cases, σ is the area coverage , and N is the number of particles. The number of particles with a given radius follows a normal distribution quite closely, as expected. A typical example of this is seen in Fig. 6.3. From Sec. 3.2, the optimal particle radius for scattering was found to be between 100 and 200 nm, so even the minimum annealing time of 45 minutes is sufficient, as seen in Table 6.1.

In Sec. 3.2 it was found that the aspect ratio of the particles plays a critical role in the absorption, with a lower radius to height ratio having less absorption. The height of the particles is given by the average roughness in Table 6.1, and reveals that while a small height change occurs between 45 and 60 minutes, there is no change between 60 and 120 minutes of annealing time. The aspect ratios for the annealing times are (8.2 ± 2.4), (8.3 ± 1.5), and (10.3 ± 2.1), respectively, showing a longer annealing time leads to larger aspect ratio (i.e. flatter particles). From Sec. 3.2.3 it was found that a smaller aspect ratio leads to less absorption, so a shorter annealing time should be used to limit this. The best choice for annealing time when considering the particle radius and aspect ratio, and the variance of these values, then is 60 minutes. This time will be used for further device fabrication.

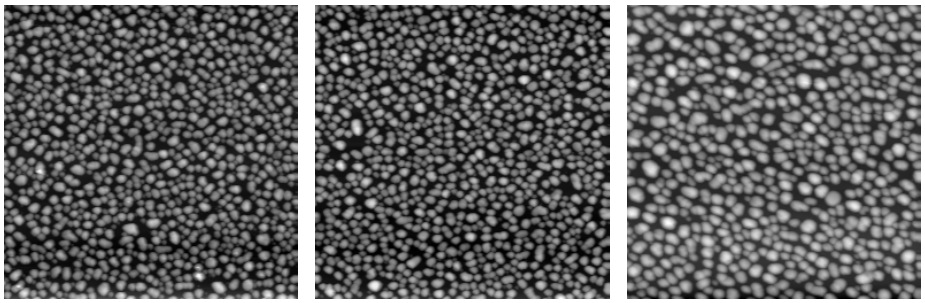

(a) (b) (c)

Figure 6.2: Examples of the AFM scans of sample (a) 1.4, (b) 1.6, and (c) 1.8 in Table 6.1. Images are of a 5x5 μm^2 area.

Sample	Anneal Time [m]	SiO_2 Thickness [nm]	Avg. Roughness [nm]	Avg. Mean Slope [deg]	Avg. Radius [nm]
Substrate	-	-	5 ± 2	1.8 ± 0.5	-
1.1	-	25	17.1 ± 0.4	22.2 ± 1.1	144 ± 32
1.2	-	50	6.5 ± 3.8	2.5 ± 0.5	-
1.3	-	100	3.8 ± 2.1	1.4 ± 0.9	-
1.4	45	0	18.8 ± 0.3	25.8 ± 0.5	155 ± 45
1.5	45	100	21.1 ± 0.7	27.0 ± 1.7	126 ± 52
1.6	60	0	19.9 ± 0.4	20.5 ± 0.8	164 ± 30
1.7	60	100	21.0 ± 0.6	26.1 ± 0.5	140 ± 6
1.8	120	0	19.2 ± 2.4	24.0 ± 2.5	197 ± 31
1.9	120	100	16.5 ± 1.5	24.7 ± 1.8	107 ± 19

Table 6.1: Particle and layer properties for varied annealing times and buffer layer thicknesses.

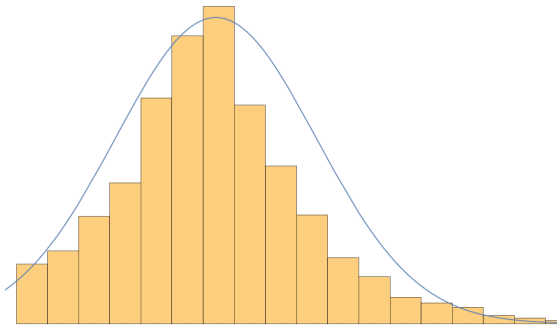

Figure 6.3: A typical histogram of particle radii and fitted normal distribution.

6.3.2 Layer Properties

The first layer of particles is deposited on a flat surface, however all subsequent layers will be affected by the morphology of the embedding material between the layers. Figs. 6.4 depict the two extreme scenarios of how underlying particle properties affect the layers on top of them. One extreme, in Fig. 6.4a, is that the deposition of embedding material, in this case SiO_2, will fill in the gaps between the particles, resulting in a flat surface for the next layer. In this case it would be expected that there is no correlation between particle positions of consecutive layers, and that the particle properties in each layer will be the same. In the other extreme, in Fig. 6.4b, the deposition of embedding material is equal across the surface, resulting in the pattern of the underlying particles being transfered to the next layer. This would result in a correlation between the position of the underlying particles and the particles in the next layers, and affect the properties of the newer particles.

Samples 1.5, 1.7, and 1.9 have a 100 nm layer of SiO_2 deposited on top of particles with the same fabrication parameters as samples 1.4, 1.6, and 1.8 respectively, allowing the surface morphology of the buffer layer to be examined. From this, insights about how particles in successive layers will deposit

(a) (b)

Figure 6.4: Two possible results from deposition on top of nanoparticles. (a) The deposition fills the gaps between the particles, resulting in a flat surface for the next deposition. (b) The deposition occurs at an equal rate across the substrate resulting in the underlying particle pattern being transfered to the deposition affecting the properties of the next layer.

themselves may be gained. In Fig. 6.5a particle radius on the buffer layer is plotted against the radius of the underlying particles. There is clearly no trend in this limited dataset, however the buffer layer particles have a bit smaller radius than the underlying particles. Fig. 6.5b shows the same sort of plot for roughness. Again there is no trend correlating the underlying roughness to the surface roughness on the buffer layer. So it appears that the underlying particle size, with a 100 nm deposition on top, does not correlate to the surface morphology of the deposited layer.

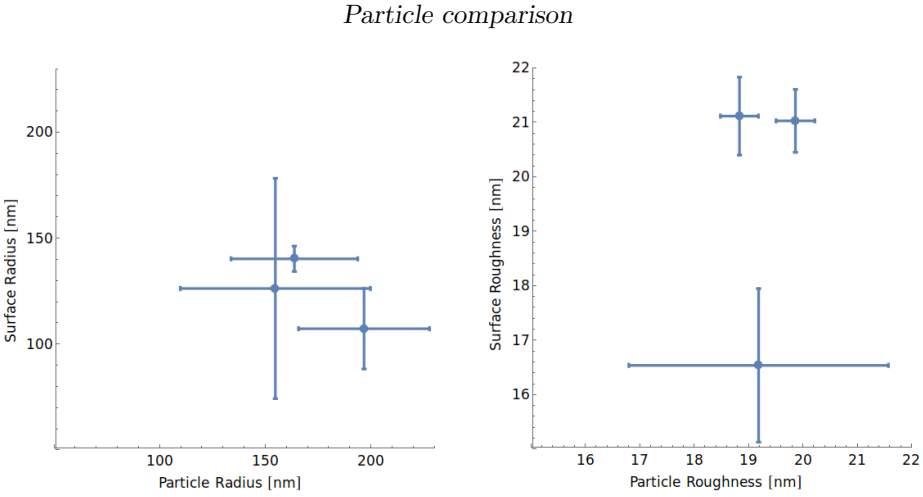

(a) (b)

Figure 6.5: The (a) radius and (b) roughness of the surface particles after a 100 nm buffer deposition against the underlying particles.

Looking at the roughness of samples 1.1, 1.2, and 1.3 do show an interesting result though. In sample 1.1, which is 25 nm of SiO_2 deposited on the glass substrate, there is a significant roughness, which is not present in samples 1.2 and 1.3 with 50 and 100 nm of SiO_2 respectively. This indicates that with more than 50 nm of SiO_2 the substrate is completely covered, and the deposited layer has

Sample	2.1	2.2	2.3	2.4	2.5	2.6	2.7	2.8	2.9	2.10
Layer Separation [nm]	50	50	50	100	100	100	150	150	200	200
Buffer Thickness [nm]	0	50	100	0	50	100	0	150	0	200

Table 6.2: Fabrication parameters for two-layered devices.

the same morphology as the substrate. With the underlying particles though, the buffer layer surface remains rough. Thus, although the underlying particles don't have a correlatable effect on the buffer layer surface morphology, they do change it relative to having no underlying particles by creating roughness.

To study how the particles deposited on the first buffer layer behave with the rough surface, the samples in Table. 6.2 were fabricated. In these devices the first layer of particles was deposited on the substrate. Then an SiO_2 layer with thickness *Layer Separation* was deposited. After forming the top layer of particles, another SiO_2 layer of *Buffer Thickness* was deposited. Each particle layer was annealed for 60 minutes. This results in devices with the schematics presented in Fig. 6.6.

Measurements of samples 2.1, 2.4, 2.7, and 2.9, seen in Table 6.3 can be used to determine any effects of the rough surface. Again, no trends are present correlating the thickness of the buffer layer to the particle properties. However, taking the average of these samples, the result can be compared to the particles created with the same fabrication parameters deposited on the substrate, sample 1.6. This shows that the top layer of particles has the same roughness, a higher slope, and a smaller radius than the particles deposited on the substrate. Due to the limited nature of this study, and the large variance in particle properties, though, a solid conclusion can not be drawn. Thus, it appears that the morphology of the surface the particles are deposited on does not play a significant role in the particle properties, and particles in different layers will have similar properties if the same fabrication parameters are used.

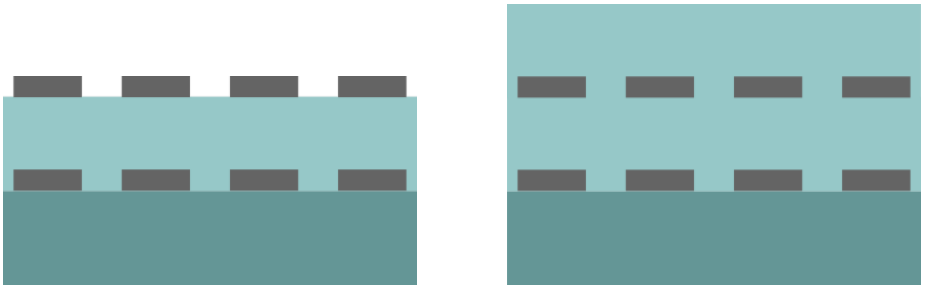

(a) (b)

Figure 6.6: Schematic of the two-layered device (a) without and (b) with an SiO_2 deposition on top of the particles

Sample	SiO_2 Thickness [nm]	Avg. Roughness [nm]	Avg. Mean Slope [deg]	Avg. Radius [nm]
2.1	50	20.9 ± 0.4	21.2 ± 0.4	142 ± 27
2.4	100	19.2 ± 1.4	25.6 ± 0.4	113 ± 22
2.7	150	20.9 ± 0.2	27.7 ± 0.3	123 ± 10
2.9	200	16.8 ± 1.0	22.9 ± 0.5	102 ± 11
Average	-	19.5 ± 0.9	24.3 ± 0.3	120 ± 19

Table 6.3: Properties of the top layer of particles with different underlying layers.

6.4 Angular Intensity Distribution

The angular intensity distribution (AID) of samples 2.2, 2.3, 2.5, 2.6, and 2.10 were measured using a PerkinElmer Lambda 950 spectrophotometer. (Sample 2.8 was not measured due to contamination.) Light of wavelengths between 700 and 1050 nm in 50 nm steps was normally incident to the sample begin measured. The results of the measurements are plotted in Fig. 6.7a. For each sample, regardless of wavelength, there is a significant forward scattering component. No other trends appear though. Fig. 6.7b shows the mean scattering intensity over all wavelengths. Here, samples 2.2 and 2.3, and 2.5 and 2.6 appear to be similar to each other. Comparing their fabrication parameters, this indicates that the top layer of SiO_2 does not affect the scattering, but the separation between the particles does have an effect. The trend indicates that as the particle separation increases more light is scattered. Light is scattered almost equally across all wavelengths, except at 140°, where a systematic dip occurs in all samples. This was likely caused by a measurement error, as there is no reason for light to not be scattered at this angle. Fig. 6.7c shows the AID averaged across samples. Here it becomes clear that wavelengths shorter than 900 nm are only scattered at 180°. Such an abrupt change in behavior between 850 and 900 nm may also indicate that the measurements taken are not reliable.

Comparing these results to those found in the HFSS models, discussed in Sec. 3.5, reveals a significant difference in the radiation patterns. In the fabricated devices, light is equally scattered across angles between 10 an 170 degrees, while in the HFSS simulations the amount of light scattered in a direction increases with the polar angle. In the HFSS simulations the frequency also did not play a major role in the radiation pattern, while in the fabricated devices wavelengths below the 900 nm threshold were not scattered at all. In both the simulated and fabricated devices the buffer layer did not impact the radiation patterns strongly, as expected. The mismatch between the simulated and measured radiation patterns indicate that the model is not accurate enough. The largest improvement to be made here would be to investigate how the particles formed on a rough surface develop. Examples of possible effects are shown in Figs. 3.39.

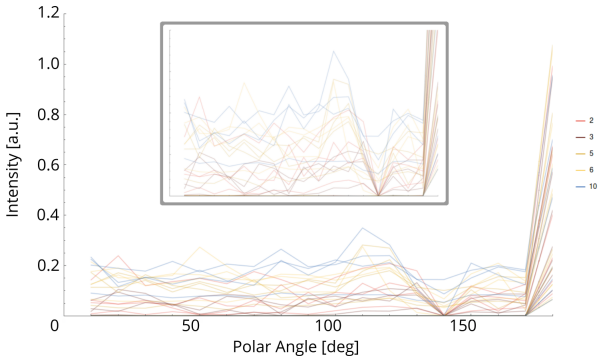

(a)

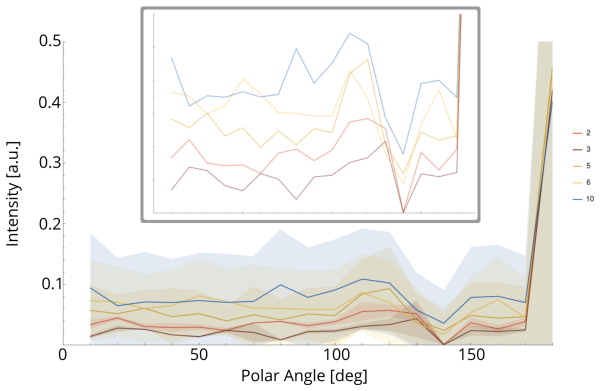

(b)

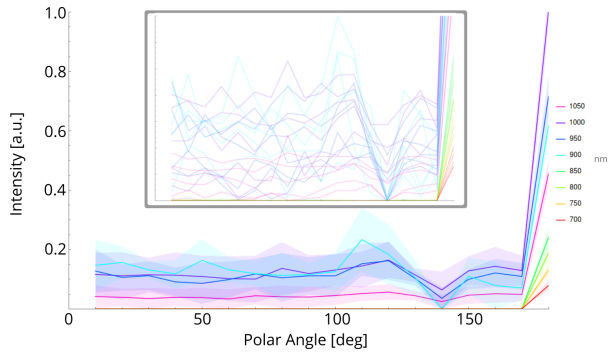

(c)

Figure 6.7: Angular intensity distribution of samples in Table 6.2. (a) shows all wavelengths, and (b) shows the mean of each sample across all wavelengths, with the shading indicating the error. **Insets:** Scaled plots showing detail. (c) The mean intensity calculated across samples with errors. **Inset:** Scaled plot of all samples.

Chapter 7

Fabrication Conclusion

To study the parameters of a fabricated reflector, one and two layer devices of self forming, silver island films were made. From the one layer devices it was found that for a buffer deposition providing sufficient coverage, the surface morphology of buffer layer does not depend on the underlying particles. Unlike the substrate, the buffer layer is quite rough though. This affects the particles of subsequent layers. Comparing the one and two layered devices, it was found that the flat substrate allows particle of larger radii to form.

The scattering properties of the two-layered devices were also investigated. For each device, a uniform scattering between 0 and 170 degrees was found, with a strong tendency to scatter at 180 degrees. Surprisingly, it was also found that all wavelength below 900 nm are only scattered to 180°, showing an abrupt change of behavior for the devices between 850 and 900 nm. This is likely caused by an inaccuracy in the measurements though. Comparing the measured results to HFSS simulations revealed that the simplification that the particles are cylinders resting on a flat surface do not represent the fabricated devices. A model incorporating the surface morphology and related particle shapes may overcome these disagreements.

Chapter 8

Conclusion

Plasmonic back reflectors have been shown to be as good as other sorts of back reflectors [7]. However, only two dimensional structures have been investigated. To understand the potential of a three dimensional structure the scattering properties were investigated. Multiple modeling methods were used to study different effects from the structure. First, the properties of a single particle were modeled using Mie theory and HFSS. From this, an optimal particle size, and constraints on the particle shape were found. Then the radiation pattern of two particles were simulated. Comparing the interference pattern from a system of ideal dipoles and that of an HFSS simulation showed that particle-particle interactions play a significant role in the scattering properties of the particles. It was also found that the scattering in the HFSS simulations remained relatively constant regardless of the particle's orientation to each other. On the other hand, the ideal dipole model showed that both the separation and relative angle of the particles play a role in the overall radiation pattern.

The effect of the lattice structure on the scattered field was then investigated. Using a new lattice summation technique it was found that the field from particles far away from the point of interest can be ignored. This allows the lattice to be designed only considering the field from nearby particles. A preliminary investigation of the fields from the near region was conducted, however no conclusions could be drawn due to its limited scope.

Several one and two layered devices were fabricated with self forming metal island films. The size and shape of the particles in these films showed a large dependence on the roughness of the deposition surface. However, the layers deposited on top of the films were not affected by the underlying particles. The devices showed a uniform scattering pattern between 10 and 170 degrees, with a large increase at 180 degrees. This shows that the random films are not strong scatterers. These results were compared with a simple HFSS model, also revealing that the surface morphology and subsequent particle shapes can not be ignored.

Appendix A

Plasmonics

Of interest is how metal nanoparticles interact with light. For the systems in this research, the properties of localized surface plasmons (LSP) are most relevant. To investigate this phenomena the path of Maier is followed [30]. LSPs are non-propagating excitations of the free electron gas. To model this, two major assumptions are made. The first is that the particle size is small compared ot the wavelength of light. From this, the electric field is assumed constant over the extent of the particle. Second, the particles are assumed to consist of a free electron gas against a fixed background of positively charged nuclei. Also assumed is that the materials being used are non-magnetic, simple media, meaning they respond isotropically, and linearly to an incident electric field. From these assumptions, the electric field from incident light will drive the system as a harmonic oscillator, with all free electrons moving as one. The kinematics equation of a damped oscillator is

$$m\ddot{\mathbf{x}} + m\gamma\dot{\mathbf{x}} = -e\mathbf{E} \tag{A.1}$$

where m is the effective mass of the electrons, x is the displacement of electron γ is a damping term representing collision of the electrons, and $-e\mathbf{E}(t)$ is the driving force caused by the incident light. If the light is a plane wave, $\mathbf{E} = \mathbf{E_0}e^{-i\omega t}$, for constant vector $\mathbf{E_0}$ the response will be

$$\mathbf{x} = \mathbf{x_0}e^{-i\omega t}, \quad \mathbf{x_0} = \frac{e\mathbf{E_0}}{m(\omega^2 + i\omega\gamma)} \tag{A.2}$$

In the material, the polarization caused by a single electron is $\mathbf{p} = -e\mathbf{x}$. If the density of free electrons is n, a macroscopic polarizability arises with

$$\mathbf{P} = -ne\mathbf{x} = -\frac{-ne^2}{m(\omega^2 + i\gamma\omega)}\mathbf{E} \tag{A.3}$$

From the assumption of linear media, the macroscopic displacement field, $\mathbf{D}$, can be related to the electric field and polarizability as

$$\mathbf{D} = \epsilon_0\mathbf{E} + \mathbf{P} \tag{A.4}$$

Where ϵ_0 is is permittivity of free space. Using equation (A.3),

$$\mathbf{D} = \epsilon_0\epsilon\mathbf{E} = \epsilon_0(1 - \frac{\omega_p^2}{\omega^2 + i\gamma\omega})\mathbf{E}, \quad \omega_p^2 = \frac{ne^2}{\epsilon_0 m} \tag{A.5}$$

Where ϵ is the relative permittivity, and ω_p is the plasma frequency. Splitting the relative permittivity into its real and imaginary components

$$\epsilon = 1 - \frac{\omega_p^2}{\omega^2 + i\gamma\omega} = \epsilon_1 + i\epsilon_2, \tag{A.6a}$$

$$\epsilon_1 = 1 - \frac{\omega_p^2\tau^2}{1 + \omega^2\tau^2}, \tag{A.6b}$$

$$\epsilon_2 = \frac{\omega_p^2\tau}{\omega(1 + \omega^2\tau^2)} \tag{A.6c}$$

Where $\tau = \gamma^{-1}$ is the characteristic time between collision events. The dielectric function is related to the complex index of refraction, $\tilde{n} = n + i\kappa$, as

$$\tilde{n} = \sqrt{\epsilon} \tag{A.7}$$

Where κ is the extinction coefficient, related to absorption. Combining equations (A.6) and (A.7) gives

$$\epsilon_1 = n^2 - \kappa^2 \tag{A.8a}$$

$$\epsilon_2 = 2n\kappa \tag{A.8b}$$

$$n^2 = \frac{1}{2}\left[\epsilon_1 \pm \sqrt{\epsilon_1^2 + \epsilon_2^2}\right] \tag{A.8c}$$

$$\kappa = \frac{\epsilon_2}{2n} \tag{A.8d}$$

For metals to retain their normal optical properties the frequency of the light driving them must be lower than the plasma frequency. Above this limit, the metals become transparent. Remaining in the $\omega < \omega_p$ regime, there are two extremes that can be examined. In the low collision limit $\omega\tau \gg 1$, giving

$$\epsilon \sim 1 - \frac{\omega_p^2}{\omega^2} \tag{A.9}$$

Because ϵ is dominantly real, $\kappa \approx 0$ and little absorption occurs. In the high collision limit $\omega\tau \ll 1$, giving

$$\epsilon \sim 1 + i\frac{\omega_p^2\tau}{\omega} \tag{A.10}$$

In which case n and κ are of similar magnitude, and significant absorption occurs. A small, implicit assumption has been made for these calculation that the energy of the incident light is less than that of the inter-band transitions of the material. For metals driven by optical frequencies, this assumption holds.

Consider now a small, spherical particle of radius a embedded in a medium with dielectric function ϵ_D and incident field $\mathbf{E} = E_0\hat{z}$. From Maxwell's equations with no sources, the electric potential, ϕ, must satisfy Laplace's equation

$$\nabla^2\phi = 0 \tag{A.11}$$

Due to the spherical symmetry of the particle, ϕ can be expressed as an expansion in Legendre polynomials, P_l

$$\phi_{in} = \sum_{l=0}^{\infty} A_l r^l P_l(\cos\theta) \tag{A.12a}$$

$$\phi_{out}(r,\theta) = \sum_{l=0}^{\infty} [B_l r^l + C_l r^{-(l+1)}] P_l(\cos\theta) \tag{A.12b}$$

Where ϕ_{in} is the potential inside the sphere, and ϕ_{out} is the potential outside the sphere. The coefficients can be determined by matching boundary conditions at the surface of the sphere, and as $r \to \infty$. Far away from the sphere the potential should be unaffected by the particle so as $r \to \infty$, $\phi_{out} \to E_0 \hat{z}$. At the surface of the sphere, the tangential and perpendicular components of the potential are required to be continuous yields. These result in

$$A_l = B_l = C_l = 0 \text{ for } l \neq 1 \tag{A.13a}$$

$$A_1 = \frac{-3\epsilon_D}{\epsilon + 2\epsilon_D} E_0 \tag{A.13b}$$

$$B_1 = -E_0 \tag{A.13c}$$

$$C_1 = \frac{\epsilon - \epsilon_D}{\epsilon + 2\epsilon_D} E_0 a^3 \tag{A.13d}$$

Plugging these into the expression for ϕ_{out}, with $P_1(x) = x$, gives

$$\phi_{out} = -E_0 r\cos\theta + \frac{\epsilon - \epsilon_D}{\epsilon + 2\epsilon_D} \frac{a^3 \cos\theta}{r^2} E_0 \tag{A.14}$$

Which is a superposition of the incident field's potential and the potential of a radiating dipole, $\mathbf{d}$. This allows the potential to be written as

$$\phi_{out} = -E_0 r\cos\theta + \frac{\mathbf{d}\cdot\mathbf{r}}{4\pi\epsilon_0\epsilon_D} \frac{1}{r^3} \tag{A.15}$$

Where

$$\mathbf{d} = \epsilon_0\epsilon_D \alpha \mathbf{E_0} = 4\pi\epsilon_0\epsilon_D a^3 \frac{\epsilon - \epsilon_D}{\epsilon + 2\epsilon_D} \mathbf{E_0} \tag{A.16}$$

With

$$\alpha = 4\pi a^3 \frac{\epsilon - \epsilon_D}{\epsilon + 2\epsilon_D} \tag{A.17}$$

α is the polarizability of the particle's dipole expansion, and exhibits a resonance at $\epsilon = -2\epsilon_D$. This is known as the *Frölich condition*. In a solar cell, this surrounding material will be transparent, so ϵ_D can be taken as a real number. Under this assumption, as ϵ_D increases, $\mathbb{R}[\epsilon]$ must increase as well to maintain resonance. Examining (A.6b), $\mathbb{R}[\epsilon] \propto (1 - \omega^{-1})$, so the resonance redshifts.

Under illumination, then, the particle will exhibit dipole radiation, with electric field

$$\mathbf{E} = \frac{k^2}{4\pi\epsilon_0\epsilon_D} (\hat{\mathbf{r}} \times \mathbf{d}) \times \hat{\mathbf{r}} \frac{e^{ikr}}{r} = -\frac{k^2}{4\pi\epsilon_0\epsilon_D} \sin\theta \frac{e^{ikr}}{r} \hat{\boldsymbol{\theta}} \tag{A.18}$$

Where k is the magnitude of the wave vector of the incident light, $\mathbf{r}$ is the position vector to the location of interest with r its magnitude, θ is the angle between $\mathbf{d}$ and $\mathbf{r}$, and $\hat{\boldsymbol{\theta}}$ is the polar direction in spherical coordinates with the dipole aligned to the z-axis.

Appendix B

Scattering

There are two main processes of interest when considering light for this problem. The first is scattering, which indicates how an incident light ray is scattered upon interaction with an object. The second is absorption. Absorption can occur in two forms. When passing through a homogeneous medium, some of the energy of light is absorbed according to Beer's Law

$$I \propto e^{-\alpha d} \tag{B.1}$$

where α is the absorption constant, and d is the distance traveled through the medium. Absorption can also occur when light is incident on a sea of free electrons, such as those found in a metal. In this case the electrons act as an oscillator, and if the frequency of the incident light is matched to the natural frequency of the electron sea, the energy of the light can be absorbed.

These two processes result in the parameters of interest for this situation, the scattering, absorption, and extinction cross-sections. These represent the effective area of the particle for each property. Scattering represents power density diverted from its original path, absorption is difference between the total power in and total power out, and extinction is the sum of the two.

B.1 Mie Theory

Consider an incident plane wave interacting with a spherical particle. As the electromagnetic field of the light and the particle interact, the field will deviate from its plane wave characteristic, scattering some of the light in different directions. To see exactly how this process occurs the course of Bohren and Huffman is followed, beginning with satisfying Maxwell's equations [24]. To simplify matters, the four four Maxwell equations can be reduced to two wave equations. Because no sources are present in the system these equations are

$$\nabla^2\mathbf{E} + k^2\mathbf{E} = 0 \tag{B.2a}$$

$$\nabla^2\mathbf{H} + k^2\mathbf{H} = 0 \tag{B.2b}$$

These equations can be further reduced to scalar wave equation. To see this first consider a vector field $\mathbf{M}$ that represents $\mathbf{E}$ or $\mathbf{B}$ with

$$\mathbf{M} = \nabla \times \mathbf{c}\psi \tag{B.3}$$

where $\mathbf{c}$ is a constant vector, and ψ is a scalar field. Then

$$\nabla \cdot \mathbf{M} = 0 \tag{B.4}$$

satisfying the divergence requirements of Maxwell without sources, and

$$\nabla^2 \mathbf{M} + k^2 \mathbf{M} = \nabla \times [\mathbf{c}(\nabla^2 \psi + k^2 \psi)] \tag{B.5}$$

Thus, $\mathbf{M}$ will satisfy the vector wave equations only when ψ satisfies the scalar wave equation

$$\nabla^2 \psi + k^2 \psi = 0 \tag{B.6}$$

Further, if another vector field $\mathbf{N}$ is related to $\mathbf{M}$ as

$$\mathbf{N} = \frac{1}{k} \nabla \times \mathbf{M} \tag{B.7}$$

then $\mathbf{M}$ and $\mathbf{N}$ have all the characteristics of the electric and magnetic fields, respectively.

Adhering to the geometry of the situation, the wave equation (B.6) is written in spherical coordinates with polar angle θ and azimuthal angle ϕ as

$$\frac{1}{r^2} \partial_r [r^2 \partial_r \psi] + \frac{1}{r^2 \sin\theta} \partial_\theta [\sin\theta \partial_\theta \psi] + \frac{1}{r^2 \sin\theta} \partial_\phi^2 \psi + k^2 \psi \tag{B.8}$$

Using separation of variables with $\psi = R(r)\Theta(\theta)\Phi(\phi)$ the Legendre polynomials $P_n^m(\cos\theta)$ and the spherical Bessel and Henkel functions J_ν, Y_ν, H_ν all satisfy Eq. (B.8). This results in even solution ψ_{emn} and odd solutions ψ_{omn}

$$\psi_{emn} = \cos(m\phi) P_n^m(\cos\theta) \mathcal{F}_n(kr) \tag{B.9a}$$

$$\psi_{omn} = \sin(m\phi) P_n^m(\cos\theta) \mathcal{F}_n(kr) \tag{B.9b}$$

where $\mathcal{F}$ is any of J_ν, Y_ν, or H_ν. The harmonic decomposition of $\mathbf{M}$ and $\mathbf{N}$ can then be found plugging Eqs. B.9 in to Eqs. (B.3) and (B.7). If the incident plane wave is polarized in the $\hat{\mathbf{x}}$ direction then it can be written in spherical coordinates as

$$\mathbf{E}_i = E_0 e^{ikr\cos\theta} \hat{\mathbf{e}}_x \tag{B.10}$$
$$\hat{\mathbf{e}}_x = \sin\theta\cos\phi \hat{\mathbf{e}}_r + \cos\theta\cos\phi \hat{\mathbf{e}}_\theta - \sin\phi \hat{\mathbf{e}}_\phi$$

and expanded in terms of the spherical harmonics as

$$\sum_{m=0}^{\infty} \sum_{n=0}^{\infty} B_{emn} \mathbf{M}_{emn} + B_{omn} \mathbf{M}_{omn} + A_{emn} \mathbf{N}_{emn} + A_{omn} \mathbf{N}_{omn} \tag{B.11}$$

with coefficients A and B. From orthogonality conditions only B_{o1n} and $_{e1n}$ survive though, resulting in the fields for the incident wave as

$$\mathbf{E}_i = E_0 \sum_{n=1}^{\infty} \frac{2n+1}{n(n+1)} (\mathbf{M}_{o1n} - i\mathbf{N}_{e1n}) \tag{B.12a}$$

$$\mathbf{H}_1 = \frac{-k}{\mu\omega} E_0 \sum_{n=1}^{\infty} i^n \frac{2n+1}{n(n+1)} (\mathbf{M}_{e1n} + i\mathbf{N}_{o1n}) \tag{B.12b}$$

At the interface of the sphere and the surrounding environment $\mathbf{E}$ and $\mathbf{H}$ must satisfy the boundary conditions

$$(\mathbf{E}_i + \mathbf{E}_s + \mathbf{E}_1) \times \hat{\mathbf{e}}_r = 0 \tag{B.13a}$$

$$(\mathbf{H}_i + \mathbf{H}_s + \mathbf{H}_1) \times \hat{\mathbf{e}}_r = 0 \tag{B.13b}$$

where $\mathbf{M}_i$ is the incident field, $\mathbf{M}_s$ is the scattered field, and $\mathbf{M}_1$ is the internal field of the particle. The scattered field can then be written in harmonics as

$$\mathbf{E}_s = \sum_{n=1}^{\infty} E_n(ia_n\mathbf{N}_{e1n} - b_n\mathbf{M}_{o1n}) \tag{B.14a}$$

$$\mathbf{H}_s = \frac{k}{\mu\omega}\sum_{n=1}^{\infty} E_n(ib_n\mathbf{N}_{o1n} + a_n\mathbf{M}_{e1n}) \tag{B.14b}$$

From the symmetry of the problem only the θ direction should matter. In this vain, let

$$\pi_n = \frac{P_n^1}{\cos\theta} \tag{B.15a}$$

$$\tau_n = \frac{dP_n^1}{d\theta} \tag{B.15b}$$

Then $(\tau_n + \pi_n)$ and $(\tau_n - \pi_n)$ are orthogonal functions that $\mathbf{E}$ and $\mathbf{H}$ can be decomposed as. The first few harmonics of these functions are seen in Fig. B.1. Notice that as n increases the number of lobes increases and the lobe at 0° narrows, and that lobes at 180° only occur in every other n. As the size of the sphere increase, more of the π and τ harmonics must be included in the solution. This results in a larger and narrower scattering profile, as seen in Fig. 1.4.

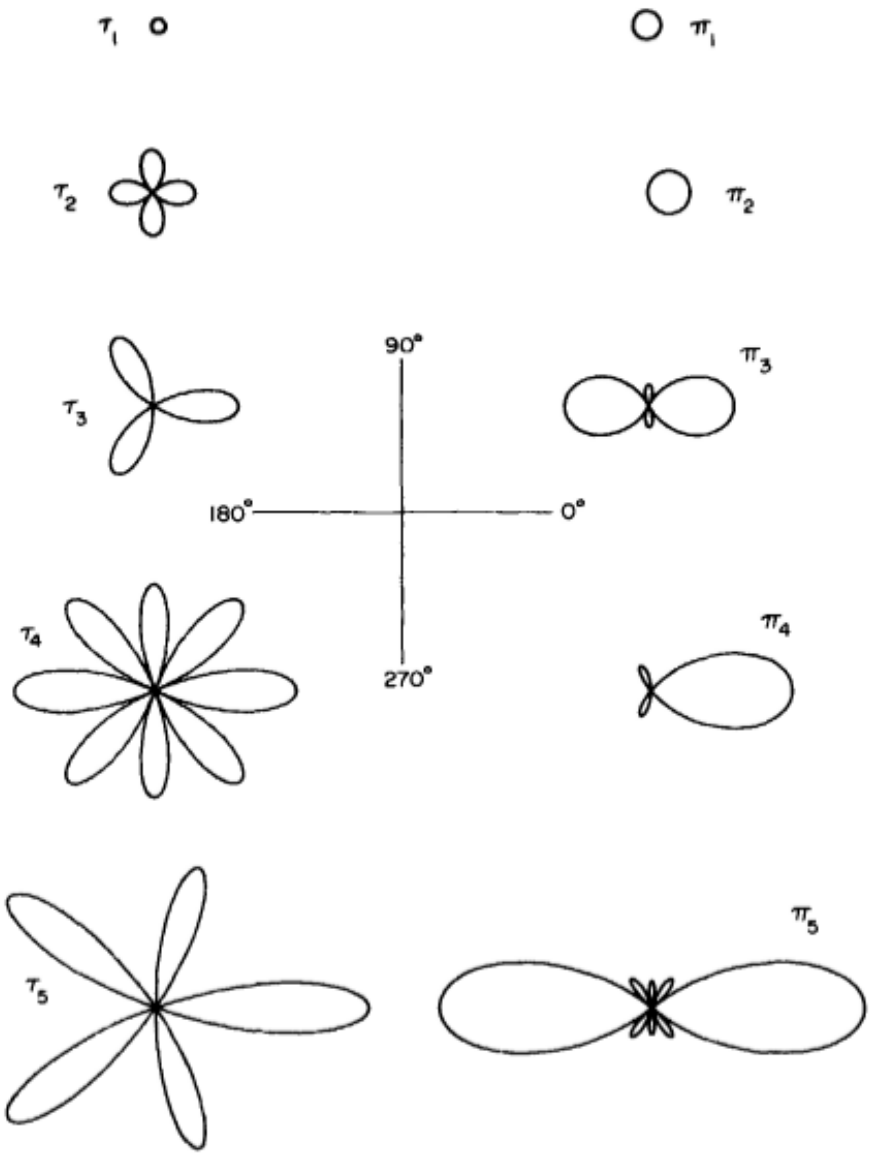

Figure B.1: Polar plots of the first five π and τ functions. The plots are to the same scale and plotted from 0 to 2π, instead of π, for ease of viewing [24, 4, p. 96].

The scattering cross section of a particle can also be determined by calculating the net rate at which electromagnetic energy crosses a spherical surface centered at the particle. This power is found to be

$$W_s = \frac{\pi |E_0|^2}{k\omega\mu} \sum_{n=1}^{\infty} (2n+1)\,\mathrm{Re}(g_n)(|a_n|^2 + |b_n|^2) \tag{B.16}$$

where a_n and b_n are the expansion coefficients of Eq. (B.14), π is $3.14\ldots$ (not to be confused with the functions π_n), and the g_n are

$$g_n = (\chi_n^* \psi_n' - \psi_n^* \chi_n') - i(\psi_n^* \psi_n' + \chi_n^* \chi_n') \tag{B.17}$$

with χ_n the Riccati-Bessel functions. This gives scattering and extinction cross-sections of

$$C_{sca} = \frac{W_s}{I_i} = \frac{2\pi}{k^2} \sum_{n=1}^{\infty} (2n+1) \left(|a_n|^2 + |b_n|^2 \right) \tag{B.18a}$$

$$C_{ext} = \frac{W_e}{I_i} = \frac{2\pi}{k^2} \sum_{n=1}^{\infty} (2n+1)\,\mathrm{Re}(a_n + b_n) \tag{B.18b}$$

where I_i is the intensity of the incident wave.

In the limiting case that the sphere is small compared to the wavelength of incident light, the electric field can be considered constant over the volume of the sphere and the expressions for the cross-sections can be simplified. Specifically, the Bessel functions can be expanded in their power series representation, and only the first few terms included. This gives simple expressions for a_n and b_n resulting in the cross-sections

$$C_{sca} = \frac{8\pi}{3} k^4 a^6 \left| \frac{\epsilon - \epsilon_m}{\epsilon + 2\epsilon_m} \right|^2 \tag{B.19a}$$

$$C_{abs} = 4\pi k a^3\,\mathrm{Im}\left[\frac{\epsilon - \epsilon_m}{\epsilon + 2\epsilon_m} \right] \tag{B.19b}$$

Evaluating the fields from this limit also gives the angular distribution of scattered light and the polarization of scattered light, seen in Figs. B.2 and B.3, respectively.

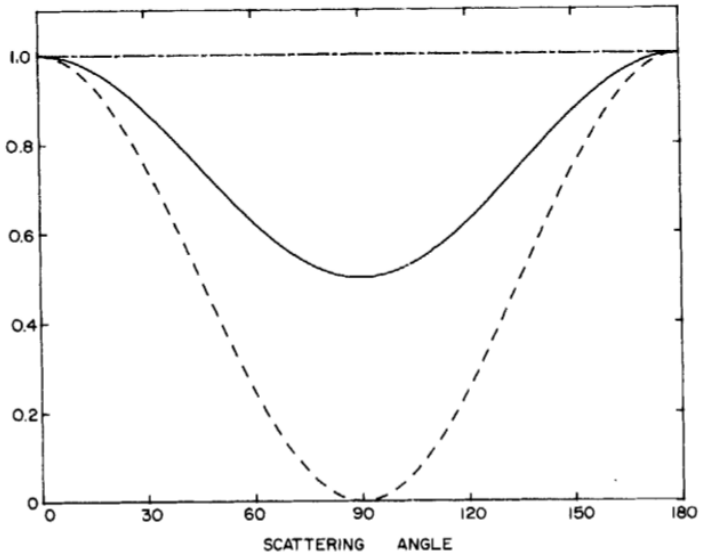

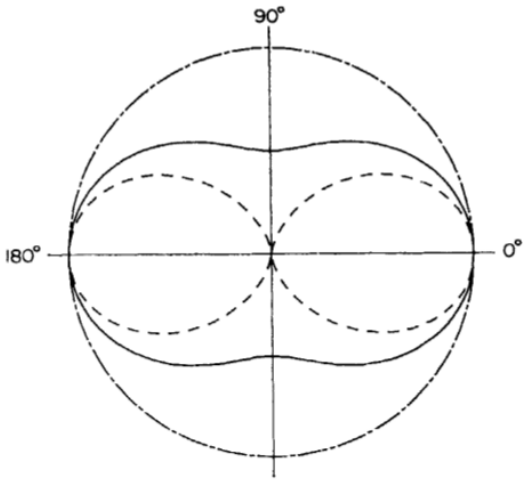

Angular distribution (normalized) of the light scattered by a sphere small compared with the wavelength: incident light polarized parallel (----) and perpendicular (—·—) to the scattering plane; (——) unpolarized incident light.

Figure B.2: From [24, Ch. 5.2]

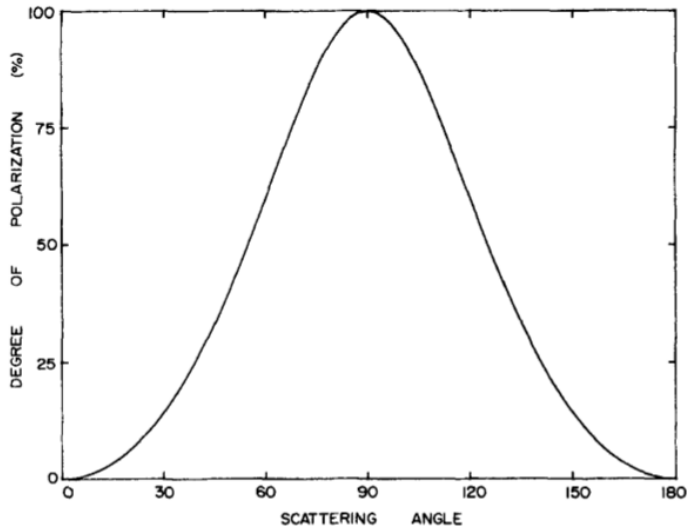

Degree of polarization of light scattered by a sphere small compared with the wavelength for incident unpolarized light.

Figure B.3: From [24, Ch. 5.2]

Appendix C

Dipole Model

To find the electric field of a system of radiating dipoles $\mathbf{p}_i$ [1], the field from each dipole, $\mathbf{E}_i$, is found at the point of interest $\mathbf{r_0}$, then summed together. In the local frame of an individual dipole, Σ_i', the radiated electric field is given by

$$\mathbf{E_i'}(\boldsymbol{\mathscr{r}}') = -\frac{p_i\omega^2\mu_0}{4\pi}\sin\theta'\frac{\exp\left(i[\omega(\frac{\mathscr{r}'}{c}-t)+\psi]\right)}{\mathscr{r}'}\hat{\boldsymbol{\theta}}' \tag{C.1}$$

where $\mathbf{p}$ defines the z-axis of Σ', ω is its oscillation frequency, $\boldsymbol{\mathscr{r}}'$ is the vector from the dipole to the point of interest in Σ', ψ is an arbitrary phase change, θ' the polar angle of $\boldsymbol{\mathscr{r}}'$, and $\hat{\boldsymbol{\theta}}'$ the polar direction unit vector. Normal weighted fonts represent the magnitude of the corresponding vector (E.g. $\mathrm{v} = |\mathbf{v}|$). An image of the system, and an individual dipole can be seen in Fig. C.1.

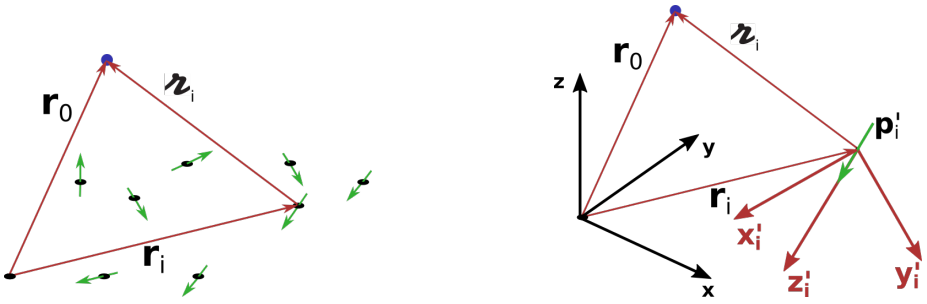

Figure C.1: (a) Depiction of an arbitrary dipole system, and (b) a focus on an individual dipole within the system.

In the global frame Σ, each dipole is displaced from the origin by $\mathbf{r}_i$. This gives the relevant position vector from $\mathbf{p}_i$ to $\mathbf{r}_0$ as $\boldsymbol{\mathscr{r}}_i = \mathbf{r}_0 - \mathbf{r}_i$. $\boldsymbol{\mathscr{r}}_i$, then, relocates $\mathbf{p}_i$ to the origin of Σ.

[1] As we all know, I is everybody's favorite word. It also happens to make a wonderful indexing variable, and pops its head up as $\sqrt{-1}$. To remain humble about this work, however, here it has only been used in the latter two contexts. Thus, an i appearing in a subscript position acts as an index, while an i appearing inline is $\sqrt{-1}$.

C.1 Frame Transformations

Because of the use of two coordinate frames, it is important to consider the role of vectors as objects in themselves. A vector $\vec{v}$ is a geometric object in itself, not requiring subjugation to a coordinate system, however, for manipulation a coordinate system is imposed upon it. This choice of coordinates system is arbitrary though, and does not affect $\vec{v}$. In this notation then, $\mathbf{v}$ represents the components of $\vec{v}$ in Σ, while $\mathbf{v}'$ represents the coordinates of $\vec{v}$ in Σ'.

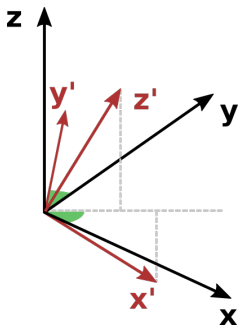

Figure C.2: The global frame Σ in black, and local dipole frame Σ' in red. As will be discussed during the construction, the angles in green are the same, and $\hat{\mathbf{x}}'$ and $\hat{\mathbf{z}}'$ have the same azimuthal angle.

Because $\mathbf{p}$ defines the z-axis of Σ', a canonical transformation from Σ to Σ' would take $\hat{\mathbf{z}}$ to $\hat{\mathbf{z}}'$. A preview of the final Σ' frame can be seen in Fig. C.2 To rotate a vector $\mathbf{v}$ in 3D, a rotation axis $\mathbf{t}$ must be defined. $\mathbf{v}$ is then rotated counter-clockwise around $\mathbf{t}$ by an angle γ. This can be accomplished by noting that only the projection of $\mathbf{v}$ onto the plane defined by $\mathbf{t}$ must change, while the component parallel to $\mathbf{t}$ is invariant.

$$\mathbf{v}_{\parallel} = \frac{\mathbf{v}\cdot\mathbf{t}}{t^2}\mathbf{t} \tag{C.2}$$

$$\mathbf{v}_{\perp} = \mathbf{v} - \mathbf{v}_{\parallel} = \mathrm{v}^i(1 - \left(\frac{t^i}{t}\right)^2)\mathbf{e}_i \tag{C.3}$$

where $\mathbf{e}_i$ are the coordinate vectors of Σ, and the Einstein summation notation has been used. The final rotated vector $\mathbf{u}$, can then be constructed by $\mathbf{u} = \boldsymbol{R}(\gamma)\mathbf{v}_{\perp} + \mathbf{v}_{\parallel}$, where $\boldsymbol{R}_{\mathbf{t}}(\gamma)$ is the 2D rotation around $\mathbf{t}$ by γ. In the $\mathbf{t}$-plane, define the coordinate axis to be the unit vectors

$$\hat{\mathbf{f}}_a = \frac{\mathbf{v}_{\perp}}{\mathrm{v}_{\perp}},\ \hat{\mathbf{f}}_b = \frac{\mathbf{t}\times\mathbf{v}_{\perp}}{t\mathrm{v}_{\perp}}$$

Rotating in the $\mathbf{t}$-plane is now simple.

$$\boldsymbol{R}_{\mathbf{t}}(\gamma) = (\cos\gamma, \sin\gamma) \tag{C.4}$$

Solving for $\mathbf{u}$ now gives

$$\begin{aligned}\mathbf{u} &= \mathbf{v}_{\parallel} + \cos\gamma\mathrm{v}_{\perp}\hat{\mathbf{f}}_a + \sin\gamma\mathrm{v}_{\perp}\hat{\mathbf{f}}_b \\ &= \cos\gamma\mathbf{v} + \frac{\sin\gamma}{t}\mathbf{t}\times\mathbf{v} + \frac{\mathbf{v}\cdot\mathbf{t}}{t^2}(1-\cos\gamma)\mathbf{t}\end{aligned} \tag{C.5}$$

This result is known as *Rodrigues' rotation formula.*

If $\mathbf{p}$ does not coincide with the z-axis, then a natural choice for the rotation vector, whose unit vector will also define the y-axis of Σ', is

$$\mathbf{t} = \hat{\mathbf{z}} \times \mathbf{p} = \begin{bmatrix} -p_y \\ p_x \\ 0 \end{bmatrix} \tag{C.6}$$

With $\hat{\mathbf{t}} = \hat{\mathbf{y}}'$. The third coordinate axis of Σ' can then be defined as

$$\hat{\mathbf{x}}' = \hat{\mathbf{y}}' \times \hat{\mathbf{z}}' = \hat{\mathbf{t}} \times \hat{\mathbf{p}} = \widehat{(\hat{\mathbf{z}} \times \mathbf{p})} \times \hat{\mathbf{p}} \tag{C.7}$$

Thus, Σ' has coordinate axes

$$\{\hat{\mathbf{x}}', \hat{\mathbf{y}}', \hat{\mathbf{z}}'\} = \{\widehat{(\hat{\mathbf{z}} \times \mathbf{p})} \times \hat{\mathbf{p}},\ \widehat{\hat{\mathbf{z}} \times \mathbf{p}},\ \hat{\mathbf{p}}\} \tag{C.8}$$

In this situation, then, a vector in Σ must be rotated an angle γ around $\mathbf{t}$ where γ is the angle between $\hat{\mathbf{z}}$ and $\mathbf{p}$. Using (C.5) and the definition of γ gives

$$\cos\gamma = \frac{\hat{\mathbf{z}} \cdot \mathbf{p}}{p},\ \sin\gamma = \frac{|\hat{\mathbf{z}} \times \mathbf{p}|}{p} = \frac{t}{p} \tag{C.9}$$

Resulting in

$$\mathbf{u} = \frac{\hat{\mathbf{z}} \cdot \mathbf{p}}{p}\mathbf{v} + \frac{\mathbf{t} \times \mathbf{v}}{p} + \frac{\mathbf{v} \cdot \mathbf{t}}{t^2}\Big(1 - \frac{\hat{\mathbf{z}} \cdot \mathbf{p}}{p}\Big)\mathbf{t} \tag{C.10}$$

Using a test vector, $\mathbf{v} = (v_x, v_y, v_z)$ and general dipole vector $\mathbf{p} = (p_x, p_y, p_z)$, in (C.10) results in

$$\begin{aligned}
u_x &= \Big[\frac{p_z}{p} + \frac{p_y^2}{p_x^2 + p_y^2}\Big(1 - \frac{p_z}{p}\Big)\Big]v_x &&+ \Big[\frac{-p_x p_y}{p_x^2 + p_y^2}\Big(1 - \frac{p_z}{p}\Big)\Big]v_y &&+ \Big[\frac{p_x}{p}\Big]v_z \\
u_y &= \Big[\frac{-p_x p_y}{p_x^2 + p_y^2}\Big(1 - \frac{p_z}{p}\Big)\Big]v_x &&+ \Big[\frac{p_z}{p} + \frac{p_x^2}{p_x^2 + p_y^2}\Big(1 - \frac{p_z}{p}\Big)\Big]v_y &&+ \Big[\frac{p_y}{p}\Big]v_z \\
u_z &= \Big[\frac{-p_x}{p}\Big]v_x &&+ \Big[\frac{-p_y}{p}\Big]v_y &&+ \Big[\frac{p_z}{p}\Big]v_z
\end{aligned}$$

where the components of $\mathbf{u}$ have been split in to their relation to the components of $\mathbf{v}$. These equations can now be represented in matrix form, giving

$$\mathbf{u} = \boldsymbol{P}\mathbf{v} = \begin{bmatrix} \frac{p_z}{p} + \frac{p_y^2}{p_x^2 + p_y^2}\Big(1 - \frac{p_z}{p}\Big) & \frac{-p_x p_y}{p_x^2 + p_y^2}\Big(1 - \frac{p_z}{p}\Big) & \frac{p_x}{p} \\ \frac{-p_x p_y}{p_x^2 + p_y^2}\Big(1 - \frac{p_z}{p}\Big) & \frac{p_z}{p} + \frac{p_x^2}{p_x^2 + p_y^2}\Big(1 - \frac{p_z}{p}\Big) & \frac{p_y}{p} \\ -\frac{p_x}{p} & -\frac{p_y}{p} & \frac{p_z}{p} \end{bmatrix} \begin{bmatrix} v_x \\ v_y \\ v_z \end{bmatrix} \tag{C.11}$$

Thus, to transform Σ to Σ', $\boldsymbol{P}$ is applied to each basis vector of Σ.

To find the coordinates of a vector $\vec{v}$ in Σ given its components in Σ', we first describe $\vec{v}$ in Σ'.

$$\mathbf{v}' = \vec{v}_{\Sigma'} = v_{x'}\hat{\mathbf{x}}' + v_{y'}\hat{\mathbf{y}}' + v_{z'}\hat{\mathbf{z}}' \tag{C.12}$$

Decomposing Σ' in terms of Σ gives

$$\begin{aligned}
\hat{\mathbf{x}}' &= x'_x\hat{\mathbf{x}} + x'_y\hat{\mathbf{y}} + x'_z\hat{\mathbf{z}} \\
\hat{\mathbf{y}}' &= y'_x\hat{\mathbf{x}} + y'_y\hat{\mathbf{y}} + y'_z\hat{\mathbf{z}} \\
\hat{\mathbf{z}}' &= z'_x\hat{\mathbf{x}} + z'_y\hat{\mathbf{y}} + z'_z\hat{\mathbf{z}}
\end{aligned} \tag{C.13}$$

where e'_a is the component of $\hat{\mathbf{e}}'$ in Σ and $\hat{\mathbf{e}}$ is a basis vector in Σ. Plugging (C.13) into (C.12) and gathering terms according the their coordinate in Σ gives a matrix equation

$$\mathbf{v} = \vec{v}_{\Sigma} = \begin{bmatrix} x'_x & y'_x & z'_x \\ x'_y & y'_y & z'_y \\ x'_z & y'_z & z'_z \end{bmatrix} \begin{bmatrix} v'_x \\ v'_y \\ v'_z \end{bmatrix} \tag{C.14}$$

where the first matrix is recognized as the components of $\hat{\mathbf{e}}'$ represented in Σ, given in Eq. (C.8), and the second matrix is $\mathbf{v}'$. Thus, given the components of a vector $\vec{v}$ in Σ', $\mathbf{v}'$, its representation in Σ is

$$\mathbf{v} = [\hat{\mathbf{x}}'_{\Sigma}\hat{\mathbf{y}}'_{\Sigma}\hat{\mathbf{z}}'_{\Sigma}]\mathbf{v}' \tag{C.15}$$

Similarly, given $\vec{v}$ in Σ, the coordinates in Σ' can be found by rotating Σ' to Σ while working in Σ'

$$\mathbf{v}' = \vec{v}_{\Sigma'} = \begin{bmatrix} x_{x'} & y_{x'} & z_{x'} \\ x_{y'} & y_{y'} & z_{y'} \\ x_{z'} & y_{z'} & z_{z'} \end{bmatrix} \begin{bmatrix} v_x \\ v_y \\ v_z \end{bmatrix} \tag{C.16}$$

To begin, notice that $\hat{\mathbf{z}}'$ can be rotated to $\hat{\mathbf{z}}$ by rotating around $\hat{\mathbf{t}} = \hat{\mathbf{y}}'$ by an angle $-\gamma$. Using Rodrigues' formula (C.5) with

$$\cos -\gamma = \cos\gamma = \frac{p_z}{p} \tag{C.17}$$

$$\sin -\gamma = -\sin\gamma = -\frac{(p_x^2 + p_y^2)^{1/2}}{p} \tag{C.18}$$

$$\hat{\mathbf{z}}_{\Sigma'} = \begin{bmatrix} -\dfrac{(p_x^2 + p_y^2)^{1/2}}{p} \\ 0 \\ \dfrac{p_z}{p} \end{bmatrix} \tag{C.19}$$

To find $\hat{\mathbf{x}}_{\Sigma'}$ and $\hat{\mathbf{y}}_{\Sigma'}$ note that by construction $\mathbf{t} = \hat{\mathbf{y}}'$ must lie in the xy-plane. Furthermore, if $\mathbf{p}$ has azimuthal angle ϕ then $\mathbf{t}$ has azimuth $\phi_t = (\frac{\pi}{2} + \phi)$. Using these relations a new frame, Σ'' can be defined in the xy-plane with

$\Sigma'' = \{\hat{\mathbf{w}}', \hat{\mathbf{y}}'\}$ and

$$\hat{\mathbf{w}}' = \hat{\mathbf{t}}_{\Sigma'} \times \hat{\mathbf{z}}_{\Sigma'} = \hat{\mathbf{y}}' \times \hat{\mathbf{z}}_{\Sigma'} = \begin{bmatrix} \frac{p_z}{p} \\ 0 \\ \frac{(p_x^2 + p_y^2)^{\frac{1}{2}}}{p} \end{bmatrix} \tag{C.20}$$

where $\hat{\mathbf{w}}$ has azimuth ϕ in Σ. Thus, $\hat{\mathbf{x}}_{\Sigma'}$ and $\hat{\mathbf{y}}_{\Sigma'}$ are related to $\hat{\mathbf{w}}$ by

$$\begin{aligned} \hat{\mathbf{x}}_{\Sigma'} &= \cos\phi\hat{\mathbf{w}}' - \sin\phi\hat{\mathbf{y}}' \\ \hat{\mathbf{y}}_{\Sigma'} &= \cos(\frac{\pi}{2} - \phi)\hat{\mathbf{w}}' + \sin(\frac{\pi}{2} - \phi)\hat{\mathbf{y}}' \\ &= \sin\phi\hat{\mathbf{w}}' + \cos\phi\hat{\mathbf{y}}' \end{aligned} \tag{C.21}$$

Using

$$\cos\phi = \frac{p_x}{(p_x^2 + p_y^2)^{1/2}}, \sin\phi = \frac{p_y}{(p_x^2 + p_y^2)^{1/2}} \tag{C.22}$$

yields

$$\hat{\mathbf{x}}_{\Sigma'} = \begin{bmatrix} \frac{p_x p_z}{p(p_x^2 + p_y^2)^{1/2}} \\ -\frac{p_y}{(p_x^2 + p_y^2)^{1/2}} \\ \frac{p_x}{p} \end{bmatrix} \tag{C.23}$$

$$\hat{\mathbf{y}}_{\Sigma'} = \begin{bmatrix} \frac{p_y p_z}{p(p_x^2 + p_y^2)^{1/2}} \\ \frac{p_x}{(p_x^2 + p_y^2)^{1/2}} \\ \frac{p_y}{p} \end{bmatrix} \tag{C.24}$$

Thus, given $\vec{v}$'s components in Σ, its components in Σ' are

$$\mathbf{v}' = \boldsymbol{T}\mathbf{v} = \begin{bmatrix} \frac{p_x p_z}{p(p_x^2 + p_y^2)^{1/2}} & \frac{p_y p_z}{p(p_x^2 + p_y^2)^{1/2}} & -\frac{(p_x^2 + p_y^2)^{1/2}}{p} \\ -\frac{p_y}{(p_x^2 + p_y^2)^{1/2}} & \frac{p_x}{(p_x^2 + p_y^2)^{1/2}} & 0 \\ \frac{p_x}{p} & \frac{p_y}{p} & \frac{p_z}{p} \end{bmatrix} \begin{bmatrix} v_x \\ v_y \\ v_z \end{bmatrix} \tag{C.25}$$

Vectors can now be easily represented in either the local dipole frame Σ', given its components in Σ by using $\boldsymbol{T}$, or represented in the global frame Σ, given the components in Σ' by using $\boldsymbol{P}$.

C.2 Multiple Dipoles

Using the frame transformations $\boldsymbol{P}$ and $\boldsymbol{T}$, any vector-valued function $\mathbf{f}'(\mathbf{r}')$ defined in a local frame Σ' that is displaced from the global origin by $\mathbf{r}$ can be represented using vectors only in the global frame. To accomplish this the local position vector to the point is interest, represented in Σ, is $\boldsymbol{\mathscr{r}} = \mathbf{r_0} - \mathbf{r}$. $\boldsymbol{\mathscr{r}}$ can then be transformed to Σ' by $\boldsymbol{\mathscr{r}}' = \boldsymbol{P}\boldsymbol{\mathscr{r}}$. $\mathbf{f}'$ is then applied to $\boldsymbol{\mathscr{r}}'$, resulting in the value of the local field at $\mathbf{r_0}$. This value must then be transformed back to Σ using $\boldsymbol{T}$. Thus,

$$\mathbf{f}(\mathbf{r}_0) = \boldsymbol{T}\mathbf{f}'(\boldsymbol{P}\boldsymbol{\mathscr{r}}) \tag{C.26}$$

Returning to the original problem now, if multiple dipoles, $\mathbf{p}_i$, are present in a system, then by using (C.26) the electric field from each one, given in (C.1), can be related to a global coordinate system, allowing them to be summed.

$$\mathbf{E}(\mathbf{r}_0) = \sum_i \mathbf{E}'_i(\boldsymbol{\mathscr{r}}'_i) = \sum_i \boldsymbol{T}\mathbf{E}'_i(\boldsymbol{P}\boldsymbol{\mathscr{r}}_i) \tag{C.27}$$

where $\boldsymbol{\mathscr{r}}_i = \mathbf{r}_0 - \mathbf{r}_i$, and $\mathbf{r}_i$ is the displacement vector to $\mathbf{p}_i$.

Appendix D

Lattice Sum

D.1 Lattice Sum

When considering the construction of a multi-layered back reflector, the width and length are much greater than its depth. This allows the approximation that each layer consists of an infinite plane of plasmonic particles. It is also likely that a carefully designed arrangement of the particles will give a more favorable scattering profile than randomly placed particles. Further, a regular lattice is likely to be an ideal structure to allow a scattering profile to be engineered due to its periodicity and reproducibility.

The proposed structure consists of several 2D layers stacked on top of each other. Thus, there are several parameters that can be adjusted in each layer: the size and shape of the particles, the lattice vectors, the parallel displacement relative to the other layers, and the spacing between the layers. One of the major issues with optimizing these parameters is that the layers are large enough to be considered infinite, creating issues when trying to find the field of even a single layer. However, if a single expression for the electric field of a single layer can be found, then the field of the whole structure, assuming each layer is decoupled from the rest, can be found with a finite sum.

In Appendix C it is shown how, given a function $\mathbf{f}'(\mathbf{r}')$ defined in a local frame Σ', it is possible to find its value in a global frame Σ given the displacement of Σ' from the global origin, the rotation of the z′- from the z-axis, and the point of interest in Σ, $\mathbf{r}_0$. This situation then, is restricted compared to that of Appendix C in that the displacement of each local frame Σ'_i is located at a lattice point instead of an arbitrary point.

D.1.1 General Method

To begin, consider a vector field $\mathbf{f}'(\mathbf{r})$ defined in a local frame Σ'. This function is then placed at each point in a 2D lattice $\tilde{\mathfrak{L}}$, defined by the vectors $\{\tilde{\mathbf{a}}_1, \tilde{\mathbf{a}}_2\} \in \mathbb{R}^3$, with global reference frame $\tilde{\Sigma}$. Thus, each lattice point can be written as $\tilde{\mathbf{r}}_i = \alpha_i^1\tilde{\mathbf{a}}_1 + \alpha_i^2\tilde{\mathbf{a}}_2$, with $\alpha^1, \alpha^2 \in \mathbb{Z}$. An illustration of this is seen in Fig. D.1a. Although we begin with a 2D lattice for simplicity, all of the ideas, and most of the calculations will be kept general enough to be expanded to a 3 dimensional lattice later on. Note, in this section indices appear as subscripts and superscripts allowing for more compact notation using Einstein's summation notation. In cases where it may be unclear as to whether a superscript is an exponent or an index, the indexed term will be placed in square brackets, e.g. $[\alpha^1]^2$ is α^1 squared.

To find the sum of all the $\mathbf{f}'_i$ at a vector $\tilde{\mathbf{r}}_0$ in $\tilde{\Sigma}$, the local vector from each lattice point

$$\boldsymbol{\imath}_i = \tilde{\mathbf{r}}_0 - \tilde{\mathbf{r}}_i \tag{D.1}$$

must be considered. However, because the $\tilde{\Sigma}_i$ only differ by a displacement, Eq. (D.1) can be thought of as collapsing each local frame to the origin as visualized in Fig. D.1b. This results in a conjugate lattice $\mathfrak{L}$ with points defined by $\mathbf{r}_i = \alpha_i^1\tilde{\mathbf{a}}_1 + \alpha_i^2\tilde{\mathbf{a}}_2 - \tilde{\mathbf{r}}_0$. At this point, to make the picture of this structure more clear, two assumptions are made without loss of generality. The first is that in images of the structure the lattice plane will be drawn horizontally, this is simply a rotation of the entire structure made for easier viewing. Second, due to the periodicity of the structure, it is assumed that the projection of $\tilde{\mathbf{r}}_0$ into $\tilde{\mathfrak{L}}$ lies in the first unit cell, i.e. in the parallelogram defined by the vectors $\tilde{\mathbf{a}}_1$ and $\tilde{\mathbf{a}}_2$.

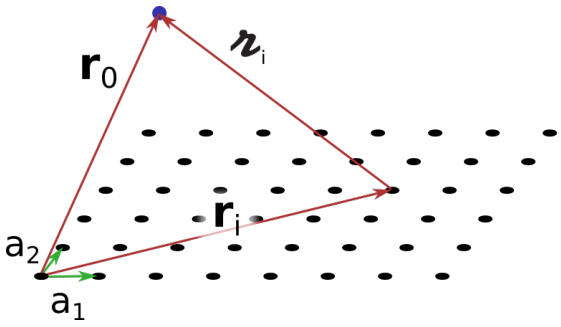

(a)

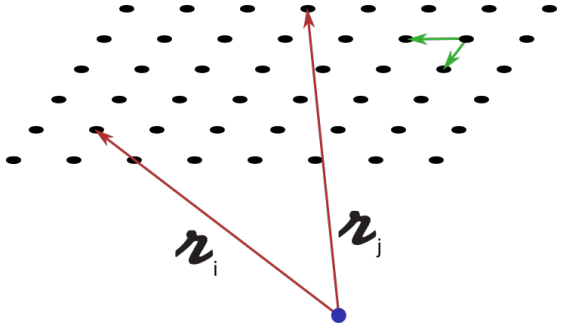

(b)

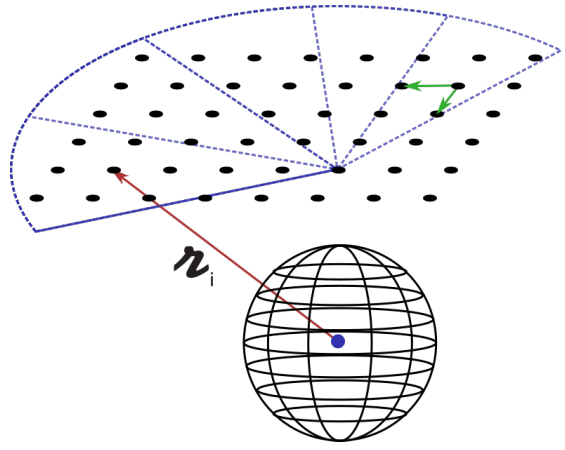

(c)

Figure D.1: Illustrations of the steps leading to the lattice summation process investigated. (a) The original lattice, with green lattice vectors. (b) Viewing the lattice points as collapsed to the origin creating a new conjugate lattice. The new conjugate lattice vectors are in green. (c) The stereographic projection that divides the conjugate lattice. The blue point in the lattice from which the divisions emanate is the projection of the origin on to the lattice plane, but is not necessarily a lattice point.

There are two main realizations driving this summation method. Underlying both is that as $\mathscr{r} \to \infty$ in any direction the distance the lattice is from the origin becomes negligible, $h \ll \mathscr{r}$ [1]. The first realization, then, is that as $\mathscr{r} \to \infty$ in some direction ϕ the distance between lattice points is constant. There are quite interesting subtleties regarding these distance that are discussed in Section D.3. Next, consider a unit sphere $\mathbb{S}$ centered at the origin of Σ with its own coordinate system $\Sigma^\dagger$ such that the $z^\dagger$-axis is directed towards and perpendicular to $\mathfrak{L}$, and the $x^\dagger$-axis is aligned with the x-axis. Then $\phi^\dagger = \phi$, and as $\mathscr{r} \to \infty$, $\boldsymbol{\mathscr{r}}$ intersects this sphere along its equator $\mathcal{E}$.

Using a stereographic projection between $\mathbb{S}$ and $\mathfrak{L}$, lattice points in $\mathfrak{L}$ are then related to points on $\mathbb{S}$. Next, $\mathbb{S}$ is divided into m regions of azimuthal width $\Delta\phi_i$, and n regions of polar width $\Delta\theta_i$ creating a grid. These grid regions can then be indexed, let them be called ρ_i. The center point of each ρ_i, $\bar{\rho}_i$, can be taken as a representative point for the entire region. This also divides $\mathfrak{L}$ in to corresponding regions. These steps are illustrated in Fig. D.1.

As $\mathscr{r} \to \infty$ then either $\alpha^1 \to \infty$ or $\alpha^2 \to \infty$, or both. Consider now $\tan\phi$.

$$\tan\phi = \frac{\mathscr{r}^1}{\mathscr{r}^2} = \frac{r_0^2 - \alpha^1 a_1^2 - \alpha^2 a_2^2}{r_0^1 - \alpha^1 a_1^1 - \alpha^2 a_2^1} \tag{D.2}$$

So either $r_0^2 \ll (\alpha^1 a_1^2 + \alpha^2 a_2^2)$, $r_0^1 \ll (\alpha^1 a_1^1 + \alpha^2 a_2^1)$, or both. If $\alpha^1/\alpha^2 = \kappa$ is constant with α^1, $\alpha^2 \neq 0$, then

$$\begin{aligned} \tan\phi &\sim \frac{\alpha^1 a_1^2 + \alpha^2 a_2^2}{\alpha^1 a_1^1 + \alpha^2 a_2^1} \\ &= \frac{\kappa a_1^2 + a_2^2}{\kappa a_1^1 + a_2^1} \end{aligned} \tag{D.3}$$

is constant. If $\alpha^2 \to \infty$ while α^1 remains constant, then $\kappa \sim 0$ and $\tan\phi \sim a_2^2/a_2^1$ is a constant. On the other hand, if $\alpha^1 \to \infty$ while α^2 remains constant then $\kappa^{-1} \sim 0$ and $\tan\phi \sim a_1^2/a_1^1$ is constant. Inverting Eq. (D.3) gives the ratio that must be maintained to remain in the ϕ direction.

$$\kappa(\phi) = -\frac{a_2^2 - a_2^1 \tan\phi}{a_1^2 - a_1^1 \tan\phi} \tag{D.4}$$

To find the distance between lattice points in a given direction, first consider the change in distance if one of the α's, α^{j_0}, is incremented by one as $\mathscr{r} \to \infty$ in the ϕ direction. To clarify the notation, $j \in J = \{1, 2\}$, $j' \in J \backslash j_0$, $k \in \{1, 2, 3\}$, $\Delta\mathscr{r}/\Delta\alpha^{j_0}$ is the change in distance as α^{j_0} is incremented by one, $\mathscr{r}(\alpha)$ is $\mathscr{r}$ given

[1] This is the strict meaning of $\ll$ from asymptotic analysis, i.e. $f \ll g\,(\text{as } n \to \infty) \iff \lim_{n\to\infty} f(n)/g(n) = 0$. The $\sim$ symbol will also be used in the strict sense, such that $f \sim g\,(\text{as } n \to \infty) \iff \lim_{n\to\infty} f(n)/g(n) = 1$

α^1, α^2, and $\mathbb{1}$ is used to indicate a sum, i.e. $a^k\mathbb{1}_k = \sum_k a^k$.

$$\begin{aligned}
\frac{\Delta r}{\Delta\alpha^{j_0}} &= r(\alpha^{j'};\, \alpha^{j_0}+1) - r(\alpha) \\
&= \left(\left[\alpha^{j'}a^k_{j'} + (\alpha^{j_0}+1)a^k_{j_0}\right]^2\mathbb{1}_k\right)^{1/2} - \left(\left[\alpha^j a^k_j\right]^2\mathbb{1}_k\right)^{1/2} \\
&= \left(\left[\alpha^j a^k_j + a^k_{j_0}\right)^2\mathbb{1}_k\right)^{1/2} - \left(\left[\alpha^j a^k_j\right]^2\mathbb{1}_k\right)^{1/2} \\
&= \left(\left[[\alpha^j a^k_j]^2 + [a^k_{j_0}]^2 + 2[\alpha^j a^k_j a^k_{j_0}]\right]\mathbb{1}_k\right)^{1/2} - \left(\left[\alpha^j a^k_j\right]^2\mathbb{1}_k\right)^{1/2} \\
&= \left(\left[\alpha^j a^k_j\right]^2\mathbb{1}_k\right)^{1/2}\left\{1 + \frac{(2\alpha^j a^k_j a^k_{j_0} + [a^k_{j_0}]^2)\mathbb{1}_k}{[\alpha^j a^k_j]^2\mathbb{1}_k}\right\}^{1/2} - \left(\left[\alpha^j a^k_j\right]^2\mathbb{1}_k\right)^{1/2}
\end{aligned}$$

Because either $\alpha^1 \to \infty$, $\alpha^2 \to \infty$, or both

$$[a^k_{j_0}]^2 \ll [\alpha^j a^k_j a^k_{j_0}] \ll [\alpha^j a^k_j]^2 \tag{D.5}$$

First using the binomial expansion then the relations in Eq. (D.5) gives

$$\begin{aligned}
\frac{\Delta r}{\Delta\alpha^{j_0}} &\sim \left(\left[\alpha^j a^k_j\right]^2\mathbb{1}_k\right)^{1/2}\left\{1 + \frac{1}{2}\frac{(2\alpha^j a^k_j a^k_{j_0} + [a^k_{j_0}]^2)\mathbb{1}_k}{[\alpha^j a^k_j]^2\mathbb{1}_k}\right\} - \left(\left[\alpha^j a^k_j\right]^2\mathbb{1}_k\right)^{1/2} \\
&= \frac{1}{2}\frac{(2\alpha^j a^k_j a^k_{j_0} + [a^k_{j_0}]^2)\mathbb{1}_k}{([\alpha^j a^k_j]^2\mathbb{1}_k)^{1/2}} \\
&\sim \frac{(\alpha^j a^k_j a^k_{j_0})\mathbb{1}_k}{([\alpha^j a^k_j]^2\mathbb{1}_k)^{1/2}} \\
&= \frac{(r^k a^k_{j_0})\mathbb{1}_k}{r} \\
&= \frac{r^1 a^1_{j_0} + r^2 a^2_{j_0} + r^3 a^3_{j_0}}{r} \\
&= \frac{\boldsymbol{r}\cdot\mathbf{a}_{j_0}}{r} \\
&= \hat{\boldsymbol{r}}\cdot\mathbf{a}_{j_0}
\end{aligned}$$

So if α^{j_0} is increased by one, then r will change by $\hat{\boldsymbol{r}}\cdot\mathbf{a}_{j_0}$, in the limit as $r \to \infty$. Because this approximation is only valid as $r \to \infty$ the lattice must be broken into a near region and a far region. In the near region, this assumption does not hold, so a direct sum of the fields will be computed. In the far region an asymptotic approximation of the field can be computed using this assumption. Remembering that $\mathbb{S}$ has been broken in to regions, a natural choice for the boundary between the near and far regions is the boundary of the region containing $\mathcal{E}$. Thus, all lattice points whose projection on to $\mathbb{S}$ is in the region also containing $\mathcal{E}$ will be considered "far away", and all other will be considered "close". This also defines the shortest distance to the far region in each direction $\boldsymbol{r}_{\beta_i}$, dictating the smallest $\{\alpha^1, \alpha^2\}$ required to enter the far region. For each ρ_i, then, choose the azimuth ϕ_i as that of $\bar{\rho}_i$ and define $\{\beta^1_i, \beta^2_i\}$ to be this minimal set of α's.

There are now $(m+1)$ regions that must be summed over: the single near region, and the m far regions. As mentioned, in the near region the sum is found

directly. And now, in each of the far regions, the distance between adjacent points in the $\mathbf{a}_{j_0}$ direction is constant with value ${}^{\Delta r}/_{\Delta\alpha^{j_0}} = \delta r_{j_0}$. Considering the sum of the points in the i^{th} region, the projection of ρ_i on to $\mathfrak{L}$ is an isosceles trapezoid with infinite height. If the sides are traced back to the projection of the origin on to $\mathfrak{L}$, as in Fig. D.2, they meet at an angle

$$\eta = 2\arcsin\left(\sin\left(\frac{\Delta\phi_i}{2}\right)\frac{1}{\cos\xi}\right) \tag{D.6}$$

where ξ is the angle between $\mathcal{E}$ and the polar angle at the distance of interest. Thus, at the γ^{th} point in ρ_i, $\cos\xi = {}^{(r_{\beta_i}+\gamma\cdot\delta r_\phi)}/_r$. However, because this sum is taking place in the far region $\xi \to 0$, so $\eta \to \Delta\phi_i$.

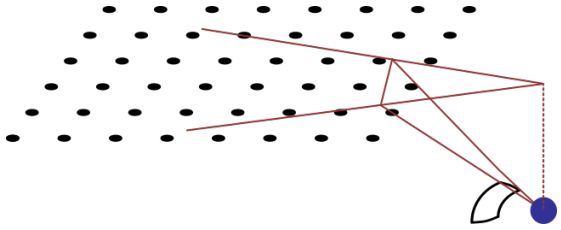

Figure D.2: The stereographic projection of one region on to to conjugate lattice. The black "square" is the region on the sphere to which the projection belongs.

In the ϕ_i direction, δr_{j_0} is constant, so the region can be broken into isosceles trapezoids of constant height δr_{j_0}. However, as r increases, so does the width of the corresponding trapezoid, and thus more lattice points are contained within the area. To account for this, the density of points when viewing the lattice in the ϕ_i direction, denoted σ_{ϕ_i}, can be found and multiplied by the area of the trapezoid A at that distance. This product represents the magnitude of $\mathbf{f}$ created by points in each trapezoid. The magnitude can then be assigned to a representative point creating a new lattice $\mathfrak{L}_R$ mimicking the original, but with radial symmetry rather than lattice symmetry.

To find the density of points along an arbitrary direction, $\sigma(\phi)$, the area each point occupies must be found. It is already known that along the ϕ direction δr_{j_0} is constant. Thus, the distance between adjacent points can be found by

$$\delta r(\phi) = \delta r_1 + \frac{1}{\kappa(\phi)}\delta r_2 = \frac{\Delta r}{\Delta\alpha^1} + \frac{\alpha^2}{\alpha^1}\frac{\Delta r}{\Delta\alpha^2} \tag{D.7}$$

This gives a linear density of points along ϕ equal to $[\delta r(\phi)]^{-1}$. $\sigma(\phi)$ then, is the inverse of the area that each point occupies, given by

$$\sigma(\phi) = [\delta r(\phi)\cdot\delta r(\phi+{}^{\pi}/_2)]^{-1} \tag{D.8}$$

The area of a trapezoid is given by $\frac{h}{2}(b_1+b_2)$, where h is the height, and b_1, b_2 are the length of the bases. In this situation the height has been defined as the distance between two points in the ϕ direction, $h = \delta r(\phi)$, and the bases are the width of the region of interest at r and $\big(r+\delta r(\phi)\big)$. Relating these distances to lattice points in region ρ_i gives

$$\begin{aligned} r(\alpha^1,\phi) &\sim r_{\beta_i} + (\alpha^1-\beta_i^1)\delta r(\phi) \\ &= r_{\beta_i} + \gamma\cdot\delta r(\phi) \\ &\sim \alpha^1\delta r(\phi),\ (\text{as } r\to\infty) \end{aligned} \tag{D.9}$$

for $\gamma = (\alpha^1 - \beta^1) \in \mathbb{N}$. Under the current assumptions $\mathscr{r} \to \infty$ and $\eta = \Delta\phi_i$, so the bases can be taken as the arc length of the circle at their respective distances. This results in

$$\begin{aligned} A(\alpha^1, \phi) &\sim \frac{\delta\mathscr{r}(\phi)}{2}\big(\alpha^1 \delta\mathscr{r}(\phi) \cdot \eta + (\alpha^1 + 1)\delta\mathscr{r}(\phi) \cdot \eta\big) \\ &= [\delta\mathscr{r}(\phi)]^2 \, \Delta\phi_i \, (\alpha^1 + \frac{1}{2}) \end{aligned} \tag{D.10}$$

Thus, the magnitude to be assigned to each point in $\mathfrak{L}_R$ is given by

$$\begin{aligned} M(\alpha^1, \phi) &= A(\phi, \alpha^1)\, \sigma(\phi) \\ &\sim \frac{\delta\mathscr{r}(\phi)}{\delta\mathscr{r}(\phi + \pi/2)} \, \Delta\phi_i \, \left(\alpha^1 + \frac{1}{2}\right) \qquad \text{(D.11)} \\ &= \frac{\delta\mathscr{r}(\phi)}{\delta\mathscr{r}(\phi + \pi/2)} \, \Delta\phi_i \, \left(\gamma + \beta + \frac{1}{2}\right) \qquad \text{(D.12)} \end{aligned}$$

Finally, the situation has become suitable to perform the actual sum over all the lattice points. However, before moving on a summary of the current steps seems in order. Originally a function $\mathbf{f}$ was placed at each point in a lattice $\mathbf{r}_i$, and the sum of the functions at some point $\mathbf{r}_0$ was to be found. First, a conjugate lattice $\mathfrak{L}$ was created in a frame Σ by realizing that for the given function only $\boldsymbol{\mathscr{r}} = \mathbf{r}_0 - \mathbf{r}_i$ is important. Then a unit sphere $\mathbb{S}$ was placed around the origin of Σ and divided into regions of angular size $\Delta\phi_i$ and $\Delta\theta_i$. Using a stereographic projection the divisions of $\mathbb{S}$ were used to divide $\mathfrak{L}$ in to corresponding regions. It was then noticed that as $\mathscr{r} \to \infty$ in any direction $\hat{\boldsymbol{\mathscr{r}}} \to \mathcal{E}$. $\mathfrak{L}$ was then divided in to one near region and m far regions using the boundary of the $\mathbb{S}$-region containing $\mathcal{E}$ as the dividing line. This dividing line was characterized by lattice constants β_i and distance $\mathscr{r}_{\beta_i}$.

It was then found that as $\mathscr{r} \to \infty$ in a certain direction the ratio of lattice constants $\kappa = {}^{\alpha^1}\!/_{\alpha^2}$, and the spacing between lattice points are constant. This was used to determine the density of points when viewing the lattice in a given direction $\sigma(\phi)$, and combined with the divisions of $\mathfrak{L}$ to determine the area of a trapezoid with height $\delta\mathscr{r}(\phi)$, at a distance $\mathscr{r}$, denoted $A(\alpha^1, \phi)$. Combining σ and A allowed a magnitude M to be assigned to each trapezoid. At this point a radial "lattice" $\mathfrak{L}_R$ was constructed that mimics $\mathfrak{L}$ by assigning the magnitude $M(\mathscr{r}, \phi)$ to points at angle $\phi = \phi_i$ and distances $\big(\mathscr{r}_{\beta_i} + \gamma\delta\mathscr{r}(\phi_i)\big)$, where ϕ is the azimuthal angle in the middle of each limiting region of $\mathbb{S}$, ρ_i, and $\gamma \in \mathbb{N}$.

Thus, the lattice sum has been transformed into a single finite sum within the near region, and m infinite sums in the far region. Further, in the far regions

because $\hat{\boldsymbol{r}}$ becomes constant as $r \to \infty$, $\hat{\mathbf{f}}$ is constant.

$$\begin{aligned}
\mathbf{F} &= \sum_i \mathbf{f}(\mathbf{r_0} - \mathbf{r_i}) \\
&\sim \sum_{i \in \text{Near}} \mathbf{f}(\boldsymbol{r}_i) + \sum_{i=1}^{m} \sum_{\gamma=0}^{\infty} M(r, \phi_i) \cdot \mathbf{f}\left((r_{\beta_i} + \gamma \cdot \delta r(\phi_i))\, \hat{\boldsymbol{r}} \right), \text{ (as } r \to \infty) \\
&= \sum_{i \in \text{Near}} \mathbf{f}(\boldsymbol{r}_i) \\
&\quad + \sum_{i=1}^{m} \sum_{\gamma=0}^{\infty} \frac{\delta r(\phi_i)}{\delta r(\phi_i + \frac{\pi}{2})} \Delta\phi_i \left(\gamma + \beta_i + \frac{1}{2} \right) \mathbf{f}\left((r_{\beta_i} + \gamma \cdot \delta r(\phi_i))\, \hat{\boldsymbol{r}} \right) \\
&= \sum_{i \in \text{Near}} \mathbf{f}(\boldsymbol{r}_i) \\
&\quad + \sum_{i=1}^{m} \Delta\phi_i \frac{\delta r(\phi_i)}{\delta r(\phi_i + \frac{\pi}{2})} \hat{\mathbf{f}}_i \sum_{\gamma=0}^{\infty} \left(\gamma + \beta_i + \frac{1}{2} \right) f\left((r_{\beta_i} + \gamma \cdot \delta r(\phi_i))\, \hat{\boldsymbol{r}} \right)
\end{aligned} \tag{D.13}$$

So the complexity of the lattice sum has been reduced to performing a single infinite sum over one index γ.

D.1.2 An Infinite 2D Lattice of Dipoles

Of interest now is what field is produced if a dipole $\mathbf{p}$ is located at each lattice point driven by a plane wave. In this scenario the dipoles do not affect each other's driving field, and the waves are assumed to travel through free space. The orientation and magnitude of every dipole is the same, and they only differ in their position, as was assumed when arriving at Eq. (D.13). Letting

$$\mathbf{E}'(\boldsymbol{r}') = -\frac{p\omega^2\mu_0}{4\pi}\sin\theta'\frac{\exp\left(i\left[\omega(\frac{r'}{c}-t)+\psi\right]\right)}{r'}\hat{\boldsymbol{\theta}}' \tag{D.14}$$

as in Eq. (A.18), then the transformations $\boldsymbol{P}$ and $\boldsymbol{T}$ from Eqs. (C.11) and (C.25) respectively, can be used to transform vectors from $\mathbf{p}$'s reference frame into Σ. Plugging Eq. (D.14) in to Eq. (D.13) results in a total field

$$\begin{aligned}\mathbf{E}_t &= \sum_{i\in\text{Near}}\mathbf{E}(\boldsymbol{r}_i)\\ &\quad+\sum_{i=1}^{m}\Delta\phi_i\frac{\delta r(\phi_i)}{\delta r(\phi_i+\frac{\pi}{2})}\boldsymbol{P}\hat{\boldsymbol{\theta}}'_i\sum_{\gamma=0}^{\infty}\left(\gamma+\beta_i+\frac{1}{2}\right)\\ &\qquad\times E\left(\left(r_{\beta_i}+\gamma\cdot\delta r(\phi_i)\right)\boldsymbol{T}\hat{\boldsymbol{r}}_i\right)\\ &= \sum_{i\in\text{Near}}\mathbf{E}(\boldsymbol{r}_i)+\sum_{i=1}^{m}\Delta\phi_i\frac{\delta r(\phi_i)}{\delta r(\phi_i+\frac{\pi}{2})}\boldsymbol{P}\hat{\boldsymbol{\theta}}'_i\cdot\mathcal{S}_i^0\end{aligned} \tag{D.15}$$

where $\mathcal{S}_i^0$ is the value of the sum.

$$\begin{aligned}\mathcal{S}_i^0 &= \sum_{\gamma=0}^{\infty}\left(\gamma+\beta_i+\frac{1}{2}\right)\cdot E\Big(\left(r_{\beta_i}+\gamma\cdot\delta r(\phi_i)\right)\boldsymbol{T}\hat{\boldsymbol{r}}_i\Big)\\ &= \sum_{\gamma=0}^{\infty}\left(\gamma+\beta_i+\frac{1}{2}\right)\frac{-p\omega^2\mu_0}{4\pi}\sin\left[\theta(\boldsymbol{T}\hat{\boldsymbol{r}}_i)\right]\\ &\qquad\times\frac{\exp\left(i\left[\frac{\omega}{c}\left(r_{\beta_i}+\gamma\cdot\delta r(\phi_i)\right)-\omega t+\psi(\phi_i,\gamma)\right]\right)}{r_{\beta_i}+\gamma\cdot\delta r(\phi_i)}\\ &= \frac{-p\omega^2\mu_0}{4\pi}\sin\left[\theta(\boldsymbol{T}\hat{\boldsymbol{r}}_i)\right]\exp\left(\frac{i\omega r_{\beta_i}}{c}\right)\exp(-i\omega t)\\ &\qquad\times\sum_{\gamma=0}^{\infty}\left(\gamma+\beta_i+\frac{1}{2}\right)\frac{\exp\left(i\left[\frac{\omega}{c}\gamma\cdot\delta r(\phi_i)+\psi(\phi_i,\gamma)\right]\right)}{r_{\beta_i}+\gamma\cdot\delta r(\phi_i)}\\ &= \frac{-p\omega^2\mu_0}{4\pi}\sin\left[\theta(\boldsymbol{T}\hat{\boldsymbol{r}}_i)\right]\exp\left(\frac{i\omega r_{\beta_i}}{c}\right)\exp(-i\omega t)\cdot\mathcal{S}_i^1\end{aligned} \tag{D.16}$$

where $\mathcal{S}_i^1$ is the value of the sum.

$$
\begin{aligned}
\mathcal{S}_i^1 &= \sum_{\gamma=0}^{\infty} \left(\gamma + \beta_i + \frac{1}{2}\right) \frac{\exp\left(i\left[\frac{\omega}{c}\gamma \cdot \delta\boldsymbol{\imath}(\phi_i) + \psi(\phi_i,\gamma)\right]\right)}{\boldsymbol{\imath}_{\beta_i} + \gamma \cdot \delta\boldsymbol{\imath}(\phi_i)} \\
&\sim \sum_{\gamma=0}^{\infty} \left(\gamma + \beta_i + \frac{1}{2}\right) \frac{\exp\left(i\left[\frac{\omega}{c}\gamma \cdot \delta\boldsymbol{\imath}(\phi_i) + \psi(\phi_i,\gamma)\right]\right)}{(\beta_i + \gamma) \cdot \delta\boldsymbol{\imath}(\phi_i)}, \text{ (as } \boldsymbol{\imath} \to \infty) \\
&= \sum_{\gamma=\beta_i}^{\infty} \left(\gamma + \frac{1}{2}\right) \frac{\exp\left(i\left[\frac{\omega}{c}(\gamma - \beta_i) \cdot \delta\boldsymbol{\imath}(\phi_i) + \psi(\phi_i,\gamma)\right]\right)}{\gamma \cdot \delta\boldsymbol{\imath}(\phi_i)} \\
&= \frac{\exp\left(-i\frac{\omega}{c}\beta_i \delta\boldsymbol{\imath}(\phi_i)\right)}{\delta\boldsymbol{\imath}(\phi_i)} \sum_{\gamma=\beta_i}^{\infty} \left(\gamma + \frac{1}{2}\right) \frac{\exp\left(i\left[\frac{\omega}{c}\delta\boldsymbol{\imath}(\phi_i)\gamma + \psi(\phi_i,\gamma)\right]\right)}{\gamma} \\
&= \frac{\exp\left(-i\frac{\omega}{c}\beta_i \delta\boldsymbol{\imath}(\phi_i)\right)}{\delta\boldsymbol{\imath}(\phi_i)} \\
&\quad \times \left\{ \begin{array}{l} \displaystyle\sum_{\gamma=\beta_i}^{\infty} \exp\left(i\left[\frac{\omega}{c}\delta\boldsymbol{\imath}(\phi_i)\gamma + \psi(\phi_i,\gamma)\right]\right) \\ \displaystyle + \frac{1}{2}\sum_{\gamma=\beta_i}^{\infty} \frac{\exp\left(i\left[\frac{\omega}{c}\delta\boldsymbol{\imath}(\phi_i)\gamma + \psi(\phi_i,\gamma)\right]\right)}{\gamma} \end{array} \right\} \\
&= \frac{\exp\left(-i\frac{\omega}{c}\beta_i \delta\boldsymbol{\imath}(\phi_i)\right)}{\delta\boldsymbol{\imath}(\phi_i)} \left\{\mathcal{S}_i^2 + \frac{1}{2}\mathcal{S}_i^3\right\}
\end{aligned}
\tag{D.17}
$$

With the sums $\mathcal{S}_i^2$ and $\mathcal{S}_i^3$ as

$$
\mathcal{S}_i^2 = \sum_{\gamma=\beta_i}^{\infty} \exp\left(i\left[\frac{\omega}{c}\delta\boldsymbol{\imath}(\phi_i)\gamma + \psi(\phi_i,\gamma)\right]\right) \tag{D.18}
$$

$$
\mathcal{S}_i^3 = \sum_{\gamma=\beta_i}^{\infty} \frac{\exp\left(i\left[\frac{\omega}{c}\delta\boldsymbol{\imath}(\phi_i)\gamma + \psi(\phi_i,\gamma)\right]\right)}{\gamma} \tag{D.19}
$$

Combining these results give the total field as

$$\mathbf{E}_t = \sum_{i\in\text{Near}} \mathbf{E}(\boldsymbol{\imath}_i) \tag{D.20}$$

$$+ \sum_{i=1}^{m} \Delta\phi_i \frac{\delta\imath(\phi_i)}{\delta\imath(\phi_i + \frac{\pi}{2})} \boldsymbol{P}\hat{\boldsymbol{\theta}}'_i \tag{D.21}$$

$$\times \frac{-p\omega^2\mu_0}{4\pi} \sin\left[\theta(\boldsymbol{T}\hat{\boldsymbol{\imath}}_i)\right] \tag{D.22}$$

$$\times \exp\left(\frac{i\omega\imath_{\beta_i}}{c}\right) \exp(-i\omega t) \tag{D.23}$$

$$\times \frac{\exp\left(-i\frac{\omega}{c}\beta_i\delta\imath(\phi_i)\right)}{\delta\imath(\phi_i)} \left\{\mathcal{S}_i^2 + \frac{1}{2}\mathcal{S}_i^3\right\}$$

$$= \sum_{i\in\text{Near}} \mathbf{E}(\boldsymbol{\imath}_i) \tag{D.24}$$

$$+ \frac{-p\omega^2\mu_0}{4\pi} e^{-i\omega t} \tag{D.25}$$

$$\times \sum_{i=1}^{m} \Delta\phi_i \frac{\exp\left(i\frac{\omega}{c}[\imath_{\beta_i} - \beta_i\delta\imath(\phi_i)]\right)}{\delta\imath(\phi_i + \frac{\pi}{2})} \cdot \sin\left[\theta(\boldsymbol{T}\hat{\boldsymbol{\imath}}_i)\right] \boldsymbol{P}\hat{\boldsymbol{\theta}}'_i \tag{D.26}$$

$$\times \left\{\mathcal{S}_i^2 + \frac{1}{2}\mathcal{S}_i^3\right\} \tag{D.27}$$

Analyzing the components of the total field is quite illuminating now. $\exp\left(i\frac{\omega}{c}[\imath_{\beta_i} - \beta_i\delta\imath(\phi_i)]\right)$ accounts for the error in the phase change from the assumption that the distance between lattice points in the near region are integer multiples of $\delta\imath(\phi_i)$. $\sin\left[\theta(\boldsymbol{T}\hat{\boldsymbol{\imath}}_i)\right]\boldsymbol{P}\hat{\boldsymbol{\theta}}'_i$ accounts for the magnitude and direction of the radiated field relative to the dipole's local frame. Also of note is the $\left[\delta\imath(\phi_i + \frac{\pi}{2})\right]^{-1}$ term which account for the density of points near the ϕ_i direction. From this point, though, no further progress can be made without explicitly knowing $\psi(\phi_i, \gamma)$, the phase change between lattice points, which is contained in $\mathcal{S}_i^2$ and $\mathcal{S}_i^3$.

D.1.3 No Phase Change

Assume there is no phase change between lattice points, i.e. $\psi = 0$. This would be a zeroth-order model of an incident plane wave normal to the lattice and linearly polarized driving the dipoles.

Finding $\mathcal{S}_i^3$

From Eq. (D.19)

$$\begin{aligned}\mathcal{S}_i^3 &= \sum_{\gamma=\beta_i}^{\infty} \frac{\exp\left(i\left[\frac{\omega}{c}\delta\mathscr{r}(\phi_i)\gamma\right]\right)}{\gamma} \\ &= \sum_{\gamma=\beta_i}^{\infty} \frac{e^{ik_i\gamma}}{\gamma} \\ &= \sum_{\gamma=1}^{\infty} \frac{e^{ik_i\gamma}}{\gamma} - \sum_{\gamma=1}^{\beta_i-1} \frac{e^{ik_i\gamma}}{\gamma}\end{aligned} \tag{D.28}$$

where $k_i = \frac{\omega}{c}\delta\mathscr{r}(\phi_i)$. The first term on the RHS of Eq. (D.28) is recognized as the Taylor series for the natural logarithm.

$$\ln(1+x) = \sum_{n=1}^{\infty} \frac{(-1)^{n+1}}{n} x^n \tag{D.29}$$

So

$$\begin{aligned}\sum_{n=1}^{\infty} \frac{e^{cn}}{n} &= -\sum_{n=1}^{\infty} \frac{(-1)^n \cdot (-1)^{n+1}}{n} e^{cn} \\ &= -\sum_{n=1}^{\infty} \frac{(-1)^{n+1}}{n} \left(-e^c\right)^n \\ &= -\ln\left(1-e^c\right)\end{aligned} \tag{D.30}$$

Thus

$$\mathcal{S}_i^3 = -\ln\left(1-e^{ik_i}\right) - \sum_{\gamma=1}^{\beta_i-1} \frac{e^{ik_i\gamma}}{\gamma} \tag{D.31}$$

The logarithmic term in the RHS of Eq. (D.31) diverges exponentially fast as $k_i \to 2\pi q$, for $q \in \mathbb{Z}$. This occurs if the spacing between lattice points in the ϕ_i direction is an integer multiple of the radiation wavelength. However, if the spacing is even slightly off, the value quickly converges. Because $-1 \leq e^{ik_i} \leq 1$ the argument of the logarithm is bound between 0 and 2. Also of note is that as $\beta_i \to \infty$, $\mathcal{S}_i^3 \to 0$. Intuitively, this occurs because the finite sum contains the largest magnitude terms in the expansion of the logarithm.

When $k_i = 0 \mod 2\pi$ in Eq. (D.28), the S_i^3 term has a harmonic series as

the first term

$$S_i^3|_{k_i=0} = \sum_{\gamma=1}^{\infty} \frac{e^{i2\pi\gamma}}{\gamma} - \sum_{\gamma=1}^{\beta_i-1} \frac{e^{i2\pi\gamma}}{\gamma}$$
$$= \sum_{\gamma=1}^{\infty} \frac{1}{\gamma} - \sum_{\gamma=1}^{\beta_i-1} \frac{1}{\gamma} \tag{D.32}$$

Using Ramanujan summation or the Cauchy principle value of the Riemann zeta function evaluated at 1, $\zeta(1)$, the harmonic series is evaluated to the Euler-Mascheroni constant $\gamma_{em} = 0.57721\ldots$. So

$$S_i^3|_{k_i=0} = \gamma_{em} - \sum_{\gamma=1}^{\beta_i-1} \frac{1}{\gamma} \tag{D.33}$$

If β_i is large, the Hurwitz zeta function can be used to approximate the second term.

Finding $\mathcal{S}_i^2$

From Eq. (D.18)

$$\mathcal{S}_i^2 = \sum_{\gamma=\beta_i}^{\infty} \exp\left(i\frac{\omega}{c}\delta\mathfrak{r}(\phi_i)\gamma\right)$$
$$= \sum_{\gamma=\beta_i}^{\infty} e^{ik_i\gamma} \tag{D.34}$$

which is a sum of unit vectors whose angle relative to the previous vector's is k_i and beginning at an angle $\beta_i k_i$. There are two situations that may occur here: either k_i is a rational multiple of 2π, or it isn't. If it is, then $k_i = {}^{2\pi p}/_{q}$ for ${}^{p}/_{q}$ in reduced form and $\{p, q\} \in \mathbb{Z} \setminus 0$. The sum then will create a closed loop with period q and cover $2\pi p$ radians. If k_i is not a rational multiple of 2π then the cycle will never close, however the values of the partial sums are still bounded. This can be thought of as the limiting case of the first situation in that both p and q go to infinity. In either case the sum will be assigned the value of the geometric center of the shape defined by the partial sums.

To find the center, the complex plane will temporarily be though of as $\mathbb{R}^2$. First, a circle is circumscribed around the shape of the partial sums. To find the center of the circle, which is also the center of the partial sums, three points on the circle can be defined. The origin will always be on the circle, as well as the point corresponding to $e^{ik_i\beta_i}$. To find the third point, observe that the tangent of the circle at the origin will pass through the point corresponding to $e^{i[k_i\beta_i - k_i/2]}$. From symmetry then, the third point will be taken as the point corresponding to $e^{i[k_i\beta_i-(k_i+\pi)]} = -e^{ik_i(\beta_i-1)}$.

Now, given three points in the plane $\{(x_1, y_1), (x_2, y_2), (x_3, y_3)\}$, the circle

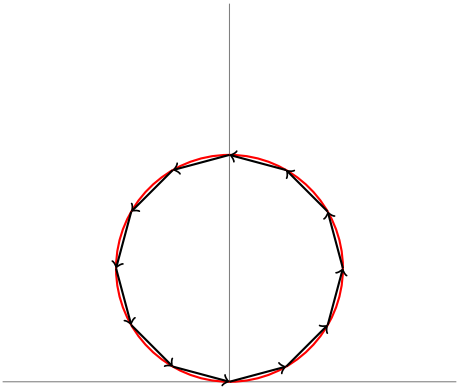

Figure D.3: A geometric series of complex exponentials and its circumscribed circle.

passing through them has center

$$x_0 = \frac{1}{2}\frac{[x_3]^2(y_2-y_1)+[x_2]^2(y_1-y_3)-(y_2-y_3)[[x_1]^2+(y_1-y_2)(y_1-y_3)]}{x_1(y_3-y_2)+x_2(y_1-y_3)+x_3(y_2-y_1)}$$

$$y_0 = \frac{1}{2}\frac{\begin{array}{c}[x_1]^2(x_3-x_2)+x_1([x_2]^2+[y_2]^2-[x_3]^2-[y_3]^2)\\ +x_3([y_1]^2-[y_2]^2)+x_2([x_3]^2+[y_3]^2-[y_1]^2)-[x_2]^2x_3\end{array}}{x_1(y_2-y_3)+x_2(y_3-y_1)+x_3(y_1-y_2)} \tag{D.35}$$

Using the points defining the circle

$$\Big\{\Big(0,0\Big),\Big(\cos(k_i\beta_i),\sin(k_i\beta_i)\Big),\Big(\cos(k_i[\beta_i-1]),\sin(k_i[\beta_i-1])\Big)\Big\}$$

the center reduces to

$$\begin{aligned} x_0 &= -\frac{1}{2}\csc(k_i)\Big[\sin(k_i[\beta_i-1])+\sin(k_i\beta_i)\Big]\\ y_0 &= \frac{1}{2}\csc(k_i)\Big[\cos(k_i[\beta_i-1])+\cos(k_i\beta_i)\Big]\end{aligned} \tag{D.36}$$

Transforming this point back in to $\mathbb{C}$ gives the center point of the shape as

$$\begin{aligned} -\frac{1}{2}\csc(k_i)\left(\Big[\sin(k_i[\beta_i-1])+\sin(k_i\beta_i)\Big]-i\Big[\cos(k_i[\beta_i-1])+\cos(k_i\beta_i)\Big]\right)\\ = \\ \frac{i}{2}\csc\left(\frac{k_i}{2}\right)e^{ik_i\left(\beta_i-\frac{1}{2}\right)}\end{aligned} \tag{D.37}$$

So

$$\mathcal{S}_i^2 = \frac{i}{2}\csc\left(\frac{k_i}{2}\right)e^{ik_i\left(\beta_i-\frac{1}{2}\right)} \tag{D.38}$$

Interestingly, a pathological case arises in the Cartesian form of $\mathcal{S}_i^2$ if $k_i = q\pi$ with q an odd integer, i.e. the spacing between lattice points is a half-wavelength. In this case the partial sums oscillate between 0 and $(-1)^{\beta_i}$, so $\mathcal{S}_i^2(k_i = q\pi) = \frac{1}{2}(-1)^{\beta_i}$, which is correctly attributed in the complex exponential form of Eq. (D.38).

The Total Field

Now that $\mathcal{S}_i^2$ and $\mathcal{S}_i^3$ have been found, Eqs. (D.38) and (D.31) can be plugged in to Eq. (D.27) to find the total field.

$$\begin{aligned}\mathbf{E}_t = &\sum_{i\in\text{Near}} \mathbf{E}(\boldsymbol{\imath}_i) \\ &+ \frac{-p\omega^2\mu_0}{4\pi} e^{-i\omega t} \\ &\quad \times \sum_{i=1}^{m} \frac{\Delta\phi_i}{2} \frac{\exp\left(i\frac{\omega}{c}[\imath_{\beta_i} - \beta_i \delta\imath(\phi_i)]\right)}{\delta\imath(\phi_i + \frac{\pi}{2})} \cdot \sin\left[\theta(\boldsymbol{T}\hat{\boldsymbol{\imath}}_i)\right] \boldsymbol{P}\hat{\boldsymbol{\theta}}_i' \\ &\quad\quad \times \left\{ \begin{array}{l} i \csc\left(\frac{k_i}{2}\right) e^{ik_i(\beta_i - \frac{1}{2})} \\ \quad + \left[\ln\left(1 - e^{ik_i}\right) + \sum_{\gamma=1}^{\beta_i - 1} \frac{e^{ik_i\gamma}}{\gamma}\right] \end{array} \right\}\end{aligned} \tag{D.39}$$

To gain insight on how the far field behaves, consider a direction where the lattice spacing approaches a quarter, half, or whole wavelength.

Quarter Wavelength If $k_i = \pi/2$

$$\begin{aligned} \csc\left(\frac{k_i}{2}\right) &= \sqrt{2} \\ e^{ik_i\left(\beta_i - \frac{1}{2}\right)} &= \frac{i^{\beta_i}(1-i)}{\sqrt{2}} \\ \ln\left(1 - e^{ik_i}\right) &= \ln\sqrt{2} - i\frac{\pi}{4} \\ \sum_{\gamma=1}^{\beta_i - 1} \frac{e^{ik_i\gamma}}{\gamma} &= \sum_{\gamma=1}^{\beta_i - 1} \frac{i^\gamma}{\gamma} \end{aligned}$$

Half Wavelength If $k_i = \pi$

$$\begin{aligned} \csc\left(\frac{k_i}{2}\right) &= 1 \\ e^{ik_i\left(\beta_i - \frac{1}{2}\right)} &= i^{2\beta_i - 1} \\ \ln\left(1 - e^{ik_i}\right) &= \ln 2 \\ \sum_{\gamma=1}^{\beta_i - 1} \frac{e^{ik_i\gamma}}{\gamma} &= \sum_{\gamma=1}^{\beta_i - 1} \frac{(-1)^\gamma}{\gamma} \end{aligned}$$

In both cases the sum over the gamma values oscillates between an envelope function, meaning that the value depends somewhat heavily on the choice of β_i.

D.1.4 Incident Plane Wave

In the previous section we assumed there was no phase change between the driving field at the lattice points. However, if a plane wave is incident on the lattice but is not normal to it, the driving field's phase will vary across the lattice. To pursue how this affects the field, consider an incident plane wave with wavelength λ_0, polar angle θ_0, and azimuthal angle ϕ_0. The phase change at a distance $\imath$ and angle ϕ is then

$$\psi(\phi, \imath) = -2\pi \frac{\imath}{\lambda_0} \sin\theta_0 \cos(\phi - \phi_0) \tag{D.40}$$

In the far region, because lattice points are reassigned, a correction must be made for the approximations used. To find this error consider adding two complex exponentials with different phase changes.

$$e^{i(a+\chi_1)} + e^{i(a+\chi_2)} = e^{ia}\left(e^{i\chi_1} + e^{i\chi_2}\right) \tag{D.41}$$

Thinking about the lattice, assume that the lattice points are symmetric about the direction ϕ_i as seen in Fig. D.4. Then the phase change of the points relative to ϕ_i is also symmetric.

$$\begin{aligned} \chi_1 &= \chi_i + \Delta\chi \\ \chi_2 &= \chi_i - \Delta\chi \end{aligned} \tag{D.42}$$

where χ_i is the distance dependent phase along ϕ_i. Plugging Eqs. (D.42) in to Eq. (D.41) gives

$$\begin{aligned} e^{i(a+\chi_1)} + e^{i(a+\chi_2)} &= e^{i(a+\chi_i)}\left(e^{i\Delta\chi} + e^{-i\Delta\chi}\right) \\ &= 2e^{i(a+\chi_i)} \cos\Delta\chi \end{aligned} \tag{D.43}$$

So an additional factor of $\cos\Delta\chi$ must be included to account for the phase change between the points. In the lattice, these phase changes accumulate as the width of region being summed over is traversed. This occurs in the $(\phi_i + \pi/2)$ direction, so

$$\begin{aligned} \Delta\chi &= \psi\left(\delta\imath\left(\phi_i + \frac{\pi}{2}\right), \left(\phi_i + \frac{\pi}{2}\right)\right) \\ &= -2\pi \frac{\delta\imath(\phi_i + \frac{\pi}{2})}{\lambda_0} \sin\theta_0 \cos(\phi_i + \frac{\pi}{2} - \phi_0) \\ &= -2\pi \frac{\delta\imath(\phi_i + \frac{\pi}{2})}{\lambda_0} \sin\theta_0 \sin(\phi_0 - \phi_i) \end{aligned} \tag{D.44}$$

At a distance $\imath$, the width of this region is $\imath\Delta\phi_i$. Thus, there are approximately

$$N_p = \frac{\imath\,\Delta\phi_i}{\delta\imath(\phi_i + \frac{\pi}{2})} \tag{D.45}$$

points across the region. Again assuming the points are symmetric about ϕ_i, then there are $(N_p/2)$ pairs of points that must be considered. Additionally, each pair is at a distance $\xi_j \delta\imath(\phi_i + \pi/2)$ from ϕ_i, with $\xi_j \leq (N_p/2) \in \mathbb{N}$. This leads to

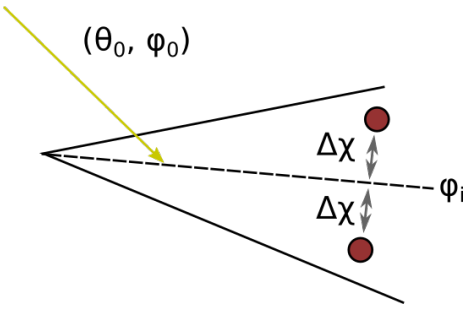

Figure D.4: Particles in the lattice are effectively reassigned along the chosen ϕ_i directions, but the phase change due to the driving field can be accounted for by considering their offset from this direction.

a total corrected phase of

$$\begin{aligned}\Delta\chi_t &= 2e^{i(a+\chi_i)}\sum_{\xi=1}^{N_p/2}\cos(\xi\Delta\chi)\\ &= 2e^{i(a+\chi_i)}\left\{\frac{\sin\left(\frac{2(N_p/2)+1}{2}\Delta\chi\right)}{2\sin\left(\frac{\Delta\chi}{2}\right)}-\frac{1}{2}\right\}\\ &= e^{i(a+\chi_i)}\left\{\frac{\sin\left(\frac{N_p+1}{2}\Delta\chi\right)}{\sin\left(\frac{\Delta\chi}{2}\right)}-1\right\}\end{aligned} \tag{D.46}$$

Because the magnitude of the sum, N_p, has already been accounted for in this method from Eq. (D.11), only the ratio between the corrected value and the magnitude is needed. This gives the needed correction as

$$\begin{aligned}\delta\chi &= \frac{\Delta\chi_t}{N_p e^{i(a+\chi_i)}}\\ &= \frac{1}{N_p}\left\{\frac{\sin\left(\frac{N_p+1}{2}\Delta\chi\right)}{\sin\left(\frac{\Delta\chi}{2}\right)}-1\right\}\end{aligned} \tag{D.47}$$

An issue arises if $\Delta\chi = 0 \mod 2\pi$ corresponding to the situation in which the particle offset corresponds to a whole wavelength. Using L'Hôpital's rule this results in

$$\delta\chi = 1 \tag{D.48}$$

as expected, though.

Using this correction to more accurately account for the phase change caused by the angle of the incident wave, $\mathcal{S}_i^3$ and $\mathcal{S}_i^2$ can now be found. The procedure is the same as that taken in Sec. D.1.3, but much messier.

Finding $\mathcal{S}_i^3$

From Eq. (D.19)

$$\mathcal{S}_i^3 = \sum_{\gamma=\beta_i}^{\infty} \frac{\exp\left(i\left[\frac{\omega}{c}\delta\mathscr{r}(\phi_i)\gamma + \psi(\phi_i,\gamma)\right]\right)}{\gamma}$$

$$\approx \sum_{\gamma=\beta_i}^{\infty} \frac{\exp\left(i\left[\frac{\omega}{c}\delta\mathscr{r}(\phi_i)\gamma - 2\pi\frac{\mathscr{r}}{\lambda_0}\sin\theta_0\cos(\phi_i-\phi_0)\right]\right)}{\gamma} \times \frac{1}{N_p}\left\{\frac{\sin\left(\frac{N_p+1}{2}\Delta\chi\right)}{\sin\left(\frac{\Delta\chi}{2}\right)} - 1\right\}$$

$$= \sum_{\gamma=\beta_i}^{\infty} \frac{\exp\left(i\left[\frac{\omega}{c}\delta\mathscr{r}(\phi_i)\gamma - 2\pi\frac{\mathscr{r}}{\lambda_0}\sin\theta_0\cos(\phi_i-\phi_0)\right]\right)}{\gamma} \frac{\delta\mathscr{r}(\phi_i+\frac{\pi}{2})}{\mathscr{r}\Delta\phi_i} \times \left\{\frac{\sin\left(\dfrac{\dfrac{\mathscr{r}\,\Delta\phi_i}{\delta\mathscr{r}(\phi_i+\frac{\pi}{2})}+1}{2}\dfrac{-2\pi\delta\mathscr{r}(\phi_i+\frac{\pi}{2})}{\lambda_0}\sin\theta_0\sin(\phi_0-\phi_i)\right)}{\sin\left(\dfrac{-2\pi\dfrac{\delta\mathscr{r}(\phi_i+\frac{\pi}{2})}{\lambda_0}\sin\theta_0\sin(\phi_0-\phi_i)}{2}\right)} - 1\right\}$$

$$= \sum_{\gamma=\beta_i}^{\infty} \frac{\exp\left(i\left[\frac{\omega}{c}\delta\mathscr{r}(\phi_i)\gamma - 2\pi\frac{\mathscr{r}}{\lambda_0}\sin\theta_0\cos(\phi_i-\phi_0)\right]\right)}{\gamma} \frac{\delta\mathscr{r}(\phi_i+\frac{\pi}{2})}{\mathscr{r}\Delta\phi_i} \times \left\{\frac{\sin\left(\left[\mathscr{r}\,\Delta\phi_i + \delta\mathscr{r}(\phi_i+\frac{\pi}{2})\right]\dfrac{-2\pi\sin\theta_0\sin(\phi_0-\phi_i)}{2\lambda_0}\right)}{\sin\left(\delta\mathscr{r}(\phi_i+\frac{\pi}{2})\dfrac{-2\pi\sin\theta_0\sin(\phi_0-\phi_i)}{2\lambda_0}\right)} - 1\right\}$$

$$= \sum_{\gamma=\beta_i}^{\infty} \frac{\exp\left(i\left[\frac{\omega}{c}\delta\mathscr{r}(\phi_i)\gamma + 2\mathscr{r}\zeta_i^1\right]\right)}{\gamma} \frac{\delta\mathscr{r}(\phi_i+\frac{\pi}{2})}{\mathscr{r}\Delta\phi_i} \times \left\{\frac{\sin\left(\left[\mathscr{r}\,\Delta\phi_i + \delta\mathscr{r}(\phi_i+\frac{\pi}{2})\right]\zeta_i^2\right)}{\sin\left(\delta\mathscr{r}(\phi_i+\frac{\pi}{2})\zeta_i^2\right)} - 1\right\} \tag{D.49}$$

where

$$\begin{aligned}\zeta_i^1 &= \frac{-2\pi \sin\theta_0}{2\lambda_0}\cos(\phi_i - \phi_0)\\ \zeta_i^2 &= \frac{-2\pi \sin\theta_0}{2\lambda_0}\sin(\phi_0 - \phi_i)\end{aligned} \tag{D.50}$$

Now, in the far region $\mathscr{r}$ can be approximated as

$$\begin{aligned}\mathscr{r}(\phi) &\sim \mathscr{r}_{\beta_i} + (\gamma - \beta_\phi)\delta\mathscr{r}(\phi), \text{ (as } \mathscr{r} \to \infty)\\ &= \big(\mathscr{r}_{\beta_i} - \beta_\phi \delta\mathscr{r}(\phi)\big) + \gamma\delta\mathscr{r}(\phi)\end{aligned} \tag{D.51}$$

And as $\beta_i \to \infty$, $(\mathscr{r}_{\beta_i} - \beta_\phi\delta\mathscr{r}(\phi)) \to 0$. Because phases are sensitive to small changes, the full $\mathscr{r}$ expression will be used, however, when appearing in the magnitude $\mathscr{r} \sim \gamma\delta\mathscr{r}(\phi)$ will be used. This gives

$$\mathcal{S}_i^3 \sim \sum_{\gamma=\beta_i}^{\infty} \frac{\exp\left(i\left[\frac{\omega}{c}\delta\mathscr{r}(\phi_i)\gamma + 2\left[\left(\mathscr{r}_{\beta_i} - \beta_i\delta\mathscr{r}(\phi_i)\right) + \gamma\delta\mathscr{r}(\phi_i)\right]\zeta_i^1\right]\right)}{\gamma}$$
$$\times \frac{\delta\mathscr{r}(\phi_i + \frac{\pi}{2})}{\gamma\delta\mathscr{r}\Delta\phi_i}$$
$$\times \left\{\frac{\sin\left(\left[\left(\mathscr{r}_{\beta_i} - \beta_i\delta\mathscr{r}(\phi_i) + \gamma\delta\mathscr{r}(\phi_i)\right)\Delta\phi_i + \delta\mathscr{r}(\phi_i + \frac{\pi}{2})\right]\zeta_i^2\right)}{\sin\left(\delta\mathscr{r}(\phi_i + \frac{\pi}{2})\zeta_i^2\right)} - 1\right\},$$
$$(\text{as } \mathscr{r} \to \infty)$$

$$= \sum_{\gamma=\beta_i}^{\infty} \exp\left(i2\zeta_i^1\left[\mathscr{r}_{\beta_i} - \beta_i\delta\mathscr{r}(\phi_i)\right]\right) \frac{\exp\left(i\gamma\delta\mathscr{r}(\phi_i)\left[\frac{\omega}{c} + 2\zeta_i^1\right]\right)}{\gamma} \frac{\delta\mathscr{r}(\phi_i + \frac{\pi}{2})}{\gamma\delta\mathscr{r}\Delta\phi_i}$$
$$\times \left\{\frac{\sin\left(\left[\mathscr{r}_{\beta_i}\Delta\phi_i - \beta_i\delta\mathscr{r}(\phi_i)\Delta\phi_i + \delta\mathscr{r}(\phi_i + \frac{\pi}{2})\right]\zeta_i^2 + \gamma\delta\mathscr{r}(\phi_i)\Delta\phi_i\,\zeta_i^2\right)}{\sin\left(\delta\mathscr{r}(\phi_i + \frac{\pi}{2})\zeta_i^2\right)} - 1\right\}$$

$$= \sum_{\gamma=\beta_i}^{\infty} e^{i2\zeta_i^1\left[\mathscr{r}_{\beta_i} - \beta_i\delta\mathscr{r}(\phi_i)\right]} \frac{e^{i\gamma\nu_i^1}}{\gamma} \frac{\delta\mathscr{r}(\phi_i + \frac{\pi}{2})}{\gamma\delta\mathscr{r}\Delta\phi_i}$$
$$\times \left\{\frac{\sin\left(\nu_i^2 + \gamma\nu_i^3\right)}{\sin\left(\delta\mathscr{r}(\phi_i + \frac{\pi}{2})\zeta_i^2\right)} - 1\right\}$$

$$= e^{i2\zeta_i^1\left[\mathscr{r}_{\beta_i} - \beta_i\delta\mathscr{r}(\phi_i)\right]} \frac{\delta\mathscr{r}(\phi_i + \frac{\pi}{2})}{\delta\mathscr{r}\Delta\phi_i}$$
$$\times \left\{\frac{1}{\sin\left(\delta\mathscr{r}(\phi_i + \frac{\pi}{2})\zeta_i^2\right)} \sum_{\gamma=\beta_i}^{\infty} \frac{e^{i\gamma\nu_i^1}}{\gamma^2} \sin\left(\nu_i^2 + \gamma\nu_i^3\right) - \sum_{\gamma=\beta_i}^{\infty} \frac{e^{i\gamma\nu_i^1}}{\gamma^2}\right\}$$

$$= e^{i2\zeta_i^1\left[\mathscr{r}_{\beta_i} - \beta_i\delta\mathscr{r}(\phi_i)\right]} \frac{\delta\mathscr{r}(\phi_i + \frac{\pi}{2})}{\delta\mathscr{r}\Delta\phi_i}$$
$$\times \left\{\begin{array}{l} \frac{1}{\sin\left(\delta\mathscr{r}(\phi_i + \frac{\pi}{2})\zeta_i^2\right)} \sum_{\gamma=\beta_i}^{\infty} \frac{1}{2i}\left[e^{i\nu_i^2} \frac{e^{i\gamma(\nu_i^1 + \nu_i^3)}}{\gamma^2} - e^{-i\nu_i^2} \frac{e^{i\gamma(\nu_i^1 - \nu_i^3)}}{\gamma^2}\right] \\ \quad - \sum_{\gamma=\beta_i}^{\infty} \frac{e^{i\gamma\nu_i^1}}{\gamma^2} \end{array}\right\}$$

$$= e^{i2\zeta_i^1\left[\mathscr{r}_{\beta_i} - \beta_i\delta\mathscr{r}(\phi_i)\right]} \frac{\delta\mathscr{r}(\phi_i + \frac{\pi}{2})}{\delta\mathscr{r}\Delta\phi_i}$$
$$\times \left\{\begin{array}{l} \frac{\csc\left(\delta\mathscr{r}(\phi_i + \frac{\pi}{2})\zeta_i^2\right)}{2i} e^{i\nu_i^2} \sum_{\gamma=\beta_i}^{\infty} \frac{e^{i\gamma(\nu_i^1 + \nu_i^3)}}{\gamma^2} \\ - \frac{\csc\left(\delta\mathscr{r}(\phi_i + \frac{\pi}{2})\zeta_i^2\right)}{2i} e^{-i\nu_i^2} \sum_{\gamma=\beta_i}^{\infty} \frac{e^{i\gamma(\nu_i^1 - \nu_i^3)}}{\gamma^2} \\ - \sum_{\gamma=\beta_i}^{\infty} \frac{e^{i\gamma\nu_i^1}}{\gamma^2} \end{array}\right\} \tag{D.52}$$

where

$$\begin{aligned}\nu_i^1 &= \delta\mathfrak{n}(\phi_i)\left[\frac{\omega}{c} + 2\zeta_i^1\right] \\ \nu_i^2 &= \left[\mathfrak{n}_{\beta_i}\Delta\phi_i - \beta_i\delta\mathfrak{n}(\phi_i)\Delta\phi_i + \delta\mathfrak{n}\left(\phi_i + \frac{\pi}{2}\right)\right]\zeta_i^2 \\ \nu_i^3 &= \delta\mathfrak{n}(\phi_i)\Delta\phi_i\,\zeta_i^2\end{aligned} \tag{D.53}$$

Each of the sums in Eq. (D.52) are now of the form

$$\sum_{\gamma=\beta_i}^{\infty}\frac{e^{i\gamma x}}{\gamma^2} = \sum_{\gamma=1}^{\infty}\frac{e^{i\gamma x}}{\gamma^2} - \sum_{\gamma=1}^{\beta_i-1}\frac{e^{i\gamma x}}{\gamma^2} \tag{D.54}$$

The first term on the right hand side (RHS) is the Taylor series of the polylogarithm function of degree 2 $\mathrm{Li}_2(e^{ix})$, also called the Dilogarithm or Spence's function. The values of $\mathrm{Li}_2(\mathrm{z})$ are seen in Fig. D.5. Compared to $\log(z)$, Li_2 is well behaved as it is convergent for all values in the complex plane.

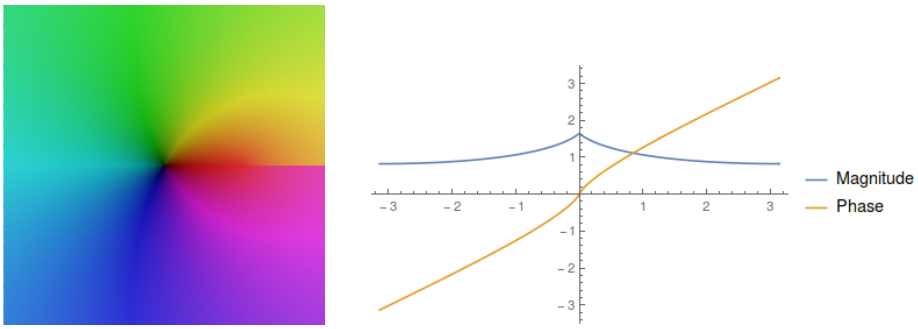

(a) (b)

Figure D.5: (a) Dilogarithm in the complex plane [31]. The color indicates phase, and the saturation magnitude. (b) The phase and magnitude of $\mathrm{Li}_2(e^{ix})$ with respect to x.

This results in

$$\begin{aligned}\mathcal{S}_i^3 \sim\; & e^{i2\zeta_i^1\left[\mathfrak{n}_{\beta_i}-\beta_i\delta\mathfrak{n}(\phi_i)\right]}\frac{\delta\mathfrak{n}(\phi_i+\frac{\pi}{2})}{\delta\mathfrak{n}\Delta\phi_i} \\ & \times\left\{\begin{array}{l} \dfrac{\csc\left(\delta\mathfrak{n}(\phi_i+\frac{\pi}{2})\zeta_i^2\right)}{2i}e^{i\nu_i^2}\left[\mathrm{Li}_2\left(e^{i\left(\nu^1+\nu^3\right)}\right) - \displaystyle\sum_{\gamma=1}^{\beta_i-1}\frac{e^{i\gamma(\nu_i^1+\nu_i^3)}}{\gamma^2}\right] \\ -\dfrac{\csc\left(\delta\mathfrak{n}(\phi_i+\frac{\pi}{2})\zeta_i^2\right)}{2i}e^{-i\nu_i^2}\left[\mathrm{Li}_2\left(e^{i\left(\nu^1-\nu^3\right)}\right) - \displaystyle\sum_{\gamma=1}^{\beta_i-1}\frac{e^{i\gamma(\nu_i^1-\nu_i^3)}}{\gamma^2}\right] \\ -\left[\mathrm{Li}_2\left(e^{i\left(\nu^1+\nu^3\right)}\right) - \displaystyle\sum_{\gamma=1}^{\beta_i-1}\frac{e^{i\gamma\nu_i^1}}{\gamma^2}\right]\end{array}\right\}\end{aligned} \tag{D.55}$$

Limiting Cases If θ_0, the polar angle of the incident wave, is 0 then ζ^1 and $\zeta^2 = 0$ causing ν^2, $\nu^3 = 0$, and $\nu^1 = k_i$. This creates a divergence due to the

csc() terms for all regions. However, taking the limit as $\theta_0 \to 0$ reveals that the terms with csc() cancel out.

$$\begin{aligned}\mathcal{S}_i^3 \to & \frac{\delta\mathscr{r}(\phi_i+\frac{\pi}{2})}{\delta\mathscr{r}\Delta\phi_i} \\ & \times \left\{ \begin{array}{l} \dfrac{\csc\left(\delta\mathscr{r}(\phi_i+\frac{\pi}{2})\zeta_i^2\right)}{2i}\left[\mathrm{Li}_2\left(e^{ik_i}\right)-\displaystyle\sum_{\gamma=1}^{\beta_i-1}\frac{e^{i\gamma k_i}}{\gamma^2}\right] \\ -\dfrac{\csc\left(\delta\mathscr{r}(\phi_i+\frac{\pi}{2})\zeta_i^2\right)}{2i}\left[\mathrm{Li}_2\left(e^{ik_i}\right)-\displaystyle\sum_{\gamma=1}^{\beta_i-1}\frac{e^{i\gamma k_i}}{\gamma^2}\right] \\ -\left[\mathrm{Li}_2\left(e^{ik_i}\right)-\displaystyle\sum_{\gamma=1}^{\beta_i-1}\frac{e^{i\gamma k_i}}{\gamma^2}\right] \end{array} \right\} \\ = & -\frac{\delta\mathscr{r}(\phi_i+\frac{\pi}{2})}{\delta\mathscr{r}\Delta\phi_i}\left[\mathrm{Li}_2\left(e^{ik_i}\right)-\sum_{\gamma=1}^{\beta_i-1}\frac{e^{i\gamma k_i}}{\gamma^2}\right] \end{aligned} \tag{D.56}$$

In contrast to the $\mathcal{S}_3$ term derived when no phase change was taken into account, Eq. (D.31), this appears to be a great improvement as the term is now convergent when $k_i = 0 \mod 2\pi$.

The $\csc() = 1/\sin()$ terms will also diverge if $\phi_i = \phi_0$, meaning the direction of interest and the azimuth of the incident light are the same. In this case ζ_i^2, ν_i^2 and $\nu_i^3 = 0$. This results in almost the same result as Eq. (D.56) with ν^1 remaining unchanged. Taking the limit as $\phi_i \to \phi_0$ gives

$$\mathcal{S}_i^3 \to -e^{i2\zeta_i^1\left[\mathscr{r}_{\beta_i}-\beta_i\delta\mathscr{r}(\phi_i)\right]}\frac{\delta\mathscr{r}(\phi_i+\frac{\pi}{2})}{\delta\mathscr{r}\Delta\phi_i}\left[\mathrm{Li}_2\left(e^{i\nu_i^1}\right)-\sum_{\gamma=1}^{\beta_i-1}\frac{e^{i\gamma\nu_i^1}}{\gamma^2}\right] \tag{D.57}$$

Finding $\mathcal{S}_i^2$

Because $\mathcal{S}_i^3$ and $\mathcal{S}_i^2$ only differ by a factor of γ^{-1}, most of the hard work has already been done when solving from $\mathcal{S}_i^3$, and a usable form of $\mathcal{S}_i^2$ can be arrived at in the same manner. From Eq. (D.18), using Eqs. (D.50), (D.51), and (D.53), and including the phase correction term gives

$$\mathcal{S}_i^2 \sim \sum_{\gamma=\beta_i}^{\infty} \exp\left(i\left[\frac{\omega}{c}\delta\mathfrak{r}(\phi_i)\gamma + 2\left[\left(\mathfrak{r}_{\beta_i} - \beta_i\delta\mathfrak{r}(\phi_i)\right) + \gamma\delta\mathfrak{r}(\phi_i)\right]\zeta_i^1\right]\right) \times \frac{\delta\mathfrak{r}(\phi_i+\frac{\pi}{2})}{\gamma\delta\mathfrak{r}\Delta\phi_i} \times \left\{\frac{\sin\left(\left[\left(\mathfrak{r}_{\beta_i} - \beta_i\delta\mathfrak{r}(\phi_i) + \gamma\delta\mathfrak{r}(\phi_i)\right)\Delta\phi_i + \delta\mathfrak{r}(\phi_i+\frac{\pi}{2})\right]\zeta_i^2\right)}{\sin\left(\delta\mathfrak{r}(\phi_i+\frac{\pi}{2})\zeta_i^2\right)} - 1\right\}, \quad (\text{as } \mathfrak{r}\to\infty)$$

$$= e^{i2\zeta_i^1\left[\mathfrak{r}_{\beta_i} - \beta_i\delta\mathfrak{r}(\phi_i)\right]}\frac{\delta\mathfrak{r}(\phi_i+\frac{\pi}{2})}{\delta\mathfrak{r}\Delta\phi_i} \times \left\{\frac{1}{\sin\left(\delta\mathfrak{r}(\phi_i+\frac{\pi}{2})\zeta_i^2\right)}\sum_{\gamma=\beta_i}^{\infty}\frac{e^{i\gamma\nu_i^1}}{\gamma}\sin\left(\nu_i^2+\gamma\nu_i^3\right) - \sum_{\gamma=\beta_i}^{\infty}\frac{e^{i\gamma\nu_i^1}}{\gamma}\right\}$$

$$= e^{i2\zeta_i^1\left[\mathfrak{r}_{\beta_i} - \beta_i\delta\mathfrak{r}(\phi_i)\right]}\frac{\delta\mathfrak{r}(\phi_i+\frac{\pi}{2})}{\delta\mathfrak{r}\Delta\phi_i} \times \left\{\begin{array}{l} \frac{\csc\left(\delta\mathfrak{r}(\phi_i+\frac{\pi}{2})\zeta_i^2\right)}{2i}e^{i\nu_i^2}\sum_{\gamma=\beta_i}^{\infty}\frac{e^{i\gamma(\nu_i^1+\nu_i^3)}}{\gamma} \\ -\frac{\csc\left(\delta\mathfrak{r}(\phi_i+\frac{\pi}{2})\zeta_i^2\right)}{2i}e^{-i\nu_i^2}\sum_{\gamma=\beta_i}^{\infty}\frac{e^{i\gamma(\nu_i^1-\nu_i^3)}}{\gamma} \\ -\sum_{\gamma=\beta_i}^{\infty}\frac{e^{i\gamma\nu_i^1}}{\gamma}\end{array}\right\} \quad (D.58)$$

Just as in Sec. D.1.3, these sums are the power series of logarithms, as in Eq. (D.30), resulting in

$$\mathcal{S}_i^2 = -e^{i2\zeta_i^1\left[\mathfrak{r}_{\beta_i} - \beta_i\delta\mathfrak{r}(\phi_i)\right]}\frac{\delta\mathfrak{r}(\phi_i+\frac{\pi}{2})}{\delta\mathfrak{r}\Delta\phi_i} \times \left\{\begin{array}{l} \frac{\csc\left(\delta\mathfrak{r}(\phi_i+\frac{\pi}{2})\zeta_i^2\right)}{2i}e^{i\nu_i^2}\left[\ln\left(1-e^{i(\nu^1+\nu^3)}\right) + \sum_{\gamma=1}^{\beta_i-1}\frac{e^{i\gamma(\nu_i^1+\nu_i^3)}}{\gamma}\right] \\ -\frac{\csc\left(\delta\mathfrak{r}(\phi_i+\frac{\pi}{2})\zeta_i^2\right)}{2i}e^{-i\nu_i^2}\left[\ln\left(1-e^{i(\nu^1-\nu^3)}\right) + \sum_{\gamma=1}^{\beta_i-1}\frac{e^{i\gamma(\nu_i^1-\nu_i^3)}}{\gamma}\right] \\ -\left[\ln\left(1-e^{i\nu^1}\right) + \sum_{\gamma=1}^{\beta_i-1}\frac{e^{i\gamma\nu_i^1}}{\gamma}\right]\end{array}\right\} \quad (D.59)$$

Limiting Cases Again, the csc() terms diverge if $\theta_0 = 0$, as occurred for $\mathcal{S}^3$. Taking the limit $\theta_0 \to 0$ reveals

$$\mathcal{S}_i^2 \to -\frac{\delta\mathscr{r}(\phi_i + \frac{\pi}{2})}{\delta\mathscr{r}\Delta\phi_i} \times \left\{ \begin{array}{l} \frac{\csc\left(\delta\mathscr{r}(\phi_i + \frac{\pi}{2})\zeta_i^2\right)}{2i}\left[\ln\left(1 - e^{ik_i}\right) + \sum_{\gamma=1}^{\beta_i - 1} \frac{e^{i\gamma k_i}}{\gamma}\right] \\ -\frac{\csc\left(\delta\mathscr{r}(\phi_i + \frac{\pi}{2})\zeta_i^2\right)}{2i}\left[\ln\left(1 - e^{ik_i}\right) + \sum_{\gamma=1}^{\beta_i - 1} \frac{e^{i\gamma k_i}}{\gamma}\right] \\ -\left[\ln\left(1 - e^{ik_i}\right) + \sum_{\gamma=1}^{\beta_i - 1} \frac{e^{i\gamma k_i}}{\gamma}\right] \end{array} \right\}$$

$$= \frac{\delta\mathscr{r}(\phi_i + \frac{\pi}{2})}{\delta\mathscr{r}\Delta\phi_i}\left[\ln\left(1 - e^{ik_i}\right) + \sum_{\gamma=1}^{\beta_i - 1} \frac{e^{i\gamma k_i}}{\gamma}\right] \tag{D.60}$$

This limit still diverges if $k_i = 0 \mod 2\pi$. In this case though the Euler-Mascheroni constant, γ_{em}, can be used as was explained in Sec. D.1.3.

Taking the limit $\phi_i \to \phi_0$ gives

$$\mathcal{S}_i^2 \to e^{i2\zeta_i^1[\mathscr{r}_{\beta_i} - \beta_i\delta\mathscr{r}(\phi_i)]}\frac{\delta\mathscr{r}(\phi_i + \frac{\pi}{2})}{\delta\mathscr{r}\Delta\phi_i}\left[\ln\left(1 - e^{i\nu_i^1}\right) + \sum_{\gamma=1}^{\beta_i - 1} \frac{e^{i\gamma\nu_i^1}}{\gamma}\right] \tag{D.61}$$

which has the same behavior as the case when $\theta_0 \to 0$ with an additional phase factor.

Note that in both limiting cases of $\mathcal{S}^2$ and $\mathcal{S}^3$ that if the limit is taken using the power series expansion of the dilogarithmic and logarithmic terms, then by using L'Hôpital's rule, the no phase change results are recovered exactly.

The Total Field

Plugging Eqs. (D.55) and (D.59) in to Eq. (D.27) gives

$$
\begin{aligned}
\mathbf{E}_t = & \sum_{i\in\text{Near}} \mathbf{E}(\boldsymbol{\imath}_i) \\
& + \frac{-p\omega^2\mu_0}{4\pi} e^{-i\omega t} \\
& \times \sum_{i=1}^{m} \Delta\phi_i \frac{\exp\left(i\frac{\omega}{c}\left[\imath_{\beta_i} - \beta_i \delta\imath(\phi_i)\right]\right)}{\delta\imath(\phi_i + \frac{\pi}{2})} \exp\left(i2\zeta^1\left[\imath_{\beta_i} - \beta_i\delta\imath\right]\right) \\
& \times \frac{\delta\imath(\phi_i + \frac{\pi}{2})}{\delta\imath(\phi_i)\Delta\phi_i} \sin\left[\theta(\boldsymbol{T}\hat{\boldsymbol{\imath}}_i)\right] \boldsymbol{P}\hat{\boldsymbol{\theta}}'_i \\
& \times \left\{ \left\{ \begin{aligned}
& \frac{-\csc\left(\delta\imath(\phi_i + \frac{\pi}{2})\zeta_i^2\right)}{2i} e^{i\nu_i^2} \\
& \qquad \times \left[\ln\left(1 - e^{i(\nu^1+\nu^3)}\right) + \sum_{\gamma=1}^{\beta_i - 1} \frac{e^{i\gamma(\nu_i^1+\nu_i^3)}}{\gamma} \right] \\
& + \frac{\csc\left(\delta\imath(\phi_i + \frac{\pi}{2})\zeta_i^2\right)}{2i} e^{-i\nu_i^2} \\
& \qquad \times \left[\ln\left(1 - e^{i(\nu^1-\nu^3)}\right) + \sum_{\gamma=1}^{\beta_i - 1} \frac{e^{i\gamma(\nu_i^1-\nu_i^3)}}{\gamma} \right] \\
& + \left[\ln\left(1 - e^{i\nu^1}\right) + \sum_{\gamma=1}^{\beta_i - 1} \frac{e^{i\gamma\nu_i^1}}{\gamma} \right]
\end{aligned} \right\} \right. \\
& \left. + \frac{1}{2} \left\{ \begin{aligned}
& \frac{\csc\left(\delta\imath(\phi_i + \frac{\pi}{2})\zeta_i^2\right)}{2i} e^{i\nu_i^2} \\
& \qquad \times \left[\mathrm{Li}_2\left(e^{i(\nu^1+\nu^3)}\right) - \sum_{\gamma=1}^{\beta_i - 1} \frac{e^{i\gamma(\nu_i^1+\nu_i^3)}}{\gamma^2} \right] \\
& - \frac{\csc\left(\delta\imath(\phi_i + \frac{\pi}{2})\zeta_i^2\right)}{2i} e^{-i\nu_i^2} \\
& \qquad \times \left[\mathrm{Li}_2\left(e^{i(\nu^1-\nu^3)}\right) - \sum_{\gamma=1}^{\beta_i - 1} \frac{e^{i\gamma(\nu_i^1-\nu_i^3)}}{\gamma^2} \right] \\
& - \left[\mathrm{Li}_2\left(e^{i(\nu^1+\nu^3)}\right) - \sum_{\gamma=1}^{\beta_i - 1} \frac{e^{i\gamma\nu_i^1}}{\gamma^2} \right]
\end{aligned} \right\} \right\}
\end{aligned}
$$

$$
\begin{aligned}
\mathbf{E}_t = & \sum_{i\in\text{Near}} \mathbf{E}(\boldsymbol{\imath}_i) \\
& + \frac{-p\omega^2\mu_0}{4\pi} e^{-i\omega t} \\
& \sum_{i=1}^{m} \frac{\exp\left(i\left[\frac{\omega}{c}+2\zeta_i^1\right]\left[\imath_{\beta_i}-\beta_i\delta\imath(\phi_i)\right]\right)}{\delta\imath(\phi_i)} \cdot \sin\left[\theta(\boldsymbol{T}\hat{\boldsymbol{\imath}}_i)\right] \boldsymbol{P}\hat{\boldsymbol{\theta}}_i' \\
& \times \left\{ \left\{ \begin{array}{l}
\left(\begin{array}{l}
\dfrac{-\csc\left(\delta\imath(\phi_i+\frac{\pi}{2})\zeta_i^2\right)}{2i} e^{i\nu_i^2} \\
\qquad \times \left[\ln\left(1-e^{i(\nu^1+\nu^3)}\right) + \displaystyle\sum_{\gamma=1}^{\beta_i-1} \frac{e^{i\gamma(\nu_i^1+\nu_i^3)}}{\gamma} \right] \\
+ \dfrac{\csc\left(\delta\imath(\phi_i+\frac{\pi}{2})\zeta_i^2\right)}{2i} e^{-i\nu_i^2} \\
\qquad \times \left[\ln\left(1-e^{i(\nu^1-\nu^3)}\right) + \displaystyle\sum_{\gamma=1}^{\beta_i-1} \frac{e^{i\gamma(\nu_i^1-\nu_i^3)}}{\gamma} \right] \\
+ \left[\ln\left(1-e^{i\nu^1}\right) + \displaystyle\sum_{\gamma=1}^{\beta_i-1} \frac{e^{i\gamma\nu_i^1}}{\gamma} \right]
\end{array} \right) \\
+ \frac{1}{2} \left(\begin{array}{l}
\dfrac{\csc\left(\delta\imath(\phi_i+\frac{\pi}{2})\zeta_i^2\right)}{2i} e^{i\nu_i^2} \\
\qquad \times \left[\mathrm{Li}_2\left(e^{i(\nu^1+\nu^3)}\right) - \displaystyle\sum_{\gamma=1}^{\beta_i-1} \frac{e^{i\gamma(\nu_i^1+\nu_i^3)}}{\gamma^2} \right] \\
- \dfrac{\csc\left(\delta\imath(\phi_i+\frac{\pi}{2})\zeta_i^2\right)}{2i} e^{-i\nu_i^2} \\
\qquad \times \left[\mathrm{Li}_2\left(e^{i(\nu^1-\nu^3)}\right) - \displaystyle\sum_{\gamma=1}^{\beta_i-1} \frac{e^{i\gamma(\nu_i^1-\nu_i^3)}}{\gamma^2} \right] \\
- \left[\mathrm{Li}_2\left(e^{i(\nu^1+\nu^3)}\right) - \displaystyle\sum_{\gamma=1}^{\beta_i-1} \frac{e^{i\gamma\nu_i^1}}{\gamma^2} \right]
\end{array} \right)
\end{array} \right\} \qquad \text{(D.62)}
\end{aligned}
$$

At this point it pays to reflect on what these results mean. The main thing to notice is that in both cases, whether a phase change is considered or not, there are situations for the far region that diverge. The easiest case of this to recognize is if the incident wave is normal to the lattice and the spacing of the lattice points is equal to an integer multiple of the incident wavelength. However, in this same situation it is likely that the near-region lattice points will be out of phase with each other. This is caused by the non-linear change in distance between lattice points near the observation point. Hence, it appears that the far-region can have a significant impact on the total field.

D.2 Reflections and Scattering of a Multilayered Lattice

In Section D.1 the radiation from a 2D lattice was considered. The radiation in that case did not interact with anything in the environment after being emitted. However, the actual back reflector will consist of plasmonic particles embedded in a layer of homogeneous material with a mirror on the bottom and the absorbing layers on top, as seen in Fig. D.6. Thus, reflections from the interfaces must be considered when determining the field within the back reflector's layers.

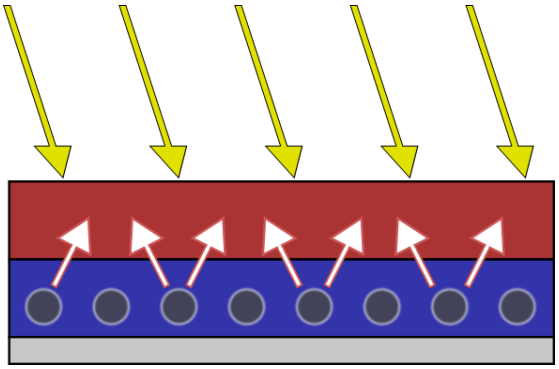

Figure D.6: Schematic of the back reflector embedded in the solar cell. The red layer represents all top layer of the cell including front-side coatings and the absorber layer. The blue layer represents the back reflector, and the silver layer is the mirror.

Each incident path that reaches the point of interest, either interacts with no particles or with at least one particle. A path that is able to reach the observation point without interacting with any particles will be called a *free light path*. Fig. D.7 illustrates one situation such that no free light paths exist due to the orientation of the incident light, the point of observation, and the particle lattice, and another situation where a free light path does exist. Assuming the

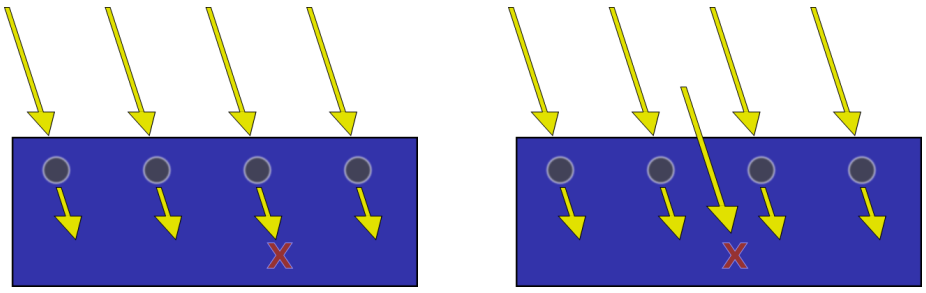

(a) (b)

Figure D.7: (a) There are no *free light paths* if the incident light, observation point, and particle lattice are arranged such that all light paths must pass through a particle position to reach the observation point. (b) A free light path exists.

lattice is made of point particles the condition that there are no free light paths

is

$$c\mathbf{I} = \boldsymbol{\imath} - \mathbf{p}_i \tag{D.63}$$

for some lattice point $\mathbf{p}_i$, where c is a scalar, $\mathbf{I}$ is the incident light vector, and $\boldsymbol{\imath}$ is the observation point. Because only the angle of the incident light is important, indicated by the arbitrary scaling factor c, this condition can be re-written as

$$\tan(\theta_I) = \frac{\left(\left[\imath^1 - \left(\alpha_i^1 a_1^1 + \alpha_i^2 a_2^1\right)\right]^2 + \left[\imath^2 - \left(\alpha_i^1 a_1^2 + \alpha_i^2 a_2^2\right)\right]^2\right)^{1/2}}{\imath^3 - z_1} \tag{D.64}$$

$$\tan(\phi_I) = \frac{\left[\imath^2 - \left(\alpha_i^1 a_1^2 + \alpha_i^2 a_2^2\right)\right]}{\left[\imath^1 - \left(\alpha_i^1 a_1^1 + \alpha_i^2 a_2^1\right)\right]} \tag{D.65}$$

So when considering the field at a point that satisfies these conditions no free light path term must be considered. If the field point does not satisfy this though, a free light path contribution must be added to the total field. This contribution can be calculated using the classical method resulting in a geometric sequence, discussed in Sec. D.2.3.

If a light path does interact with a particle the geometric series approach will not work. Instead, the path of the each light ray can be "unfolded", as seen in Fig. D.8a. When performing this unfolding, the original layer is inverted with respect to the normal of the interface, causing a mirroring effect. This creates two 1D sub-lattices, one with an even number of reflections in its path, and the other with an odd number of reflections. This situation is seen in Fig. D.8b. Because these 1D sub-lattices occur for each particle, a 3D virtual lattice can be created.

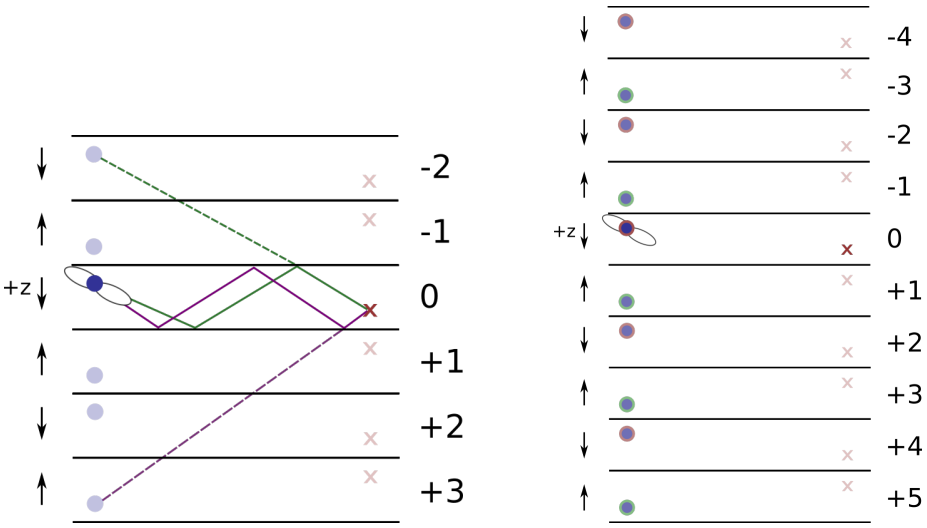

(a) (b)

Figure D.8: (a) Example of unfolding the layer. The green and purple rays are scattered from the particle and subsequently reach the point of observation. The arrows on the left indicate the positive z-direction, which is inverted in every reflection. The numbers on the right indicate the virtual layer number, the absolute value of which indicates the number of reflections which have occurred. (b) The two 1D sub-lattices created from the unfolding process. The even lattice points are highlight in red, while the odd points are in green.

D.2.1 Virtual Lattice

Consider a set of point sources within a layer where each point scatters incident light the same way, given by the *scattering function*, S. Through the unfolding process, a 3D *virtual lattice* is created, with each real lattice point having an infinite string of virtual lattice points above and below it, as seen in Fig. D.9.

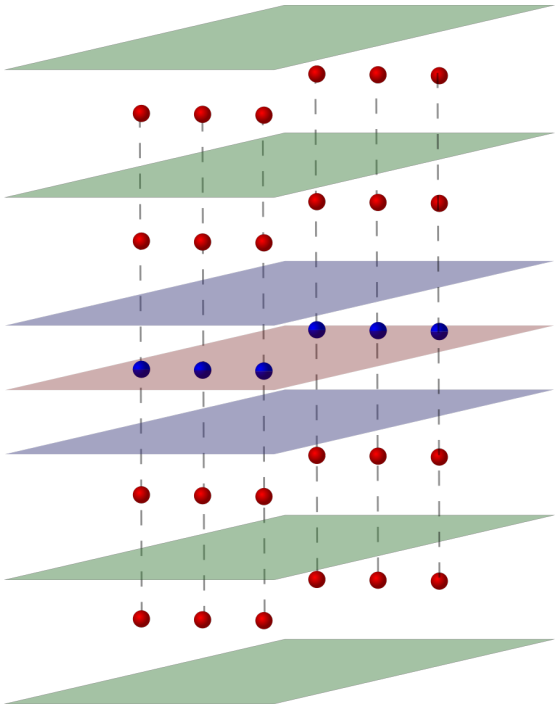

Figure D.9: The virtual lattice created by unfolding the reflections from the real lattice. The original lattice points are indicated by the blue points lying in the red plane with blue layer boundaries. The virtual lattice is indicated by the green layer boundaries and red particles.

If the height of the layer is h, then the vertical spacing between the points in each sub-lattice is $2h$. Thus, the two virtual lattices created are defined by the original lattice vectors $\mathbf{a}'_1 = \mathbf{a}_1$ and $\mathbf{a}'_2 = \mathbf{a}_2$, and the third vector

$$\mathbf{a}'_3 = 2h\frac{\mathbf{a}_1 \times \mathbf{a}_2}{|\mathbf{a}_1 \times \mathbf{a}_2|} \tag{D.66}$$

The only difference between the even and odd lattices is the observation point relative to them, depicted in Fig. D.10. The observation point of the even sub-lattice being $\boldsymbol{r}_0$, and the observation point of the odd sub-lattice being

$$\boldsymbol{r}'_0 = \boldsymbol{r}_0 + r_0^3\frac{\mathbf{a}_1 \times \mathbf{a}_2}{|\mathbf{a}_1 \times \mathbf{a}_2|} \tag{D.67}$$

Assuming the $\mathbf{a}_1$ and $\mathbf{a}_2$ vectors lie in the x-y plane, this means

$$\begin{aligned}\boldsymbol{r}'_0 &= \boldsymbol{r}_0 + \left(0,\, 0,\, r_0^3\right) \\ &= \left(r_0^1, r_0^2, 2r_0^3\right)\end{aligned} \tag{D.68}$$

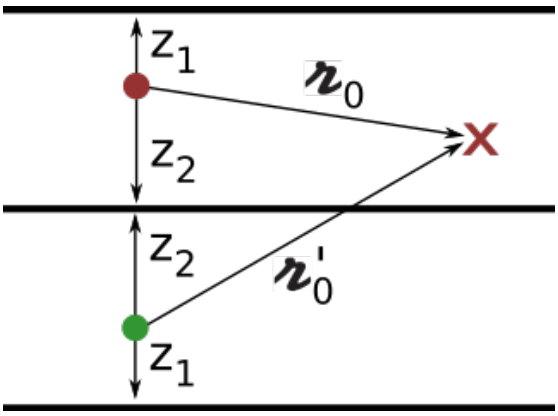

Figure D.10: The observation point relative to the even lattice, with origin indicated by the red circle, and odd lattice, with origin in green.

Caution must be taken when thinking about the coordinate system of the odd lattice though. Because it was created through an inversion process the handedness of the coordinate system is opposite to the original (i.e. If the original coordinate system was right-handed, the coordinate system of the odd lattice is left-handed.). Luckily none of the relevant parameters depend on the handedness of the coordinate system, but it is something to keep in mind.

D.2.2 Infinite 3D Lattice

In section D.1.1 the general method for summing the field of a 2D lattice was considered. However, nothing in the discussion there was inherently 2 dimensional. Thus, using the same line of reasoning the 3D analog of this method can be established.

1. Move problem to conjugate lattice with vectors $\boldsymbol{\imath}_i = \mathbf{r}_0 - \mathbf{r}_i$, where $\mathbf{r}_0$ is the point of interest and $\mathbf{r}_i$ is the i^{th} lattice point.
2. Define a distance that separates the near and far regions, $\imath_\beta$.
3. Define angular divisions of a sphere, $\Delta\theta_i$ and $\Delta\phi_j$, centered at the origin. Project these divisions onto the far region of the lattice.
4. Sum over the volumes, called pyramidal frustums, within each division whose height is equal to the separation of lattice points in that direction.

There are only two difference in these steps between the 3D and 2D cases. First is that the sum is now taking place in both the θ and ϕ directions where as in the 2D case the sum only occurred in the ϕ direction. And second is that the shapes created by the lattice division is a right pyramidal frustum, seen in Fig. D.11 rather than a trapezoid.

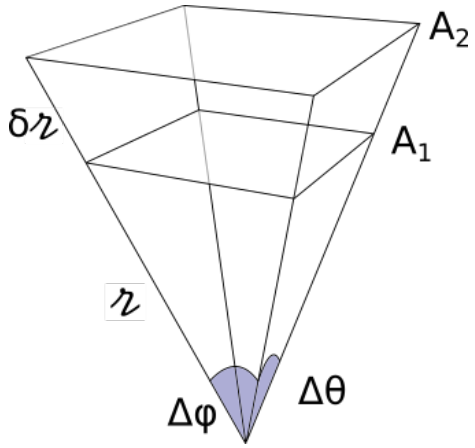

Figure D.11: A right pyramidal frustum with base areas A_1 and A_2.

In analogy to using the area of the trapezoid to define the magnitude of each mocked lattice point, the volume of a right pyramidal frustum with height $h$and base areas A_1 and A_2 is

$$V = \frac{h}{3}\left(A_1 + A_2 + \sqrt{A_1 A_2}\right) \tag{D.69}$$

with

$$\begin{aligned} A_1 &= [\imath\Delta\theta]\,[\imath\Delta\phi] \\ &= \imath^2\Delta\phi\Delta\theta \qquad \text{(D.70a)} \\ A_2 &= [(\imath+\delta\imath)\Delta\theta]\,[(\imath+\delta\imath)\Delta\phi] \\ &= (\imath+\delta\imath)^2\Delta\phi\Delta\theta \qquad \text{(D.70b)} \end{aligned}$$

So the volume of a frustum at the γ^{th} lattice point in the (θ, ϕ) direction is

$$\begin{aligned} V &= \frac{\delta r}{3}\left[(r^2\Delta\theta\Delta\phi + r + \delta r)^2\Delta\theta\Delta\phi + \left[r^2\Delta\theta\Delta\phi\cdot(r+\delta r)^2\Delta\theta\Delta\phi\right]^{1/2}\right] \\ &= \delta r\Delta\theta\Delta\phi\left(r^2 + r\delta r + \frac{\delta r^2}{3}\right) \end{aligned} \tag{D.71}$$

It pays to pause here and think about how the far region boundary is chosen. In the 2D case the observation point could move perpendicular to the lattice infinitely far away, as in Fig. D.12. This made the choice of β significant, such that the lateral distance r_β, and the actual distance r, to the far region were similar. This became the case when the distance from the observation point to the lattice became negligible compared to the lateral distance of the far field. In this case, though, the lattice is 3D so the observation point is periodically bound in all directions. There is no perpendicular direction to move into. Thus, β should be chosen such that the size of the unit cell of the lattice is small compared to the r_β.

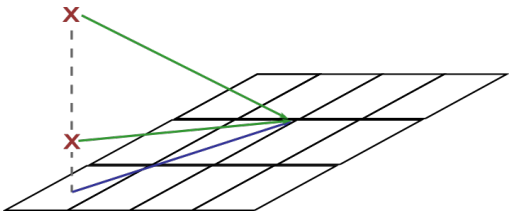

Figure D.12: The distance the observation point is from the lattice plays a significant role in the 2D case, however in the 3D case this freedom is removed.

So, just as in the 2D case

$$\begin{aligned} r &\to r_\beta + \gamma\delta r \\ &\to (\beta+\gamma)\delta r \,(\text{as } r \to \infty) \end{aligned} \tag{D.72}$$

giving

$$\begin{aligned} V &= \delta r\Delta\theta\Delta\phi\left((\beta+\gamma)^2\delta r^2 + (\beta+\gamma)\delta r\cdot\delta r + \frac{\delta r^2}{3}\right) \\ &= \Delta\theta\Delta\phi\delta r^3\left(\gamma^2 + (2\beta+1)\gamma + (\beta^2+\beta+\frac{1}{3})\right) \end{aligned}$$

Continuing with the process developed for the 2D lattice, the volume of a single point in the (θ, ϕ) direction is

$$v = \delta r(\theta,\phi)\,\delta r(\theta+\pi/2,\phi)\,\delta r(\theta,\phi+\pi/2) \tag{D.73}$$

giving a point density of $\rho = v^{-1}$. So the magnitude of the γ^{th} volume in the (θ, ϕ) direction is

$$\begin{aligned} M(\gamma,\theta,\phi) &= V\rho \\ &= \frac{\delta r^2(\theta,\phi)\Delta\theta\Delta\phi}{\delta r(\theta+\pi/2,\phi)\delta r(\theta,\phi+\pi/2)} \\ &\quad\times\left(\gamma^2 + (2\beta+1)\gamma + (\beta^2+\beta+\frac{1}{3})\right) \end{aligned} \tag{D.74}$$

Now, to find the sum over in the (θ, ϕ) direction,

$$\begin{aligned} F(\theta,\phi) &= \sum_{\gamma=0}^{\infty} M(\gamma,\theta,\phi)\mathbf{f}(\boldsymbol{r}) \\ &= \sum_{\gamma=0}^{\infty} \frac{\delta r^2(\theta,\phi)\cdot\Delta\theta\Delta\phi}{\delta r(\theta+\pi/2,\phi)\delta r(\theta,\phi+\pi/2)} \\ &\quad \times \left(\gamma^2+(2\beta+1)\gamma+(\beta^2+\beta+\frac{1}{3})\right)\mathbf{f}(\boldsymbol{r}) \\ &= \frac{\delta r^2(\theta,\phi)\cdot\Delta\theta\Delta\phi}{\delta r(\theta+\pi/2,\phi)\delta r(\theta,\phi+\pi/2)}\hat{\mathbf{f}}(\theta_i,\phi_j) \\ &\quad \times \sum_{\gamma=0}^{\infty}\left(\gamma^2+(2\beta+1)\gamma+(\beta^2+\beta+\frac{1}{3})\right) f(\boldsymbol{r}) \end{aligned} \tag{D.75}$$

giving the sum of the entire lattice as

$$\begin{aligned} F &= \sum_{i\in\text{Near}} \mathbf{F}_i + \sum_{\theta_i}\sum_{\phi_j} F(\theta,\phi) \\ &= \sum_{i\in\text{Near}} \mathbf{F}_i + \sum_{\theta_i}\sum_{\phi_j} \frac{\delta r^2(\theta_i,\phi_j)\cdot\Delta\theta_i\Delta\phi_j}{\delta r(\theta_i+\pi/2,\phi_j)\delta r(\theta_i,\phi_j+\pi/2)}\hat{\mathbf{f}}(\theta_i,\phi_j) \\ &\qquad \times \sum_{\gamma=0}^{\infty}\left(\gamma^2+(2\beta_{i,j}+1)\gamma+(\beta_{i,j}^2+\beta_{i,j}+\frac{1}{3})\right) f(\boldsymbol{r}) \end{aligned} \tag{D.76}$$

D.2.3 Field From Reflections

Free Light Paths

To determine whether a free light path exists the angles of the near and far regions are considered. If there are no near region particles or far region directions with the same angles as the incident light, then a free light path is considered to exist. This is a simplification that ignores both the geometric and scattering cross section of the particles. To include these effects, a radius around each lattice point could be considered to shade the observation point.

Consider an incident plane wave with normal vector at angle (θ_0, ϕ_0) with wavelength λ_0 and traveling through a medium with index of refraction n_0, as in Fig. D.13. Two possible 1D sub-lattices are created, $\mathfrak{L}'$, having an even number of reflections, and $\mathfrak{L}''$ having an odd number of reflections, before reaching the observation point.

From Eq. (D.40), the phase change of the incident light with distance is

$$\delta\psi(d, \phi) = -2\pi \frac{d}{\lambda_0} \sin\theta_0 \cos(\phi - \phi_0) \tag{D.77}$$

The distance between origin points of incident light in both lattices is

$$\Delta d = 2h \tan\theta \tag{D.78}$$

where $h = z_1 + z_2$. This gives a lattice change between consecutive lattice points of

$$\Delta\psi = \delta\psi(\Delta d, \phi_0) = -2\pi \frac{2h \tan\theta}{\lambda_0} \sin\theta_0 \tag{D.79}$$

As the light propagates through the layer a distance ℓ, it transforms as

$$\mathcal{R}(\ell, m_1, m_2) = e^{-\eta\ell} \cdot e^{ik\ell} \cdot r_1^{m_1} r_2^{m_2} \tag{D.80}$$

where the first term is the absorption of energy from the Beer-Lambert Law with absorption constant η, the second term is the phase change of the light due to its optical path with k the wavenumber, and the third term is the absorption due to reflection, described by Fresnel's equation, with m_1 and m_2 the number of reflections off the top and bottom interfaces, respectively.

Because of the regular spacing of origin points, the distance traveled and number of reflections is simple to calculate. For each complete cycle of the of the light traveling through the layer it travels a total distance of

$$\Delta\ell = 2\frac{h}{\cos\theta} \tag{D.81}$$

Now, consider a ray, in either lattice, traveling from the j^{th} origin point to the zeroth origin point, which has the direct path to the observation point. This path will have originated a distance $d_j = j\Delta d$ away from the zeroth origin point, traveled $\ell_j = j\Delta\ell$ and undergone $n_1 = n_2 = j$ reflections off each interface. Using Eq. (D.80), this results in the field

$$\begin{aligned} E'_j &= E'_0 \cdot e^{ij\Delta\psi} \cdot e^{-j\eta\Delta\ell} \cdot e^{ijk\Delta\ell} \cdot r_1^j r_2^j \\ &= E'_0 C^j \end{aligned} \tag{D.82}$$

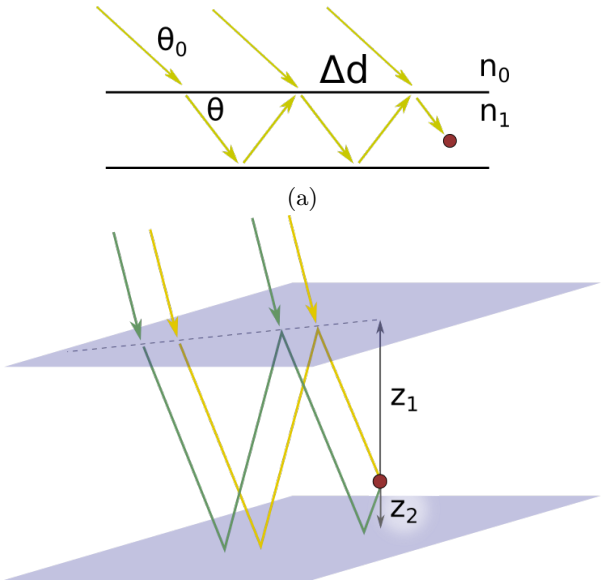

(a)

(b)

Figure D.13: The paths leading to a free light path in (a) 2D, viewed from the side, and (b) 3D perspectives. The yellow paths, with origin points constituting $\mathfrak{L}'$, will always have an even number of reflections before reaching the observation point, while the green path will always have an odd number of reflections, with origin points making up $\mathfrak{L}''$.

where $\mathbb{D} = 0$ because there have been $2j$ total reflections, and

$$C = e^{i\Delta\psi} e^{-\eta\Delta\ell} \cdot e^{ik\Delta\ell} \cdot r_1 r_2 \tag{D.83}$$

The total field at the 0^{th} origin point is then

$$\begin{aligned} E_0 &= \sum_{j=0}^{\infty} E'_j \\ &= \sum_{j=0}^{\infty} E'_0 \cdot C^j \\ &= E'_0 \frac{1}{1-C} \end{aligned} \tag{D.84}$$

Because the magnitude of $C < 1$ due to the absorption and reflection terms, the sum of a geometric series is valid to use. For a general complex number Ae^{iB}

$$\left[1 - Ae^{iB}\right]^{-1} = \left[1 + A^2 - 2A\cos B\right]^{-1/2} \exp\left(i \arctan\left[\frac{A\sin B}{1 - A\cos B}\right]\right) \tag{D.85}$$

In this case

$$\begin{aligned} A &= e^{-\eta\Delta\ell} r_1 r_2 \\ B &= \Delta\psi + k\Delta\ell \end{aligned} \tag{D.86}$$

Limiting Case In (D.85) an issue arises if $A = 1$ and $B = 0 \mod 2\pi$ indicating there is no energy loss form reflections or absorption, and the driven phase change and optical path phase change are coordinated such that each origin point is in phase. Using a power series expansion to the quadratic term $\sin B/(1 - \cos B) \to \pm\infty$ as $B \to 0$. Whether the term approaches positive or negative infinity depends on which direction B approaches zero. As $B \to \pm\infty$ the arctan term goes to $\pm\pi/2$. However, the $(1 + A^2 - 2A\cos B)$ term, in this case, goes to 0, resolving the issue.

From the 0^{th} origin point the light must still travel to the observation point. For $\mathfrak{L}'$ this path has no further reflections and a distance

$$\ell'_{-1} = \frac{z_1}{\cos\theta} \tag{D.87}$$

For $\mathfrak{L}'$ there is an additional reflection off the bottom interface, $n_2 = 1$, and has a distance of

$$\ell''_{-1} = \frac{z_1 + 2z_2}{\cos\theta} \tag{D.88}$$

The direction of the electric field in the $\mathfrak{L}'$ lattice the E-field will have the same orientation as the incident light. However, the E-field in the $\mathfrak{L}''$ path will be rotated 180° around the normal vector of the interface. Finally, there will be a phase shift of the incident light of the two lattices because of the spatial offset of their origin points. From the observation point, the 0^{th} origin point in the $\mathfrak{L}$ lattice has a lateral distance of

$$d'_{-1} = z_1 \tan\theta \tag{D.89}$$

and in the $\mathfrak{L}''$ lattice of

$$d''_{-1} = (z_1 + 2z_2)\tan\theta \tag{D.90}$$

Thus, the phase change of the incident light caused by the $\left(d''_{-1} - d'_{-1}\right) = 2z_2 \tan\theta$ offset is

$$\psi'' = \psi' - 2\pi\frac{2z_2\tan\theta}{\lambda_0}\sin\theta_0\cos\left(\phi - \phi_0\right) \tag{D.91}$$

So, the final fields from the free light path lattices of $\mathfrak{L}'$ and $\mathfrak{L}''$, respectively are

$$\mathbf{E}' = E_0 \cdot e^{-\eta\ell'} e^{ik\ell'} e^{i\psi'} \hat{\mathbf{e}} \tag{D.92a}$$

$$\mathbf{E}'' = E_0 \cdot e^{-\eta\ell''} e^{ik\ell''} e^{i\psi''} r_2 \, \hat{\mathbf{e}}'' \tag{D.92b}$$

where $\hat{\mathbf{e}}$ is the unit vector of the incident electric field, and $\hat{\mathbf{e}}''$ is the reflected unit vector found by rotating $\hat{\mathbf{e}}$ by $(\pi - 2\theta_0)$ around the incident plane normal. Plugging these into the fields at the observation point gives

$$\mathbf{E}' = E'_0 \frac{e^{-\eta\ell'} e^{ik\ell'} e^{i\psi'}}{1 - e^{i\Delta\psi} e^{-\eta\Delta\ell} \cdot e^{ik\Delta\ell} \cdot r_1 r_2} \hat{\mathbf{e}} \tag{D.93a}$$

$$\mathbf{E}'' = E'_0 \frac{e^{-\eta\ell''} e^{ik\ell''} e^{i\psi''} r_2}{1 - e^{i\Delta\psi} e^{-\eta\Delta\ell} \cdot e^{ik\Delta\ell} \cdot r_1 r_2} \hat{\mathbf{e}}'' \tag{D.93b}$$

E_0' is the electric field just after the incident field is transmitted through the interface, so is given by

$$E_0' = E_{inc} t \tag{D.94}$$

where t represents the transmission. Both the reflection and transmission terms come from the Fresnel equations

$$r_s = \frac{n_1 \cos\theta_i - n_2 \cos\theta_t}{n_1 \cos\theta_i + n_2 \cos\theta_t} \tag{D.95a}$$

$$t_s = \frac{2n_1 \cos\theta_i}{n_1 \cos\theta_i + n_2 \cos\theta_t} \tag{D.95b}$$

$$r_p = \frac{n_2 \cos\theta_i - n_1 \cos\theta_t}{n_1 \cos\theta_t + n_2 \cos\theta_i} \tag{D.95c}$$

$$t_p = \frac{2n_1 \cos\theta_i}{n_1 \cos\theta_t + n_2 \cos\theta_1} \tag{D.95d}$$

for s- and p-polarized light respectively. Thus, the total electric field of the free paths is given by

$$\begin{aligned}
\mathbf{E}_{free} &= \mathbf{E}' + \mathbf{E}'' \\
&= \sum_{\epsilon\in\{s,p\}} E_{0,\epsilon}' \frac{e^{-\eta\ell'} e^{ik\ell'} e^{i\psi'}}{1 - e^{i\Delta\psi} e^{-\eta\Delta\ell} \cdot e^{ik\Delta\ell} \cdot r_{1,\epsilon} r_{2,\epsilon}} \hat{\mathbf{e}}_\epsilon \\
&\qquad + E_{0,\epsilon}' \frac{e^{-\eta\ell''} e^{ik\ell''} e^{i\psi''} r_{2,\epsilon}}{1 - e^{i\Delta\psi} e^{-\eta\Delta\ell} \cdot e^{ik\Delta\ell} \cdot r_{1,\epsilon} r_{2,\epsilon}} \hat{\mathbf{e}}_\epsilon'' \\
&= E_{inc} \sum_{\epsilon\in\{s,p\}} \frac{A_\epsilon t_\epsilon}{1 - e^{i\Delta\psi} e^{-\eta\Delta\ell} \cdot e^{ik\Delta\ell} \cdot r_{1,\epsilon} r_{2,\epsilon}} \\
&\qquad \times \left[e^{-\eta\ell'} e^{ik\ell'} e^{i\psi'} \hat{\mathbf{e}}_\epsilon + e^{-\eta\ell''} e^{ik\ell''} e^{i\psi''} r_{2,\epsilon} \hat{\mathbf{e}}_\epsilon'' \right]
\end{aligned} \tag{D.96}$$

where A_ϵ is the fraction of incident light polarized in the ϵ direction.

Interacting Paths

We again consider a field of radiating dipoles as in Sec. D.1.2. It is important to realize here, to stay consistent with the free lights paths, that the orientation of the dipole is the same as that of the incident field. When thinking of the path the light makes to reach the observation point, there is also a major difference between this case and the 2D case considered in Sec. D.1. In the 2D case, it was implicitly assumed that the observation point lay outside the lattice plane. Thus, once a wave was emitted from a lattice point, it did not interact with anything else. In this case however, all radiation coming from a certain direction in the virtual lattice must interact with each particle having a point in the virtual lattice in that that direction as well. This is depicted in Fig. D.14. In reality, in both cases, the radiation scattered in other directions will be re-scattered back in the direction of the observation point. This leads to a discretized version of Feynman's path integral formulation. Instead of going this route though, a first order approximation will be taken such that re-scattered fields are considered weak and neglected. Scattered fields will also be considered

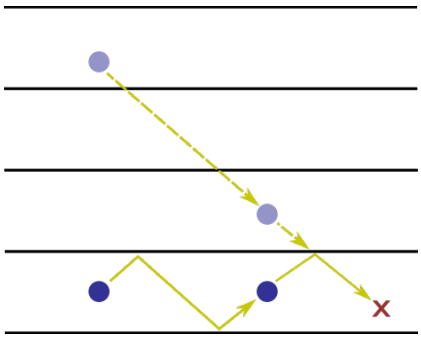

Figure D.14: In the virtual lattice, if a light path must pass through a lattice point it indicates that in the real lattice it interacted with a particle.

weak compared to the incident driving field, so the radiation from each of the lattice points will be a dipole driven by the incident field.

Using dipole radiation, Eq. (D.14), as the scattering function in Eq. (D.76) and accounting for reflections and absorption using (D.80) gives

$$\begin{aligned}\mathbf{E}_{int} = &\sum_i \sum_j \frac{\delta r^2(\theta_i,\phi_j)\cdot\Delta\theta_i\Delta\phi_j}{\delta r(\theta_i+\pi/2,\phi_j)\delta r(\theta_i,\phi_j+\pi/2)}\boldsymbol{P}\hat{\boldsymbol{\theta}'}_{i,j}\\ &\times\sum_{\gamma=0}^{\infty}\left(\gamma^2+(2\beta_{i,j}+1)\gamma+(\beta_{i,j}^2+\beta_{i,j}+\frac{1}{3})\right)\\ &\times E\left(\left(r_{\beta_{i,j}}+\gamma\cdot\delta r(\theta_i,\phi_j)\right)\boldsymbol{T}\hat{\boldsymbol{r}}_{i,j}\right)\\ &\times\exp\left[-\eta\left(r_{\beta_{i,j}}+\gamma\delta r(\theta_i,\phi_j)\right)\right]r_1^{m_1}r_2^{m_2}\\ =&\sum_i\sum_j\frac{\delta r^2(\theta_i,\phi_j)\cdot\Delta\theta_i\Delta\phi_j}{\delta r(\theta_i+\pi/2,\phi_j)\delta r(\theta_i,\phi_j+\pi/2)}\boldsymbol{P}\hat{\boldsymbol{\theta}'}_{i,j}\mathcal{S}^0_{i,j}\end{aligned}\tag{D.97}$$

with

$$\mathcal{S}^0_{i,j} = e^{-i\omega t}\sum_{\gamma=0}^{\infty}\left(\gamma^2+(2\beta_{i,j}+1)\gamma+(\beta_{i,j}^2+\beta_{i,j}+\frac{1}{3})\right)$$
$$\times\frac{-p\omega^2\mu_0}{4\pi}\sin\left(\theta(\boldsymbol{T}\boldsymbol{r}_{i,j})\right)$$
$$\times\frac{\exp\left(i\left[\frac{\omega}{c}\left(r_{\beta_{i,j}}+\gamma\delta r(\theta_i,\phi_j)\right)+\psi(\phi_j,\boldsymbol{r})\right]\right)}{r_{\beta_{i,j}}+\gamma\delta r(\theta_i,\phi_j)}$$
$$\times\exp\left[-\eta\left(r_{\beta_{i,j}}+\gamma\delta r(\theta_i,\phi_j)\right)\right]r_1^{m_1}r_2^{m_2}$$

$$= e^{-i\omega t}\exp\left[i\frac{\omega}{c}r_{\beta_{i,j}}\right]\exp\left[-\eta r_{\beta_{i,j}}\right]$$
$$\times\frac{-p\omega^2\mu_0}{4\pi}\sin\left(\theta(\boldsymbol{T}\boldsymbol{r}_{i,j})\right)$$
$$\times\sum_{\gamma=0}^{\infty}\left(\gamma^2+(2\beta_{i,j}+1)\gamma+(\beta_{i,j}^2+\beta_{i,j}+\frac{1}{3})\right)$$
$$\times\frac{\exp\left(i\left[\frac{\omega}{c}\gamma\delta r(\theta_i,\phi_j)+\psi(\phi_j,\boldsymbol{r})\right]\right)}{r_{\beta_{i,j}}+\gamma\delta r(\theta_i,\phi_j)}$$
$$\times\exp\left[-\eta\gamma\delta r(\theta_i,\phi_j)\right]r_1^{m_1}r_2^{m_2} \tag{D.98}$$

The values of m_1 and m_2 can be found by counting the virtual layer, L, the γ^{th} lattice point in the (θ,ϕ) direction is in, depicted in Fig. D.15.

$$L(\gamma) = L_\beta + \gamma\frac{\delta r\cos\theta}{h} \tag{D.99}$$

where L_β is the layer of the β point, and $(\delta r\cos\theta/h)$ is necessarily an integer due to the regular geometry of the virtual lattice.

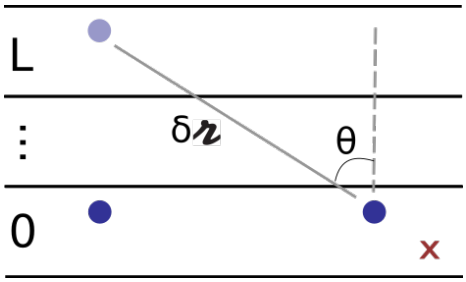

Figure D.15: Determining the layer the γ^{th} point lies in.

Thinking about how many reflections occur on each boundary from the L^{th} virtual layer reveals

$$m_1 = \left|\left\lfloor\frac{L}{2}\right\rfloor\right|$$
$$m_2 = \left|\left\lfloor\frac{L+1}{2}\right\rfloor\right|$$

L	-3	-2	-1	0	1	2	3
$m_1(L)$	2	1	1	0	0	1	1
$m_2(L)$	1	1	0	0	1	1	2

Table D.1: Example values of $m_1(L)$ and $m_2(L)$ indicating the number of reflections off each interface.

Examining these terms, and the physical situation, m_1 and m_2 are always within one of each other. Separating these terms for each sub-lattice also allows further simplification. In the even sub-lattice $L/2$ is an integer so

$$m_{1,e}(L) = m_{2,e}(L) = \left|\frac{L}{2}\right| = \left|\frac{L_\beta}{2} + \gamma\frac{\delta r \cos\theta}{2h}\right| \tag{D.100}$$

indicating that all points contained in the even sub-lattice are reflected from each interface an equal number of times. In the odd sub-lattice $[(L \pm 1)/2]$ is an integer, so

$$m_{1,d}(L) = \left|\frac{L-1}{2}\right| = \left|\frac{L_\beta - 1}{2} + \gamma\frac{\delta r \cos\theta}{2h}\right| \tag{D.101a}$$

$$m_{2,d}(L) = \left|\frac{L+1}{2}\right| = \left|\frac{L_\beta + 1}{2} + \gamma\frac{\delta r \cos\theta}{2h}\right| \tag{D.101b}$$

These results are made more clear by examining some values of $m_1(L)$ and $m_2(L)$, shown in Table D.1.

In Eqs. (D.100) and (D.101) both terms inside the absolute value have the same sign, so the absolute value can be split into two terms. Further, because $\gamma \geq 0$, it can be pulled out from the absolute value. This gives the final reflection counts as

$$m_{1,e} = \left|\frac{L_\beta}{2}\right| + \gamma\left|\frac{\delta r \cos\theta}{2h}\right| \tag{D.102a}$$

$$m_{2,e} = \left|\frac{L_\beta}{2}\right| + \gamma\left|\frac{\delta r \cos\theta}{2h}\right| \tag{D.102b}$$

$$m_{1,d} = \left|\frac{L_\beta - 1}{2}\right| + \gamma\left|\frac{\delta r \cos\theta}{2h}\right| \tag{D.102c}$$

$$m_{2,d} = \left|\frac{L_\beta + 1}{2}\right| + \gamma\left|\frac{\delta r \cos\theta}{2h}\right| \tag{D.102d}$$

For convenience of notation, let $m'_{i,l}$ be the first term on the RHS in each of these equations, and $m''_{i,l}$ be the second term, excluding the γ factor. Thus, each of the RHS's can be written as $m_{i,l} = m'_{i,l} + \gamma m''_{i,l}$.

Plugging the results for m_1 and m_2 into Eq. D.98 gives

$$\begin{aligned}\mathcal{S}^0_{i,j} = e^{-i\omega t}\exp\left[i\frac{\omega}{c}\boldsymbol{\imath}_{\beta_{i,j}}\right]\exp\left[-\eta\boldsymbol{\imath}_{\beta_{i,j}}\right] r_1^{m_1'} r_2^{m_2'} \\ \times \frac{-p\omega^2\mu_0}{4\pi}\sin\left(\theta(\boldsymbol{T}\boldsymbol{\imath}_{i,j})\right) \\ \times \sum_{\gamma=0}^{\infty}\left(\gamma^2 + (2\beta_{i,j}+1)\gamma + (\beta_{i,j}^2+\beta_{i,j}+\frac{1}{3})\right) \\ \times \frac{\exp\left[i\left[\gamma\frac{\omega}{c}\delta\imath(\theta_i,\phi_j)+\psi(\phi_j,\gamma)\right]\right]}{\boldsymbol{\imath}_{\beta_{i,j}}+\gamma\delta\imath(\theta_i,\phi_j)} \\ \times \exp\left[-\eta\gamma\delta\imath(\theta_i,\phi_j)\right] r_1^{\gamma m_1''} r_2^{\gamma m_2''}\end{aligned}$$

As in the 2D analysis from (D.40)

$$\psi(\phi,\boldsymbol{\imath}) = -2\pi\frac{\imath}{\lambda_0}\sin\theta_0\cos(\phi_j-\phi_0) \tag{D.103}$$

where $\imath$ in this case is the lateral distance from the origin given by $\imath = (\boldsymbol{\imath}_\beta + \gamma\delta\imath)\sin\theta$. So

$$\begin{aligned}\mathcal{S}^0_{i,j} = e^{-i\omega t}\exp\left[i\frac{\omega}{c}\boldsymbol{\imath}_{\beta_{i,j}}\right]\exp\left[-\eta\boldsymbol{\imath}_{\beta_{i,j}}\right] \\ \times \exp\left[-i2\pi\frac{\boldsymbol{\imath}_{\beta_{i,j}}\sin\theta_i}{\lambda_0}\sin\theta_0\cos(\phi_j-\phi_0)\right] r_1^{m_1'} r_2^{m_2'} \\ \times \frac{-p\omega^2\mu_0}{4\pi}\sin\left(\theta(\boldsymbol{T}\boldsymbol{\imath}_{i,j})\right) \\ \times \sum_{\gamma=0}^{\infty}\left(\gamma^2 + (2\beta_{i,j}+1)\gamma + (\beta_{i,j}^2+\beta_{i,j}+\frac{1}{3})\right)\frac{\left[\nu^1_{i,j}\right]^\gamma e^{i\zeta^1_{i,j}\gamma}}{\boldsymbol{\imath}_{\beta_{i,j}}+\gamma\delta\imath(\theta_i,\phi_j)}\end{aligned} \tag{D.104}$$

with

$$\nu^1_{i,j} = \exp\left[-\eta\delta\imath(\theta_i,\phi_j)\right] r_1^{m_1''} r_2^{m_2''} \tag{D.105a}$$

$$\zeta^1_{i,j} = \frac{\omega}{c}\delta\imath(\theta_i,\phi_j) - 2\pi\frac{\delta\imath(\theta_i,\phi_j)\sin\theta_i}{\lambda_0}\sin\theta_0\cos(\phi_j-\phi_0) \tag{D.105b}$$

Again letting $\mathscr{r}_{\beta_{i,j}} \to \beta_{i,j}\delta\mathscr{r}(\theta_i,\phi_j)$ gives

$$\begin{aligned}
\mathcal{S}^0_{i,j} &= e^{-i\omega t}\exp\left[i\frac{\omega}{c}\mathscr{r}_{\beta_{i,j}}\right]\exp\left[-\eta\mathscr{r}_{\beta_{i,j}}\right] \\
&\quad\times\frac{-p\omega^2\mu_0}{4\pi}\sin\left(\theta(\boldsymbol{T}\boldsymbol{\mathscr{r}}_{i,j})\right) \\
&\quad\times\exp\left[-i2\pi\frac{\mathscr{r}_{\beta_{i,j}}\sin\theta_i}{\lambda_0}\sin\theta_0\cos(\phi_j-\phi_0)\right]r_1^{m_1'}r_2^{m_2'} \\
&\quad\times\sum_{\gamma=0}^{\infty}\left(\gamma^2+(2\beta_{i,j}+1)\gamma+(\beta_{i,j}^2+\beta_{i,j}+\frac{1}{3})\right)\frac{\left[\nu^1_{i,j}\right]^\gamma e^{i\zeta^1_{i,j}\gamma}}{(\beta_{i,j}+\gamma)\delta\mathscr{r}(\theta_i,\phi_j)} \\
&= e^{-i\omega t}\exp\left[i\frac{\omega}{c}\mathscr{r}_{\beta_{i,j}}\right]\exp\left[-\eta\mathscr{r}_{\beta_{i,j}}\right] \\
&\quad\times\frac{-p\omega^2\mu_0}{4\pi}\sin\left(\theta(\boldsymbol{T}\boldsymbol{\mathscr{r}}_{i,j})\right) \\
&\quad\times\exp\left[-i2\pi\frac{\mathscr{r}_{\beta_{i,j}}\sin\theta_i}{\lambda_0}\sin\theta_0\cos(\phi_j-\phi_0)\right]r_1^{m_1'}r_2^{m_2'} \\
&\quad\times\sum_{\gamma=\beta_{i,j}}^{\infty}\left((\gamma-\beta_{i,j})^2+(2\beta_{i,j}+1)(\gamma-\beta_{i,j})+(\beta_{i,j}^2+\beta_{i,j}+\frac{1}{3})\right) \\
&\qquad\qquad\times\frac{\left[\nu^1_{i,j}\right]^{\gamma-\beta_{i,j}}e^{i\zeta^1_{i,j}(\gamma-\beta_{i,j})}}{\gamma\delta\mathscr{r}(\theta_i,\phi_j)}
\end{aligned} \tag{D.106}$$

and

$$(\gamma-\beta_{i,j})^2+(2\beta_{i,j}+1)(\gamma-\beta_{i,j})+(\beta_{i,j}^2+\beta_{i,j}+\frac{1}{3})=\gamma^2+\gamma+\frac{1}{3} \tag{D.107}$$

so

$$\begin{aligned}
\mathcal{S}^0_{i,j} &= e^{-i\omega t}\exp\left[i\frac{\omega}{c}\mathscr{r}_{\beta_{i,j}}\right]\exp\left[-\eta\mathscr{r}_{\beta_{i,j}}\right] \\
&\quad\times\frac{-p\omega^2\mu_0}{4\pi}\sin\left(\theta(\boldsymbol{T}\boldsymbol{\mathscr{r}}_{i,j})\right) \\
&\quad\times\exp\left[-i2\pi\frac{\mathscr{r}_{\beta_{i,j}}\sin\theta_i}{\lambda_0}\sin\theta_0\cos(\phi_j-\phi_0)\right]r_1^{m'_1}r_2^{m'_2} \\
&\quad\times\sum_{\gamma=\beta_{i,j}}^{\infty}\left(\gamma^2+\gamma+\frac{1}{3}\right)\frac{\left[\nu^1_{i,j}\right]^{\gamma-\beta_{i,j}}e^{i\zeta^1_{i,j}(\gamma-\beta_{i,j})}}{\gamma\delta\mathscr{r}(\theta_i,\phi_j)} \\
&= e^{-i\omega t}\exp\left[i\frac{\omega}{c}\mathscr{r}_{\beta_{i,j}}\right]\exp\left[-\eta\mathscr{r}_{\beta_{i,j}}\right]\frac{\left[\nu^1_{i,j}\right]^{-\beta_{i,j}}e^{-i\zeta^1_{i,j}\beta_{i,j}}}{\delta\mathscr{r}(\theta_i,\phi_j)} \\
&\quad\times\frac{-p\omega^2\mu_0}{4\pi}\sin\left(\theta(\boldsymbol{T}\boldsymbol{\mathscr{r}}_{i,j})\right) \\
&\quad\times\exp\left[-i2\pi\frac{\mathscr{r}_{\beta_{i,j}}\sin\theta_i}{\lambda_0}\sin\theta_0\cos(\phi_j-\phi_0)\right]r_1^{m'_1}r_2^{m'_2} \\
&\quad\times\sum_{\gamma=\beta_{i,j}}^{\infty}\left(\gamma+1+\frac{1}{3\gamma}\right)\left[\nu^1_{i,j}\right]^{\gamma}e^{i\zeta^1_{i,j}\gamma} \\
&= e^{-i\omega t}\exp\left[i\frac{\omega}{c}\mathscr{r}_{\beta_{i,j}}\right]\exp\left[-\eta\mathscr{r}_{\beta_{i,j}}\right]\frac{\left[\nu^1_{i,j}\right]^{-\beta_{i,j}}e^{-i\zeta^1_{i,j}\beta_{i,j}}}{\delta\mathscr{r}(\theta_i,\phi_j)} \\
&\quad\times\frac{-p\omega^2\mu_0}{4\pi}\sin\left(\theta(\boldsymbol{T}\boldsymbol{\mathscr{r}}_{i,j})\right) \\
&\quad\times\exp\left[-i2\pi\frac{\mathscr{r}_{\beta_{i,j}}\sin\theta_i}{\lambda_0}\sin\theta_0\cos(\phi_j-\phi_0)\right]r_1^{m'_1}r_2^{m'_2} \\
&\quad\times\mathcal{S}^1_{i,j}
\end{aligned}\tag{D.108}$$

with

$$\mathcal{S}^1_{i,j}=\sum_{\gamma=\beta_{i,j}}^{\infty}\left(\gamma+1+\frac{1}{3\gamma}\right)\left[\nu^1_{i,j}\right]^{\gamma}e^{i\zeta^1_{i,j}\gamma}\tag{D.109}$$

Accounting for the phase change error given by Eq. (D.47) with

$$N_p=\frac{\mathscr{r}\Delta\phi}{\delta\mathscr{r}(\theta,\phi+\frac{\pi}{2})}\frac{\mathscr{r}\Delta\theta}{\delta\mathscr{r}(\theta+\frac{\pi}{2},\phi)}\tag{D.110a}$$

$$\Delta\chi=-2\pi\frac{\delta\mathscr{r}(\theta,\phi+\frac{\pi}{2})\sin\theta}{\lambda_0}\sin\theta_0\sin(\phi_0-\phi)\tag{D.110b}$$

gives

$$\begin{aligned}\delta\chi &= \frac{\delta\mathfrak{r}(\theta,\phi+\frac{\pi}{2})\delta\mathfrak{r}(\theta+\frac{\pi}{2},\phi)}{\mathfrak{r}^2\Delta\phi\Delta\theta} \\ &\quad\times\left\{\frac{\sin\left(\left[\mathfrak{r}^2\Delta\phi\Delta\theta+\delta\mathfrak{r}(\theta,\phi+\frac{\pi}{2})\delta\mathfrak{r}(\theta+\frac{\pi}{2},\phi)\right]\zeta_{i,j}^2\right)}{\sin\left(\delta\mathfrak{r}(\theta,\phi+\frac{\pi}{2})\zeta_{i,j}^2\right)}-1\right\} \\ &= \frac{\delta\mathfrak{r}(\theta,\phi+\frac{\pi}{2})\delta\mathfrak{r}(\theta+\frac{\pi}{2},\phi)}{\gamma^2\delta\mathfrak{r}^2(\theta,\phi)\Delta\phi\Delta\theta} \\ &\quad\times\left\{\frac{\sin\left(\left[\gamma^2\delta\mathfrak{r}^2(\theta,\phi)\Delta\phi\Delta\theta+\delta\mathfrak{r}(\theta,\phi+\frac{\pi}{2})\delta\mathfrak{r}(\theta+\frac{\pi}{2},\phi)\right]\zeta_{i,j}^2\right)}{\sin\left(\delta\mathfrak{r}(\theta,\phi+\frac{\pi}{2})\zeta_{i,j}^2\right)}-1\right\}\end{aligned} \tag{D.111}$$

with

$$\zeta_{i,j}^2 = -\frac{2\pi\sin\theta_i}{2\delta\mathfrak{r}(\theta_i,\phi_j+\frac{\pi}{2})\lambda_0}\sin\theta_0\sin(\phi_0-\phi_j) \tag{D.112}$$

and $\mathfrak{r}\to\gamma\delta\mathfrak{r}$ because the sum in $\mathcal{S}^0$ begins at 0. Multiplying the term in the

sum of $\mathcal{S}^0$ in Eq. D.108 gives

$$
\begin{aligned}
\mathcal{S}^1_{i,j} = & \sum_{\gamma=\beta_{i,j}}^{\infty} \left(\gamma + 1 + \frac{1}{3\gamma}\right) \frac{\delta\mathfrak{r}(\theta_i, \phi_j + \frac{\pi}{2})\delta\mathfrak{r}(\theta_i + \frac{\pi}{2}, \phi_j)}{\gamma^2 \delta\mathfrak{r}^2(\theta_i, \phi_j)\Delta\phi_j\Delta\theta_i} \left[\nu^1_{i,j}\right]^{\gamma} e^{i\zeta^1_{i,j}\gamma} \\
& \times \left\{ \frac{\sin\left(\left[\gamma^2\delta\mathfrak{r}^2(\theta_i, \phi_j)\Delta\phi_j\Delta\theta_i + \delta\mathfrak{r}(\theta_i, \phi_j + \frac{\pi}{2})\delta\mathfrak{r}(\theta_i + \frac{\pi}{2}, \phi_j)\right]\zeta^2_{i,j}\right)}{\sin\left(\delta\mathfrak{r}(\theta_i, \phi_j + \frac{\pi}{2})\zeta^2_{i,j}\right)} - 1 \right\} \\
= & \frac{\delta\mathfrak{r}(\theta_i, \phi_j + \frac{\pi}{2})\delta\mathfrak{r}(\theta_i + \frac{\pi}{2}, \phi_j)}{\delta\mathfrak{r}^2(\theta_i, \phi_j)\Delta\phi_j\Delta\theta_i} \\
& \times \sum_{\gamma=\beta_{i,j}}^{\infty} \left(\frac{1}{\gamma} + \frac{1}{\gamma^2} + \frac{1}{3\gamma^3}\right) \left[\nu^1_{i,j}\right]^{\gamma} e^{i\zeta^1_{i,j}\gamma} \\
& \times \left\{ \frac{\sin\left(\left[\gamma^2\delta\mathfrak{r}^2(\theta_i, \phi_j)\Delta\phi_j\Delta\theta_i + \delta\mathfrak{r}(\theta_i, \phi_j + \frac{\pi}{2})\delta\mathfrak{r}(\theta_i + \frac{\pi}{2}, \phi_j)\right]\zeta^2_{i,j}\right)}{\sin\left(\delta\mathfrak{r}(\theta_i, \phi_j + \frac{\pi}{2})\zeta^2_{i,j}\right)} - 1 \right\} \\
= & \frac{\delta\mathfrak{r}(\theta_i, \phi_j + \frac{\pi}{2})\delta\mathfrak{r}(\theta_i + \frac{\pi}{2}, \phi_j)}{\delta\mathfrak{r}^2(\theta_i, \phi_j)\Delta\phi_j\Delta\theta_i} \\
& \times \sum_{\gamma=\beta_{i,j}}^{\infty} \left(\frac{1}{\gamma} + \frac{1}{\gamma^2} + \frac{1}{3\gamma^3}\right) \left[\nu^1_{i,j}\right]^{\gamma} e^{i\zeta^1_{i,j}\gamma} \\
& \times \left\{ \begin{array}{l}
\left[\dfrac{\exp\left[i\delta\mathfrak{r}(\theta_i, \phi_j + \frac{\pi}{2})\delta\mathfrak{r}(\theta_i + \frac{\pi}{2}, \phi_j)\zeta^2_{i,j}\right]}{2i\sin\left(\delta\mathfrak{r}(\theta_i, \phi_j + \frac{\pi}{2})\zeta^2_{i,j}\right)} \right. \\
\qquad \left. \times \exp\left[i\gamma^2\delta\mathfrak{r}^2(\theta_i, \phi_j)\Delta\phi_j\Delta\theta_i\zeta^2_{i,j}\right] \right] \\
- \left[\dfrac{\exp\left[-i\delta\mathfrak{r}(\theta_i, \phi_j + \frac{\pi}{2})\delta\mathfrak{r}(\theta_i + \frac{\pi}{2}, \phi_j)\zeta^2_{i,j}\right]}{2i\sin\left(\delta\mathfrak{r}(\theta_i, \phi_j + \frac{\pi}{2})\zeta^2_{i,j}\right)} \right. \\
\qquad \left. \times \exp\left[-i\gamma^2\delta\mathfrak{r}^2(\theta_i, \phi_j)\Delta\phi_j\Delta\theta_i\zeta^2_{i,j}\right] \right] \\
\quad - 1
\end{array} \right\}
\end{aligned}
$$

$$\mathcal{S}^1_{i,j} = \frac{\delta\mathscr{r}(\theta_i, \phi_j + \frac{\pi}{2})\delta\mathscr{r}(\theta_i + \frac{\pi}{2}, \phi_j)}{\delta\mathscr{r}^2(\theta_i, \phi_j)\Delta\phi_j\Delta\theta_i}$$

$$\times \left\{ \begin{array}{l} \left[\begin{array}{l} \dfrac{\exp\left[i\delta\mathscr{r}(\theta_i, \phi_j + \frac{\pi}{2})\delta\mathscr{r}(\theta_i + \frac{\pi}{2}, \phi_j)\zeta^2_{i,j}\right]}{2i\sin\left(\delta\mathscr{r}(\theta_i, \phi_j + \frac{\pi}{2})\zeta^2_{i,j}\right)} \\ \quad \times \displaystyle\sum_{\gamma=\beta_{i,j}}^{\infty} \left(\frac{1}{\gamma} + \frac{1}{\gamma^2} + \frac{1}{3\gamma^3}\right) \left[\nu^1_{i,j}\right]^\gamma e^{i\zeta^1_{i,j}\gamma} \\ \quad\quad \times \exp\left[i\gamma^2\delta\mathscr{r}^2(\theta_i, \phi_j)\Delta\phi_j\Delta\theta_i\zeta^2_{i,j}\right] \end{array} \right] \\ - \left[\begin{array}{l} \dfrac{\exp\left[-i\delta\mathscr{r}(\theta_i, \phi_j + \frac{\pi}{2})\delta\mathscr{r}(\theta_i + \frac{\pi}{2}, \phi_j)\zeta^2_{i,j}\right]}{2i\sin\left(\delta\mathscr{r}(\theta_i, \phi_j + \frac{\pi}{2})\zeta^2_{i,j}\right)} \\ \quad \times \displaystyle\sum_{\gamma=\beta_{i,j}}^{\infty} \left(\frac{1}{\gamma} + \frac{1}{\gamma^2} + \frac{1}{3\gamma^3}\right) \left[\nu^1_{i,j}\right]^\gamma e^{i\zeta^1_{i,j}\gamma} \\ \quad\quad \times \exp\left[-i\gamma^2\delta\mathscr{r}^2(\theta_i, \phi_j)\Delta\phi_j\Delta\theta_i\zeta^2_{i,j}\right] \end{array} \right] \\ - \displaystyle\sum_{\gamma=\beta_{i,j}}^{\infty} \left(\frac{1}{\gamma} + \frac{1}{\gamma^2} + \frac{1}{3\gamma^3}\right) \left[\nu^1_{i,j}\right]^\gamma e^{i\zeta^1_{i,j}\gamma} \end{array} \right\} \tag{D.113}$$

There are nine terms being summed with the forms

$$\sum_\gamma \frac{x^\gamma e^{i\gamma} e^{\pm i\gamma^2}}{\gamma}, \quad \sum_\gamma \frac{x^\gamma e^{i\gamma} e^{\pm i\gamma^2}}{\gamma^2}, \quad \sum_\gamma \frac{x^\gamma e^{i\gamma} e^{\pm i\gamma^2}}{\gamma^3} \tag{D.114a}$$

$$\sum_\gamma \frac{x^\gamma e^{i\gamma}}{\gamma}, \quad \sum_\gamma \frac{x^\gamma e^{i\gamma}}{\gamma^2}, \quad \sum_\gamma \frac{x^\gamma e^{i\gamma}}{\gamma^3} \tag{D.114b}$$

Unfortunately, the terms with the exponential factors $e^{i\gamma^2}$ in Eqs. (D.114a) do not have a closed form. However, because $x = \nu^1 < 1$, using the Comparison test, the terms still converge. The terms without the exponential factors in Eqs (D.114b) we have seen before and take the form of polylogarithmic functions $\mathrm{Li}_n(z)$ where Li_1 is the normal logarithm, Li_2 is the dilogarithm, and

$$\mathrm{Li}_3(z) = \sum_{k=1}^{\infty} \frac{z^k}{k^3} \tag{D.115}$$

can be seen in Fig. D.16.

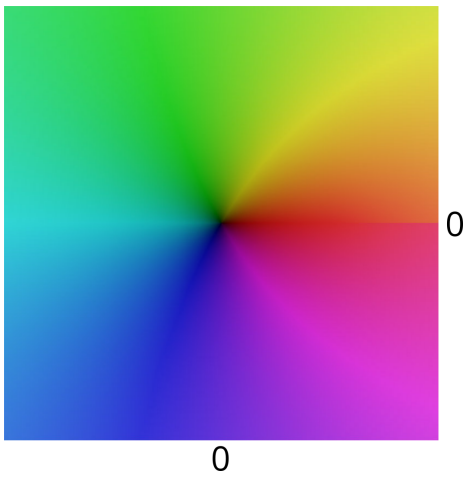

Figure D.16: The polylogarithmic function Li_3 on the complex plane. The hue represents the phase, and saturation the magnitude [32].

Combining the results of $\mathcal{S}^0$ and $\mathcal{S}^1$ gives a total field of

$$
\begin{aligned}
\mathbf{E}_{int} = \sum_i \sum_j & \frac{\delta\mathscr{r}^2(\theta_i,\phi_j)\cdot\Delta\theta_i\Delta\phi_j}{\delta\mathscr{r}(\theta_i+\pi/2,\phi_j)\delta\mathscr{r}(\theta_i,\phi_j+\pi/2)}\boldsymbol{P}\hat{\boldsymbol{\theta}'}_{i,j} \\
& \times \frac{-p\omega^2\mu_0}{4\pi}\sin\left(\theta(\boldsymbol{T}\boldsymbol{\mathscr{r}}_{i,j})\right) \\
& \times e^{-i\omega t}\exp\left[i\frac{\omega}{c}\mathscr{r}_{\beta_{i,j}}\right]\exp\left[-\eta\mathscr{r}_{\beta_{i,j}}\right]\frac{\left[\nu^1_{i,j}\right]^{-\beta_{i,j}}e^{-i\zeta^1_{i,j}\beta_{i,j}}}{\delta\mathscr{r}(\theta_i,\phi_j)} \\
& \times \exp\left[-i2\pi\frac{\mathscr{r}_{\beta_{i,j}}\sin\theta_i}{\lambda_0}\sin\theta_0\cos(\phi_j-\phi_0)\right]r_1^{m'_1}r_2^{m'_2} \\
& \times \frac{\delta\mathscr{r}(\theta_i,\phi_j+\frac{\pi}{2})\delta\mathscr{r}(\theta_i+\frac{\pi}{2},\phi_j)}{\delta\mathscr{r}^2(\theta_i,\phi_j)\Delta\phi_j\Delta\theta_i} \\
\times \Bigg\{ & \left[\frac{\exp\left[i\delta\mathscr{r}(\theta_i,\phi_j+\frac{\pi}{2})\delta\mathscr{r}(\theta_i+\frac{\pi}{2},\phi_j)\zeta^2_{i,j}\right]}{2i\sin\left(\delta\mathscr{r}(\theta_i,\phi_j+\frac{\pi}{2})\zeta^2_{i,j}\right)}\right. \\
& \quad \times\sum_{\gamma=\beta_{i,j}}^{\infty}\left(\frac{1}{\gamma}+\frac{1}{\gamma^2}+\frac{1}{3\gamma^3}\right)\left[\nu^1_{i,j}\right]^{\gamma}e^{i\zeta^1_{i,j}\gamma} \\
& \quad \left.\times\exp\left[i\gamma^2\delta\mathscr{r}^2(\theta_i,\phi_j)\Delta\phi_j\Delta\theta_i\zeta^2_{i,j}\right]\right] \\
- & \left[\frac{\exp\left[-i\delta\mathscr{r}(\theta_i,\phi_j+\frac{\pi}{2})\delta\mathscr{r}(\theta_i+\frac{\pi}{2},\phi_j)\zeta^2_{i,j}\right]}{2i\sin\left(\delta\mathscr{r}(\theta_i,\phi_j+\frac{\pi}{2})\zeta^2_{i,j}\right)}\right. \\
& \quad \times\sum_{\gamma=\beta_{i,j}}^{\infty}\left(\frac{1}{\gamma}+\frac{1}{\gamma^2}+\frac{1}{3\gamma^3}\right)\left[\nu^1_{i,j}\right]^{\gamma}e^{i\zeta^1_{i,j}\gamma} \\
& \quad \left.\times\exp\left[-i\gamma^2\delta\mathscr{r}^2(\theta_i,\phi_j)\Delta\phi_j\Delta\theta_i\zeta^2_{i,j}\right]\right] \\
& -\sum_{\gamma=\beta_{i,j}}^{\infty}\left(\frac{1}{\gamma}+\frac{1}{\gamma^2}+\frac{1}{3\gamma^3}\right)\left[\nu^1_{i,j}\right]^{\gamma}e^{i\zeta^1_{i,j}\gamma}
\end{aligned}
\Bigg\} \tag{D.116a}
$$

$$
\begin{aligned}
\mathbf{E}_{int} = \sum_i \sum_j \boldsymbol{P}\hat{\boldsymbol{\theta}'}_{i,j} e^{-i\omega t} \exp\left[i\frac{\omega}{c}\boldsymbol{\imath}_{\beta_{i,j}}\right] \exp\left[-\eta \boldsymbol{\imath}_{\beta_{i,j}}\right] \frac{\left[\nu^1_{i,j}\right]^{-\beta_{i,j}} e^{-i\zeta^1_{i,j}\beta_{i,j}}}{\delta\boldsymbol{\imath}(\theta_i,\phi_j)} \\
\times \exp\left[-i2\pi\frac{\boldsymbol{\imath}_{\beta_{i,j}}\sin\theta_i}{\lambda_0}\sin\theta_0\cos(\phi_j-\phi_0)\right] r_1^{m'_1} r_2^{m'_2} \\
\times \frac{-p\omega^2\mu_0}{4\pi}\sin\left(\theta(\boldsymbol{T}\boldsymbol{\imath}_{i,j})\right) \\
\times \left\{ \begin{array}{l}
\left[\begin{array}{l}
\dfrac{\exp\left[i\delta\boldsymbol{\imath}(\theta_i,\phi_j+\frac{\pi}{2})\delta\boldsymbol{\imath}(\theta_i+\frac{\pi}{2},\phi_j)\zeta^2_{i,j}\right]}{2i\sin\left(\delta\boldsymbol{\imath}(\theta_i,\phi_j+\frac{\pi}{2})\zeta^2_{i,j}\right)} \\
\quad\times\displaystyle\sum_{\gamma=\beta_{i,j}}^{\infty}\left(\frac{1}{\gamma}+\frac{1}{\gamma^2}+\frac{1}{3\gamma^3}\right)\left[\nu^1_{i,j}\right]^{\gamma} e^{i\zeta^1_{i,j}\gamma} \\
\qquad\times\exp\left[i\gamma^2\delta\boldsymbol{\imath}^2(\theta_i,\phi_j)\Delta\phi_j\Delta\theta_i\zeta^2_{i,j}\right]
\end{array}\right] \\
-\left[\begin{array}{l}
\dfrac{\exp\left[-i\delta\boldsymbol{\imath}(\theta_i,\phi_j+\frac{\pi}{2})\delta\boldsymbol{\imath}(\theta_i+\frac{\pi}{2},\phi_j)\zeta^2_{i,j}\right]}{2i\sin\left(\delta\boldsymbol{\imath}(\theta_i,\phi_j+\frac{\pi}{2})\zeta^2_{i,j}\right)} \\
\quad\times\displaystyle\sum_{\gamma=\beta_{i,j}}^{\infty}\left(\frac{1}{\gamma}+\frac{1}{\gamma^2}+\frac{1}{3\gamma^3}\right)\left[\nu^1_{i,j}\right]^{\gamma} e^{i\zeta^1_{i,j}\gamma} \\
\qquad\times\exp\left[-i\gamma^2\delta\boldsymbol{\imath}^2(\theta_i,\phi_j)\Delta\phi_j\Delta\theta_i\zeta^2_{i,j}\right]
\end{array}\right] \\
-\left[\ln\left(1-\nu^1_{i,j}e^{i\zeta^1_{i,j}}\right)+\displaystyle\sum_{\gamma=1}^{\beta_{i,j}-1}\frac{\left[\nu^1_{i,j}\right]^{\gamma} e^{i\zeta^1_{i,j}\gamma}}{\gamma}\right] \\
-\left[\mathrm{Li}_2\left(\nu^1_{i,j}e^{i\zeta^1_{i,j}}\right)+\displaystyle\sum_{\gamma=1}^{\beta_{i,j}-1}\frac{\left[\nu^1_{i,j}\right]^{\gamma} e^{i\zeta^1_{i,j}\gamma}}{\gamma^2}\right] \\
-\frac{1}{3}\left[\mathrm{Li}_3\left(\nu^1_{i,j}e^{i\zeta^1_{i,j}}\right)+\displaystyle\sum_{\gamma=1}^{\beta_{i,j}-1}\frac{\left[\nu^1_{i,j}\right]^{\gamma} e^{i\zeta^1_{i,j}\gamma}}{\gamma^3}\right]
\end{array} \right\}
\end{aligned}
\tag{D.116b}
$$

Remember that this result accounts for each of the four sub-lattices that must be summed together to find the entire field. There is the even and odd sub-lattice caused by the reflections, and the s- and p-polarized driving fields which affects the reflections and scattering.

Limiting Cases Again issues arise if $\zeta^2 = 0$ which occurs if $\theta_0 = 0$ or $\phi_j = \phi_0$. using L'Hôpital's rule on the problem factors gives

$$
\pm\frac{\exp\left[\pm i\delta\boldsymbol{\imath}(\theta_i,\phi_j+\frac{\pi}{2})\delta\boldsymbol{\imath}(\theta_i+\frac{\pi}{2},\phi_j)\zeta^2_{i,j}\right]}{2i\sin\left(\delta\boldsymbol{\imath}(\theta_i,\phi_j+\frac{\pi}{2})\zeta^2_{i,j}\right)} \to \frac{\delta\boldsymbol{\imath}(\theta_i+\frac{\pi}{2},\phi_j)}{2}, \text{ (as } \zeta^2_{i,j}\to 0)
\tag{D.117}
$$

Notice also that because absorption has been accounted for by ν^1, there are no divergent terms as occurred in the 2D case of Sec. D.1.2, unless $\nu^1 = 1$.

By assuming the distance change between particles is constant we have arrived at an analytic expression for the magnitude of each direction in the far region. By studying this expression the dependence of the electric field on the lattice structure can be gleaned. By using calculus of variations, then, the optimal structure to create a given radiation pattern could be found. These efforts are thwarted, unfortunately, by the behavior of the separation function $\delta\mathscr{r}$, which turns out to be very complicated.

D.3 The Separation Function

Notice that no actual predications have been made yet about the field produced by a lattice. This is due to the unruly nature of the $\delta\mathfrak{r}$ function describing the separation between lattice points in a given direction. This bad behavior is exhibited because, naturally, $\delta\mathfrak{r}$ is defined only in the directions for which a lattice point exists.

D.3.1 2D Separation Function

The lattice point directions are composed of *rational combinations* of the lattice vectors,

$$\phi = \arctan\left(\frac{\alpha^i a_i^2}{\alpha^i a_i^1}\right) \tag{D.118}$$

Because the α-space is discrete, $\alpha^i \in \mathbb{Z}$, but the angular space of the lattice is continuous, there are "holes" for angles ϕ that do not correspond to a lattice point. This creates an everywhere discontinuous set, similar to the Cantor set. Further, though, there is a fractal nature to this function due to the translation invariance of the lattice. This results in a function that, even though it is defined on a dense set in ϕ-space, can not be represented by a continuous function. A plot of $\delta\mathfrak{r}$ for lattice vectors $(1,0)$ and $(0,1)$ and $0 \leq \alpha^1, \alpha^2 \leq 100$ can be seen in Fig. D.17.

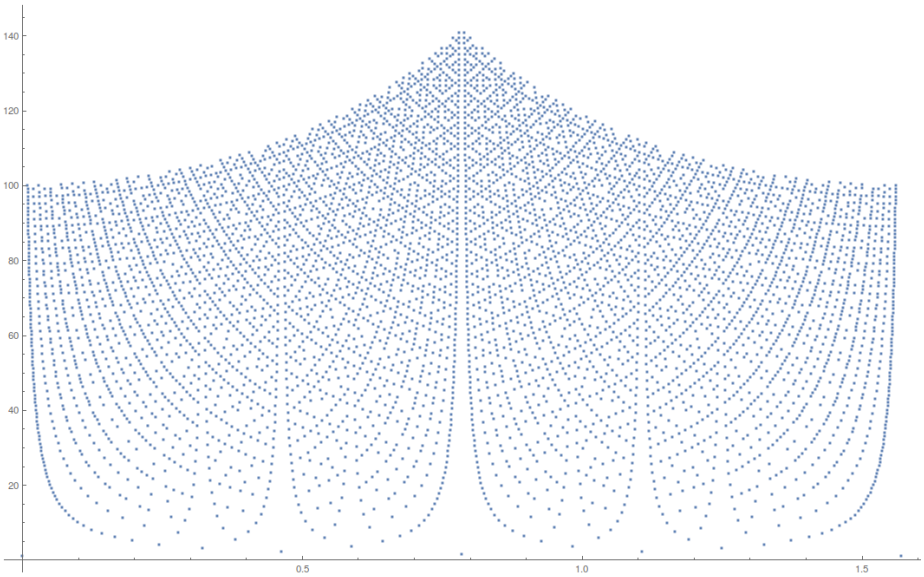

Figure D.17: Separation function with $a_1 = (1,0)$, $a_2 = (0,1)$, and $0 \leq \alpha^1, \alpha^2 \leq 100$. Due to symmetry of the lattice vectors, only the first quadrant $0 \leq \phi \leq \pi/2$ is relevant. The x-axis is ϕ and the y-axis is the separation in arbitrary units.

The behavior of $\delta\mathfrak{r}$ forces a careful evaluation of the directions chosen as representatives for each region. In fact, $\delta\mathfrak{r}$ will end up dictating these choices. To make the situation tractable, a limit will be imposed on the maximum separation. All angles whose separation fall under this value will be considered,

and the rest will be ignored. An issue may arise here in that although the strongest directions of radiation are being considered, a countably infinite number of weaker directions are being ignored, and these ignored direction may have a significant contribution when added together.

Although the behavior of $\delta\mathfrak{r}$ is infinitely discontinuous, it transforms with the lattice vectors in a smooth manner. There are four parameters that affect $\delta\mathfrak{r}$: the length and angle of each lattice vector. When evaluating the change of $\delta\mathfrak{r}$ issues arise because, looking in a fixed direction, if the lattice vector changes a lattice point that was present suddenly disappears. This leads to discontinuities in the derivatives of $\delta\mathfrak{r}$ similar to the discontinuities in the function itself. To solve this, instead of fixing the direction of interest when taking partial derivatives, the lattice point is fixed, i.e. α_1 and α_2 are fixed, and the direction of observation is allowed to vary.

From the definition of $\delta\mathfrak{r}(\phi)$ being the separation between points in the ϕ direction, an equivalent definition of $\delta\mathfrak{r}$, compared to Eq. (D.7), can be written as

$$\delta\mathfrak{r}(\phi) = \left[\left[\alpha^i a_i^j\right]^2 \mathbb{1}_j\right]^{1/2} \tag{D.119}$$

assuming that Eq. (D.3) holds. Changing $\delta\mathfrak{r}$ and ϕ into functions of the length and angles of the lattice vectors, defined in Fig. D.18 results in

$$\begin{aligned}\delta\mathfrak{r} &= \left[\left[\alpha^1 a_1 \cos\eta_1 + \alpha^2 a_2 \cos\eta_2\right]^2 + \left[\alpha^1 a_1 \sin\eta_1 + \alpha^2 a_2 \sin\eta_2\right]^2\right]^{1/2} \\ &= \left[\left[\alpha^1 a_1\right]^2 + \left[\alpha^2 a_2\right]^2 + 2\alpha^1\alpha^2 a_1 a_2 \cos\left(\eta_1 - \eta_2\right)\right]^{1/2}\end{aligned} \tag{D.120}$$

and

$$\phi = \arctan\left[\frac{\alpha^1 a_1 \sin\eta_1 + \alpha^2 a_2 \sin\eta_2}{\alpha^1 a_1 \cos\eta_1 + \alpha^2 a_2 \cos\eta_2}\right] \tag{D.121}$$

where $a_i^1 = a_i \cos\eta_i$ and $a_i^2 = a_i \sin\eta_i$.

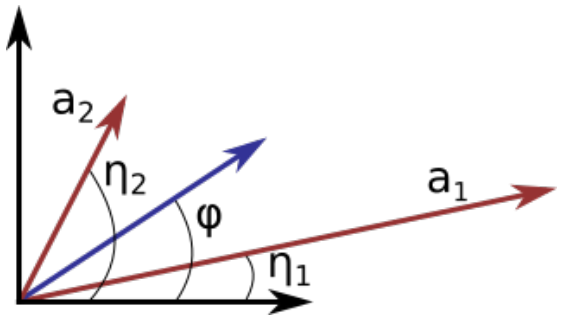

Figure D.18: Variable definitions used in the alternative definition of the separation function, Eq. (D.119).

To see how the lattice changes with each of these variables the derivative of

$\delta\mathscr{r}$ and ϕ can be taken with respect to each of a_1, a_2, η_1, and η_2. This results in

$$\frac{d(\delta\mathscr{r})}{da_1} = \frac{\alpha^1\left[\alpha^1 a_1 + \alpha^2 a_2\cos\left(\eta_1-\eta_2\right)\right]}{\delta\mathscr{r}} \tag{D.122}$$

$$\frac{d(\delta\mathscr{r})}{da_2} = \frac{\alpha^2\left[\alpha^2 a_2 + \alpha^1 a_1\cos\left(\eta_1-\eta_2\right)\right]}{\delta\mathscr{r}} \tag{D.123}$$

$$\frac{d(\delta\mathscr{r})}{d\eta_1} = -\frac{\alpha^1\alpha^2 a_1 a_2\sin\left(\eta_1-\eta_2\right)}{\delta\mathscr{r}} \tag{D.124}$$

$$\frac{d(\delta\mathscr{r})}{d\eta_2} = \frac{\alpha^1\alpha^2 a_1 a_2\sin\left(\eta_1-\eta_2\right)}{\delta\mathscr{r}} \qquad = -\frac{d(\delta\mathscr{r})}{d\eta_1} \tag{D.125}$$

and

$$\frac{d\phi}{da_1} = \frac{\alpha^1\alpha^2 a_2\sin\left(\eta_1-\eta_2\right)}{\delta\mathscr{r}^2} \tag{D.126}$$

$$\frac{d\phi}{da_2} = -\frac{\alpha^1\alpha^2 a_1\sin\left(\eta_1-\eta_2\right)}{\delta\mathscr{r}^2} \qquad = -\frac{a_1}{a_2}\frac{d\phi}{da_1} \tag{D.127}$$

$$\frac{d\phi}{d\eta_1} = \frac{\alpha^1 a_1\left[\alpha^1 a_1 + \alpha^2 a_2\cos\left(\eta_1-\eta_2\right)\right]}{\delta\mathscr{r}^2} \tag{D.128}$$

$$\frac{d\phi}{d\eta_2} = \frac{\alpha^2 a_2\left[\alpha^2 a_2 + \alpha^1 a_1\cos\left(\eta_1-\eta_2\right)\right]}{\delta\mathscr{r}^2} \tag{D.129}$$

D.3.2 3D Separation Function

In analogy to the 2D case, in a three dimensional lattice each lattice vector can be defined in spherical coordinates, giving a more natural representation for the lattice summation. Using the magnitude, and polar and azimuthal angles, (a, υ, η), the separation function is

$$\delta\mathscr{r} = \left[\left(\sum_i \alpha^i a_i \sin\upsilon_i\cos\eta_i\right)^2 + \left(\sum_i \alpha^i a_i \sin\upsilon_i\sin\eta_i\right)^2 + \left(\sum_i \alpha^i a_i\cos\upsilon_i\right)^2\right]^{1/2} \tag{D.130}$$

the polar angle is

$$\theta = \arctan\frac{\sum_i \alpha^i a_i\sin\upsilon_i}{\left[\left(\sum_i \alpha^i a_i\sin\upsilon_i\cos\eta_i\right)^2 + \left(\sum_i \alpha^i a_i\sin\upsilon_i\sin\eta_i\right)^2\right]^{1/2}} \tag{D.131}$$

and the azimuthal angle is

$$\phi = \arctan\frac{\sum_i \alpha^i a_i\sin\upsilon_i\sin\eta_i}{\sum_i \alpha^i a_i\sin\upsilon_i\cos\eta_i} \tag{D.132}$$

This gives derivatives

$$\frac{d(\delta\mathfrak{r})}{da_{i_0}} = \frac{\alpha_{i_0}}{\delta\mathfrak{r}} \left[\begin{array}{l} \left(\sum_i \alpha^i a_i \sin\upsilon_i \cos\eta_i\right) \sin\upsilon_{i_0} \cos\eta_{i_0} \\ + \left(\sum_i \alpha^i a_i \sin\upsilon_i \sin\eta_i\right) \sin\upsilon_{i_0} \sin\eta_{i_0} \\ + \left(\sum_i \alpha^i a_i \cos\upsilon_i\right) \cos\upsilon_{i_0} \end{array} \right] \tag{D.133a}$$

$$\frac{d(\delta\mathfrak{r})}{d\upsilon_{i_0}} = \frac{\alpha_{i_0}}{\delta\mathfrak{r}} \left[\begin{array}{l} \left(\sum_i \alpha^i a_i \sin\upsilon_i \cos\eta_i\right) a^{i_0} \cos\upsilon_{i_0} \cos\eta_{i_0} \\ + \left(\sum_i \alpha^i a_i \sin\upsilon_i \sin\eta_i\right) a^{i_0} \cos\upsilon_{i_0} \sin\eta_{i_0} \\ - \left(\sum_i \alpha^i a_i \cos\upsilon_i\right) a^{i_0} \sin\upsilon_{i_0} \end{array} \right] \tag{D.133b}$$

$$\frac{d(\delta\mathfrak{r})}{d\eta_{i_0}} = \frac{\alpha^{i_0} a_{i_0} \sin\upsilon_{i_0}}{\delta\mathfrak{r}} \left[\begin{array}{l} - \left(\sum_i \alpha^i a_i \sin\upsilon_i \cos\eta_i\right) \sin\eta_{i_0} \\ + \left(\sum_i \alpha^i a_i \sin\upsilon_i \sin\eta_i\right) \cos\eta_{i_0} \end{array} \right] \tag{D.133c}$$

$$\frac{d\theta}{da_{i_0}} = \frac{\alpha^{i_0}}{\delta\mathfrak{r}} \left[\begin{array}{l} \left[\left(\sum_i \alpha^i a_i \sin\upsilon_i \cos\eta_i\right)^2 + \left(\sum_i \alpha^i a_i \sin\upsilon_i \sin\eta_i\right)^2\right]^{1/2} \cos\upsilon_{i_0} \\ - \cot\theta \sin\upsilon_{i_0} \left(\cos\eta_{i_0} + \sin\eta_{i_0}\right) \end{array} \right] \tag{D.134a}$$

$$\frac{d\theta}{d\upsilon_{i_0}} = \frac{-\alpha_{i_0} a_{i_0}}{\delta\mathfrak{r}} \left[\begin{array}{l} \left[\left(\sum_i \alpha^i a_i \sin\upsilon_i \cos\eta_i\right)^2 + \left(\sum_i \alpha^i a_i \sin\upsilon_i \sin\eta_i\right)^2\right]^{1/2} \sin\upsilon_{i_0} \\ + \cot\theta \cos\upsilon_{i_0} \left(\cos\eta_{i_0} + \sin\eta_{i_0}\right) \end{array} \right] \tag{D.134b}$$

$$\frac{d\theta}{d\eta_{i_0}} = \frac{\cot\theta \alpha^{i_0} a_{i_0} \sin\upsilon_{i_0}}{\delta\mathfrak{r}} \left(\sin\eta_{i_0} - \cos\eta_{i_0}\right) \tag{D.134c}$$

$$\begin{aligned} \frac{d\phi}{da_{i_0}} = & \frac{\alpha^{i_0} \sin\upsilon_{i_0}}{\left(\sum_i \alpha^i a_i \sin\upsilon_i \cos\eta_i\right)^2 + \left(\sum_i \alpha^i a_i \sin\upsilon_i \sin\eta_i\right)^2} \\ & \times \left[\sin\eta_{i_0} \sum_i \alpha^i a_i \sin\upsilon_i \cos\eta_i - \cos\eta_{i_0} \sum_i \alpha^i a_i \sin\upsilon_i \sin\eta_i\right] \end{aligned} \tag{D.135a}$$

$$\frac{d\phi}{d\upsilon_{i_0}} = \frac{\alpha^{i_0} a_{i_0} \cos \upsilon_{i_0}}{\left(\sum_i \alpha^i a_i \sin \upsilon_i \cos \eta_i\right)^2 + \left(\sum_i \alpha^i a_i \sin \upsilon_i \sin \eta_i\right)^2} \times \left[\sin \eta_{i_0} \sum_i \alpha^i a_i \sin \upsilon_i \cos \eta_i - \cos \eta_{i_0} \sum_i \alpha^i a_i \sin \upsilon_i \sin \eta_i\right] \tag{D.135b}$$

$$\frac{d\phi}{d\eta_{i_0}} = \frac{\alpha^{i_0} a_{i_0} \sin \upsilon_{i_0}}{\left(\sum_i \alpha^i a_i \sin \upsilon_i \cos \eta_i\right)^2 + \left(\sum_i \alpha^i a_i \sin \upsilon_i \sin \eta_i\right)^2} \times \left[\cos \eta_{i_0} \sum_i \alpha^i a_i \sin \upsilon_i \cos \eta_i + \sin \eta_{i_0} \sum_i \alpha^i a_i \sin \upsilon_i \sin \eta_i\right] \tag{D.135c}$$

D.3.3 Method Analysis

Model Accuracy

When developing the lattice summation technique there were three levels of "accuracy" that can be used. The first considers only the particles in the directions defining the far region. Then, a magnitude function was incorporated to account for all the particles in the region. And finally, a phase change factor was incorporated that accounted for the particles along the width of each region. In the 3D case the free light paths can also be made more accurate by accounting for the particle size. By only including the free light path if the incident wave angle are outside some solid angle of the designated lattice points, instead of using a delta function.

Divergent Terms

In certain cases we saw that logarithmic terms diverge when parameters are coordinated such that fields from each lattice point are in phase. This created a harmonic series. This arose from the assumption that the distance from each lattice point changes linearly. In reality, however this assumption does not hold and there is a small change in the distance. This causes a different phase change between adjacent points, and eliminates the divergence of the series.

Region Widths

In the 2D case, region boundaries are easy to determine. From the direction of interest, travel to the nearest included point in a clockwise and counter-clockwise direction, then divide each distance in half. The 3D case uses the same method, but is a bit more difficult to determine because of the extra degrees of freedom. To do this, first all included points were projected from the origin on to the unit cell. These are the blue points in Fig. D.19a Then the lattice vectors were projected on to each of the unit cell faces. This created a basis for each of the faces, as one of the lattice vectors is always perpendicular to a face. For points lying within a face of the unit cell, the nearest point in each of the cardinal directions (+1 and -1 times the basis vectors) was found, and the region distance divided in two. These are the red points in Fig. D.19a. Line segments were then placed at each of these points perpendicular to the direction from the point. Each of these line segments then intersect two others, forming a parallelogram which determines the region.

If a point lays on an edge, then two faces needed to be considered to determine the region. In this case, for each face a region is marked by taking the segments half ways to the nearest point in that face and the nearest points on the edge. This results in two regions, the union of which is taken as the region for the point. Finally, if the point lies on a corner, the nearest point on each of the three edges are used as references. This results in three regions, the union of which is taken. Each of these type of regions are marked in Fig. D.19a by the green area.

Finally, notice that in the summation technique the region width always appears as $\Delta\phi\Delta\theta$, indicating that what is important is the steradians. This is also evident in the derivations, as the reason the region width is important is to account for the regions area at different lengths from the origin. So, the

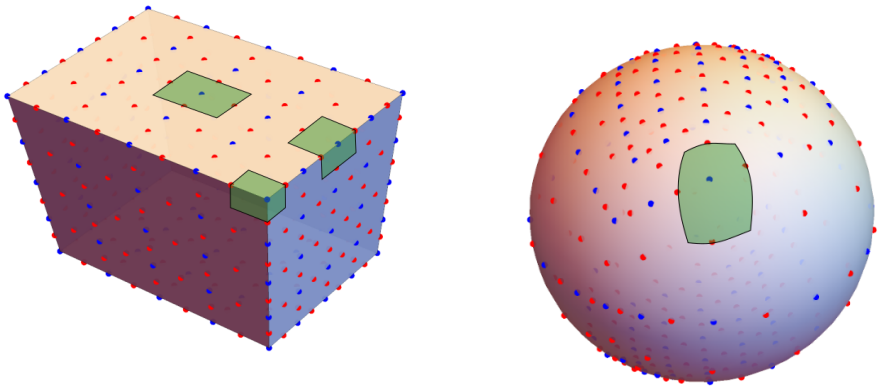

(a) (b)

Figure D.19: (a) The included lattice points projected on to the unit cell. The actual lattice points are in blue, the region boundaries are in red, and examples of different associated regions are shaded in green. (b) The lattice points, boundary points, and a region projected on to the unit sphere.

regions widths are obtained by projecting the regions on to the unit sphere and measuring the steradians covered, as seen in Fig. D.19b.

Bibliography

[1] Yinan Zhang Nicholas Stones Baohua Jia Shanhui Fan Min Gu. "Towards ultra-thin plasmonic silicon wafer solar cells with minimized efficiency loss". In: *Scientific Reports* (May 13, 2014). DOI: 10.1038/srep04939.

[2] Arno Smets. *Light Trapping*. University Lecture. 2015.

[3] Iddo Diukman Meir Orenstein. "How front side plasmonic nanostructures enhance solar cell efficiency". In: *Solar Energy Materials & Solar Cells* (May 12, 2011). DOI: 10.1016/j.solmat.2011.05.019.

[4] Arno Smets Klaus Jäger Olindo Isabella Renè van Swaaij Miro Zeman. *Solar Energy: The Physics and Engineering of Photovoltaic Conversion Technologies and Systems*. 2016.

[5] Hairen Tan Efthymia Psomadaki Olindo Isabella Marinus Fischer Pavel Babal Ravi Vasudevan Miro Zeman Arno H. M. Smets. "Micro-textures for efficient light trapping and improved electrical performance in thin-film nanocrystalline silicon solar cells". In: *Applied Physics Letters* (Oct. 23, 2013). DOI: 10.1063/1.4826639.

[6] Olaf Berger Daniel Inns Armin Aberle. "Commercial white paint as a back surface reflector for thin-film solar cells". In: *Solar Energy Materials & Solar Cells* (May 8, 2007). DOI: 10.1016/j.solmat.2007.04.008.

[7] *Towards lambertian internal light scattering in solar cells using coupled plasmonic and dielectric nanoparticles as back reflector*. IEEE, June 16, 2013. DOI: 10.1109/PVSC.2013.6744092.

[8] Harry A. Atwater Albert Polman. "Plasmonics for improved photovoltaic devices". In: *Nature Materials* (Feb. 19, 2010). DOI: 10.1038/nmat2629.

[9] T.L. Temple G.D.K. Mahanama H.S. Reehal D.M. Bagnall. "Influence of localized surface plasmon excitation in silver nanoparticles on the performance of silicon solar cells". In: *Solar Energy Materials & Solar Cells* (July 22, 2009). DOI: 10.1016/j.solmat.2009.07.014.

[10] P. Mandal S. Sharma. "Progress in plasmonic solar cell efficiency improvement: A status review". In: *Renewable and Sustainable Energy Reviews* (July 21, 2016). DOI: 10.1016/j.rser.2016.07.031.

[11] Venu Gopal Achanta. "Plasmonic quasicrystals". In: *Progress in Quantum Electronics* (Dec. 13, 2014). DOI: 10.1016/j.pquantelec.2014.12.002.

[12] S. Pillai M.A. Green. "Plasmonics for photovoltaic applications". In: *Solar Energy Materials & Solar Cells* (Mar. 21, 2010). DOI: 10.1016/j.solmat.2010.02.046.

[13] Alessio Paris Alessandro Vaccari Antonino Calá Lesina Enrico Serra Lucia Calliari. "Plasmonic Scattering by Metal Nanoparticles for Solar Cells". In: *Plasmonics* (Mar. 8, 2012). DOI: 10.1007/s11468-012-9338-4.

[14] Sharayanan. URL: https://commons.wikimedia.org/wiki/File:Mie_scattering.svg (visited on 10/21/2016).

[15] Hairen Tan Rudi Santbergen Arno H. M. Smets Miro Zeman. "Plasmonic Light Trapping in Thin-film Silicon Solar Cells with Improved Self-Assembled Silver Nanoparticles". In: *Nanoletters* (June 27, 2012). DOI: 10.1021/nl301521z.

[16] Rudi Santbergen Hairen Tan Miro Zeman Arno H. M. Smets. "Enhancing the driving field for plasmonic nanoparticles in thin-film solar cells". In: *Optics Express* (June 30, 2014). DOI: 10.1364/OE.22.0A1023.

[17] Z. Starowicz G. Kulesza-Matlak M. Lipiński. "Optimization Studies on Enhanced Absorption in Thin Silicon Solar Cell by Plasmonic Silver Nanoparticles for the Front Side Configuration". In: *Plasmonics* (Apr. 15, 2015). DOI: 10.1007/s11468-015-9996-0.

[18] Constantine A. Balanais. *Antenna Theory: Analysis and Design*. John Wiley & Sons, 2005. ISBN: 0-471-66782-X.

[19] *Generalized Ray Interpretation of Floquet Modes for Two-Dimensions, infinite Phased Array Antennas*. International Symposium of Electromagnetic Theory. 2013.

[20] Philip Laven. *MiePlot*. URL: http://www.philiplaven.com/mieplot.htm (visited on 05/10/2017).

[21] *An Introduction to HFSS: Fundamental Principles, Concepts, and Use*. English. Version ANSYS Electromagnetics Suite 17.0. ANSYS Inc. 2009.

[22] R.W. Christy P.B. Johnson. "Optical Constants of the Noble Metals". In: *Physical Review B* (). DOI: 10.1103/PhysRevB.6.4370.

[23] Celine Pahud Olindo Isabella Ali Naqavi Franz-Josef Haug Miro Zeman Hans Peter Herzig Cristophe Ballif. "Plasmonic silicon solar cells: impact of material quality and geometry". In: *Optics Express* (July 16, 2013). DOI: 10.1364/OE.21.00A786.

[24] Craig Bohren Donald Huffman. *Absorption and Scattering of Light by Small Particles*. John Wiley & Sons, Inc., 1983. ISBN: 978-0-471-29340-8.

[25] N. J. A. Sloane. *Sequence A001970*. URL: https://oeis.org/A175549 (visited on 10/15/2017).

[26] Gerald Kreindl Thomas Glinsner Ron Miller. "Next-generation lithography: Making a good impression". In: *Nature Photonics* (Jan. 2010).

[27] R. Santbergen T. L. Temple R. Liang A. H. M. Smets R. A. C. M. M. van Swaaij M. Zeman. "Application of plasmonic silver island films in thin-film silicon solar cells". In: *Journal of Optics* (Jan. 12, 2012). DOI: 10.1088/2040-8978/14/2/024010.

[28] Hairen Tan. *Materials and Light Management for High Efficiency Thin-Film Silicon Solar Cells*. 2015.

[29] Hairen Tan Laura Sivec Baojie Yan Rudi Santbergen Miro Zeman Arno H.M. Smets. "Improved light trapping in microcrystalline silicon solar cells by plasmonic back reflector with broad angular scattering and low parasitic absorption". In: *Applied Physics Letters* (Apr. 18, 2013). DOI: 10.1063/1.4802451.

[30] Stefan A. Maier. *Plasmonics: Fundamentals and Applications*. Springer Science+Business LLC., 2007. ISBN: 978-0387-33150-8.

[31] Jan Homann. *Complex Polylog*. URL: https://commons.wikimedia.org/wiki/File:Complex_polylog2.jpg (visited on 08/22/2017).

[32] Jan Homann. *Complex Polylog*. URL: https://commons.wikimedia.org/wiki/File:Complex_polylog3.jpg (visited on 08/22/2017).

[33] Brian Kahn. "Earth's CO_2 Passes the 400 PPM Threshold — Maybe Permanently". In: *Scientific American* (Sept. 27, 2016). URL: http://www.scientificamerican.com/article/earth-s-co2-passes-the-400-ppm-threshold-maybe-permanently/ (visited on 10/05/2016).

[34] Rob Monroe. *Note on Reaching the Annual Low Point*. Scripps Institute of Oceanography. Sept. 23, 2016. URL: https://scripps.ucsd.edu/programs/keelingcurve/2016/09/23/note-on-reaching-the-annual-low-point/ (visited on 10/05/2016).

[35] Robert Fares. "The Price of Solar Is Declining to Unprecedented Lows". In: *Scientific American* (Aug. 27, 2016). URL: https://blogs.scientificamerican.com/plugged-in/the-price-of-solar-is-declining-to-unprecedented-lows/ (visited on 10/10/2016).

[36] *The Economics of Grid Defection: When and Where Distributed Solar Generation Plus Storage Competes with Traditional Utility Service*. Feb. 2014.

[37] SCU, ed. *Science for Environment Policy: What are Barriers to Solar Energy Adoption?* European Commission, Jan. 14, 2016.

[38] *Photovoltaic Report*. Fraunhofer Institute for Solar Energy Systems, June 6, 2016. URL: https://www.ise.fraunhofer.de/de/downloads/pdf-files/aktuelles/photovoltaics-report-in-englischer-sprache.pdf (visited on 10/13/2016).

[39] Galen Barbose Naïm Darghouth. "Tracking the Sun IX: The Installed Price of Residential and Non-Residential Photovoltaic Systems in the United States". In: (Aug. 2016).

[40] *ANSYS Electronics Desktop Online Help*. English. Version ANSYS Electromagnetics Suite 17.0. ANSYS Inc. Dec. 2015.